

Understanding Rock-Fluid Interactions

in

Tight Oil Formations

by

Ali Habibi

A thesis submitted in partial fulfillment of the requirements for the degree of

Doctor of Philosophy

in

Petroleum Engineering

Department of Civil and Environmental Engineering

University of Alberta

© Ali Habibi, 2018

Abstract

Combination of horizontal drilling and hydraulic fracturing has led to improved oil recovery from unconventional resources over the past decade. In spite of the huge amount of oil in-place, the primary oil recovery factor is very low (3-10 % of initial oil in-place) in unconventional resources. This is due to ultra-low permeability, complex pore structure, and oil-wet (or mixed-wet) behavior of tight formations. To guarantee economically long term oil production from tight formations, enhanced oil recovery (EOR) techniques should be implemented as soon as fracturing operations start. The first step to develop any EOR technique is to understand the wettability of tight formations. The next step is to investigate interactions among reservoir fluids, rock surface, and fracturing fluids.

This study aims at understanding the (i) wettability of Montney (MT) tight rocks at core-scale and pore-scale and (ii) mechanisms responsible for oil displacement from these rocks using CO₂ and surfactant solutions. First, spontaneous imbibition tests and contact angle measurements are conducted to evaluate the wettability of and oil recovery from the MT tight rocks. Next, the Derjaquin, Landau, Verwey, and Overbeek (DLVO) theory is applied to investigate how mineral heterogeneity affects wettability of the MT rocks. Finally, two EOR techniques are used to investigate further oil recovery from the MT rocks after water spontaneous imbibition. These techniques use CO₂ and non-ionic octylphenol ethoxylate (OPE) surfactant solutions. Different experiments are designed to study the rock-fluid interactions at bulk-phase and core-scale conditions.

The spontaneous imbibition results show that water can imbibe into the oil-saturated core plugs and produce oil up to 45% of initial oil in-place while oil cannot imbibe into the water-saturated core plugs. These observations suggest the water-wet behavior for the oil (or water)-saturated core plugs. The water contact angles calculated (using DLVO theory) for the solid surface/water/oil system confirm the water-wet behavior of the core plugs. Disjoining pressures calculated for this system also show that water film covering the rock surface is stable.

Investigating CO₂-oil interactions at bulk-phase conditions shows high oil swelling factor (up to 1.390) at reservoir conditions (2000 psig and 50C). The results of cyclic CO₂ tests also show that oil recovery factor from oil-saturated core plugs is high (up to 66% of original oil in-place). The proposed mechanisms for oil production are: 1) oil swelling as a result of CO₂ dissolution into the oil, and 2) evaporation of oil components and expelling out of core plugs.

Investigating the surfactant solutions-oil interactions at bulk-phase and core-scale conditions shows that mixed non-ionic octylphenol ethoxylate (OPE) surfactants can spontaneously imbibe into the oil-saturated core plugs. The final oil recovery factor from mixed surfactant solutions is higher than that for reference case (water without surfactants). In addition to (i) decreasing IFTs for mixed surfactant solutions and (ii) preferentially wetting the rock surface by mixed surfactant solutions, additional mechanisms are responsible for improved oil recovery. The higher oil recovery factor for the mixed solutions can be explained by (i) improved adsorption tendency of mixed

surfactants on the rock surface due to the existence of OPE15 (soluble in oil), (ii) formation of small micelles (100-200 nm) in mixed solutions. The existence of small mixed micelles facilitates surfactant imbibition into narrow pores ($P_{\text{throat}} < 100 \text{ nm}$) for oil expulsion.

Preface

A version of Chapter 2 is published as Habibi, A., Binazadeh, M., Dehghanpour, H., Bryan, D., Uswak, G. (2016). "Advances in Understanding Wettability of Tight Oil Formations: A Montney Case Study", *SPE Reservoir Evaluation and Engineering*, 19(4), 583-603. I was responsible for conducting experiments, analyzing the experimental data, writing and editing the paper. Mojtaba Binazadeh was responsible for reviewing and editing the paper. Donald Bryan and Gordon Uswak were responsible for securing company approvals for publishing the paper. Hassan Dehghanpour was responsible for supervising the research, reviewing the paper, and providing technical feedbacks.

A version of Chapter 3 is published as Habibi, A., and Dehghanpour. H. (2018). "Wetting Behavior of Tight Rocks: From Core-scale to Pore-scale", *Water Resources Research*, 54, 9162-9186. I was responsible for conducting experiments, analyzing the experimental data, writing MATLAB codes, writing and editing the paper. Hassan Dehghanpour was responsible for reviewing the paper and providing technical feedbacks.

A version of Chapter 4 is published as Habibi, A., Yassin, M. R., Dehghanpour, H., Bryan, D. (2017). "Experimental Investigation of CO₂-Oil Interactions in Tight Rocks: A Montney Case Study", *Fuel*, 203, 853-867. I was responsible for conducting experiments, analyzing the experimental data, writing and editing the paper. Mahmood Reza Yassin was responsible for conducting the visualization of CO₂-oil interactions in the visual cell. Hassan Dehghanpour was responsible for reviewing the paper and providing technical feedbacks. Donald Bryan was responsible for securing company approvals for publication of the paper.

A version of Chapter 5 is submitted as Habibi, A., Esparza, Y., Boluk, Y., Dehghanpour. H. "Interfacial Interactions of Mixed Nonionic Surfactants in Nano-scale Pores", *Fuel* [Submitted: November 2018]. I was responsible for conducting experiments, analyzing the experimental data, writing and editing the paper. Yussef Esparza was responsible for conducting the isothermal titration calorimetry tests. Hassan Dehghanpour and Yaman Boluk were responsible for reviewing the paper and providing technical feedbacks.

To Fatemeh

Acknowledgements

I wish to express my sincere thanks to my supervisor, Dr. Hassan Dehghanpour, whose ideas, feedbacks, and mentorship provided impetus for this research study. Your energetic attitude and organized thoughts helped me develop a systematic way of thinking about and approaching to problems. I would like to thank Dr. Yaman Boluk for providing me the opportunity to collaborate with his group. I am also thankful to my examining committee, Dr. Kishore K. Mohanty, Dr. Qi Liu, Dr. Juliana Leung, and Dr. Japan Trivedi for their insightful advice.

I would like to thank my parents for teaching me how to be resilient in tough situations. I never forget your gracious support in my life. God bless you.

I would like to express my utmost gratitude to my beloved wife, Fatemeh Jafari, for her infinite patience and constant love. Without your support, it would be impossible for me to accomplish what I have today. Thanks to my beloved little son, Sajjad, for accompanying me on this journey.

I would like to appreciate my past and present colleagues (Obinna Ezulike, Yingkun Fu, Yanmin Xu, Ebrahim Ghanbari, Mahdie Mojarrad, Ashkan Zolfaghari, Mahmood Reza Yassin, Momotaj Begum, Ali Javaheri, Mingxiang Xu, Sara Eghbali, Hamidreza Yarveicy, and Yue Shi) for their insightful contributions and fruitful discussions.

I am deeply thankful to Mohammad Hossein Bitarfan, Zahra Sohrabi, Fahimeh Behboudi, and Behnam Khorshidi for their support and friendship over the course of my PhD program.

I am grateful to Cenovus Energy Inc., Flotek Chemistry, Natural Sciences and Engineering Research Council of Canada (NSERC) and Natural Resources Canada (NRCan) for supporting this study.

Table of Contents

Chapter 1 General Introduction	1
1.1. Overview	1
1.1.1. Tight Oil Formation	1
1.1.2. Hydraulic Fracturing	3
1.1.3. Fracturing Fluid	4
1.1.4. Montney Formation	6
1.2. Research Motivation	6
1.3. Research Objectives	7
1.4. Organization of Thesis	8
Chapter 2 Understanding Wettability of Tight Oil Formations: A Montney Case Study	10
2.1. Introduction	10
2.2. Materials	12
2.2.1. Core Properties	12
2.2.2. Fluid Properties	19
2.3. Methodology	19
2.3.1. Spontaneous Imbibition on Fresh Core Plugs	19
2.3.2. Spontaneous Imbibition of Brine (or Oil) Into Oil(or Brine)-Saturated Samples	21
2.3.3. Contact Angle Measurement	21
2.3.4. Surface Analysis and Elemental Mapping	22
2.4. Results and Discussions	23
2.4.1. Spontaneous Imbibition of Brine and Oil in Fresh Plugs	23
2.4.2. SEM/EDS Analysis	27
2.4.3. Contact Angle Measurement	32
2.4.4. Spontaneous Imbibition of Brine Into Oil-Saturated Samples	34
2.4.5. Scaling Groups	38
2.4.6. Effect of Layering on Oil Production	40

2.5.	Proposed Laboratory Procedure for Wettability Evaluation of Tight Rocks	41
2.6.	Significance of Results for Field Applications.....	42
2.7.	Conclusions.....	43
Chapter 3 Wetting Behavior of Tight Rocks: From Core-Scale to Pore-Scale.....		45
3.1.	Introduction	45
3.2.	Review of Previous Spontaneous Imbibition and Contact Angle Results	49
3.3.	DLVO Theory and Wettability	50
3.4.	Materials and Methods	54
3.4.1.	Core Properties.....	54
3.4.2.	Pure Minerals.....	54
3.4.3.	Fluid Properties.....	55
3.5.	Methodology.....	55
3.5.1.	Step1: Visualization of Rock Surface	55
3.5.2.	Step2: Implementing the DLVO Theory for the Wettability Evaluation	56
3.5.3.	Step3: AFM Analysis.....	57
3.6.	Results and Discussion	59
3.6.1.	Step1: Rock Surface Analysis	59
3.6.2.	Step 2: DLVO Theory and Wettability.....	66
3.6.3.	Step 3: AFM Analysis.....	76
3.7.	Conclusions.....	82
Chapter 4 CO ₂ -Oil Interactions in Tight Rocks: An Experimental Study		84
4.1.	Introduction	84
4.2.	Materials.....	86
4.2.1.	Core Properties.....	86
4.2.2.	Fluid Properties.....	86
4.3.	Methodology.....	87
4.3.1.	CCE Tests	87

4.3.2. Visualization of CO ₂ - Oil Interactions in Visual Cell	90
4.3.3. CO ₂ Soaking Experiments Using Oil-saturated Core Plugs	91
4.3.4. CO ₂ Cyclic Process.....	92
4.4. Results and Discussions	95
4.4.1. CCE Tests	95
4.4.2. Visualization of CO ₂ -Oil and N ₂ -Oil Interactions in the Visual Cell	100
4.4.3. CO ₂ Soaking Experiments Using Oil-Saturated Core Plugs	108
4.4.4. Cyclic CO ₂ Process.....	112
4.5. Conclusions.....	116
Chapter 5 Imbibition Oil Recovery From Tight Rocks by Non-ionic Surfactant Systems	118
5.1. Introduction	118
5.2. Materials and Methods	120
5.2.1. Materials	120
5.2.2. Methods.....	122
5.3. Results and Discussions	125
5.3.1. Surface Tension and Interfacial Tension	125
5.3.2. Micelle Size Distribution	129
5.3.3. Isothermal Titration Calorimetry	130
5.3.4. Wettability Evaluation.....	133
5.3.5. Imbibition Oil-recovery Test	139
5.4. Conclusions.....	143
Chapter 6 Conclusions and Recommendations	145
6.1. Conclusions.....	145
6.1.1. Wettability and Surface Forces	145
6.1.2. CO ₂ -Oil Interactions	146
6.1.3. OPE Surfactant Solutions-Oil Interactions.....	146
6.2. Significance for the Field Application	146

6.3. Recommendations	147
References	149
Appendix A: SEM Images of Layered Core Plugs	169
Appendix B: Surface Forces.....	172
Appendix C: Surface Tension of Surfactant Solutions	183

List of Tables

Table 1.1. Properties of fracturing fluid chemical additive[12].	5
Table 2.1. Petrophysical properties of well 1 and well 2-MT Formation.....	14
Table 2.2. Physical properties of reservoir brine.	19
Table 2.3. Physical properties of crude oil.	19
Table 2.4. Comparison of oil and brine capillary pressure ratio obtained from imbibition data and Young-Laplace equation.	26
Table 2.5. Air/ brine and air/ oil contact angle for fresh, oil-saturated and brine-saturated samples.	33
Table 2.6. Inverse bond number for samples of well 1 and well 2.	39
Table 3.1. Petrophysical properties of the core plugs.....	54
Table 3.2. Mineral composition of the core plugs. Heavy minerals can be rutile, anatase, ankerite, rhodochrosite, and fluorapatite.	54
Table 3.3. Ion composition of the saline reservoir brine.	55
Table 3.4. Hamaker constants of materials used for calculation of van der Waals forces [114, 146, 147].....	66
Table 3.5. Oil Hamaker constants used for calculation of van der Waals forces [114, 146].....	66
Table 3.6. Calculated contact angles using Eq. 11 for solid surface/air/water system.	67
Table 3.7. Zeta potential (ζ_i) values measured for the solid powder/water and water/oil pairs. 73	
Table 3.8. The water contact angles calculated for solid surface/water/oil systems using Eq. 11.	76
Table 3.9. Roughness analysis of the minerals in dry conditions	79
Table 3.10. The adhesion forces measured between the tip of the cantilever and the pure quartz, pure calcite, and the MT thin section.	81
Table 4.1. Petrophysical properties of the Montney core plugs. The diameter of core plugs is 3.8 cm.....	86
Table 4.2. Physiochemical properties of the Montney crude oil.....	87
Table 4.3. Compositional analysis of the Montney crude oil.....	87
Table 4.4. CO ₂ mole% and temperature of CO ₂ -oil mixtures in CCE tests.	89
Table 4.5. Measured bubble-point pressure and swelling factor obtained from CCE tests	99
Table 4.6. Oil recovery factor for soaking experiments with CO ₂ . 7.9 moles of CO ₂ is required for pressurizing the visual cell to 2000 psig at 50°C.	109

Table 4.7. Normalized injected volume of CO ₂ for cyclic CO ₂ process conducted at 1000 psig/21°C and 1400 psig/50°C.	114
Table 5.1. Petrophysical properties of the MT core plugs	120
Table 5.2. TOC content and mineral composition of the core plugs	121
Table 5.3. Properties of tested octylphenol ethoxylate surfactants at 25°C [277].....	121
Table 5.4. Mean size of micelles formed in the mixed surfactant solutions.....	130
Table 5.5. Oil contact angles measured for the mixed solutions at different concentrations....	135
Table 5.6. Wetting parameters calculated for the OPE70 and OPE100 solutions prepared in 1,000 ppm NaCl solutions.	137
Table 5.7. Calculated wetting parameters for mixed surfactant solutions	139

List of Figures

Figure 1.1. Major tight oil formations located in Canada and the US [4].....	2
Figure 1.2. Historical oil production in the US through 2012 and projection of oil production through 2040. 1 million barrels (oil)= $158,987 \text{ m}^3$ [5].	2
Figure 1.3. Schematic geological section of conventional, tight, and shale gas and oil resources [6].....	3
Figure 1.4. Schematic view of fractures created during hydraulic fracturing in a horizontal well [9].....	3
Figure 1.5. Advantages and disadvantages of fracturing with (a) water and (b) CO_2	4
Figure 1.6. An example of aqueous fracturing fluid formulation [11].	5
Figure 1.7. The Montney Formation located in the western Canadian sedimentary basin[14]....	6
Figure 2.1. Approximate location of core samples on the well logs for (a) well 1 and (b) well 2.	13
Figure 2.2. Porosity distribution for well 1 and well 2 drilled in the MT formation	15
Figure 2.3. Rock mineralogy of samples from: (a) well 1 and (b) well 2. Quartz and carbonates are the main components of samples from both wells.	17
Figure 2.4. Clay fraction of total clay composition for samples from: (a) well 1 and (b) well 2. Total clay of samples from well 1 is composed of illite/mica, illite/smectite and kaolinite. Total clay of samples from well 2 is composed of illite/smectite and kaolinite.	17
Figure 2.5. Thin sections of siltstone samples taken from well 1 at: (a) 1568.89 m, (b) 1571.89 m, (c) 1578.26 and (d) 1585.18 m. Blue, white, grey, yellow and black are pores, quartz, carbonates, feldspars and organic matter/pyrite, respectively.	18
Figure 2.6. Thin sections of siltstone samples taken from well 2 at: (a) 2380.24 m, (b) 2384.87 m, (c) 2390.9 m and (d) 2402.5 m.	18
Figure 2.7. Schematic view of the experimental set-up used for spontaneous imbibition experiments on fresh samples.	20
Figure 2.8. Counter-current imbibition cells used for soaking of (a) brine-saturated and (b) oil-saturated samples in oil and brine, respectively.	21
Figure 2.9. Normalized imbibed volume of (a) Brine (Well 1), (b) Oil (Well 1), (c) Brine (Well 2) and Oil (Well 2) in fresh samples.....	23
Figure 2.10. Wettability index for samples from (a) well 1 and (b) well 2. Oil and brine wettability index are close 0.5 for most the samples.....	24
Figure 2.11. Oil/brine capillary pressure ratio from Young-Laplace equation versus oil/brine capillary pressure ratio from the imbibition data.	27

Figure 2.12. Sample 7 (depth of 1578.26 m) from well 1 under (a) SE beam, (b) BSE beam and (c) EDS analysis. Presence of Fe and S in part (c) shows the presence of pyrite in the sample. Pyrite is shown in part (b) by brighter spots.....	29
Figure 2.13. Sample 9 (depth of 1583.79 m) from well 1 under (a) SE beam, (b) BSE beam and (c) EDS analysis. The big chunk of pure carbon is expected to be organic matter.	30
Figure 2.14. Sample 4 (depth of 2388.75 m) from well 2 under (a) SE beam, (b) BSE beam and (c) EDS analysis. The pure carbon in subplot (c) suggests the presence of organic matter in the sample.	31
Figure 2.15. Complex pore wall of a random MT sample. Pores are surrounded with quartz, carbonates and feldspars. Quartz and feldspars tend to be water-wet while carbonates are expected to be oil-wet.	32
Figure 2.16. Contact angle of (a) brine/air and (b) oil/air on the surface of fresh sample. The brine droplet partially wets the rock surface while the oil droplet completely spreads on rock surface.....	33
Figure 2.17. Liquid/Liquid Contact angle of (a) oil and (b) brine. Brine-saturated sample is strongly oil repellent and water-wet.	34
Figure 2.18. Contact angle of the brine droplet equilibrated on the surface of the core immersed in oil for (a) well 1 and (b) well 2.....	34
Figure 2.19. Oil-saturated samples immersed in brine (a) at the beginning of the experiment and (b) 30 days after starting the experiment	35
Figure 2.20. Oil droplets are expelled out of the rock due to spontaneous imbibition of brine into the oil-saturated samples. Oil is produced from specific layers in some samples.	36
Figure 2.21. Estimated oil recovery during spontaneous imbibition versus time for samples from (a) well 1 and (b) well 2	36
Figure 2.22. Brine-saturated samples immersed in oil (a) at the beginning of the experiment and (b) 30 days after starting the experiment	37
Figure 2.23. Distribution of oil and water inside cores where spontaneous counter-current imbibition is driven by (a) capillary forces; (b) capillary-gravity forces and (c) gravity forces.....	40
Figure 2.24. Normalized oil recovery versus dimensionless time given by Ma et al. [63] for samples from (a) well 1 and (b) well 2	40
Figure 2.25. Cross section of a layered MT sample. Layer 1 contains more quartz, feldspars; layer 2 contains more pyrite, quartz, feldspars; layer 3 contains more quartz, feldspars, and carbonates	41

Figure 3.1. (a) Contact region between two fluids and a solid surface. The extrapolated meniscus makes the macroscopic contact angle with the solid surface. (b) Profile of meniscus and thin film in transition zone (Modified after [81]).	46
Figure 3.2. The study area in the Montney Formation located in the western Canadian sedimentary basin (modified after [109]).	49
Figure 3.3. Film of fluid 1 covers the rock surface in the presence of fluid 2.	51
Figure 3.4. A typical force-distance plot measured with AFM	58
Figure 3.5. The thin sections prepared from the core plugs drilled at (a) 1571.89 m depth under plane polarized light (left) and cross polarized light (right), (b) 1578.26 m depth under plane polarized light (left) and cross polarized light (right), and (c) 1578.26 m depth under plane polarized light (left) and cross polarized light (right). Images presented in parts (b) and (c) are from two different spots of the same thin section sample. Blue areas shown under plane polarized light represent the pores. Areas surrounded by red, orange, and green dashed lines are quartz or feldspar, carbonates and feldspars, respectively.	61
Figure 3.6. SEM images from core plug 2 (depth of 1578.26 m). “Q”, “C”, “F”, “Ca” and “OG” stand for quartz, clay, feldspars, carbonates and organic matter/HR, respectively. Three areas are magnified to show the minerals surrounding the pores.....	64
Figure 3.7. (a) An SEM image taken from core plug 2, (b) magnified view of mica located in the rock sample, and (c) fibrous illite accumulated on the mica surface.	64
Figure 3.8. Pore-throat size distribution of core plug 2 (depth of 1758.26 m) measured by MICP method. 23%, 55%, and 15% of pores have the throat radius smaller than 100 nm, in the range of 100-1000 nm, and larger than 1000 nm, respectively.	65
Figure 3.9. Calculated disjoining pressure versus separation distance for (a) pure calcite, (b) clays, (c) HR, (d) pure quartz, and (e) the MT rock sample.	69
Figure 3.10. Calculated disjoining pressure versus separation distance for (a) water imbibition into the dry core plugs and (b) oil imbibition into the dry core plugs when $A_{H(oil)} = 4.5 \times 10^{-20}$ J, and (c) oil imbibition into the dry core plugs when $A_{H(oil)} = 9.0 \times 10^{-20}$ J.....	70
Figure 3.11. The total disjoining pressure for the solid surface/oil/water system when $A_{H(oil)} = 4.5 \times 10^{-20}$ J.....	72
Figure 3.12. The total disjoining pressure for the solid surface/oil/water system when $A_{H(oil)} = 9.0 \times 10^{-20}$ J.....	72
Figure 3.13. The total disjoining pressure-distance profile for the solid surface/water/oil when $A_{H(oil)} = 4.5 \times 10^{-20}$ J.	75

Figure 3.14. The total disjoining pressure-distance profile for the solid surface/water/oil when $A_{H(oil)} = 9.0 \times 10^{-20}$ J.....	75
Figure 3.15. (a) A light image of quartz slide and a tip contacting the surface, (b) an AFM height mode (forward) image taken from the pure quartz slide, (c) 3D surface topography of the quartz slide, and (d) the force-distance profile for a point marked on the quartz slide.	78
Figure 3.16. (a) A light image of the calcite crystal, (b) 3D surface topography of the calcite crystal, (c) marked points on a pure calcite crystal used for force measurement, and (d) a force-distance profile for a point marked on the calcite surface.	80
Figure 3.17. (a) A light image of the Montney thin section, (b) 3D surface topography of the Montney thin section, (c) marked points on the thin section used for force measurement, and (d) a force-distance profile for a point marked on the tin section.	81
Figure 4.1. The experiments are divided into bulk-phase characterization and flow in porous media.....	86
Figure 4.2. Schematic of the PVT cell.	90
Figure 4.3. Custom-designed visual cell and its components. The diameter of sight glass is 4.8 cm.....	91
Figure 4.4. Schematic view of the cyclic CO_2 set-up.....	94
Figure 4.5. Densities of crude oil measured using the PVT cell at different temperatures and pressures.....	96
Figure 4.6. Comparison between the measured and calculated oil density.....	96
Figure 4.7. Measured relative volume versus pressure at three different concentrations of CO_2 in the mixture at 50°C.....	98
Figure 4.8. Measured relative volume at different temperatures for CO_2 mole % of (a) 58.82 and (b) 71.06.	98
Figure 4.9. Mass fraction of original oil and CO_2 -oil mixtures measured by simulated distillation column.	100
Figure 4.10. CO_2 -oil interface at reservoir temperature (50°C). (a) There is 235 cc (0.78 mole) of oil in the cell when there is no CO_2 in the cell at atmospheric pressure ($P=0$ psig). (b) We inject 6.4 moles of CO_2 to increase the pressure from 0 psig to 2000 psig and then close the CO_2 injection valve. Oil EF is 1.23 at 2000 psig. Rapid expansion of oil after introducing the CO_2 into the visual cell is explained by natural convection mechanism. (c) Due to further CO_2 dissolution into the oil phase, pressure of visual cell declines from 2000 psig to 1707 psig after 5 hours. Rapid pressure decline during 5 hours is explained by convection mechanism. Oil EF is	

1.32 at 1707 psig. The dashed line shows the level of CO ₂ -oil interface at different conditions.	102
Figure 4.11. Pressure profile of CO ₂ -oil mixture at 50°C. The pressure of visual cell declines from 2000 psig to 1707 psig after 5 hours. Rapid pressure decline during 5 hours is explained by convection mechanism.....	103
Figure 4.12. N ₂ -oil interface at reservoir temperature (50°C) and different pressures. (a) There is 295 cc (0.98 mole) of oil in the cell before injecting N ₂ at atmospheric pressure (P=0 psig) (b) 1.46 mole of N ₂ is injected to increase the atmospheric pressure to 2000 psig. Oil EF is equal to 1.0 at this pressure. (c) We inject 0.65 mole of N ₂ to increase the pressure from 1863 psig to 3000 psig. Oil EF is equal to 1.0. The dashed line shows the level of N ₂ -oil interface at different conditions.....	105
Figure 4.13. (a) Solid precipitates deposited at the CO ₂ -oil interface at 1707 psig and 50°C. Brown area below CO ₂ -oil interface is mainly a mixture of oil and CO ₂ and black dots highlighted by circles are solid precipitates attached on the sight glass. (b) Solid precipitates mixed with oil deposited at the bottom of visual cell after finishing the CO ₂ -oil test.....	106
Figure 4.14. (a) SE image and (b) the results of EDS analysis on the solid precipitates. Black and white areas represent the highest and lowest concentrations of each element, respectively.	107
Figure 4.15. Conducting IP-143 test for measuring asphaltene content. The asphaltene content of oil samples before and after contact with CO ₂ are 2.2 and 2.1 wt.%, respectively. The asphaltene content of solid precipitates at the bottom of the visual cell (Figure 4.13) is 14.0 wt.%.....	107
Figure 4.16. Side view of S1 surface soaked in CO ₂ at 2000 psig and 50°C at (a) initial state, (b) after 1 day (c) after 3 days, and (d) after 5 days.....	109
Figure 4.17. Oil droplets condensed on the top surface of the cell during soaking of S1 core sample in CO ₂	110
Figure 4.18. Pressure profiles for cyclic CO ₂ tests conducted at 1400 psig/50°C and 1000 psig/21°C.....	113
Figure 4.19. Oil production profile for cyclic CO ₂ processes at 1000 psig/21°C and 1400 psig/50°C.....	115
Figure 4.20. Mass fraction of the original oil and the oil produced from the first cycle measured by simulated distillation column.....	116
Figure 5.1. Surface tensions of mixed solutions versus surfactant concentrations: (a) OPE15-OPE70 and (b) OPE15-OPE100 with 1:1 mixing ratio.....	126

Figure 5.2. IFT measured between the oil and OPE70 solutions versus surfactant concentration	127
Figure 5.3. IFT measured between the oil and OPE100 solutions versus surfactant concentration	127
Figure 5.4. IFT values measured between the oil and (a) OPE15-OPE70 and (b) OPE15-OPE100 solutions with 1:1 mixing ratio versus surfactant concentration.	128
Figure 5.5. Mean size of micelles formed in the (a) OPE70 and (b) OPE100 surfactant solutions versus NaCl concentration.	130
Figure 5.6. ITC curves of (a) OPE70, (b) OPE100, (c) OPE15-OPE70, and (d) OPE15-OPE100 solutions titrated into 1,000 ppm NaCl solution with and without 1% rock particles.	132
Figure 5.7. Liquid/liquid contact angle of an oil droplet on an end-piece of the MT rock immersed in (a) 1,000 ppm NaCl solution (reference case) and (b) 1,000 ppm NaCl solution with 10^{-2} molar OPE70. The oil droplet completely spreads on the rock surface immersed in 1,000 ppm NaCl solution, indicating strongly oil-wet behavior.	134
Figure 5.8. Oil contact angle measured on oil-saturated end-pieces of the MT rock samples immersed in OPE70 and OPE100 solutions. Oil droplets completely spread on the surface when the oil-saturated end-pieces are immersed in the water.	135
Figure 5.9. Oil recovery-time profiles for (a) single and (b) mixed surfactant solutions prepared in 1,000 ppm NaCl solution.	141
Figure 5.10. Pore size distribution measured by MICP method for the MT core plugs drilled at depth of (a) 2068.39, (b) 2074.99, (c) 2130.46, (d) 2138.85 m, (e) 2149.54 m.	143
Appendix A1. SEM/EDS analysis shows that layer 1 is mainly composed of quartz, feldspar, and carbonate grains.	169
Appendix A2. SEM/EDS analysis shows that layer 2 is mainly composed of pyrite, quartz, and feldspar.	170
Appendix A3. SEM/EDS analysis shows layer 3 is composed of quartz, feldspar, carbonates, and organic matter.	171
Appendix B1. (a) SEM image of a multi-mineral pore from core plug 3 (2380.24 m) and (b) its elemental mapping. The concentration of Si and O is high at the left side of the pore while the concentration of Fe and S is high at the right side of the pore. Therefore, the highlighted pore in this figure is surrounded by quartz (left side) and pyrite (FeS_2) (right side).	172
Appendix B2. (a) SEM image of multi-mineral pores from core plug 5 (2393.94 m) and (b) its elemental mapping. Pores are surrounded by carbonates, feldspars and pyrite. The	

concentration of carbonates in the left side of the figure is high as shown by black color in Ca, Mg, C and O elemental maps. The concentration of feldspars is relatively high in the upper right side of pores as shown by black color in Al, Si, O and K elemental maps. Concentration of pyrite at the lower corner of pores is high as shown by black color in Fe and S elemental maps.	173
Appendix B3. The total disjoining pressure-distance profiles calculated for (a) calcite, (b) clays, (c) HR, (d) quartz, and (e) the MT rock surface for the solid surface/air/oil system.....	174
Appendix B4. The total disjoining pressure-distance profiles calculated for the solid surface/air/oil system when (a) $A_{H(oil)} = 5.0 \times 10^{-20}$ J, (b) $A_{H(oil)} = 5.2 \times 10^{-20}$ J, (c) $A_{H(oil)} = 6.0 \times 10^{-20}$ J, (d) $A_{H(oil)} = 7 \times 10^{-20}$ J, and (e) $A_{H(oil)} = 8 \times 10^{-20}$ J.	175
Appendix B5. The total disjoining pressure-distance profiles calculated for the solid surface/oil/water system when (a) $A_{H(oil)} = 4.5 \times 10^{-20}$ J, (b) $A_{H(oil)} = 5.0 \times 10^{-20}$ J, (c) $A_{H(oil)} = 5.2 \times 10^{-20}$ J, (d) $A_{H(oil)} = 6.0 \times 10^{-20}$ J, (e) $A_{H(oil)} = 7 \times 10^{-20}$ J, (f) $A_{H(oil)} = 8 \times 10^{-20}$ J, and (g) $A_{H(oil)} = 9 \times 10^{-20}$ J.	177
Appendix B6. The total disjoining pressure-distance profiles calculated for pure (a) calcite, (b) clays, (c) HR, (d) quartz, and (e) rock surface for the solid surface/oil/water system.	178
Appendix B7. The total disjoining pressure –distance profiles calculated for pure (a) calcite, (b) clays,(c) HR, (d) quartz, and (e) rock surface for the solid surface/water/oil system.	179
Appendix B8. The total disjoining pressure-distance profiles calculated for (a) $A_{H(oil)} = 4.5 \times 10^{-20}$ J, (b) $A_{H(oil)} = 5.0 \times 10^{-20}$ J,(c) $A_{H(oil)} = 5.2 \times 10^{-20}$ J, (d) $A_{H(oil)} = 6.0 \times 10^{-20}$ J, (e) $A_{H(oil)} = 7 \times 10^{-20}$ J, (f) $A_{H(oil)} = 8 \times 10^{-20}$ J, and (g) $A_{H(oil)} = 9 \times 10^{-20}$ J for the solid surface/water/oil system.....	181
Appendix B9. Contribution of the surface forces to the total disjoining pressure when $A_{H(oil)} = 5.2 \times 10^{-20}$ J for (a) the rock surface/air/oil, (b) the rock surface/air/water, (c) the rock surface/oil/water, and (d) the rock surface/water/oil systems.....	182
Appendix C1. Surface tension measured for the surfactant solutions prepared with (a) OPE70 and (b) OPE100.	183
Appendix C2. Oil recovery-time curves for (a) single and (b) mixed surfactant solutions prepared in DI water.....	183

Chapter 1 General Introduction

1.1. Overview

This section briefly presents an overview of tight formations in North America and defines technical terms used in this work.

1.1.1. *Tight Oil Formation*

Tight oil formations refer to low permeability (<0.1 mD) sandstones, siltstones, and shales containing trapped crude oil. The depth of tight oil formations range from 1,000 m to 4,000 m. **Figure 1.1** shows the major producing tight oil formations located in Canada and the US. Oil production from tight formations has made US crude supply to exceed 10% of global oil production [1]. **Figure 1.2** shows the history of oil production in the US from conventional resources and the forecast of oil production from tight oil formations. It is expected that the oil production from tight formations increases by 2020 up to 9.6 million barrel per day. It is also expected that produced oil volume from tight formations will be significantly higher than that from other resources within 2020-2040.

Figure 1.3 shows the relative location of conventional and unconventional formations. Conventional oil production is designed to extract crude oil from permeable rock formations using a production well. However, conventional oil production techniques do not work properly for tight formations [2] because oil and gas cannot easily flow through their poorly connected small pores. During the last decade, horizontal drilling and multi-stage hydraulic fracturing techniques have been used by the industry to expand the oil production from tight formations [3].

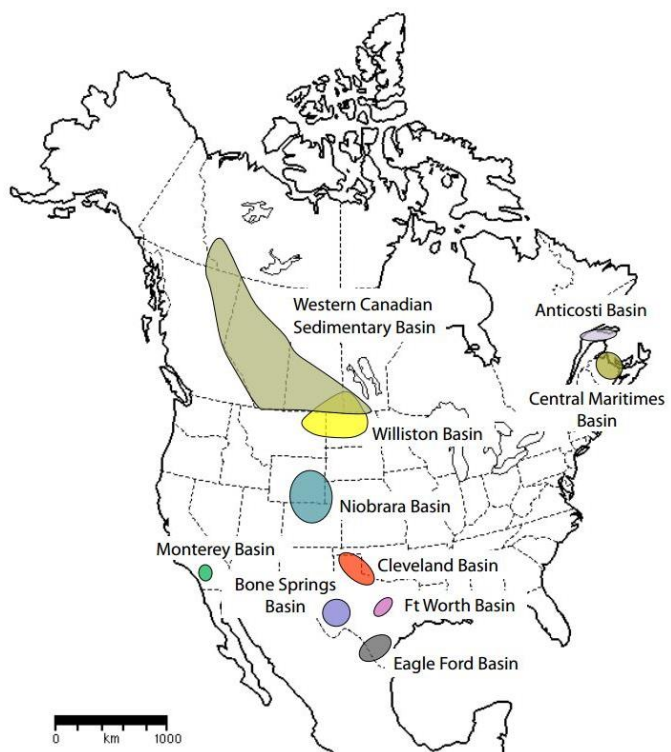


Figure 1.1. Major tight oil formations located in Canada and the US [4].

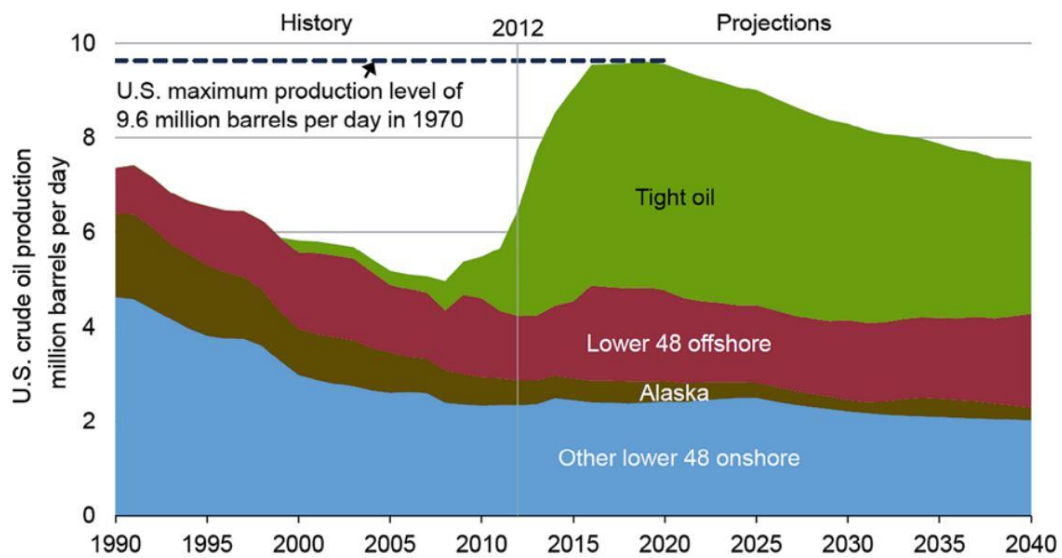


Figure 1.2. Historical oil production in the US through 2012 and projection of oil production through 2040. 1 million barrels (oil)=158,987 m³[5].

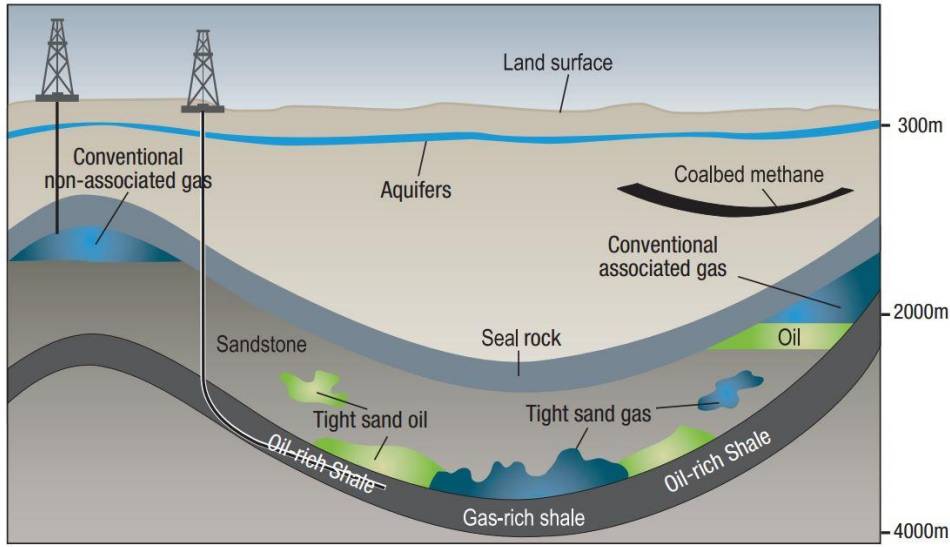


Figure 1.3. Schematic geological section of conventional, tight, and shale gas and oil resources [6].

1.1.2. *Hydraulic Fracturing*

Hydraulic fracturing is a stimulation process for creating new fractures in a reservoir or opening existing natural fractures [7, 8]. During hydraulic fracturing, a mixture of fracturing fluid (aqueous and non-aqueous), proppant (typically silica sand), and chemical additives is injected from a horizontal well into the tight formation to create fractures (**Figure 1.4**).

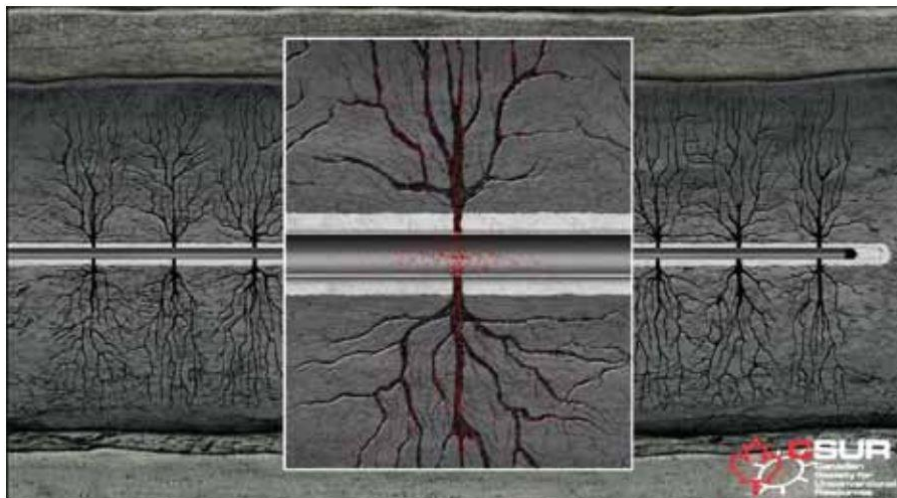


Figure 1.4. Schematic view of fractures created during hydraulic fracturing in a horizontal well [9].

1.1.3. *Fracturing Fluid*

Aqueous (water-based) and non-aqueous (CO_2 , N_2 , oil-based) fracturing fluids have been used to optimize well productivity in the oil and gas industry. To choose the proper fracturing fluid formulation several parameters such as reservoir properties (rock mineralogy, concentration of clays and total organic carbon, and type of clays), cost and availability of fluids need to be considered.

Figure 1.5 shows the advantages and disadvantages of fracturing with water and CO_2 . Although water is cheap and more available compared with other non-aqueous fluids, low recovery of injected water during flow-back process may be a concern for fracturing with water. CO_2 has higher miscibility with oil and injectivity to the reservoir compared with water. However, high mobility ratio of CO_2 can lead to poor oil recovery due to early CO_2 breakthrough.

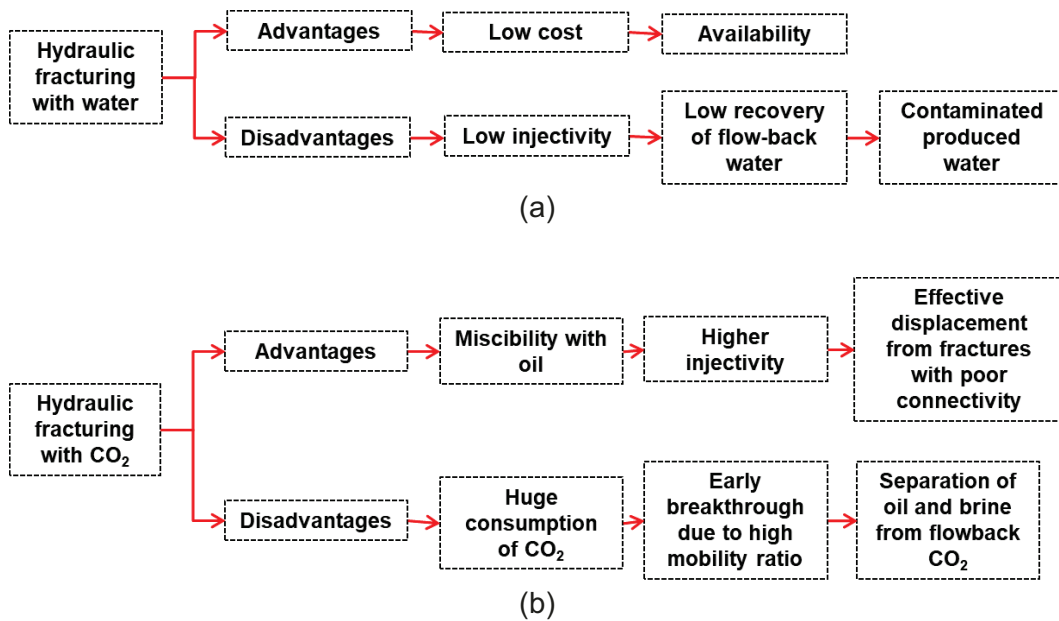


Figure 1.5. Advantages and disadvantages of fracturing with (a) water and (b) CO_2 .

Fracturing with aqueous fluids generally requires a significant amount of water. For example, 20,000 m^3 of water is required for fracking a tight gas well. This amount of water can be alternatively used to grow 9 acres of corn in a year [10]. Although this huge amount of water use in fracturing operations can be put to good alternate uses, water is still the most common fracturing fluid due to its low cost and availability [8].

Different types of chemical are generally added to aqueous fracturing fluid depending on the rock characteristics. A typical fracturing fluid has a very low concentration of between 3 and 12 chemical additives (**Figure 1.6**). Each additive serves a specific purpose as listed in **Table 1.1**. For example, friction reducer added to water (called slickwater) facilitates transport of water and proppants into the target zone at a higher rate and leads to less pressure loss compared with water without friction reducer.

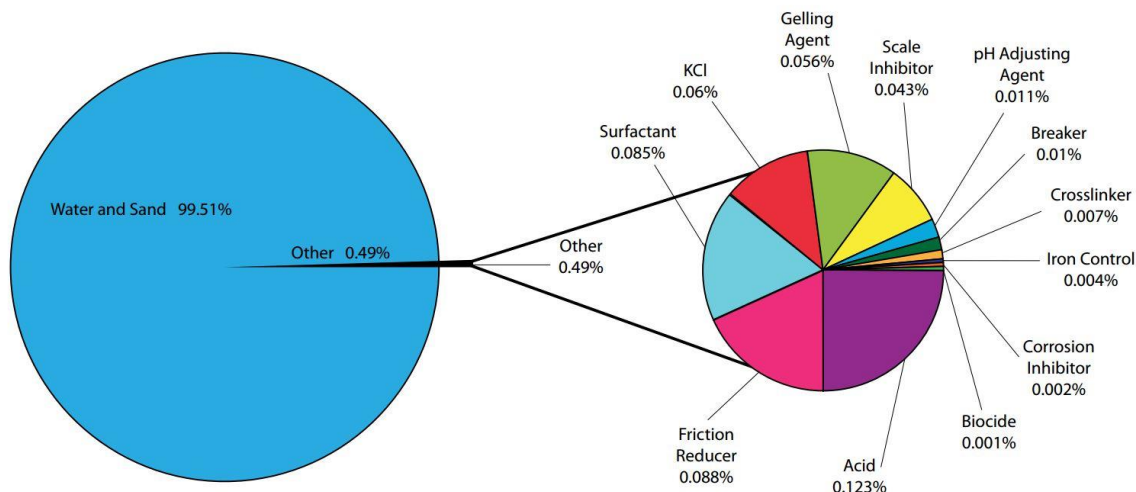


Figure 1.6. An example of aqueous fracturing fluid formulation [11].

Table 1.1. Properties of fracturing fluid chemical additive[12].

Additive	Purpose
Acid	Dissolving minerals and initiating cracks in the rock
Acid/corrosion inhibitor	Protecting casing from corrosion
Biocide	Eliminating bacteria in water to prevent formation of corrosive by-products
Breaker	Delaying the breakdown of gels
Clay/shale stabilizer	Avoiding clay swelling
Crosslinker	Maintaining proper viscosity when temperature increases
Friction reducer	Reducing friction in pipe
Gel	Thickening the fracturing fluid to suspend the proppant
Iron control	Preventing precipitation of metal oxide
Non-emulsifier	Separating oil-water mixtures (emulsions)
pH adjusting agent	Maintaining the effectiveness of other additives
propping agent	Keeping fractures open
Scale inhibitor	Preventing scale in pipe and formation
Surfactant	Reducing interfacial tension

1.1.4. Montney Formation

The Montney Formation located in the Western Canadian Sedimentary Basin (WCSB) is thin-bedded siliciclastic lithologies up to 250-300 m thick (**Figure 1.7**). The Montney Formation extended from east (Alberta) to west (British Columbia) is stacked siltstone and very fine sandstone. These layers overlie a deeper basinal facies of fine grained, organic-rich mudstone/shale, cut by lowstand turbidite sandstones. Most recent drilling activities are focused on oil and gas plays in this formation[5]. The Montney tight oil play (covering an area of more than 90,000 km²) has an estimated 2,133 tcf of natural gas, 28.9 billion bbl of natural gas liquids, and 136.3 billion bbl of oil in-place in the province of Alberta [13].

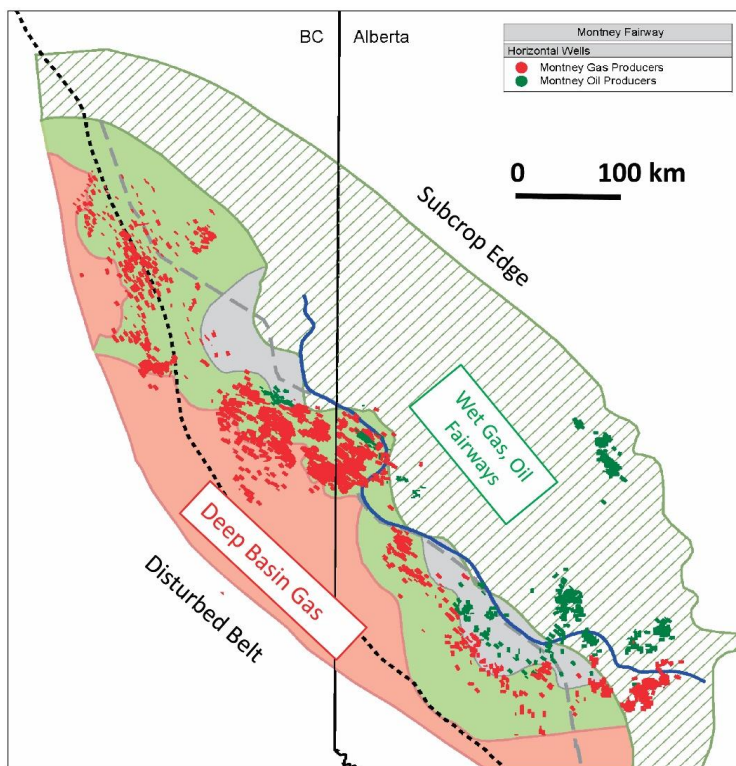


Figure 1.7. The Montney Formation located in the western Canadian sedimentary basin[14].

1.2. Research Motivation

Oil production rate from tight oil formations declines rapidly when wells are placed on production. To guarantee economically long term oil production from these formations, enhanced oil recovery (EOR) techniques should be implemented during fracturing

operations. Improving oil recovery during fracturing operations requires understanding the interactions among fracturing fluids, reservoir fluids, and reservoir rocks. Understanding rock-fluid interactions enable us to develop a proper fracturing fluid formulation for improving oil recovery from tight rocks. It is crucial to evaluate natural wettability behavior of tight rocks prior to investigating the rock-fluid interactions. Although several authors have studies natural wettability of tight rocks, there are still gaps in the proper understanding of rock-fluid interactions in tight rocks.

First, there is ongoing debate about reliable methods for characterizing the natural wettability of tight rocks. It is challenging to evaluate wettability of tight rocks using conventional methods because tight rocks have complex pore structure (composed of hydrophilic and hydrophobic pore networks) and low permeability. Second, the effect of surface forces on wettability behavior of tight rock is poorly understood. The stability of thin film of oil/water covering the rock surface is not investigated for heterogeneous rock samples. It is also unclear how mineral heterogeneity affects the stability of the thin film. Third, the effect of fracturing fluid formulation becomes important once the natural wettability of tight rocks is evaluated.

In this study, the interactions between oil and CO₂ (non-aqueous) and surfactant solutions (aqueous) are investigated. Characterizing the bulk-phase behavior of CO₂-oil mixtures helps us understand the physics of CO₂-oil interactions at the core-scale. Moreover, the non-ionic surfactant solution-oil interactions at the bulk-phase and core scale are poorly understood for tight rocks. It is required to explore the mechanisms controlling the improved oil recovery from tight rocks by CO₂ and surfactant solutions.

1.3. Research Objectives

To understand the physics of rock-fluid interactions in tight rocks, the objectives of this research include:

- Evaluating the natural wettability behavior of downhole core plugs drilled from the Montney tight oil Formation.
- Understanding the role of mineral heterogeneity and intermolecular forces at solid/liquid and liquid/liquid interfaces on wettability behavior of the Montney tight rocks.

- Understanding the mechanisms controlling oil displacement from tight rocks during (i) cyclic CO₂ injection and (ii) soaking with non-ionic surfactant solutions.

1.4. Organization of Thesis

This work is divided into six chapters. All chapters (except the first and last) are published or under review in peer-reviewed journals. Some chapters repeat the same figures, tables, and texts.

Chapter 1 provides a general introduction, defines general technical terms used in the hydraulic fracturing operations, and presents the research motivation and objectives of the research.

The objective of chapter 2 is to develop a laboratory protocol for evaluating the wettability of tight oil rocks reliably. This chapter presents the results of (i) comparative spontaneous imbibition tests conducted on fresh, water-saturated, and oil-saturated core plugs, using reservoir rock and fluids, (ii) air/liquid and liquid/liquid contact angles, and (iii) SEM/EDS analyses to investigate wettability behavior of the Montney tight oil play.

The objective of chapter 3 is to understand how mineral heterogeneity and intermolecular forces acting at solid/liquid and liquid/liquid interfaces can affect the wettability behavior of the Montney tight rocks. This chapter presents the results of (i) pore-scale visualizations on thin section samples and SEM/EDS analyses, (ii) adhesion forces measured for the rock surface and pure minerals using atomic force microscopy (AFM) analysis, and (iii) calculated intermolecular forces by applying the Derjaquin, Landau, Verwey, and Overbeek (DLVO) theory.

The objective of chapter 4 is to understand CO₂-oil interactions at different experimental conditions, and explain how these interactions can lead to improved oil recovery. This chapter presents the results of (i) CO₂-oil interactions at the bulk-phase conditions using a PVT cell and a custom-designed visual cell, (ii) oil recovery factor from oil-saturated core plugs soaked in CO₂, and (iii) oil recovery from oil-saturated core plugs by conducting the cyclic CO₂ process.

The objectives of chapter 5 are to investigate (i) how OPE solutions affect wettability of tight rocks and IFT between reservoir fluids and (ii) how mixing of OPE surfactants

results in improved oil recovery from tight rocks. This chapter presents the results of (i) surface and interfacial tensions measurement of non-ionic octylphenol ethoxylate (OPE) surfactant solutions, (ii) particle size distribution of micelles formed in surfactant solutions, (iii) isothermal titration calorimetry (ITC) experiments for evaluation of surfactant adsorption on the rock surface, (iv) liquid/liquid contact angle measurements to characterize the wettability of rock surface exposed to different surfactant solutions, and (v) imbibition oil-recovery experiments using oil-saturated downhole Montney core plugs.

Chapter 6 presents the key conclusions drawn from this work and recommendations for future studies.

The references from all chapters are presented at the end of chapter six. The appendices are also presented after the references.

Chapter 2 Understanding Wettability of Tight Oil Formations: A Montney Case Study

2.1. Introduction

The soaring global energy demand and decreasing conventional oil production have motivated the industry to produce hydrocarbons from unconventional resources such as tight oil reservoirs, which have emerged as abundant and reliable source of energy. For example, the Montney tight oil play (covering an area of more than 90,000 km²) has an estimated in-place hydrocarbon resources of almost 2,133 tcf of natural gas, 28.9 billion bbl of natural gas liquids, and 136.3 billion bbl of oil in the province of Alberta [13]. Primary oil production from tight oil reservoirs is between 5-10 % of original oil in-place [15, 16]. Therefore, it is essential to develop new enhanced oil recovery techniques for unconventional resources. A key factor that determines the outcome of any EOR technique is the natural wettability of rock matrix. Thus understanding and characterizing wettability of rock, and its interactions with treatment and fracturing fluids are crucial for reservoir development operations.

Ultimately, the outcome of a hydraulic fracturing operation strongly depends on the wettability of the rock-fluid system. Wettability is the tendency of a fluid to preferentially wet the rock surface in the presence of other fluid(s) [17, 18]. Wettability impacts (a) the microscopic distribution of fluid phases at the pore scale, (b) the irreducible water saturation, (c) efficiency of an immiscible displacement such as water flooding, (d) rock-fluid properties such as capillary pressure and relative permeability, and (e) electrical properties of porous media [19-25]. In tight reservoirs, the fluids-rock interactions become more complex as their porosity and permeability are usually very low. As the size of pore-throats decreases to less than 100 nm, the effect of surface forces on surface wettability becomes more pronounced and cannot be neglected [26].

Wettability of a fluid-rock system can be evaluated by measuring (a) equilibrium contact angle [19], (b) Amott wettability index [27], (c) USBM (United States Bureau of Mines) index [28], (d) spontaneous imbibition [29], (e) hysteresis of the relative permeability curves [30], and (f) nuclear magnetic relaxation (NMR) [31]. It is difficult to apply the

common conventional methods, involving forced displacements, for evaluating wettability of tight rocks. This is mainly due to the complex pore structure and low porosity and permeability of tight rocks. Contact angle measurement is the simplest technique for wettability evaluation but may need complementary analysis, as it does not necessarily represent the wettability of the effective pore network [32, 33]. Recent studies show that comparative imbibition tests can provide useful information regarding the wettability of tight formations [33-36].

To stimulate a tight formation, a large volume of fracturing fluid is pumped into the horizontal wells to create fractures [37]. Then, the wells may be soaked with fracturing fluid for a period of time (soaking time) to allow imbibition of fracturing fluid into the rock and possibly counter-current displacement of hydrocarbons toward the fractures. Soaking a fractured reservoir with fracturing fluid leads to spontaneous imbibition of fracturing fluid into the rock matrix. There is a considerable debate going on regarding the effect of soaking process on oil production after hydraulic fracturing operations. Spontaneous imbibition may result in fluid loss and formation damage [38-44]. Up to 70% of fracturing fluid may be retained in the rock matrix due to the high capillary pressure in extremely small pores (less than 100 nm). This phenomenon is called water blockage and can reduce the relative permeability of hydrocarbon and consequently decrease oil production rate [45]. On the other hand, spontaneous imbibition of fracturing fluid has been considered as a driving force for enhanced oil recovery [15, 46-48]. Furthermore, recent experiments [34, 49], field data analyses [50], and simulation studies [51] suggest that extended shut-in of gas wells in the Horn River Basin results in immediate gas production, suggesting expelling of gas by fracturing water imbibition.

The counter-current imbibition of fracturing fluid into tight rock matrix can be performed in laboratory to evaluate the fracturing fluid-rock wettability and to simulate the soaking process in the reservoir. There is a dearth in the literature about the wettability evaluation of tight oil plays. As an example, the wettability of the Montney (MT) tight oil play is poorly understood. In this study, we evaluated the wettability of several core plugs from the MT tight oil play by performing systematic and comparative imbibition experiments and by measuring contact angle of different fluid-rock systems. We also simulated the shut-in period in the field by soaking the samples with different fluids in

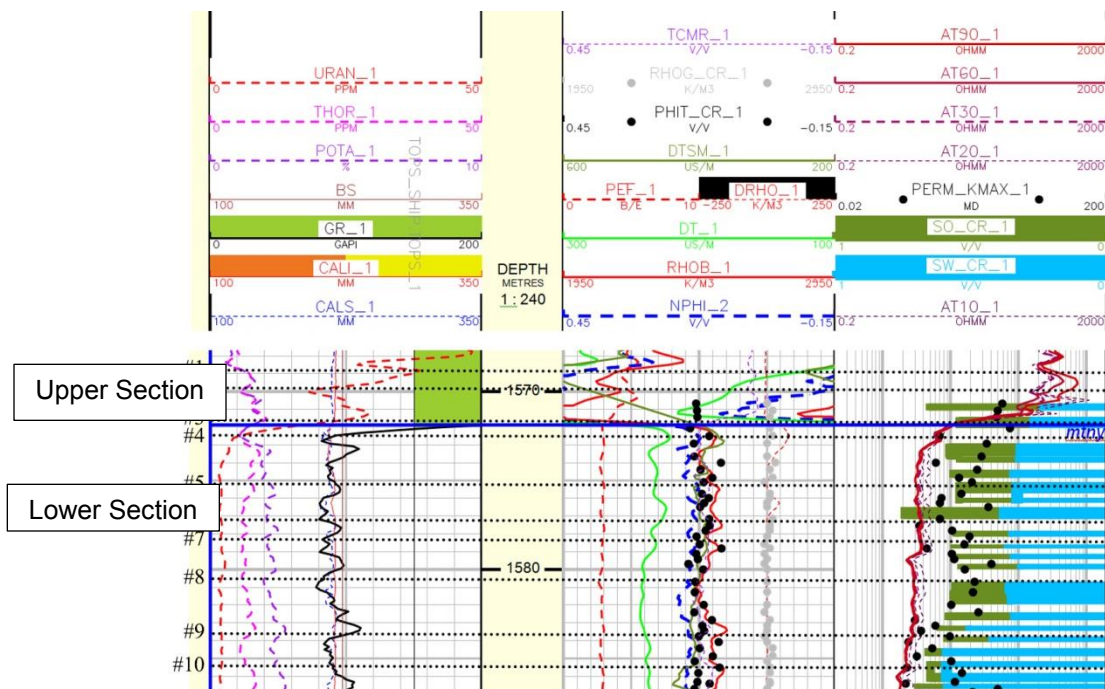
the laboratory. Finally, we discussed the factors controlling water and oil imbibition into the MT tight oil samples.

2.2. Materials

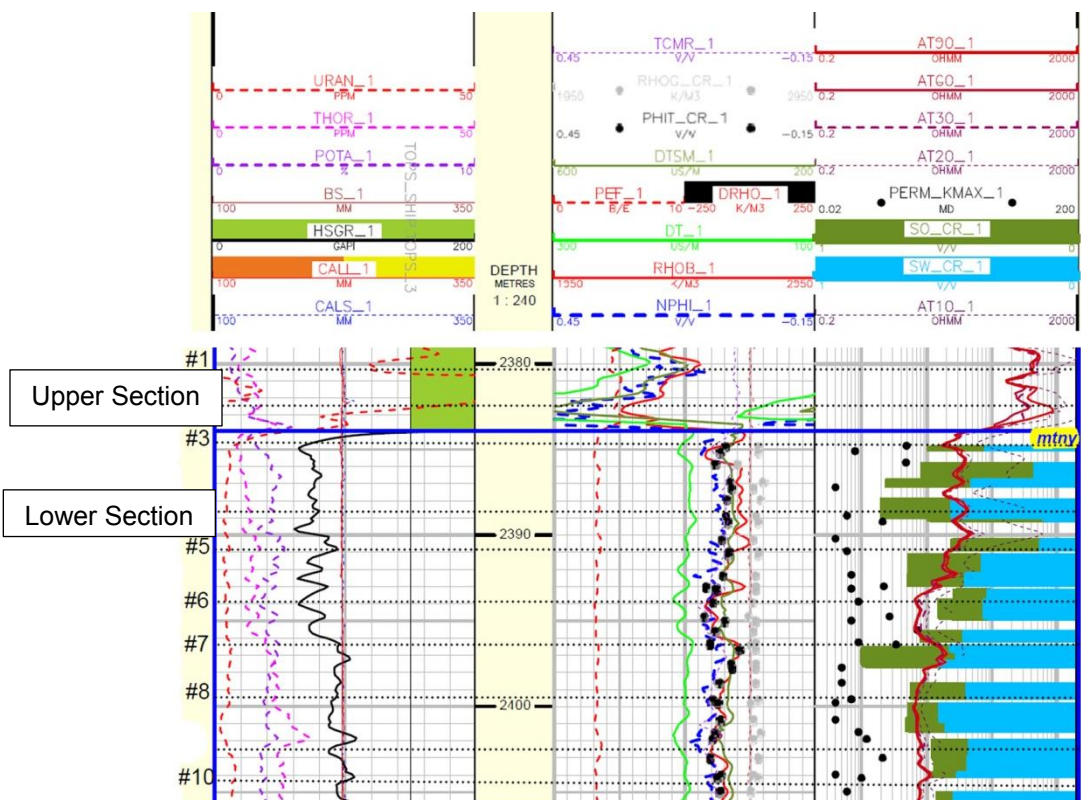
2.2.1. Core Properties

We used fresh core samples from two different wells drilled at different depths (1568.89-1585.18 m and 2380.24- 2404.62 m) in the MT formation and cut 15 plugs using Nitrogen for consistent and comparative imbibition experiments. **Figure 2.1** shows the location of core samples on the well logs for wells 1 and 2. The third track of the logs shows the measured values of oil and water saturations from core analyses. Water saturation increases with the depth and indicates the capillary-gravity equilibrium within geologic time scales. The upper section of the logs shows higher values of resistivity and uranium concentration compared with the lower section. High values of uranium log may be related to the presence of organic materials. For the lower section, relatively lower values in uranium concentration indicates lower amounts of organic materials. Neutron and density porosity logs almost overlap and show a uniform trend in the lower section. In general, the samples from well 1 have higher porosity compared with samples from well 2 based on neutron and density porosity logs, and this is consistent with the laboratory results listed in **Table 2.1** and shown in **Figure 2.2**.

Table 2.1 lists the petrophysical properties of the two wells. These measured values are provided by the Core Laboratories service company. As can be seen in **Table 2.1**, samples of well 1 are more porous and permeable than samples of well 2.



(a)



(b)

Figure 2.1. Approximate location of core samples on the well logs for (a) well 1 and (b) well 2.

Porosity of each sample was measured using Helium gas. **Figure 2.2** compares the normal distribution of porosity for the two wells, and we observe a wide distribution of porosity for the two wells. Permeability variations are the result of variable diagenesis process, in particular the amount of cement, and also the amount of clay. All of the samples are siltstones deposited in storm dominated conditions. The facies is a Hummocky Cross Stratified (HCS) siltstone facies deposited in a lower to middle shoreface setting [52]. The Dykstra-Parsons parameter for well 1 and well 2 is 0.972 and 0.797, respectively. Higher value of Dykstra-Parson coefficient represents more heterogeneous reservoir [25]. Although both wells are categorized as heterogeneous reservoirs, the order of heterogeneity of well 1 is more than well 2.

Table 2.1. Petrophysical properties of well 1 and well 2-MT Formation

Well 1					Well 2				
No.	Depth(m)	Permeability (k_{air} - mD)	Porosity (Helium-Fraction)	Grain Density- Kg/m^3	No.	Depth(m)	Permeability (k_{air} - mD)	Porosity (Helium-Fraction)	Grain Density- Kg/m^3
1	1568.89	4.98	0.155	2720	1	2380.24	0.127	0.0724	2720
2	1569.92	7.53	0.17	2710	2	2382.39	0.036	0.044	2716
3	1571.89	0.61	0.102	2730	3	2384.87	0.092	0.064	2716
4	1572.67	2.08	0.14	2690	4	2388.75	0.197	0.087	2710
5	1575.12	0.35	0.127	2710	5	2390.9	0.422	0.088	2714
6	1577.14	1.14	0.153	2700	6	2393.94	0.054	0.0762	2722
7	1578.26	2.27	0.159	2700	7	2396.25	0.071	0.078	2729
8	1580.64	0.3	0.122	2710	8	2399.39	0.088	0.076	2721
9	1583.79	1.48	0.152	2710	10	2404.62	0.083	0.056	2708
10	1585.18	1.31	0.152	2710					

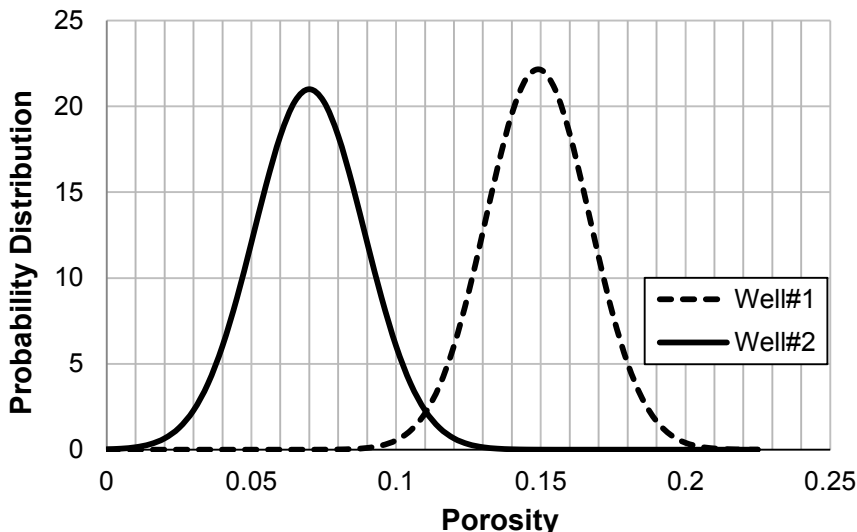


Figure 2.2. Porosity distribution for well 1 and well 2 drilled in the MT formation

Figure 2.3 and **Figure 2.4** plot the mineral concentrations of well 1 and well 2 versus depth of samples based on XRD analysis. The results of XRD analysis are provided by the Core Laboratories service company. The main minerals in the samples of well 1 are quartz (50-55 wt. %), dolomite (13-25 wt. %), clay minerals (10-22 wt. %), and feldspars (10-13 wt. %). **Figure 2.4a** shows that clay minerals of the samples from well 1 are categorized in three types: mixed layer of illite/mica (51-74 % of total clay), mixed layer of illite/smectite (20-32 % of total clay) and kaolinite (0-26 % of total clay). Illite/smectites mixed layers can adsorb water and swell, but we did not observe any swelling in our experiments. Kaolinite, on the other hand, does not swell in the presence of water but may detach from the rock matrix occasionally. Samples of well 2 are mainly comprised of quartz (33-55 wt. %), dolomite (15-29 wt. %), calcite (4.5-12.5 wt. %), clay minerals (9-21.5 wt. %) and feldspars (9.5-14 wt. %). Clay minerals of samples taken from well 2 are illite/muscovite mixed layers (9-28 % of total clay) and kaolinite (72-91 % of total clay), as shown in **Figure 2.4b**.

Quartz content is higher in samples of well 1 as compared with samples of well 2. In addition, samples from well 2 have a wider variation of quartz content as opposed to the samples from well 1. Furthermore, concentration of carbonates (calcite and dolomite) in samples from well 2 is higher than those from well 1. The total clay contents for both wells are similar.

Figure 2.5 and **Figure 2.6** show high magnification view of thin sections under plane light performed on the samples from different depths of well 1 and well 2, respectively. Blue areas shown in **Figure 2.5** and **Figure 2.6** represent pores. The higher population of blue areas in the thin section of well 1 samples (**Figure 2.5**) as compared with that of well 2 samples (**Figure 2.6**) is consistent with relatively higher porosity of well 1 samples, as reported in Table 1 (porosity range of 0.102-0.17 and 0.044-0.088 for samples of well 1 and well 2, respectively). Moreover, the pores in samples of well 1 appear to be more connected which is consistent with the higher average permeability of these samples reported in Table 1 (0.3- 7.53 mD and 0.036- 0.422 mD for samples from well 1 and well 2, respectively).

Quartz, feldspars, carbonates (dolomite/calcite), and organic matter (kerogen or bitumen)/pyrite are indicated by white, yellow, grey, and black grains in the thin section images under plane light, respectively. The dominant mineral in **Figure 2.5** and **Figure 2.6** is quartz. Extensive distribution of quartz in thin section images is in agreement with rock mineralogy data in **Figure 2.3**. Yellow grains representing feldspars in thin section images are more dominant for well 2 samples than well 1 samples which is in agreement with the data in **Figure 2.3**. Generally, the population of greyish grains in samples from well 2 is more than that in samples from well 1, and this confirms the higher percentage of carbonates (dolomite/calcite) in samples of well 2 which supports the data in **Figure 2.3**. Black areas in thin section images are expected to be pyrite/organic matter (kerogen or bitumen). The pyrite contents of samples from well 1 and well 2 are within the range of 1-3 % wt. and 0.75-2 % wt., respectively (**Figure 2.3**). To investigate the presence of pyrite and organic matter, we conducted surface and elemental mapping analysis on different rock samples which are discussed in details in section 2.4.2. SEM/EDS analysis.

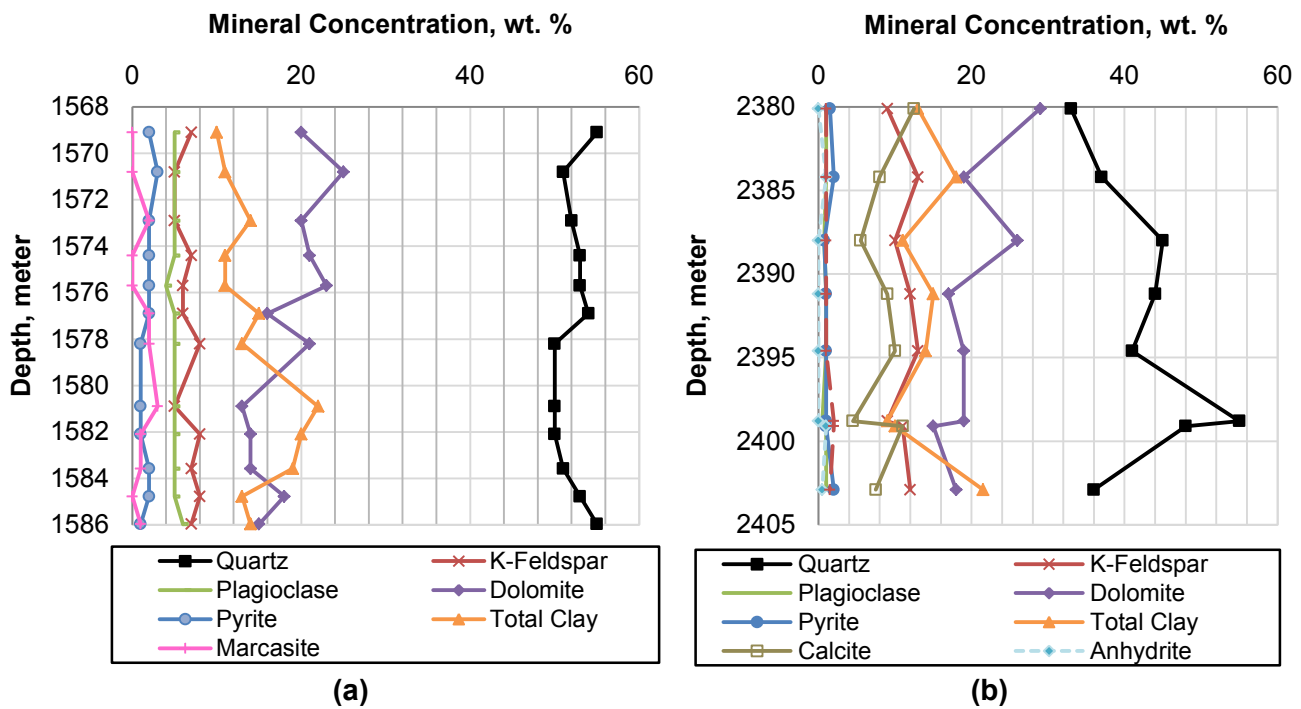


Figure 2.3. Rock mineralogy of samples from: (a) well 1 and (b) well 2. Quartz and carbonates are the main components of samples from both wells.

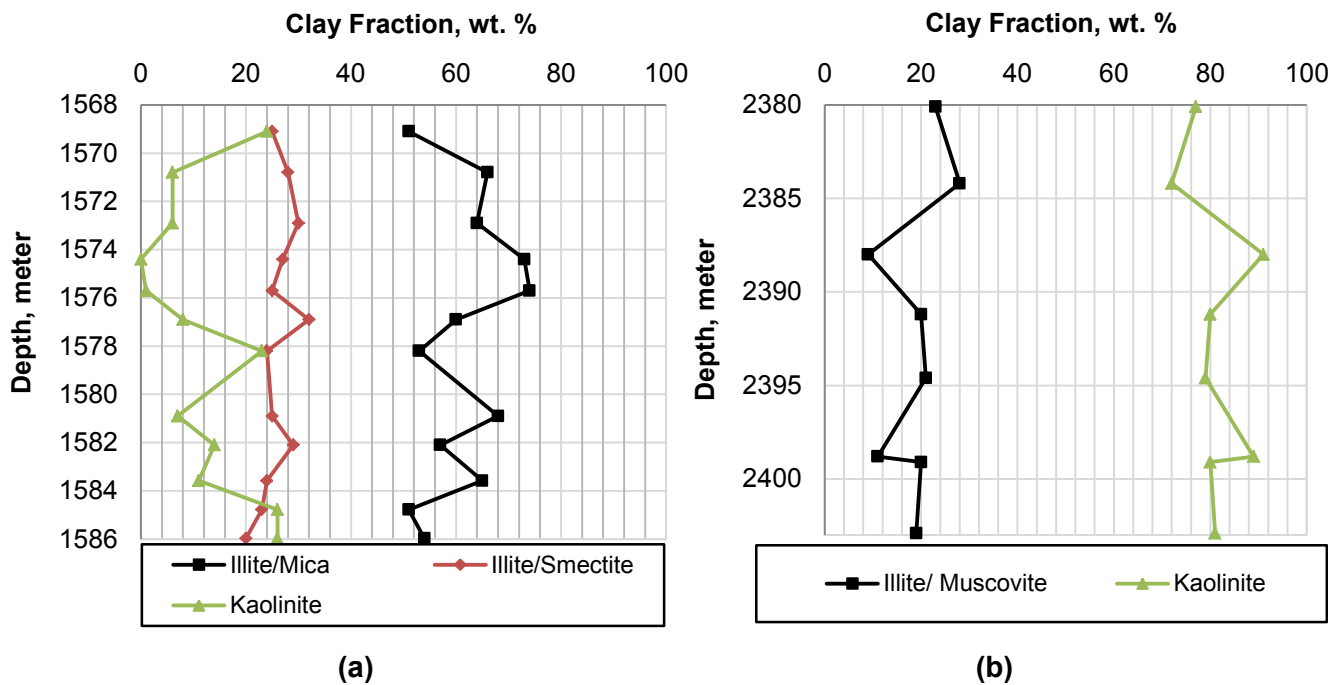


Figure 2.4. Clay fraction of total clay composition for samples from: (a) well 1 and (b) well 2. Total clay of samples from well 1 is composed of illite/mica, illite/smectite and kaolinite. Total clay of samples from well 2 is composed of illite/smectite and kaolinite.

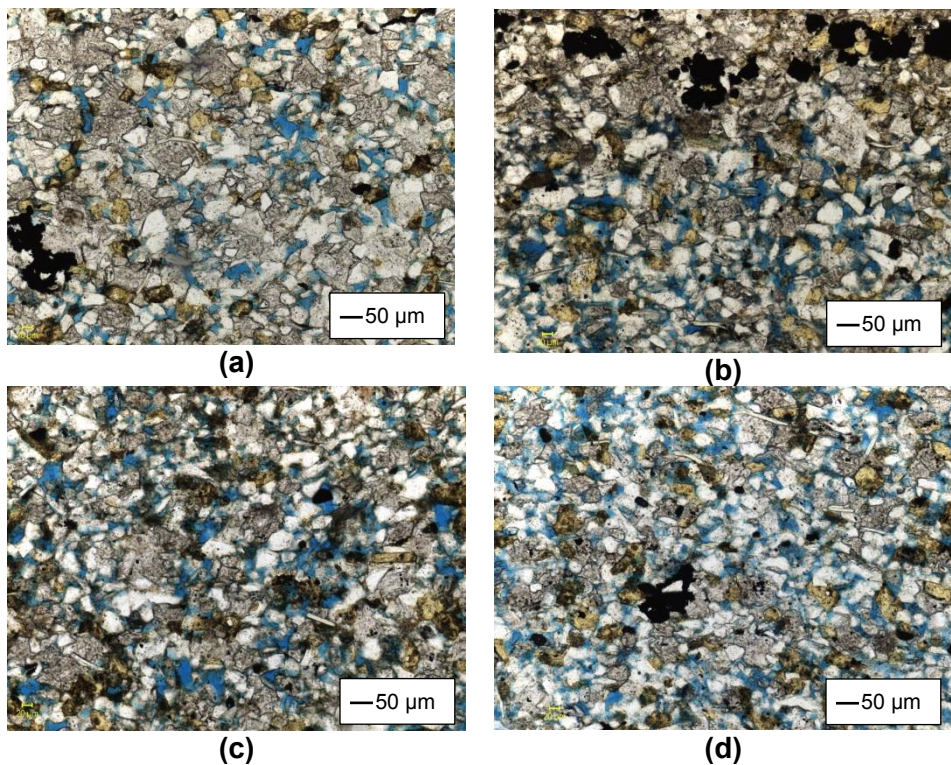


Figure 2.5. Thin sections of siltstone samples taken from well 1 at: (a) 1568.89 m, (b) 1571.89 m, (c) 1578.26 and (d) 1585.18 m. Blue, white, grey, yellow and black are pores, quartz, carbonates, feldspars and organic matter/pyrite, respectively.

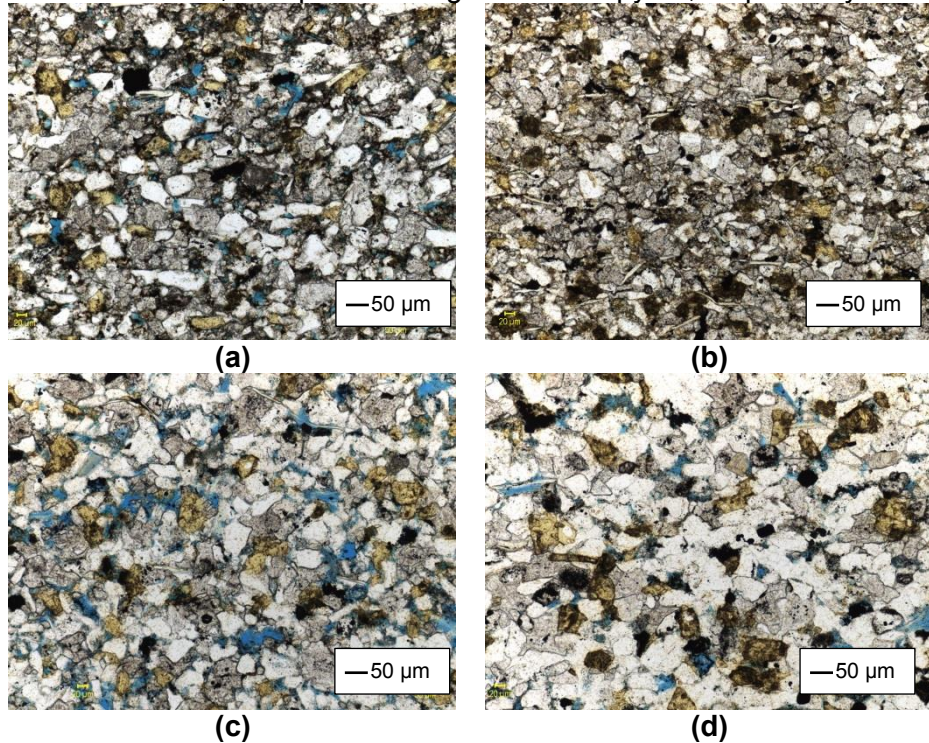


Figure 2.6. Thin sections of siltstone samples taken from well 2 at: (a) 2380.24 m, (b) 2384.87 m, (c) 2390.9 m and (d) 2402.5 m.

2.2.2. Fluid Properties

We used crude oil and reservoir brine as imbibition fluids. **Table 2.2** and Table 2.3 list the physicochemical properties of the fluids used for imbibition experiments. Reservoir brine is a highly saline water and the produced oil from these two wells is characterized as light oil (API=37.96).

Table 2.2. Physical properties of reservoir brine.

Property	Value
Total Dissolved Solids, mg/L	136,630
Observed pH	6.71
Relative Density (25 °C)	1.100
Salinity %	13.94
Total Alkalinity as CaCO ₃ , mg/L	1,433.33
Surface Tension, mN/m	70.1

Table 2.3. Physical properties of crude oil.

Property	Value
Color of Clean Oil	Dark Brown
API Gravity (15 °C)	37.96
Relative Density	0.834
Absolute Viscosity (25 °C), mPa.S	3.55
Surface Tension, mN/m	26.8

2.3. Methodology

First, we measured and compared spontaneous imbibition of oil and brine into twin core plugs. Then, we visualized and measured spontaneous imbibition of brine (or oil) into the plugs partly saturated with oil (or brine) obtained from the first part. Finally, we performed the contact angle measurements on cores at different saturation conditions.

2.3.1. Spontaneous Imbibition on Fresh Core Plugs

We measured spontaneous imbibition of oil and brine into fresh twin plugs (partially saturated with air) drilled from the cores of the two wells. We cut 19 plugs using nitrogen and stored them in the plastic wrap to preserve initial conditions of the rock samples and control weathering and evaporation. However, the core samples were not totally preserved at the reservoir conditions. Oil and brine may partly be evaporated and, cores may partially be saturated with air. We did not use any solvent to clean the rock

samples to avoid changing the initial wetting affinity of the samples. [53] showed that some petrophysical (grain density and permeability) and geochemical properties of the Montney samples changed after solvent-extraction of as-received samples with toluene and methanol.

Measured contact angle data under the laboratory conditions may be different from those under the reservoir conditions due to change of pressure, temperature and fluid saturation. Temperature affects the contact angle significantly but the effect of temperature is not investigated in this study. Pressure does not have a strong effect of contact angle [15]. Initial oil (or brine) saturation of rock samples may affect the wettability behavior of samples. We observed that saturating the samples with brine make them more water-wet while saturating the samples with oil make them more oil-wet. To interpret the spontaneous imbibition results on fresh and oil- (or brine) saturated samples, we performed the contact angle measurements at similar experimental conditions (liquid saturation, temperature and pressure).

We used the plugs (6 cm in length and 3.8 cm in diameter) drilled horizontally from the full-diameter cores. Then, we cut each plug into half to prepare twin plugs with similar petrophysical properties, and placed one plug of each twin set in the imbibition cell filled with reservoir brine and the other plug in the imbibition cell filled with the reservoir oil. The mass gain is recorded by an accurate electronic balance for the period of at least three months. **Figure 2.7** shows the set-up used for the imbibition tests on fresh samples. The experiments were performed at room pressure and temperature.

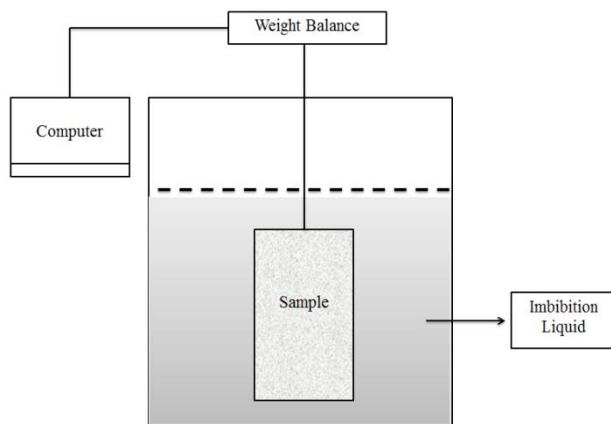


Figure 2.7. Schematic view of the experimental set-up used for spontaneous imbibition experiments on fresh samples.

2.3.2. Spontaneous Imbibition of Brine (or Oil) Into Oil(or Brine)-Saturated Samples

After the imbibition tests on fresh plugs, we placed the plugs, partially saturated with oil (or brine), in imbibition cells filled with brine (or oil), as shown in **Figure 2.8**. These tests are called soaking tests in this chapter. The expelled volume of oil during brine imbibition and that of brine during oil imbibition was collected at the top and bottom of the cells, respectively (**Figure 2.8**). The volume of produced oil and water was measured at different times during the soaking test.

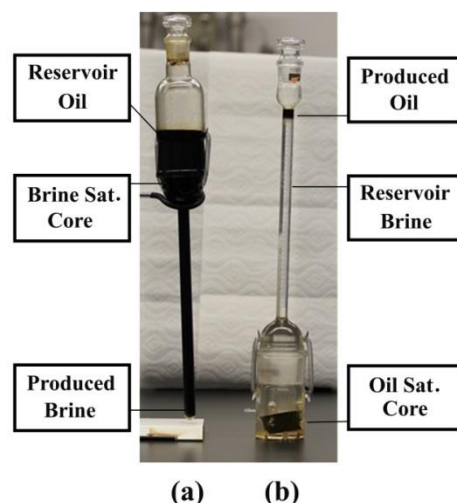


Figure 2.8. Counter-current imbibition cells used for soaking of (a) brine-saturated and (b) oil-saturated samples in oil and brine, respectively.

2.3.3. Contact Angle Measurement

We performed contact angle measurement for different combinations of fluids-rock systems by analyzing the droplet profile equilibrated on the rock surface using a high-resolution camera. We investigated the wetting affinity by visualizing the contact angle of:

- Brine or oil droplet on fresh core samples in the presence of air (air/brine and air/oil contact angle). For fresh samples, we polished the fresh sample and injected an oil (or brine) droplet on the rock surface. We monitored the shape of droplet and recorded the final oil/brine droplet on the rock surface after reaching equilibrium.

- Brine or oil droplet on cores saturated with brine in presence of air to observe the effect of soaking with brine (air/brine and air/oil contact angle). Similarly, we visualized brine or oil droplet on cores saturated with oil in presence of air to observe the effect of soaking with oil (air/brine and air/oil contact angle). For oil-(or brine) saturated samples, we initially soaked the rock samples with oil (or brine), we injected an oil (or brine) droplet on the rock surface, in the presence of air, and monitored the shape of droplet by time. After the equilibrium, we took the picture with a high-resolution camera and analyzed the picture with an image analyzer software to calculate the angle between droplet and rock surface.
- Brine (or oil) droplet on cores immersed in oil (or brine). For oil/brine contact angle measurements on brine saturated sample, we initially soaked the samples with brine; then put them in a glass vessel filled with brine. Brine saturated samples were mounted to the top part of the cell. The oil droplet was inserted using a J-shape needle at the bottom of the vessel below the rock surface. The buoyancy force that arises from the density contrast of the brine and oil helps the oil droplet to attach to the rock surface. Then, oil droplet was left for 20 hours to equilibrium in the system before taking measurements. Finally, we took the pictures and analyzed them using an image analyzer software. For brine droplet, we put the brine saturated samples in the vessel filled with kerosene and inserted brine droplet at the top of vessel. Here we used kerosene as the reservoir oil was not transparent enough to visualize the water droplet.

2.3.4. *Surface Analysis and Elemental Mapping*

We used the end pieces of the core samples for scanning electron microscopy (SEM) and energy-dispersive X-ray spectroscopy (EDS) analysis using Tescan Vega-3W instrument. The instrument has secondary electron (SE), backscattered electron (BSE) and EDS electron beams for surface characterization. SE images are routinely used for analyzing the surface morphology while the BSE images are used to distinguish between heavy and light components. EDS also provides the elemental mapping of the surface and is used as a complementary test for the XRD analysis to explore the presence of organic matter on the rock surface.

2.4. Results and Discussions

This section presents and discusses the results of the imbibition tests on fresh samples and the samples partly saturated with brine or oil. We also present the results of contact angle measurements for different fluid-rock systems. Moreover, we conducted SEM/EDS analysis to further investigate the effect of rock elements on brine/oil imbibition in the MT samples.

2.4.1. Spontaneous Imbibition of Brine and Oil in Fresh Plugs

In **Figure 2.9**, we plot versus time the normalized imbibed volume obtained by dividing the imbibed volume of oil or brine by the sample pore volume. Comparative analysis of the imbibition profiles leads to the following key observations:

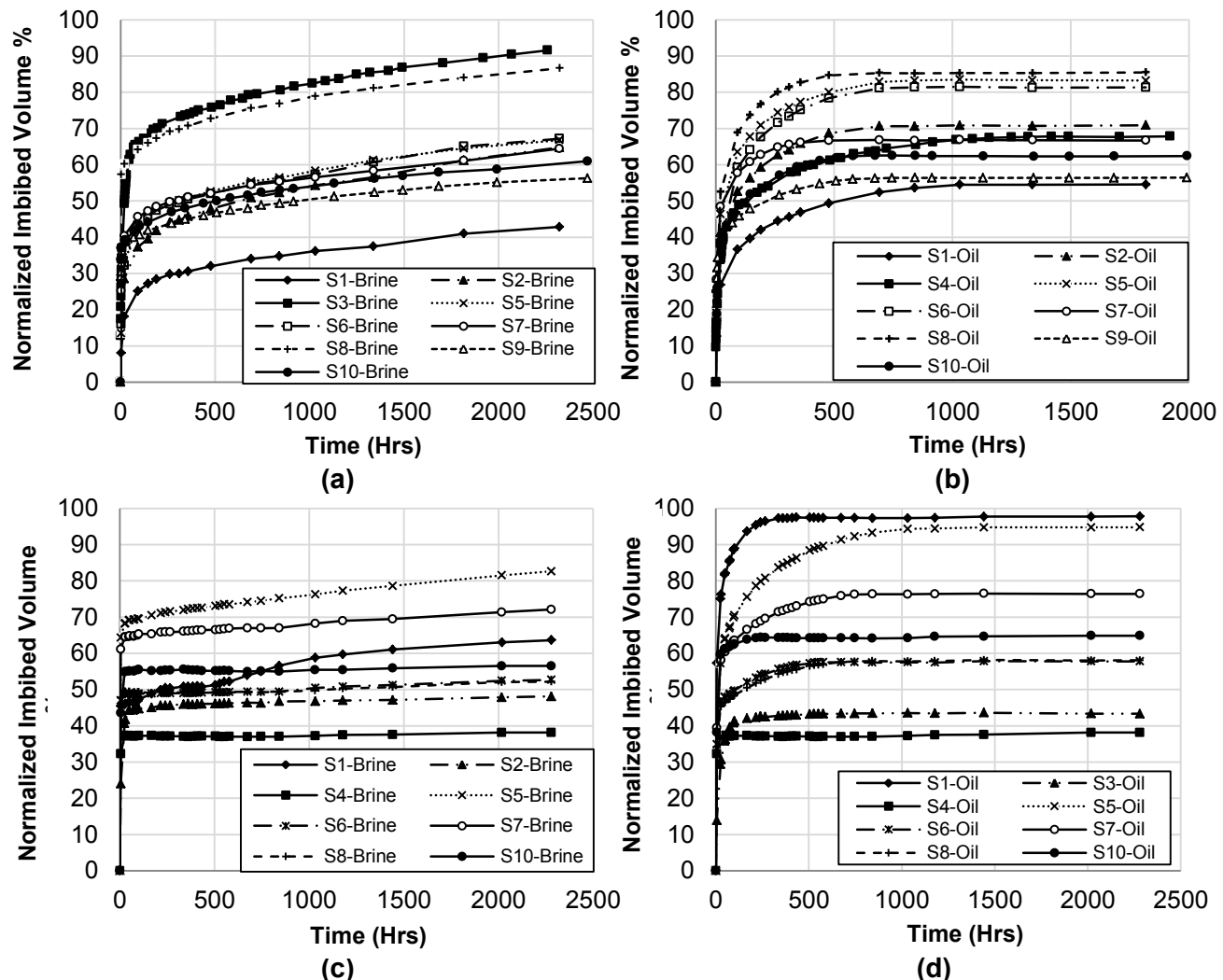


Figure 2.9. Normalized imbibed volume of (a) Brine (Well 1), (b) Oil (Well 1), (c) Brine (Well 2) and Oil (Well 2) in fresh samples.

Mixed-wet behavior: Both oil and brine imbibe spontaneously into the core plugs from the two wells. This indicates that the surface of the rock pore network has a similar affinity to both oil and brine. To compare the affinity of the MT samples to oil and brine, we use the wettability indices defined by Lan et al. [41]:

$$\text{Wetting affinity index of brine (WI}_b\text{)} = \frac{I_b}{I_b+I_o} \quad (1)$$

$$\text{Wetting affinity index of oil (WI}_o\text{)} = \frac{I_o}{I_b+I_o} \quad (2)$$

Where, I_b and I_o are normalized imbibed volume of brine and oil, respectively. In **Figure 2.10**, we plot the wettability indices of brine and oil versus depth for the samples from the two wells. In general, the wettability indices for oil and brine are close to 0.5 and this indicates similar affinities to both oil and brine. However, the wetting affinity of oil is slightly higher than that of brine for some samples, and this difference appears to be more pronounced for samples taken from lower depths.

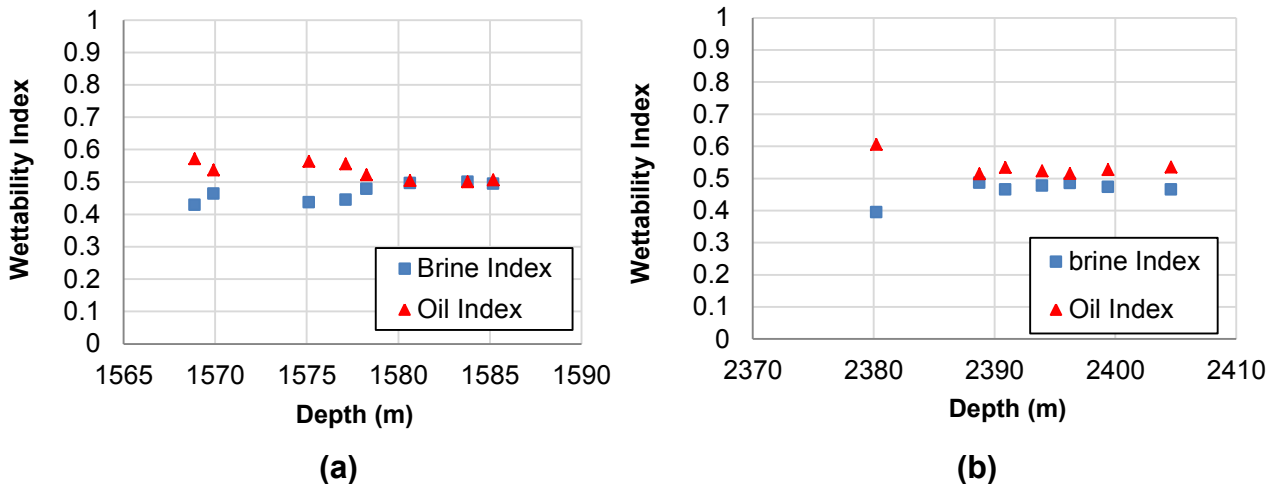


Figure 2.10. Wettability index for samples from (a) well 1 and (b) well 2. Oil and brine wettability index are close 0.5 for most the samples.

Oil reaches to equilibrium faster than brine: Comparing oil and brine imbibition profiles shows that in general, oil reaches to the equilibrium state faster than brine, and this is more pronounced for samples of well 1. We observe two main regions in the brine imbibition profiles. In the first region, brine quickly imbibes into the rock, while in the second region, the imbibition rate is very slow, and interestingly the profiles seem to be

linear (see for example, samples S3 and S8 in **Figure 2.9a**). It should be noted that the brine profile of some samples shows a plateau (for example, S4 and S10 in **Figure 2.9c**). On the other hand, oil imbibition arrives at the equilibrium state relatively fast in most of the samples, and we do not observe the slow linear region (region 2) which was observed in the brine case.

Faster oil imbibition cannot be explained by capillary-driven imbibition models: Handy [54] modeled spontaneous imbibition for one dimensional water-air systems and showed that the imbibed volume at the early time of imbibition (region 1) is proportional to the square root of time. Schembre et al. [55] derived an expression for imbibed volume (Q) as a function of capillary pressure (P_c), porosity (\emptyset), effective fluid permeability (K), fluid saturation (S), contact surface area (A_c), viscosity (μ) of fluid, and time (t):

$$Q = \left[\frac{2 P_c \emptyset K S A_c^2}{\mu} \right]^{0.5} t^{0.5} \quad (3)$$

$$m(\text{slope}) = \left[\frac{2 P_c \emptyset K S A_c^2}{\mu} \right]^{0.5} \quad (4)$$

Therefore, m represents the imbibition rate and can be obtained by plotting the imbibed volume versus square root of time. The ratio of imbibition slope for oil and brine is given by

$$SR(\text{slope ratio}) = \frac{m_o}{m_b} = \left[\frac{\frac{P_{co} \emptyset_o K_o S_o A_c^2}{\mu_o}}{\frac{P_{cb} \emptyset_b K_b S_b A_c^2}{\mu_b}} \right]^{0.5} \quad (5)$$

Assuming constant \emptyset , K , S , and A_c for twin plugs and rearranging Eq. 5 give the ratio between oil and brine capillary pressure:

$$\left(\frac{P_{co}}{P_{cb}} \right)_{\text{Imbibition}} = \left(\frac{m_o}{m_b} \right)^2 \frac{\mu_o}{\mu_b} \quad (6)$$

The ratio of oil and brine capillary pressures can also be approximated using Young-Laplace equation assuming constant average pore diameter for oil and brine imbibition:

$$\left(\frac{P_{co}}{P_{cb}} \right)_{\text{Young-Laplace}} = \frac{\sigma_o \cos \theta_o}{\sigma_b \cos \theta_b} \quad (7)$$

Where σ is surface tension of fluid and θ is contact angle of fluid on the rock surface. Surface tension of oil and brine are listed in **Table 2.2** and **Table 2.3**, respectively. Contact angle of oil and brine droplet on different fresh samples are also listed in **Table 2.5**.

Table 2.4. Comparison of oil and brine capillary pressure ratio obtained from imbibition data and Young-Laplace equation.

	Sample No.	Slope Ratio (SR)	$\left(\frac{P_{co}}{P_{cb}}\right)_{Imbibition}$	$\left(\frac{P_{co}}{P_{cb}}\right)_{Young-Laplace}$
Well 1	1	1.06	3.97	0.54
	2	1.04	3.81	0.56
	5	1.04	3.87	0.56
	6	1.02	3.71	0.42
	7	1.02	3.71	0.43
	8	1	3.55	0.39
	9	1.04	3.88	0.42
	10	0.85	2.58	0.43
	1	1.09	4.26	0.43
	4	0.96	3.42	0.48
Well 2	5	0.98	3.48	0.40
	6	0.99	3.41	0.41
	7	0.98	3.67	0.39
	8	1.02	3.55	0.40
	10	1	3.42	0.40

In **Table 2.4** and **Figure 2.11**, we compare $\frac{P_{co}}{P_{cb}}$ determined from Eqs. 6 and 7, and observe a surprising behavior. Based on the Young-Laplace equation, $\frac{P_{co}}{P_{cb}}$ is between 0.39 to 0.56 while, based on imbibition experiments, $\frac{P_{co}}{P_{cb}}$ is between 2.57 to 4.26. This discrepancy between capillary pressure ratio obtained from imbibition data and Young-Laplace equation can be explained by considering the assumptions made for deriving the capillary pressure ratios. We assumed that capillary pressure is the only mechanism for fluid imbibition and that oil and brine imbibe into the same pore networks. Higher capillary pressure ratio based on imbibition data may be referred to the presence of organic matter. Oil imbibes faster into the rock samples if there is a connected pore network of organic matter [56]; and thus capillary pressure ratio will be higher based on the imbibition data.

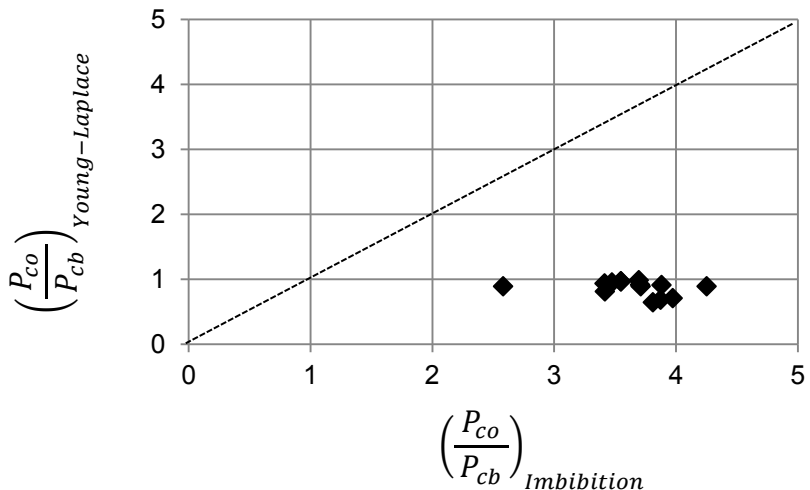


Figure 2.11. Oil/brine capillary pressure ratio from Young-Laplace equation versus oil/brine capillary pressure ratio from the imbibition data.

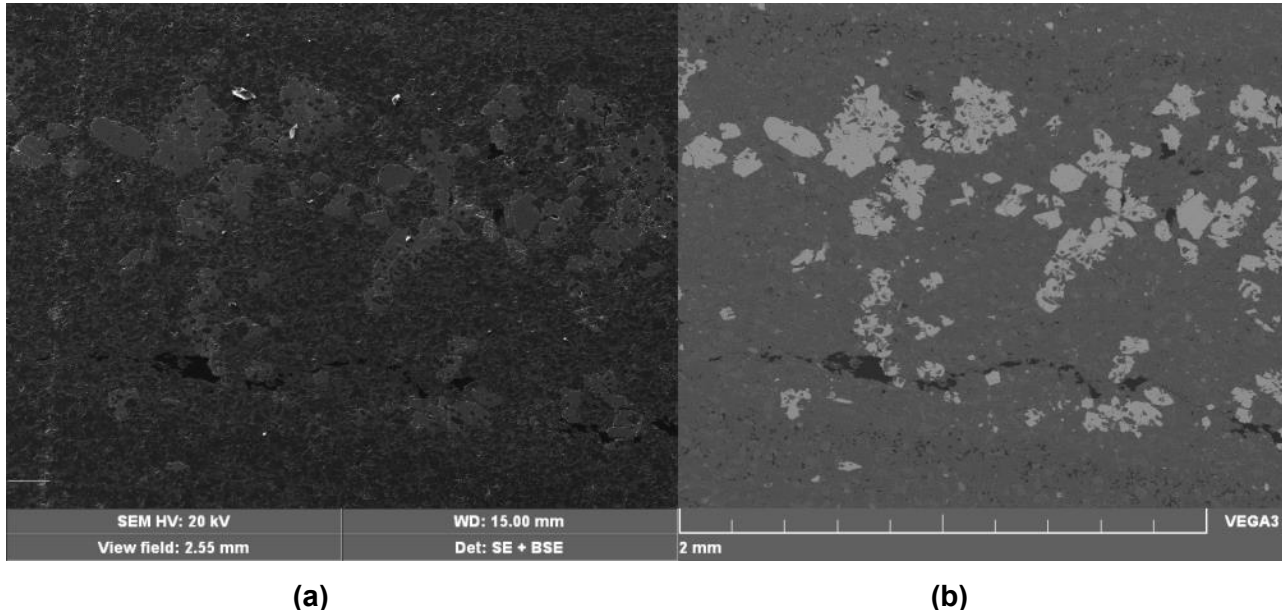
2.4.2. SEM/EDS Analysis

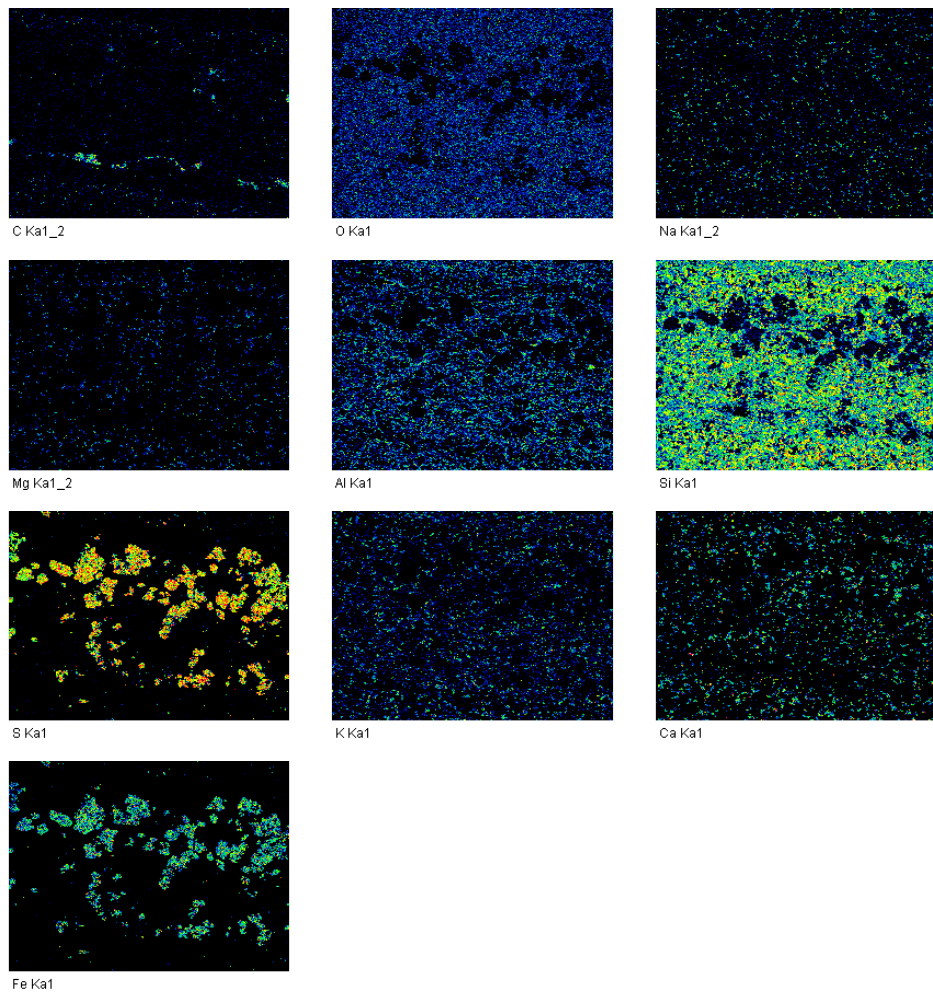
To understand the possible reasons for comparable affinity of samples to oil and brine, we performed SEM/EDS on the rock samples. **Figure 2.12-Figure 2.14** show the SE images, BSE images, and elemental mapping of samples using EDS analysis. We used sample 7 (depth of 1578.26 m) from well 1 (**Figure 2.12**), sample 9 (depth of 1583.79 m) from well 1 (**Figure 2.13**) and sample 4 (depth of 2388.75 m) from well 2 (**Figure 2.14**) for conducting SEM/EDS analysis. SE images provide topographical information and, BSE reveals the compositional variations in the samples. Bright spots in BSE images (**Figure 2.12b**, **Figure 2.13b**, and **Figure 2.14b**) represent heavy materials (such as pyrite) while dark spots represent lighter components (organic matter). **Figure 2.12c** shows the presence of Fe and S elements at the bright spots observed in BSE analysis (**Figure 2.12b**). Therefore, these bright spots are pyrite.

Figure 2.12c shows the elemental mapping of sample 7 from well 1. Si is uniformly distributed in the map while Fe and S (pyrite) are present at specific locations where Si does not exist. Interestingly, Ca, Mg, and C (carbonate components) exist between Si elements (silica components). This mixed distribution suggests that quartz and carbonate components are mixed with each other and form a complex structure. This observation is consistent with spatial distribution of quartz and dolomite grains observed in the thin sections shown in **Figure 2.5** and **Figure 2.6**, and can be used to explain the

observed mix-wet behavior. **Figure 2.15** highlights two complex pores (blue areas) surrounded by quartz (white grains) and carbonate components (grey grains). In general, quartz tends to be water-wet while the carbonate minerals such as dolomite tend to be oil-wet [18]. Therefore, the observed mix-wet behavior may be explained by wetting affinity of mix-wet grains.

We also observe a dark strip extended along the sample in SE image (**Figure 2.12a**). EDS analysis on this sample shows the presence of pure carbon element, which may represent organic matter since other components such as oxygen are absent (**Figure 2.12c**). **Figure 2.13** and **Figure 2.14** illustrate the presence of organic matter in other samples.





(c)

Figure 2.12. Sample 7 (depth of 1578.26 m) from well 1 under (a) SE beam, (b) BSE beam and (c) EDS analysis. Presence of Fe and S in part (c) shows the presence of pyrite in the sample. Pyrite is shown in part (b) by brighter spots.

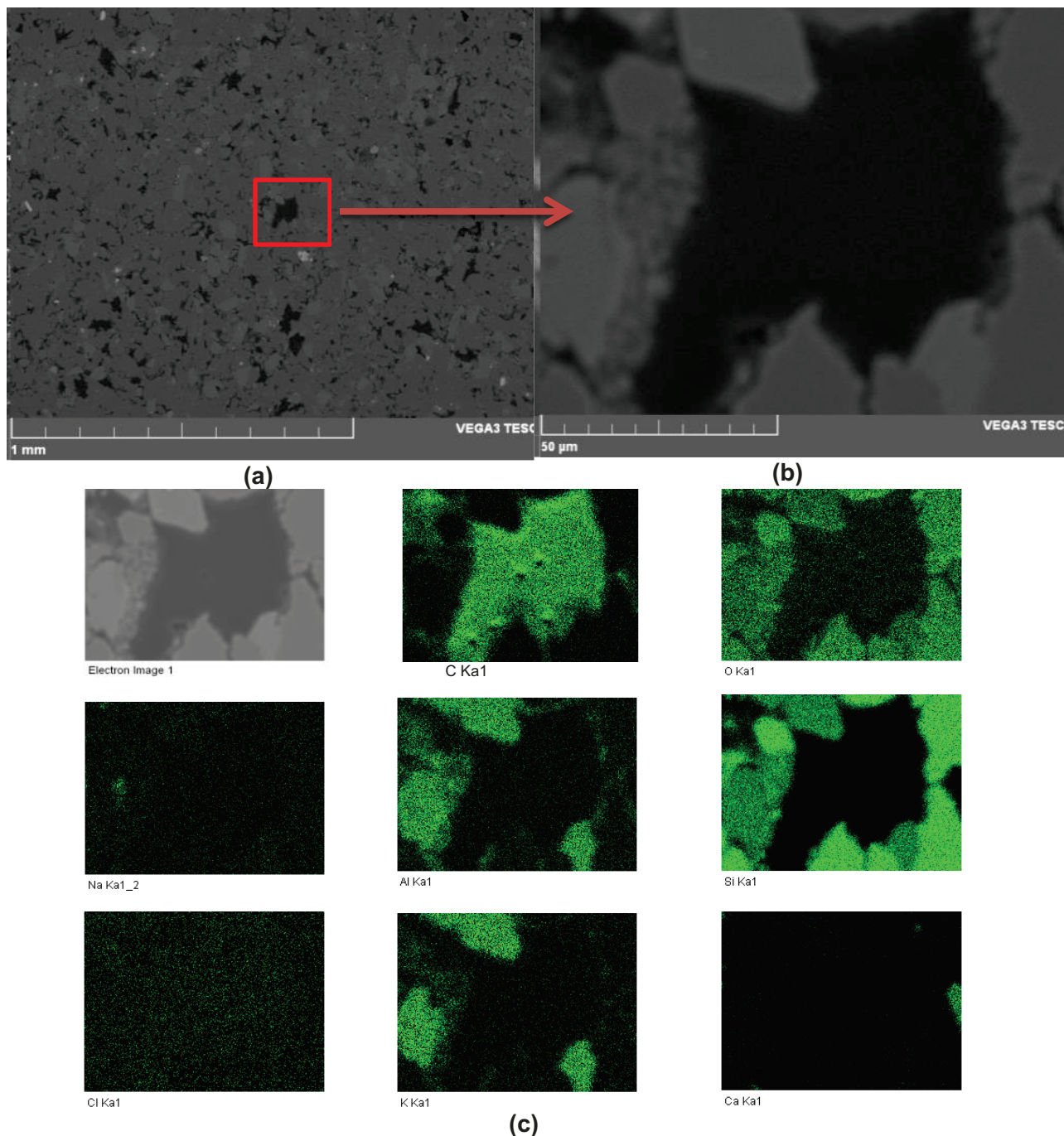
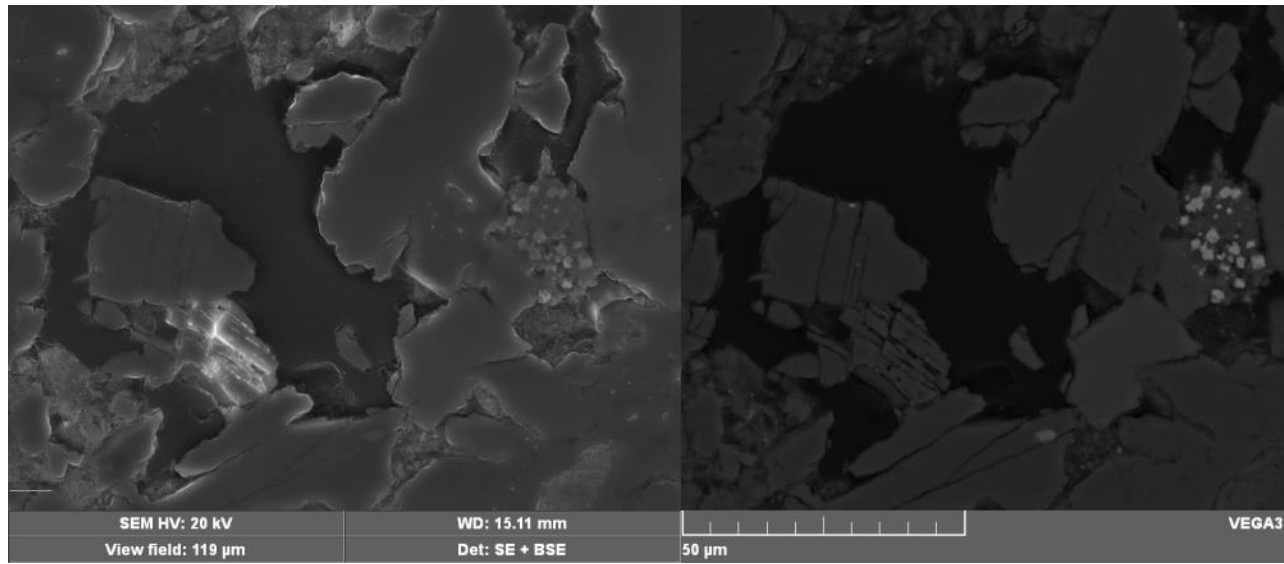
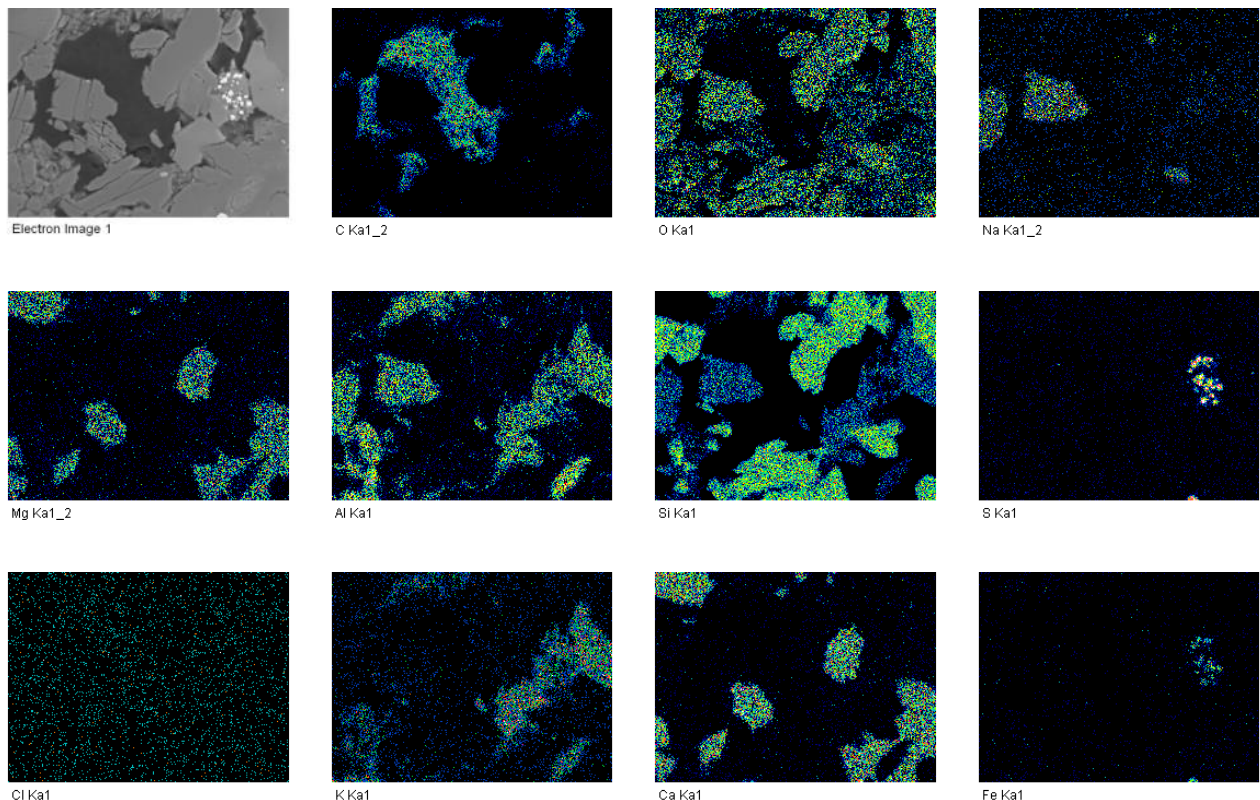


Figure 2.13. Sample 9 (depth of 1583.79 m) from well 1 under (a) SE beam, (b) BSE beam and (c) EDS analysis. The big chunk of pure carbon is expected to be organic matter.



(a)

(b)



(c)

Figure 2.14. Sample 4 (depth of 2388.75 m) from well 2 under (a) SE beam, (b) BSE beam and (c) EDS analysis. The pure carbon in subplot (c) suggests the presence of organic matter in the sample.

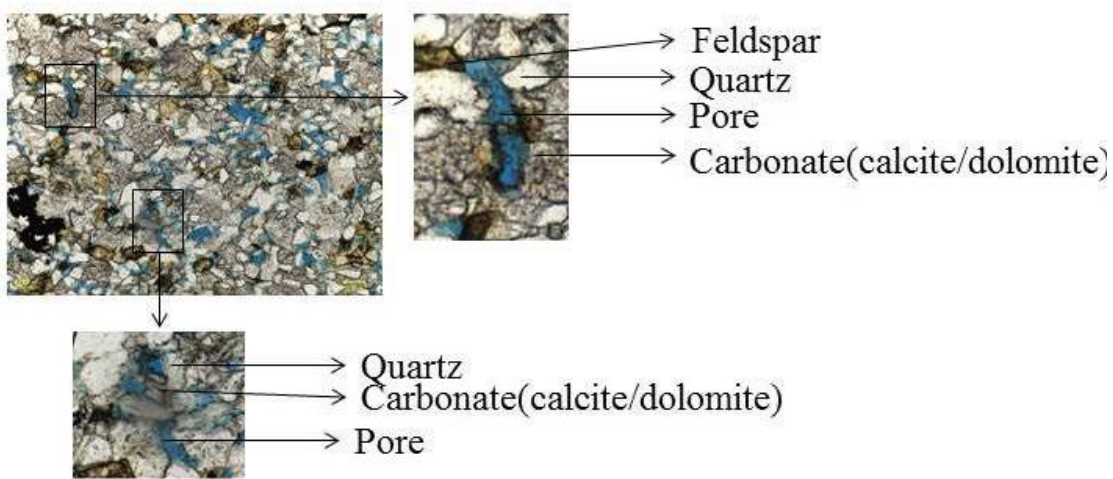


Figure 2.15. Complex pore wall of a random MT sample. Pores are surrounded with quartz, carbonates and feldspars. Quartz and feldspars tend to be water-wet while carbonates are expected to be oil-wet.

2.4.3. Contact Angle Measurement

First, we measured air/brine and air/oil contact angles on fresh samples. **Table 2.5** lists the measured values of contact angles for oil and brine. Oil droplet totally spreads on the rock surface while brine partially wets the sample. **Figure 2.16** shows this phenomenon for a random sample. The results indicate that the affinity of the fresh samples to oil is higher than that to brine, and this is in agreement with the general observation in **Figure 2.9** that oil imbibes faster than brine in these samples.

Second, we measured air/brine and air/oil contact angles on saturated samples (after spontaneous imbibition) to observe the effect of soaking with brine and oil. In the case of brine-saturated samples, oil totally spreads on the rock surface while; brine droplet forms a measurable, but smaller, contact angle on the rock surface. The decrease in brine contact angle reveals that aging in water increases the rock affinity to water. In the case of oil-saturated samples, oil spreads on the rock surface while brine forms a droplet with higher contact angle. Therefore, aging in oil decreases the rock affinity to water.

Third, we measured the contact angle of brine/oil in brine-saturated samples to mimic the reservoir conditions. **Figure 2.17** shows equilibrated droplets of crude oil and brine on the rock surface immersed in brine and kerosene, respectively. In order to visualize the water droplet, we used kerosene instead of crude oil. Brine droplet tends to spread

on the rock surface in the presence of kerosene while oil droplet tends to minimize its interfacial contact with rock in the presence of brine. **Figure 2.18** shows the contact angle of brine (in the presence of kerosene) on the rock surface versus depth for the two wells. The brine contact angles change from 30° to 63° . Interestingly, in contrast to the results of the previous tests on fresh samples, here the results show that the rock samples are strongly oil repellent when immersed in brine. To investigate this discrepancy, we measured and compared imbibition of brine and oil into oil-saturated and brine-saturated samples, respectively.

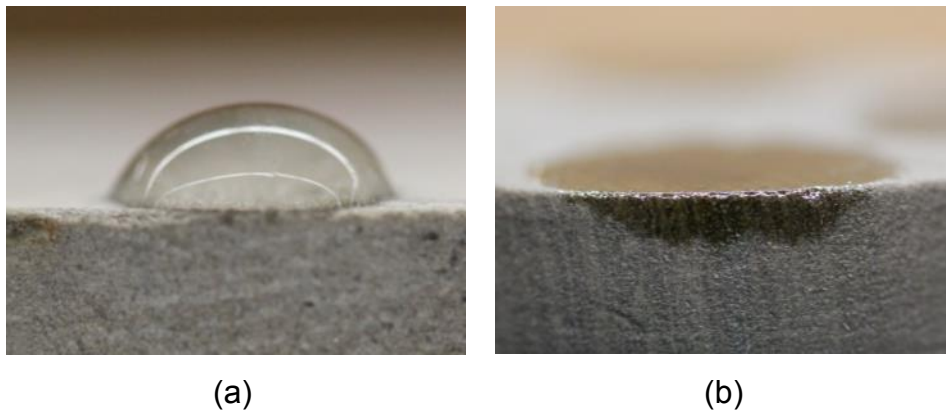


Figure 2.16. Contact angle of (a) brine/air and (b) oil/air on the surface of fresh sample. The brine droplet partially wets the rock surface while the oil droplet completely spreads on rock surface.

Table 2.5. Air/ brine and air/ oil contact angle for fresh, oil-saturated and brine-saturated samples.

No.	Oil on fresh sample	Oil on brine saturates sample	Oil on oil- saturated sample	Brine on fresh sample	Standard Error	Brine on brine- saturated sample	Standard Error	Brine on oil- saturated sample	Standard Error
Well 1	1	0	0	44	0.61	31	0.58	60	1.37
	2	0	0	34	1.58	27	0.19	73	0.84
	3	0	0	---	0.99	22	0.45	---	---
	4	0	---	0	0.23	---	---	73	0.35
	5	0	0	46	1.00	22	1.03	75	0.50
	6	0	0	26	0.81	14	0.81	72	0.50
	7	0	0	23	1.99	20	0.82	73	0.99
	8	0	0	15	1.49	13	1.59	66	1.95
	9	0	0	29	1.19	10	0.94	66	1.82
	10	0	0	25	1.54	17	1.03	76	0.50
Well 2	1	0	0	25	0.92	21	0.80	74	1.82
	2	0	0	---	0.79	25	0.99	----	----
	3	0	0	0	41	1.79	----	76	0.63
	4	0	0	0	34	1.73	27	1.05	74
	5	0	0	0	21	0.72	24	1.03	93
	6	0	0	0	23	1.00	37	1.38	103
	7	0	0	0	12	0.37	24	1.37	86
	8	0	0	0	17	1.18	25	0.26	103
	10	0	0	0	17	0.67	26	0.65	74
									0.61

2.4.4. Spontaneous Imbibition of Brine Into Oil-Saturated Samples

We immersed the oil-saturated plugs in brine, and observed expelled oil droplets initially on the rock surface as shown in **Figure 2.19** and **Figure 2.20**. As the imbibition progresses, oil droplets detach from the rock surface and accumulate at the top of the imbibition cells, as shown in **Figure 2.19b**. Here, we define oil recovery as the volume of produced oil divided by the volume of oil initially in the plug samples. **Figure 2.21** shows how the estimated oil recovery change versus soaking time for samples from well 1 and well 2.

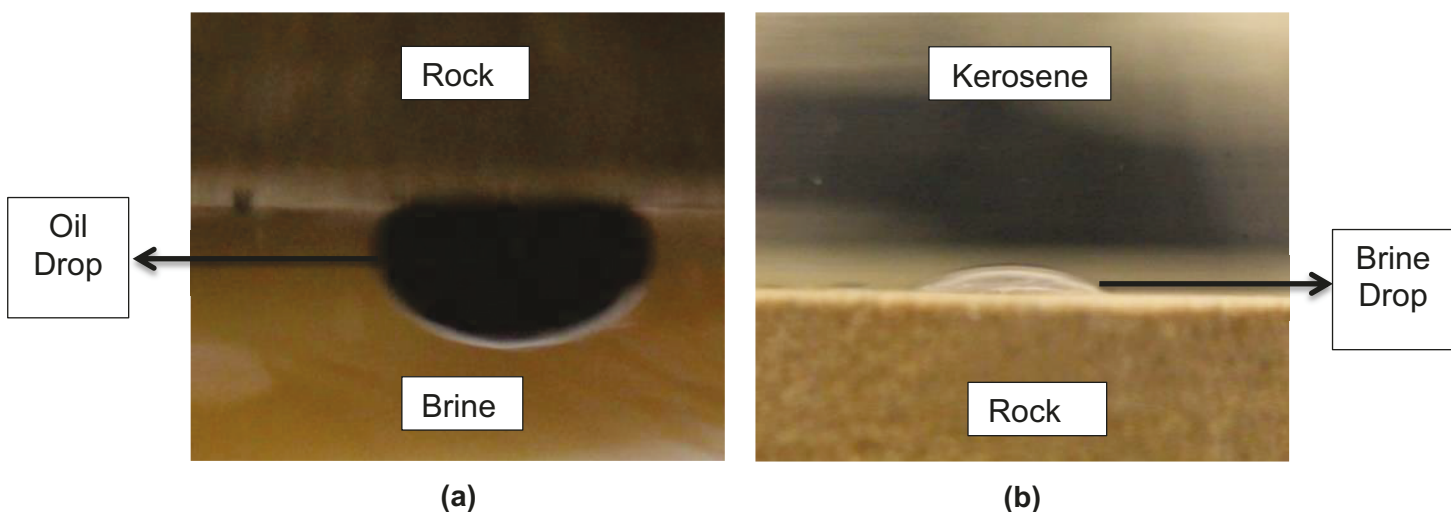


Figure 2.17. Liquid/Liquid Contact angle of (a) oil and (b) brine. Brine-saturated sample is strongly oil repellent and water-wet.

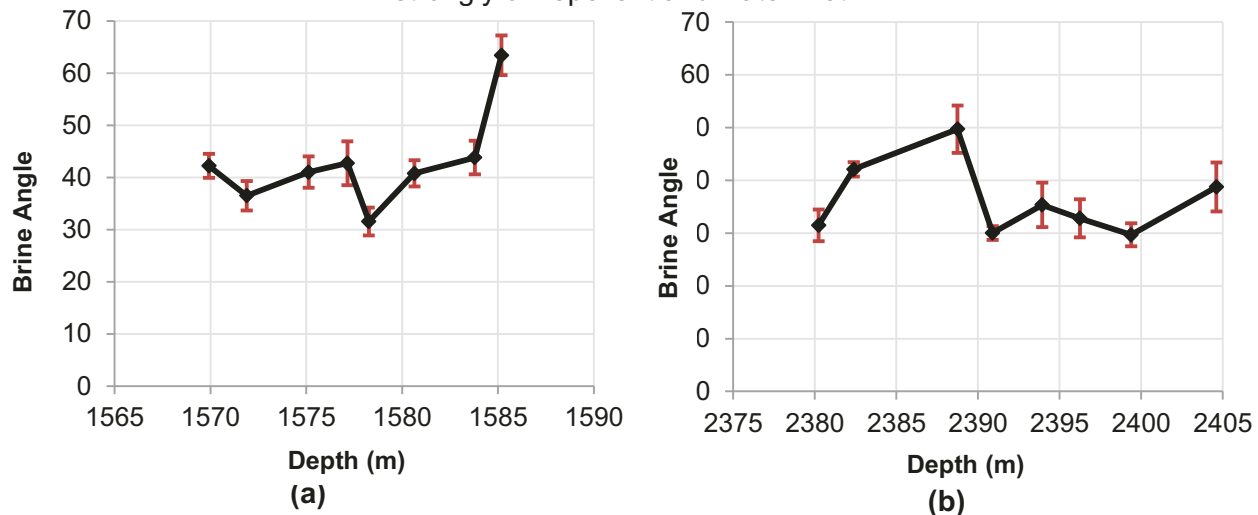


Figure 2.18. Contact angle of the brine droplet equilibrated on the surface of the core immersed in oil for (a) well 1 and (b) well 2.

The oil recovery is in the range of 25 % to 45 % and most of the experiments reach to the equilibrium after one month of soaking in brine. Therefore, more than 50 % of the initial oil remains in the samples mainly because the imbibition force is not strong enough to displace the oil residing in small oil-wet pores. Furthermore, part of the oil in water-wet pores can be trapped by imbibing water due to snap-off mechanism. It should be noted that there are some sources of error in this experiment which results in underestimation of the produced oil. First, some of the small oil droplets do not detach from the rock surface, due to low buoyancy force, and therefore, do not accumulate at the top of the cell. Second, some oil droplets attach to the neck of cells due to the curvature of the glass. We tried to reduce such errors by slightly shaking the imbibition cells.

We also immersed brine-saturated samples into oil as shown in **Figure 2.22**, and did not observe accumulation of brine droplets at the bottom of cells. Apparently, oil cannot imbibe into the brine-saturated samples. It could be that some little amount of brine was produced; however they might attach to the glass surface and could not form a visible bulk of brine at the bottom of the cell. Regardless of possible attachment of brine on the glass surface, the volume of produced brine was negligible as compared with the volume of recovered oil.



Figure 2.19. Oil-saturated samples immersed in brine (a) at the beginning of the experiment and (b) 30 days after starting the experiment

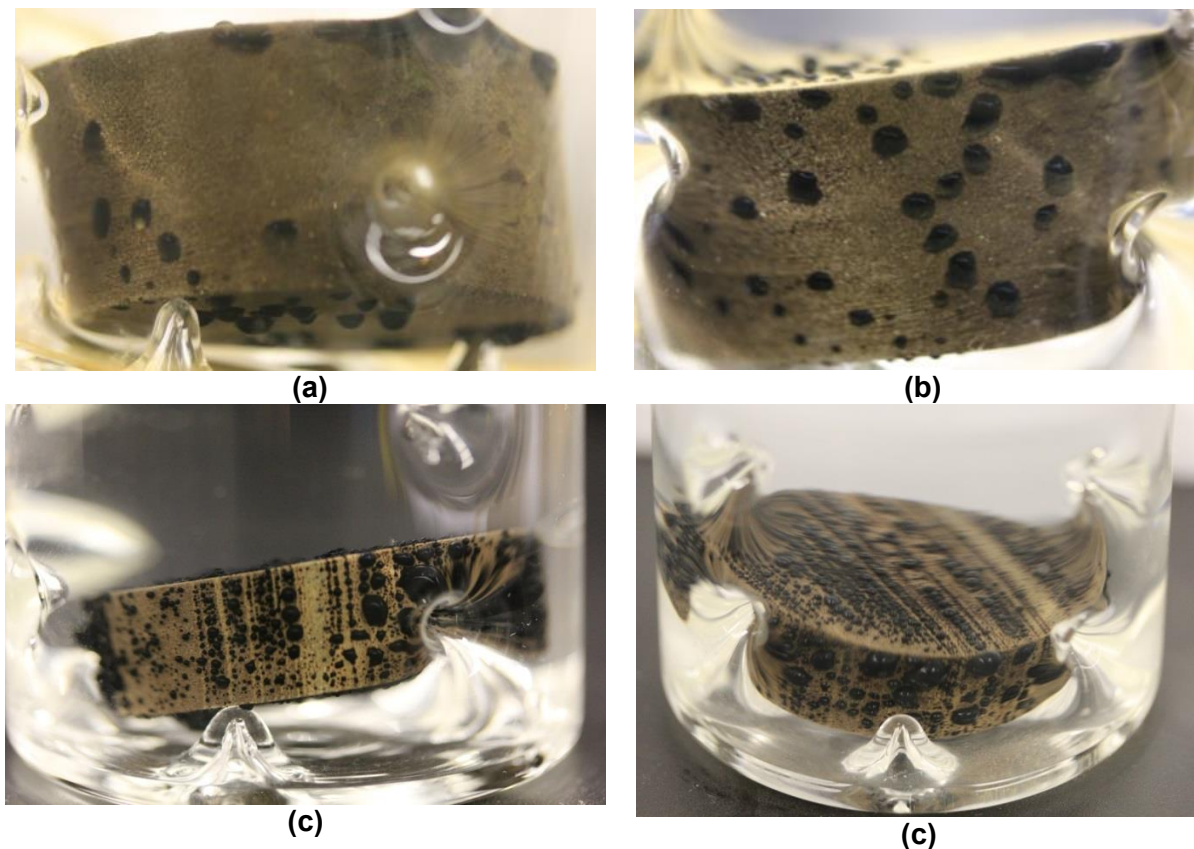


Figure 2.20. Oil droplets are expelled out of the rock due to spontaneous imbibition of brine into the oil-saturated samples. Oil is produced from specific layers in some samples.

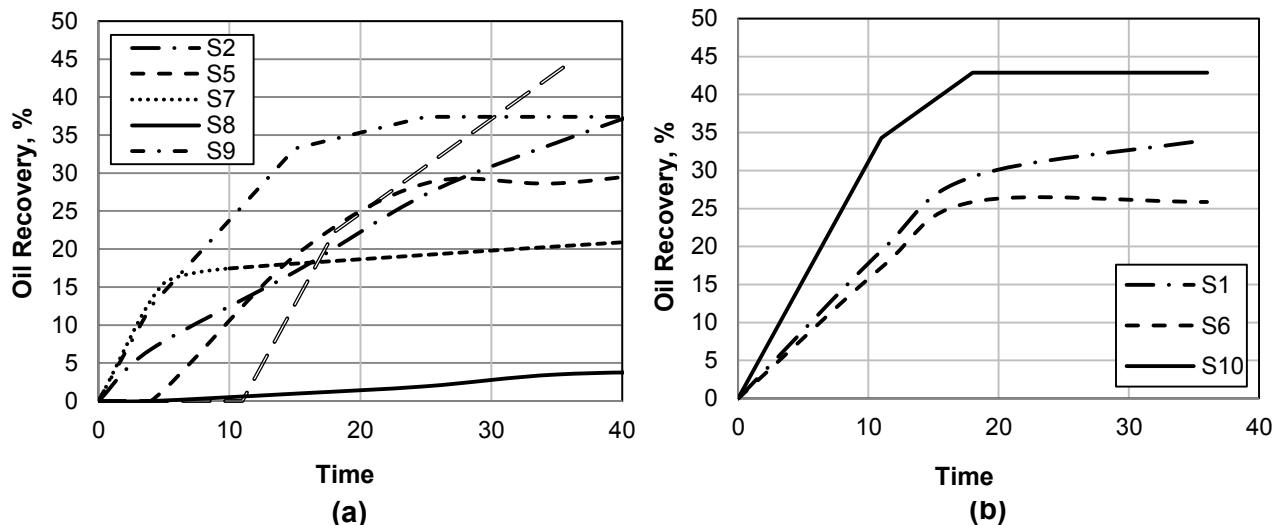


Figure 2.21. Estimated oil recovery during spontaneous imbibition versus time for samples from (a) well 1 and (b) well 2.

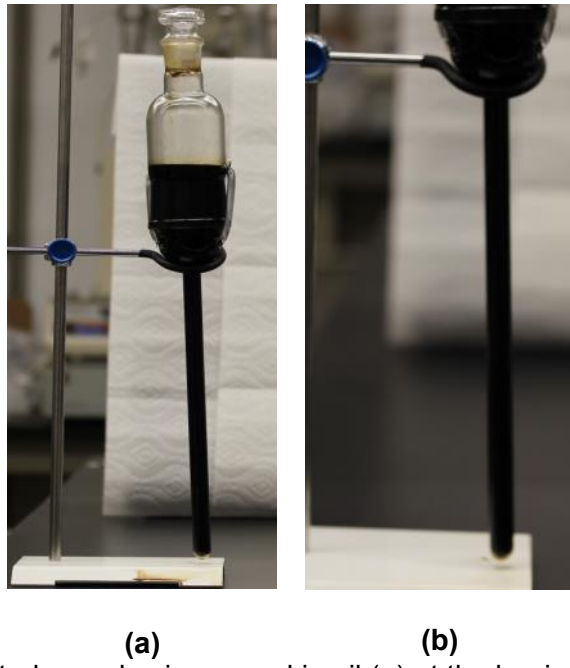


Figure 2.22. Brine-saturated samples immersed in oil (a) at the beginning of the experiment and (b) 30 days after starting the experiment

There are two main driving forces for fluid displacement during spontaneous imbibition: capillary force and gravity force. To investigate the relative effect of gravity and capillary forces during counter-current imbibition process, we use inverse Bond number [57-59] defined as:

$$N_B^{-1} = C_1 \frac{\sigma_{ob} \cos \theta}{(\Delta\rho)gH} \sqrt{\frac{\varphi}{K_{abs}}} \quad (8)$$

where $C_1=0.4$ for capillary tube model, $\Delta\rho$ the difference in density of oil and water (Kg/m^3), σ_{ob} is interfacial tension (N/m), g is gravity (m/s^2), H is height of the core (m), φ is porosity (fraction), and K_{abs} is absolute permeability (m^2). Generally, capillary forces are dominant for $N_B^{-1} > 5$, gravity and capillary forces are active for $0.2 < N_B^{-1} < 5$, and gravity is dominant for $N_B^{-1} < 0.2$ (Schechter et al., 1994). **Table 2.6** shows the calculated inverse Bond number for all samples from the two wells. The calculated inverse Bond number value is much higher than 5 for all samples. Therefore, capillary forces are dominant during the spontaneous imbibition in partly saturated samples.

Figure 2.20 shows that oil is expelled from all faces of the rock samples. Schechter et al. [58] proposed three different patterns for oil and brine displacement (**Figure 2.23**) during imbibition based on relative strength of capillary and gravity forces. Based on the pictures shown in **Figure 2.20**, our experimental results match with **Figure 2.23a** where oil is expelled from all directions. Therefore, both qualitative and quantitative analyses prove that in our experiments capillarity is the dominant force, and gravity effect is negligible.

2.4.5. Scaling Groups

Scaling groups have been applied to predict the oil recovery at the field scale by use of spontaneous imbibition data. Different types of scaling groups have been identified for different types of porous media [60-63]. The imbibition data depend on petrophysical properties (porosity and permeability) of rock, fluid properties (viscosity, interfacial tension) and experimental conditions (size of samples, shape of sample and boundary conditions). The [63] scaling group is defined as:

$$t_D = C_2 t \sqrt{\frac{K_{abs}}{\phi} \frac{\sigma_{ob}}{\sqrt{\mu_o \mu_w}} \frac{1}{L_c^2}} \quad (9)$$

$$L_c = \frac{Ld}{2\sqrt{d^2 + 2L^2}} \quad (10)$$

where t_D is dimensionless time, $C_2 = 0.018849$, t is the actual time (min) of imbibition, K is the absolute permeability (mD), ϕ is the rock porosity, σ is the interfacial tension (dyne/cm), μ_o is the oil viscosity (cp), μ_w is the water viscosity (cp), L_c is the characteristic length, L is the length of sample (cm) and d is the diameter of sample (cm). Normalized oil recovery (R_N) is also defined as:

$$R_N = \frac{R}{R_\infty} \quad (11)$$

where R is the oil recovery (cc) at each time step and R_∞ is the ultimate oil recovery (cc). We plotted the spontaneous imbibition data using Ma et al. [63] scaling equation. **Figure 2.24** shows the normalized oil recovery (R_N) versus dimensionless time (t_D) for samples from well 1 and well 2. The scaling does not result in the convergence of the

imbibition data onto a single curve for samples from well 1. Scaled imbibition data are relatively scattered for samples of well 1 (**Figure 2.24a**). In contrast, scaling results in the convergence of the imbibition data onto a single curve for samples of well 2 (**Figure 2.24b**). One possible reason for the observed scattering may be neglecting the effect of wettability. Wetting affinities of samples from well 1 may be different and this is not accounted for in the scaling equation. In addition, the heterogeneity of the samples from well 1 is more than those from well 2 and can explain the scattering of oil recovery data.

Table 2.6. Inverse bond number for samples of well 1 and well 2.

	Sample	N_B^{-1}
Well 1	1	159
	2	72
	3	309
	5	520
	6	237
	7	163
	8	508
	9	112
	10	40
Well 2	1	446
	2	725
	4	382
	5	292
	6	682
	7	720
	8	422
	10	562

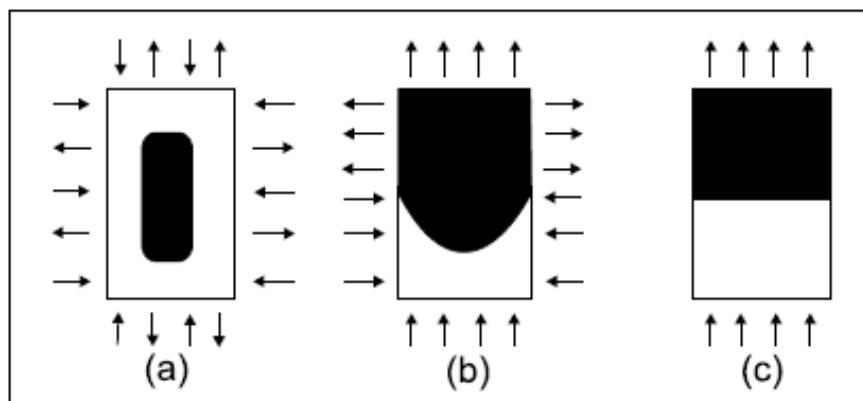


Figure 2.23. Distribution of oil and water inside cores where spontaneous counter-current imbibition is driven by (a) capillary forces; (b) capillary-gravity forces and (c) gravity forces.

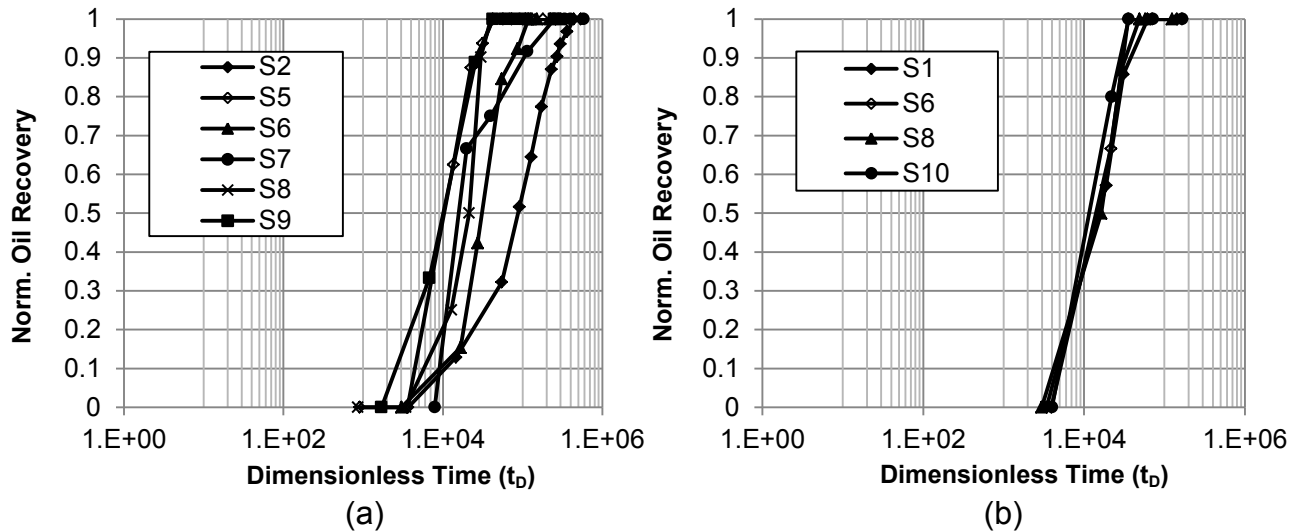


Figure 2.24. Normalized oil recovery versus dimensionless time given by Ma et al. [63] for samples from (a) well 1 and (b) well 2.

2.4.6. Effect of Layering on Oil Production

Figures 2.20c and d show that oil is preferentially produced from some layers of the samples soaked in brine. The layered structure of an example sample is visible in **Figure 2.25**. It appears that water is preferentially imbibed into the layers with lighter color, and oil is produced from the layers with darker color. There are two main reasons for presence of layers in the rock samples: (i) the difference in concentration of different minerals and (ii) the difference in porosity and permeability of layers. To address the first reason, we conducted SEM/EDS analysis on the three different layers (**Figure 2.25**) to investigate the mineralogy of different layers. Certainly, there are some differences in minerals concentration in different layers; for instance, the concentration of pyrite in layer 2 is higher than that in other layers. Pyrite shows the mixed-wet behavior and may be responsible for brine imbibition and oil recovery whiles other minerals such as quartz and carbonates are randomly distributed in other layers. We did not observe distinct difference in the quartz and carbonates composition in the layers, as shown in **Appendix A**.

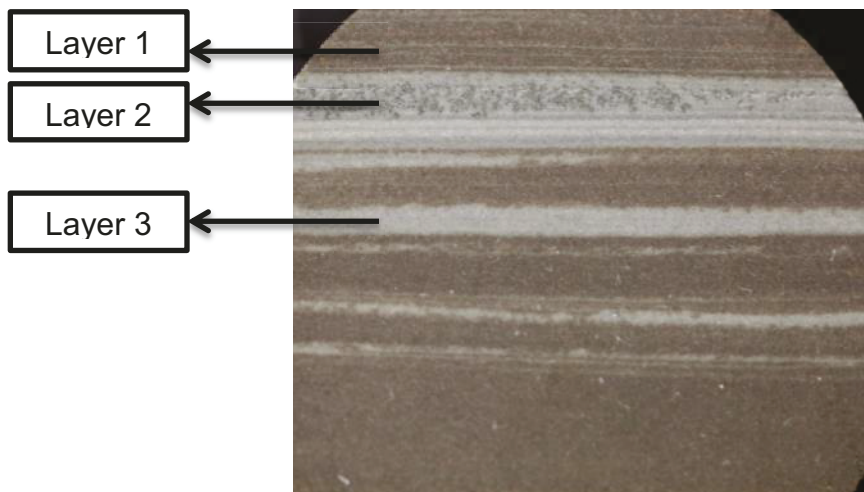


Figure 2.25. Cross section of a layered MT sample. Layer 1 contains more quartz, feldspars; layer 2 contains more pyrite, quartz, feldspars; layer 3 contains more quartz, feldspars, and carbonates

2.5. Proposed Laboratory Procedure for Wettability Evaluation of Tight Rocks

We conclude that systematic measurement of contact angles and spontaneous imbibition on rock samples is essential for better understanding of the wettability of tight rocks. We propose the measurement of both air/liquid (air/brine or air/oil) and liquid/liquid (oil/brine) contact angles. In addition, two types of imbibition experiments are proposed as: oil and brine imbibition into the fresh samples and oil (or brine) imbibition into the brine- (or oil) saturated samples.

Air/liquid contact angle measurements may represent the wettability of fresh samples, mainly saturated with air. Comparative wetting affinity of oil and brine is evaluated by conducting the imbibition experiments on twin fresh samples. One plug of each twin sample is immersed into the brine and another plug is immersed into the oil. Imbibed volume of brine (or oil) is measured and plotted versus time. Comparison of WI_b and WI_o reveals the wetting behavior of fresh samples. If the $WI_o > WI_b$, then fresh samples are preferentially oil-wet, and if $WI_b > WI_o$, fresh samples are preferentially water-wet. If $WI_b \approx WI_o \approx 0.5$, the samples are mixed-wet.

Liquid/liquid contact angle on oil (or brine)-saturated cores shows the preferential tendency of the rock surface to the liquid phases. To understand the wetting affinity of the effective pore network, spontaneous imbibition on oil (or brine)-saturated samples is proposed. Oil-saturated plugs are immersed in the brine and brine-saturated plugs are immersed in the oil. Oil will be produced if brine can imbibe into the oil-saturated samples and displace the oil out. In contrast, brine will be produced if oil can spontaneously imbibe into the samples and displace the brine out. Although spontaneous imbibition is time consuming, its results are more reliable than other conventional methods which require application of external forces such as high pressure injection, which may alter the pore network of the rock.

To have more representative data for field applications, we recommend spontaneous imbibition on oil-(or brine) saturated samples and liquid/liquid contact angle measurements under reservoir conditions. To complement the wettability tests, we recommend conducting detailed analysis of SEM/EDS and thin section images to investigate the existence possible relationships between the core-scale wettability and pore-scale features. For instance, we explained the mixed-wet behavior of the Montney core samples by observation of multi-mineral pores in thin section and SEM/EDS images.

2.6. Significance of Results for Field Applications

Understanding the wettability behavior of tight oil rocks can help the industry to select the optimum fracturing and treatment fluids, and to optimize the soaking and flowback processes. The results suggest that the Montney rock samples show the mixed-wet behavior at 1) pore scale due to the presence of multi-mineral pores, and 2) core scale due to the presence of thin layers with different wettabilities. The results show that counter-current spontaneous imbibition of brine into the oil-saturated samples can effectively displace and expel the oil out of the samples. This process may occur when the wells are soaked with aqueous fracturing fluids. Our observations suggest that fracturing operations with aqueous fluids may assist oil production due to imbibition of fracturing fluid into the matrix. The results of brine imbibition tests can be used for prediction of oil recovery at the field scale by application of scaling groups. Produced oil volume from the small rock samples in the laboratory can be used to estimate the oil

recovery at the field by using the plot of normalized oil recovery versus dimensionless time.

2.7. Conclusions

We conducted systematic and comparative imbibition experiments on core samples from two different wells drilled in the Montney Formation, which led to the following results:

- The fresh samples have similar affinities to oil and brine. It can be explained by the complex pore structure of the MT samples as observed in the thin section images. The images show that a significant number of pores are between different grains such as quartz and dolomite. In general, it is known that quartz tends to be water-wet while carbonate minerals tend to be oil-wet.
- Oil imbibes faster than brine into fresh samples. It cannot be explained by Young-Laplace-based imbibition models. Therefore, additional mechanisms such as adsorption of oil on organic matter can be responsible for the observed quick oil uptake. The presence of organic matter is evident in the SEM/EDS images. Furthermore, this result is consistent with complete spreading of oil on the surface of fresh samples in the presence of air.
- Spontaneous imbibition of brine into the oil-saturated samples results in oil production. This indicates the strong affinity of oil-saturated samples to brine. Interestingly, although oil completely spreads on the surface and imbibes quickly into the fresh samples (partly saturated with air), it cannot imbibe into the brine-saturated samples. However, brine imbibes spontaneously into and expels the oil out of the oil-saturated samples. The measured oil recovery is in the range of 25 % to 45 % and most experiments reach equilibrium after one month of soaking in brine. The remaining oil is expected to be trapped in small oil-wet pores and also in the strongly water-wet pores due to the snap-off mechanism.
- Some rock samples have a layered structure and oil is preferentially produced from specific layers. This indicates the effect of layering on oil production. The pictures of oil-saturated samples immersed in brine suggest that brine is preferentially imbibed into certain layers (usually with lighter color), and oil is produced from other layers (usually with a darker color). This observation

indicates that the layered structure can result in mixed-wet behavior at the core scale.

Chapter 3 Wetting Behavior of Tight Rocks: From Core-Scale to Pore-Scale

3.1. Introduction

Wettability is the tendency of a fluid to preferentially wet a solid surface in the presence of other fluid(s) [64, 65]. Understanding the wettability of natural rocks has significant applications in petroleum reservoir engineering [66-68], cleanup of underground reservoirs contaminated by non-aqueous phase liquids (NAPL) [69, 70], and CO₂ sequestration in subsurface geological formations [71-74]. Wettability impacts (a) the fluids distribution at the pore scale, (b) the irreducible water saturation, (c) efficiency of an immiscible displacement such as water flooding in hydrocarbon reservoirs, (d) rock-fluid properties such as capillary pressure and relative permeability, and (e) electrical properties of porous media [75]. There is a wide spectrum in wettability states changing from strongly water-wet to strongly oil-wet states. Four general wettability states are water-wet, fractional-wet, mixed-wet, and oil-wet. In the water-wet state, water fills the smaller pores and dead ends, and forms a thin film on the rock surface while oil exists in the larger pores stretching out on the water film [65]. In the fractional-wet state [76], the spatial distribution of the wettability is random with respect to pore size and minerals [77]. In the mixed-wet state [78], small pores in the rock are water-wet and saturated with water while the larger pores are oil-wet and saturated with oil [79]. In the oil-wet state, oil fills the smaller pores and forms a thin film of oil on the pore walls while water exists in the larger pores [65].

Young equation relates the contact angle, θ , to interfacial tension values:

$$\cos \theta = \frac{\sigma_{sv} - \sigma_{sl}}{\sigma_{lv}} \quad (1)$$

Here, σ_{sv} , σ_{sl} , and σ_{lv} are the solid/vapor, solid/liquid, and liquid/vapor interfacial tensions, respectively. To apply this equation, it is assumed that solid surface is smooth, homogeneous, non-deformable, and insoluble in the liquid [80]. The Young equation provides a macroscopic contact angle (**Figure 3.1a**).

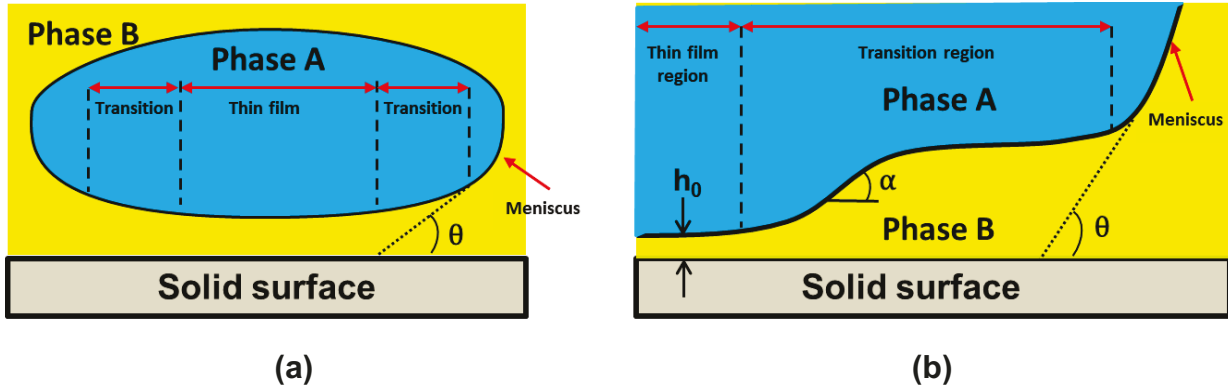


Figure 3.1. (a) Contact region between two fluids and a solid surface. The extrapolated meniscus makes the macroscopic contact angle with the solid surface. (b) Profile of meniscus and thin film in transition zone (Modified after [81]).

The surface forces acting on the solid/liquid (phase A) and liquid (phase A)/liquid (phase B) interfaces within the transition zone can modify the shape of the local angles in the vicinity of three-phase contact line at the microscopic scale [82]. Therefore, the macroscopic contact angle can be different from the local microscopic angles at the three-phase contact line (**Figure 3.1b**).

The effect of surface forces (acting between two interfaces) on the stability of the liquid film coating the solid surface becomes more important when the size of pore-throat decreases to less than 100 nm [26, 83]. In unconventional resources (e.g. tight oil formations and shales), the wettability evaluation becomes more challenging [84-86] since (i) a significant portion of pores has the throat radius less than 1 μm , and (ii) there exists a wide spectrum of components with different wetting affinities such as organic matter and clays. So far, macro (mm)-scale contact angles measured by sessile drop and captive bubble methods have been used to evaluate the wettability behavior of rocks. Several parameters such as roughness of the solid surface, the drop (bubble) size, and environmental vibration affect the contact angle measurements. Therefore, contact angles measured by routine methods provide an average wettability for a rock-fluid system. A recent study [87] evaluated the micro-scale variation in wettability of Bakken tight oil formation by live imaging of water contact angles with an environmental field emission scanning electron microscope (E-FESEM). They measured the contact angles of oil and water micro-droplets on small samples cut from core plugs. The live imaging of water condensation/evaporation experiments on cryogenically frozen rock

samples is applied to measure the micro-scale contact angles. Measuring contact angles at the micro-scale using the E-FESEM can be more representative of rock-fluid interactions in tight rocks compared with routine methods. Although working with the E-FESEM and preparing rock samples are not as simple as routine methods, the results of contact angles measured at the micro scale can explain how mineral heterogeneity and surface roughness affect the wettability behavior in tight rocks. Previous studies show that the Bakken Formation is generally oil-wet or intermediate-wet [48, 88] at the macro-scale. Deglint et al., [87] showed that the water contact angles measured for dolomite crystal and potassium feldspar grains in the Bakken rock samples are approximately 68° and 95° , respectively. The oil contact angle measured for cryogenically frozen oil ranged from 109° to 130° . Although the literature is enriched by the wettability evaluation of tight rocks at the macro scale during the last decade, the wettability behavior of tight rocks at the pore scale is not well understood. To explain how intermolecular forces behave in the narrow pore systems, we take into account the forces acting at the solid/liquid and liquid/liquid interfaces by implementing the Derjaquin, Landau, Verwey, and Overbeek (DLVO) theory. This theory enables us to understand the stability of the film coating the solid surface.

The oil reservoirs were considered for many years as strongly water-wet formations because oil was migrated into formations filled originally with water [20, 89, 90]. In a strongly water-wet system, a water film separates the rock surface from oil. The water film collapses when oil comes into the contact with the rock surface [91]. As capillary pressure (pressure difference between non-wetting phase and wetting phase) increases, water film thickness decreases until capillary pressure reaches its critical point. By exceeding from critical capillary pressure, the water film collapses into molecularly-adsorbed water monolayers. Then, the oil polar components such as asphaltenes contact directly with the pore walls, adsorb irreversibly onto the pore walls, and change the wettability to the oil-wet state [29, 81, 89, 91, 92]. Small pores and corners of the pore space remain water-wet due to the high capillary pressure required for the water displacement, leading to mixed-wet conditions. Although fluid flow in mixed-wet systems has been extensively modeled for estimation of capillary pressure and relative permeabilities [67, 93-97], few studies investigated experimentally multi-

phase flow in mixed-wet synthetic rocks [98, 99] and real rocks [100-103]. Different methods have been implemented to prepare a mixed-wet system including (1) mixing the oil-wet sands treated with octadecyltrichlorosilane solutions and water-wet sands at different ratios [98, 99], (2) freezing the initial water followed by flushing with a stable chemical group to make the pore surface hydrophobic [101], and (3) doping the oil with fatty acids and aging the cores overnight to make them mixed-wet [103].

In addition to the intermolecular forces acting at the solid/liquid and liquid/liquid interfaces separated by an interlayer film, the type of solid surface affects the wettability state. Most sedimentary rocks are not uniform with respect to mineralogy and they are composed of a wide range of minerals such as carbonates, quartz, and clay. These heterogeneous solid surfaces present different surface forces compared with pure minerals. The effect of mineral heterogeneity on the wettability of downhole core plugs is poorly understood. To understand how mineralogy affects the wettability at the sub-micron scale, we compare the adhesion forces (F_{adh}) measured for different pure minerals with those measured for real heterogeneous rock surfaces by conducting atomic force microscopy (AFM) analysis. AFM analysis is used as an accurate tool at the sub-micron resolution i) to visualize the pore structure on tapping mode and ii) to measure adhesion forces between the tip of the cantilever and a solid surface on the contact mode [104-108].

The objective of this chapter is to understand how mineral heterogeneity and intermolecular forces acting at solid/liquid and liquid/liquid interfaces can affect the wettability behavior of tight rocks. First, we review the results of our previous experiments conducted on downhole core plugs collected from two wells drilled in the Montney (MT) tight oil formation. Second, we conduct pore-scale visualizations on thin section samples and SEM/EDS analyses. Third, we apply the DLVO theory to explain the spontaneous imbibition results by calculating the intermolecular forces acting at solid/liquid and liquid/liquid interfaces. We investigate how mineral heterogeneity can influence the stability of a thin film covering the rock surface. Fourth, we measure adhesion forces for the main minerals of the MT rock samples, i.e. quartz and calcite, by performing AFM analysis to understand how pure minerals behave at pore scale.

Finally, we compare the adhesion forces measured for the pure minerals with those measured for thin sections of the rock samples.

3.2. Review of Previous Spontaneous Imbibition and Contact Angle Results

In our previous paper [100], we evaluated wettability of the core plugs collected from two wells drilled in the MT tight oil Formation (**Figure 3.2**). Here, we summarize the main conclusions from the previous experiments.

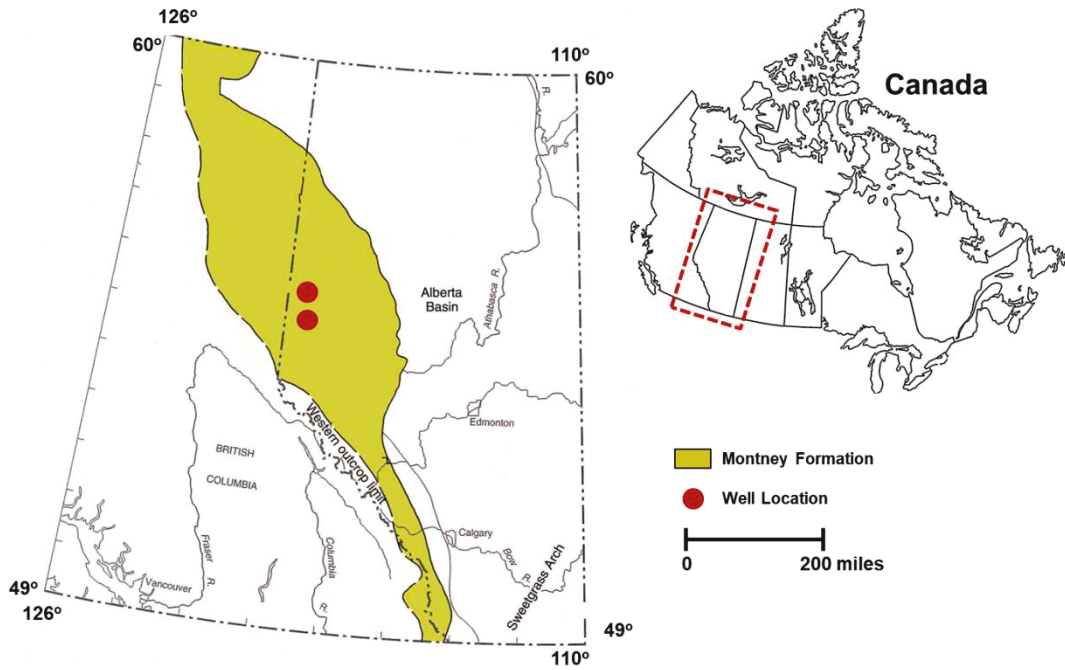


Figure 3.2. The study area in the Montney Formation located in the western Canadian sedimentary basin (modified after [109]).

We conducted a series of spontaneous imbibition tests using reservoir oil, reservoir brine, and 15 downhole core plugs to compare the wetting affinity of the core plugs. We did not clean the core plugs with solvent since the natural wetting affinity of the intact core plugs changes as a result of solvent treatment [110]. We cut each full-length core plug into half to prepare twin plugs with similar petrophysical properties, and place one plug of each twin set in the imbibition cell filled with the reservoir brine and the other plug in the imbibition cell filled with the reservoir oil. The mass gain is recorded by an

accurate electronic balance for the period of at least three months. The results of spontaneous imbibition tests conducted on dry core plugs showed that oil and brine imbibe into the core plugs similarly. The wetting indices calculated based on the total imbibed volume of oil and brine into each set of twin core plugs are close to 0.5, indicating the similar wetting affinity of the dry core plugs to oil and brine which suggests mixed-wet behavior.

Next, we performed contact angle (CA) measurements on polished end-pieces of the core plugs using Attension Theta (Biolin Scientific) equipped with Navitar lens (1984×1264 pixel resolution) and an LED light source. The results of CA measurements showed that the oil droplets completely spread on while the brine partially wets the MT end-pieces. The contact angle results support the mixed-wet behavior observed from the spontaneous imbibition tests.

Finally, we performed spontaneous imbibition tests on oil-saturated (or brine-saturated) core plugs. We placed the oil-saturated (or brine-saturated) core plugs into the imbibition cells filled with the reservoir brine (or oil). Then, we periodically measured the volume of oil produced during brine imbibition and that of brine during oil imbibition. We observed that the brine can imbibe into the oil-saturated core plugs and expel the oil out while the oil cannot imbibe into the brine-saturated core plugs and displace the brine. The oil recovery factor was in the range of 25% to 45%. Therefore, the core plugs tends to be water-wet when saturated with oil and brine.

3.3. DLVO Theory and Wettability

Here, we apply the Derjaguin, Landau, Verwey, and Overbeek (DLVO) theory for the rock surface/fluid 1/fluid 2 system to investigate the stability of fluid 1 (water or oil) film separating the rock surface from fluid 2 (oil or water) during the spontaneous imbibition test as shown in **Figure 3.3..** The thickness of the film covering the rock surface is usually very small (<< 100nm thick) compared with the size of pores [90].

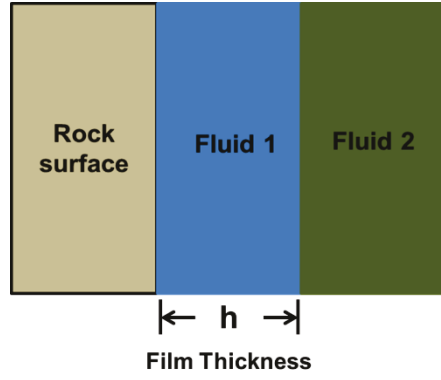


Figure 3.3. Film of fluid 1 covers the rock surface in the presence of fluid 2.

The pressure required to resist the attractive forces between fluid 1 and rock surface and to lift fluid 1 film (**Figure 3.3.**) from the rock surface is the disjoining pressure [111]. The film of fluid covering the rock surface is stable when the disjoining pressure (P_t) is positive while it is unstable when the disjoining pressure becomes negative. The repulsive and attractive forces are dominant when P_t is positive and negative, respectively. P_t is the summation of the van der Waals, electrostatic (double layer), and structural forces:

$$P_t(h) = F_{VDW}(h) + F_{DL}(h) + F_S(h) \quad (2)$$

Here, P_t , F_{VDW} , F_{DL} , F_S , and h are the total disjoining pressure, van der Waals forces, double layer forces, structural forces, and the separation distance between the rock surface and fluid 2, respectively.

F_{VDW} between two dissimilar objects separated by a third surface can be attraction (negative) or repulsion (positive). The van der Waals contribution of the disjoining pressure is dominant at the longer distance from the rock surface when the film of fluid covering the rock surface is thick. F_{VDW} between two parallel plates is calculated as [112]

$$F_{VDW}(h) = \frac{-A_H \left(15.96 \frac{h}{\lambda_{lw}} + 2 \right)}{12\pi h^3 \left(1 + 5.32 \frac{h}{\lambda_{lw}} \right)^2} \quad (3)$$

where A_H is the Hamaker constant for the system, h is the separation distance between the rock surface and fluid 2 layer, λ_{lw} is the London-wavelength and is assumed to be 100 nm [112].

To calculate the Hamaker constant based on the traditional approach, the geometric mean of the interactions for each media with itself is calculated. The Hamaker constant for a film of material 3 between material 1 and 2 is given by

$$A_H = (A_{11}^{0.5} - A_{33}^{0.5})(A_{22}^{0.5} - A_{33}^{0.5}) \quad (4)$$

where A_{11} , A_{22} , and A_{33} are Hamaker constants of the rock surface, fluid 2, and fluid 1 film, respectively. The values of parameters presented in Eq. 4 are provided for different materials in the literature [81, 91, 113-115]. However, Hamaker constant for the heterogeneous rock samples is not reported in the literature, and its measurement is out of the scope of this study. So, $A_{H(\text{rock})}$ is assumed to be the weighted average of Hamaker constants for the main minerals composing the rock sample as

$$A_{H(\text{rock})} = \frac{\sum_{i=1}^n C_i \times (A_H)_i}{\sum_{i=1}^n C_i} \quad (5)$$

where C_i and $(A_H)_i$ stand for the concentration and the Hamaker constant of component i , respectively.

F_{DL} between charged surfaces can be either attraction (negative) or repulsion (positive) depending on the pH and salinity of the electrolyte medium [91, 116, 117]. The double layer forces for a constant potential can be calculated using the reduced surface potentials of fluid 2/fluid 1 and rock/fluid 1 pairs as [118]

$$F_{DL}(h) = n_b k_B T \left[\frac{2\psi_{r1}\psi_{r2} \cosh(kh) - \psi_{r1}^2 - \psi_{r2}^2}{(\sinh(kh))^2} \right] \quad (6)$$

where n_b , k_B , T , ψ_{r1} , ψ_{r2} , κ , and h are the ionic density of fluid 1, Boltzmann constant (1.38×10^{-23} J/K), absolute temperature (293.15 K in this study), reduced surface potential for fluid 2/fluid 1 pair, reduced surface potential for rock/fluid 1 pair, the reciprocal Debye-Huckel length, and the separation distance between rock surface and fluid 2 layer (m), respectively. The reciprocal Debye-Huckel double layer length is calculated as

$$\kappa^{-1} = \sqrt{\frac{\epsilon_0 \epsilon k_B T}{\sum_{i=1}^n C_{i,0} e^2 Z_i^2}} \quad (7)$$

where ϵ_0 , ϵ , $C_{i,0}$, e , and Z_i are the vacuum dielectric constant (8.85×10^{-12} F/m), the dielectric constant of fluid 1 (80.1 at 20°C in this study), number density (# ion/m³), the electron charge (1.6×10^{-19} C), and the valency of ions, respectively.

To calculate the reduced surface potential, we measure the zeta potential of fluid 2/fluid 1 and rock/fluid 1 pairs. The reduced surface potentials are calculated as

$$\Psi_{ri} = \frac{e\zeta_i}{k_B T} \quad (8)$$

where ζ_i is the zeta potential (mV) for a pair of components.

The repulsive F_S increases when the thick water film collapses into molecularly thin film of fluid 1. Then, fluid 1 forms a thin film covering the rock surface. F_S is calculated for water [90] as

$$F_{S-water}(h) = A_s \left(e^{\frac{-h}{h_s}} \right) \quad (9)$$

where A_s and h_s are the structural forces coefficient, and the characteristic decay length, respectively. In this study, we assume the values suggested in the literature [81] as 1.5×10^{10} Pa for A_s and 0.05 nm for h_s .

F_S is also calculated for oil [119] as

$$F_{S-oil}(h) = C_1 \times e^{-h/\lambda_1} + C_2 \times e^{-h/\lambda_2} \quad (10)$$

where C_1 and λ_1 are the magnitude and the decay length of short-range forces for the exponential model, respectively. C_2 and λ_2 are the magnitude and decay length of the long-range forces, respectively. These parameters are evaluated by fitting the experimental data. We assume the values suggested in the literature [119] as 8.86×10^7 Pa and 2.87×10^6 Pa for C_1 and C_2 , respectively. λ_1 and λ_2 are assumed to be 0.10 nm and 0.35 nm, respectively.

The contact angle is derived by a direct integration of the augmented Young-Laplace equation as [120]

$$\cos \theta = 1 + \frac{1}{\sigma} \int_{h_o}^{h_p} P_t(h) dh \quad (11)$$

where h_o and h_p are the thickness of the very thin stable film of a fluid covering the solid surface (The thickness of monolayer water film is approximately 3.5 Angstroms) and the thickness of the layer where the disjoining pressure is important (P_t is close to zero), respectively. σ stands for surface tension and interfacial tension for air/liquid and liquid/liquid conditions, respectively.

3.4. Materials and Methods

3.4.1. Core Properties

Thin section, SEM/EDS, and AFM analyses and zeta potential measurements are conducted using downhole core plugs collected from two wells drilled in the MT Formation. **Table 3.1** lists the petrophysical properties of the core plugs used in this study. Quartz and carbonates (calcite and dolomite) are the main components of the core plugs evaluated by x-ray diffraction (XRD) analysis (**Table 3.2**). More details about the mineralogy of the core plugs are provided elsewhere [100].

Table 3.1. Petrophysical properties of the core plugs.

Sample No.	Depth(m)	Permeability ($k_{\text{air}} \times 10^{-3}$, $(\mu\text{m})^2$)	Porosity (Helium)
1	1571.89	0.602	0.102
2	1578.26	2.240	0.159
3	2380.24	0.125	0.0724
4	2390.9	0.416	0.088
5	2393.94	0.053	0.0762

Table 3.2. Mineral composition of the core plugs. Heavy minerals can be rutile, anatase, ankerite, rhodochrosite, and fluorapatite.

Mineral (wt%)	Sample No.				
	1	2	3	4	5
Quartz	51	50	33	44	41
K-Feldspar	5	8	9	12	13
Plagioclase	5	5	1	1	1
Calcite	0	0	12.5	9	10
Dolomite & Fe-Dolomite	25	21	29	17	19
Pyrite	3	1	1.5	1	1
Illite/Smectite	3	3	0	0	0
Illite/Mica	7	7	3	3	3
Kaolinite	1	3	10	12	11
Heavy Minerals	0	0	1	1	1

3.4.2. Pure Minerals

Pure calcite and pure quartz are purchased from Sigma Aldrich with the purity of 99% to measure the zeta potential used for calculation of the electrical double layer forces. Moreover, the fresh and clean calcite crystal (MTI Corporation, US) and quartz slides (TED Pella Inc., US) are used to measure the adhesion force by using atomic force microscope.

3.4.3. Fluid Properties

The MT crude oil and reservoir brine are used for the zeta potential measurements. Reservoir brine is a highly saline water (TDS= 136,630 ppm) and the produced oil from these two wells is characterized as light oil (API=37.96). **Table 3.3** lists the concentration of cations and anions of saline reservoir brine evaluated with the flame atomic absorption spectrophotometry (EPA SW-848 7000B) and the ion chromatography (SM 4110B) methods, respectively.

Table 3.3. Ion composition of the saline reservoir brine.

Cations		Anions	
Ion	mg/L	Ion	mg/L
Na	46,200.0	Cl	84,867.0
K	1,260.0	Br	126.0
Ca	1,670.0	I	66.7
Mg	1,030.0	HCO ₃	1,748.0
Ba	1.2	SO ₄	744.0
Sr	28.7	CO ₃	
Fe	2.1	OH	

3.5. Methodology

First, pore-scale visualizations are conducted using thin section and SEM/EDS images. Second, the DLVO theory is applied to explain the mixed-wet and water-wet behavior of the core plugs at dry and wet initial conditions, respectively. To calculate the total disjoining pressure, the zeta potential for different suspensions is measured. Third, the adhesion forces for quartz and calcite are measured by performing AFM analysis, and the values are compared with those measured for the thin section of the rock samples.

3.5.1. Step1: Visualization of Rock Surface

3.5.1.1. Thin Section Analysis

Thin layers of the core plugs are cut by using a diamond saw to prepare thin sections. Then, each thin flat layer is glued to a glass slide using epoxy. The thickness of the thin section is adjusted to 30 μm using a grinder and a fine abrasive grit. The section is then placed in a holder and spun on a polishing machine until a suitable polish is achieved. Blue epoxy is used for identification of pores.

To analyze the thin sections, Nikon ECLISPSE 50i POL polarizing microscope is used, which is equipped with a digital camera, and an ELMO P10 Visual Presenter image capturing. The thin sections are visualized under plane and cross polarized lights.

3.5.1.2. SEM/EDS Analysis

The end-pieces of the core plugs are used for SEM/EDS analyses using Zeiss Sigma field emission scanning electron microscope (FE-SEM) equipped with secondary electron (SE) and energy dispersive x-ray spectrometry (EDS) electron beams. SE images are routinely used for analyzing the surface morphology. EDS also provides the elemental mapping of the surface. The SEM/EDS analyses are conducted on three different spots for each sample.

3.5.2. Step2: Implementing the DLVO Theory for the Wettability Evaluation

3.5.2.1. Zeta Potential Measurements

To investigate the wettability behavior of the core plugs based on the DLVO theory, the van der Waals, double layer, and structural forces are calculated. To calculate the double layer forces, the zeta potentials of i) rock powder/water suspensions (ζ_1 in Eq. 8) and ii) the oil emulsion in water (ζ_2) are measured by using a Malvern Zetasizer Nano ZS. The tests are performed at 20°C and atmospheric pressure. The results of zeta potential measurements enable us to calculate the double layer forces (Eq. 6). Water is an electrolyte medium while rock powder and the oil are the dispersant particles and droplets, respectively.

Several studies have investigated the effect of temperature on zeta potential of intact natural sandstones [121], intact natural carbonates [122], intact granite [123], pure Ottawa and Fontainebleau sands [124], and pure minerals including quartz, calcite, and kaolinite [125]. [125]observed that zeta potentials of quartz, calcite, and kaolinite increase in magnitude by increasing the temperature at low salinity (0.01 M NaCl concentration). They also measured the zeta potential of these pure minerals at different pressures ranged from atmospheric pressure to 513 KPa. By increasing the pressure, zeta potentials of quartz and kaolinite show decreasing and increasing trends in magnitude, respectively. However, calcite shows complex behavior in aqueous solutions. Zeta potential of calcite decreases in magnitude when pressure is less than 310 KPa; while it tends to increase when pressure is more than 310 KPa. In addition to

temperature and pressure, salinity of aqueous phase controls the zeta potential of minerals. Further studies are required to estimate the zeta potential of water at the reservoir conditions.

Five different solid powder/water suspensions are prepared for the zeta potential measurements by mixing pure calcite powder (Sigma Aldrich), pure quartz powder (Sigma Aldrich), mixture of pure kaolinite and pure smectite (Sigma Aldrich), petroleum coke powder (99% purity, crystalline, particle size < 325 US mesh, Alfa Aesar), and the MT rock powder with water. The contribution of double layer forces on total disjoining pressure decreases by increasing the salinity of the reservoir brine [81]. Therefore, the suspensions are prepared with the reservoir brine diluted 1000 times to emphasize on the effect of double layer forces on the stability of water film. First, a core plug is crushed and ground to prepare rock powder with the particle size of 907 ± 60.57 nm. Next, a solid powder/water suspension is prepared with 0.03 wt% of rock powder by mixing the rock powder with water using a vortex mixer for 5 minutes to make sure that the suspension stays stable during the zeta potential measurement. To prepare the oil emulsion in water, 2 mL of the reservoir oil is added into 10 mL of water and is mixed using a vortex mixer for 5 minutes. Then, the prepared solid powder/water suspension or the oil emulsion is placed in the Malvern Zetasizer and the zeta potential is measured immediately after mixing the substances to avoid i) deposition of the powder at the bottom of the cell and ii) coalescence of oil droplets and formation of oil layer on top of water [91]. The pH of solutions is 6.5-7 for all the samples, and the pH is not changed during zeta potential measurements.

3.5.3. Step3: AFM Analysis

The adhesion forces are measured between the tip of a cantilever and different minerals by conducting AFM analysis (AFM, Dimension Edge, Bruker, USA) in the contact mode. The AFM data are analyzed using Nanoscope Analysis software (V.1.40). All force measurements are conducted in air and at room temperature ($20\pm2^\circ\text{C}$). Contact mode tips (Pointprobe, Silicon SPM-Sensor, NanoWorld AG, Switzerland) are used in this study. This uncoated standard tip is designed for contact mode imaging and for high sensitivity force measurements due to a low force constant. The resonance frequency

and force constant of the tip are 13 KHz and 0.2 N/m, respectively. The thickness, length and width of the tip are 2 μ m, 450 μ m, and 50 μ m, respectively. The scan area is set to 5 μ m \times 5 μ m, and the scan rate is kept constant at 1 Hz to obtain stable images. The adhesion forces between the tip and a solid surface are measured by recording the deflection of the cantilever as a function of tip-sample distance. The deflection of cantilever can be related to the force between the tip and the surface by Hooke's law. **Figure 3.4** shows a typical force-distance plot in approach and retract stages. In the approach stage, tip of the cantilever is brought close to surface. At large separation distance, no interaction forces are detected (A) and the cantilever does not deflect in this part of the approach stage. As the tip-surface distance decreases and the tip reaches close to the surface, interaction forces such as van der Waals and electrostatic interactions become significant (B). When the attractive forces exceed the spring constant of the cantilever, the tip contacts the surface. The vertical distance between C and D represents the attractive forces. The tip stays in contact with the surface until the retract stage starts from E. As the retract stage continues, the gradient of the adhesion forces at a specific point (F) becomes less than the spring constant of the cantilever. At this point, the tip pulls off from the surface to its equilibrium position (G). The value of adhesion or pull-off forces can be related to the surface energy [126-129]. More details about the adhesion force measurement have been described in the literature [104, 105, 130].

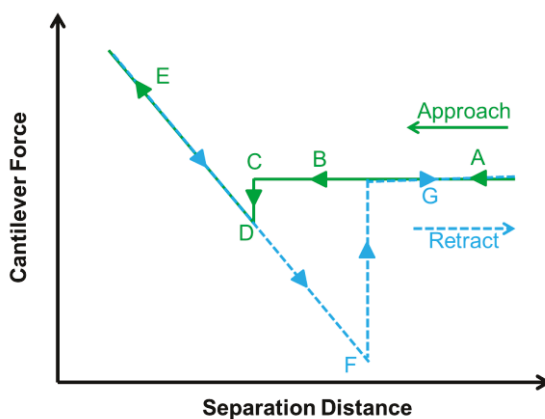


Figure 3.4. A typical force-distance plot measured with AFM

To evaluate the effect of mineralogy on adhesion forces, three different surfaces are selected for the force-distance measurements. First, the force measurements are conducted on clean calcite crystal (MTI Corporation, US) and quartz slides (TED Pella Inc., US). Then, very smooth uncovered thin sections are prepared and the force-distance measurements are performed. Finally, the adhesion forces measured for pure minerals are compared with those for the thin sections.

3.6. Results and Discussion

3.6.1. Step1: Rock Surface Analysis

To explain the spontaneous imbibition results observed in our previous study [100], we investigate the effect of rock mineralogy on wetting behavior. Here, we visualize the pores and identify the mineralogy of the pore walls by thin section and SEM/EDS analyses.

3.6.1.1. Thin Section Analysis

The polarized light microscopy is used for identification of minerals in thin sections. Since minerals show different colors under cross polarized light, we capture images of the thin sections prepared from the core plugs under plane polarized light (PPL) and cross polarized light (XPL) as shown in **Figure 3.5**. Blue areas represent pores in plane polarized images since we used blue epoxy during preparation of thin sections to identify the pores. It is hard to distinguish quartz and feldspars under XPL and PPL analyses. Quartz and feldspars show white and blue colors under plane and cross polarized light, respectively. Carbonates (dolomites/calcite) show brown and rainbow colors under plane and cross polarized light, respectively. The black areas may represent pyrite or organic matter/hydrocarbon residue (HR) under plane polarized light. The pore walls highlighted in **Figure 3.5** suggest the existence of multi-mineral pores, surrounded by quartz, feldspars and carbonates. To understand the wetting behavior of the multi-mineral pores, it is important to evaluate the wetting affinity of individual minerals. Minerals such as quartz, clays (except kaolinite), and mica tend to be more water-wet while carbonates and organic matter/HR tend to be more oil-wet [65]. It is expected that the heterogeneity in the minerals forming the pore walls leads to heterogeneity in wetting behavior of the pores. The spontaneous imbibition results

conducted on dry core plugs showed similar wetting affinity of the core plugs to oil and brine since wetting affinity index of brine and oil were close to 0.5. However, the spontaneous imbibition results conducted on oil-(or brine) saturated core plugs showed that the oil cannot imbibe spontaneously into the brine-saturated core plugs while brine can imbibe spontaneously into the oil-saturated core plugs. The oil recovery factor was up to 45% indicating that more than 50% of the oil was left in the pores. One reason is that a portion of the oil volume is trapped by snap-off mechanism during water imbibition into the water-wet pores. Another reason for retaining the oil in the pores can be the mixed-wet behavior of the core plugs. We hypothesize that these multi-mineral pores are responsible for the mixed-wet behavior of the core plugs. To understand how the contrast in mineralogy affects the wetting affinity of the heterogeneous rocks, we evaluate the stability of the thin films of water and oil coating the rock surface by calculating the total disjoining pressure.

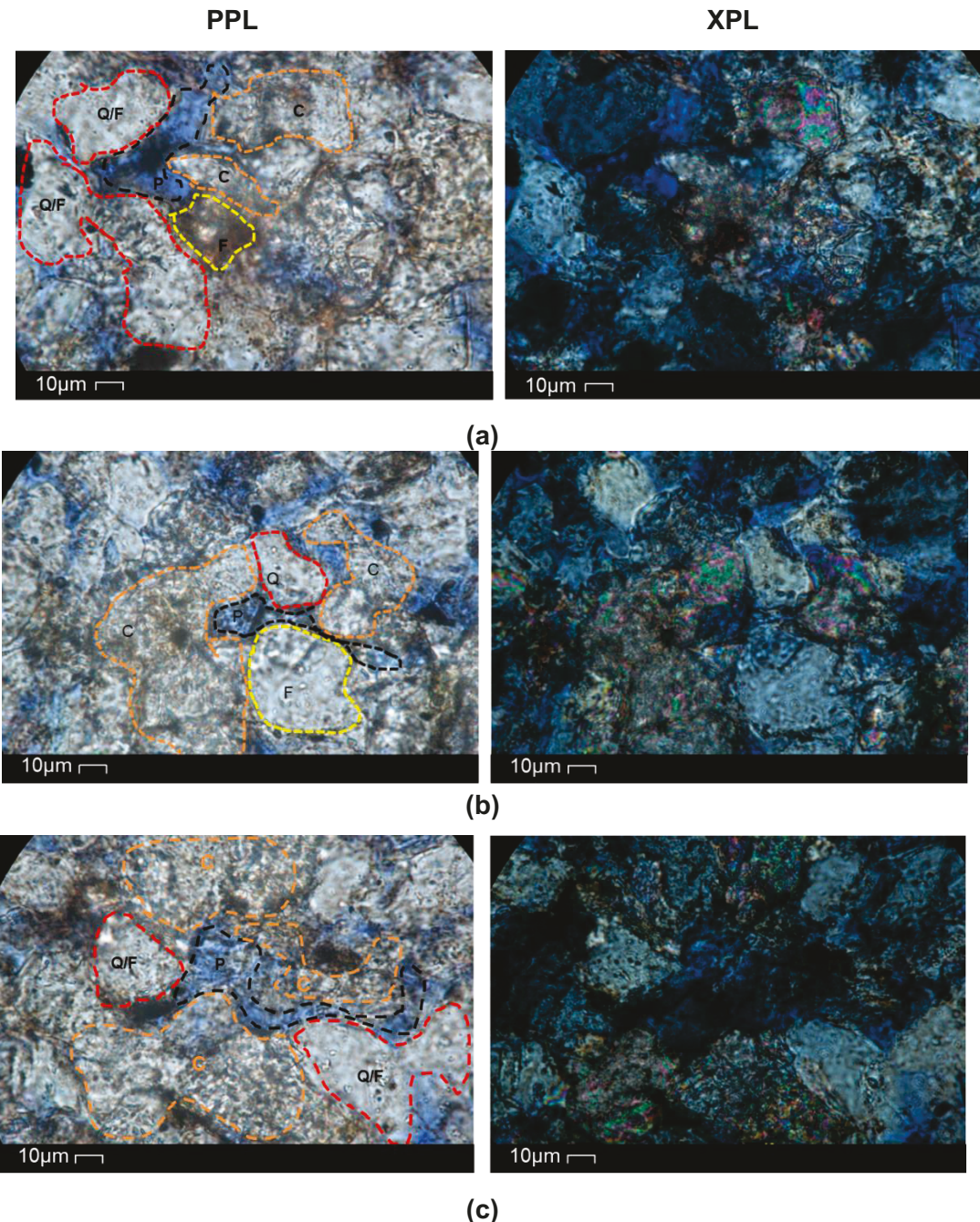


Figure 3.5. The thin sections prepared from the core plugs drilled at (a) 1571.89 m depth under plane polarized light (left) and cross polarized light (right), (b) 1578.26 m depth under plane polarized light (left) and cross polarized light (right), and (c) 1578.26 m depth under plane polarized light (left) and cross polarized light (right). Images presented in parts (b) and (c) are from two different spots of the same thin section sample. Blue areas shown under plane polarized light represent the pores. Areas surrounded by red, orange, and green dashed lines are quartz or feldspar, carbonates and feldspars, respectively.

3.6.1.2. SEM/EDS Analysis

In the next step, we perform SEM/EDS analysis on end-pieces of the core plugs (i) to identify the pores which cannot be identified by thin section analysis, and (ii) to evaluate the minerals surrounding the pores. **Figure 3.6** shows the SE images conducted on core plug 2 (depth of 1578.26 m). Pores located in zone 1 (shown with dashed circle) are surrounded by clay minerals which are not categorized as kaolinite. First, the shape of clays does not look like pseudo-hexagonal plates. Second, potassium exists in the elemental map of this zone, representing non-kaolinite clay minerals. These clays can be categorized as illite/mica or illite/smectite. Previous studies show that clays are divided into hydrophilic and hydrophobic clays in term of wetting affinity. Illite and smectite can retain the bounding water and remain water-wet even after contact with oil while kaolinite can behave differently [131-133]. Phyllosilicate kaolinite is composed of a single tetrahedral silicon-oxygen (siloxane) and an octahedral aluminum-oxygen (gibbsite) sheets. Several studies have been conducted to investigate the wettability of water/oil droplets on kaolinite surfaces [134-136]. Šolc et al. [137] conducted molecular dynamics (MD) simulations to study the wettability behavior of the basal kaolinite. The results showed that water droplets spread on the octahedral sheet, indicating that gibbsite surface is fully hydrophilic; while water droplets form a microscopic contact angle of 105° on the tetrahedral sheet, indicating that the siloxane is hydrophobic. The hydrogen bonds between water molecules are stronger than those between water hydrogens and the siloxane surface, leading to hydrophobic behavior in siloxane surface. Consistently, Greathouse et al. [138] showed the preference of organic molecules to adsorb on the siloxane surface by conducting MD simulations.

Illite/mica and illite/smectite have higher surface charge density, specific area, and cation exchange capacity than kaolinite [132, 139]. The range of illite/smectite, illite/mica and kaolinite concentrations in the MT core plugs are 0-3 wt%, 3-7 wt%, and 1-12 wt%, respectively as listed in **Table 3.2**. So, the pores located in illite/smectite and kaolinite are expected to be water-wet and oil-wet, respectively.

If we assume rectangular shape for pores located in zone 1, the longest pore in zone 1 is 1.87 µm and 116 nm in length and width, respectively. Most of the pores are less than

$1\mu\text{m}$ in length. Moreover, pores located in zones 2 and 3 are multi-mineral pores which may lead to mixed-wet behavior as discussed before.

Figure 3.7 shows the SEM images taken from core plug 2. The circle highlighted with dashed line in **Figure 3.7b** shows flaky edge of a mica crystal. Mica (very rich in aluminum) has tetrahedral-octahedral-tetrahedral (TOT) units like clays and has phyllosilicate structure. **Figure 3.7c** shows the fibrous illite growing from the mica surface. Illite known as the pore bridging clays can be formed as a result of mica and K-feldspar dissolution. The way of handling and drying the core plugs strongly affect the morphology of illite. Drying core plugs with air changes the morphology of illite and leads to accumulation of illite on pore walls [140, 141].

Figure 3.8 shows the pore-throat radius distribution of this core plug evaluated by mercury intrusion capillary pressure (MICP) method. Around 80% of pores have the throat radius less than $1\mu\text{m}$. According to the size of pore throats observed in zone 1 of **Figure 3.6**, water-wet clays may form a significant portion of pores with throat radius of less than $1\mu\text{m}$. Therefore, brine imbibition into the small pores surrounded by clays is expected to take place at the later time of imbibition process. Additional images taken from core plug 3 (depth of 2380.24 m) and core plug 5 (depth of 2393.94 m) are presented in the **Appendix B**.

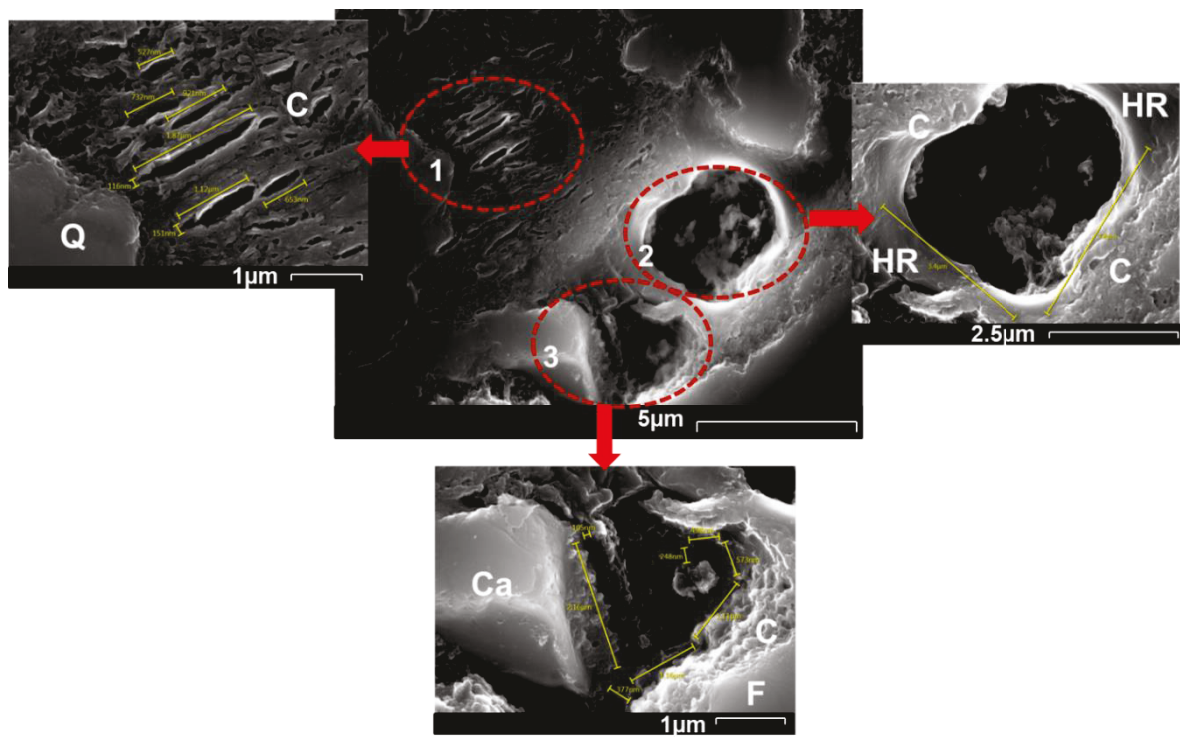


Figure 3.6. SEM images from core plug 2 (depth of 1578.26 m). “Q”, “C”, “F”, “Ca” and “OG” stand for quartz, clay, feldspars, carbonates and organic matter/HR, respectively. Three areas are magnified to show the minerals surrounding the pores.

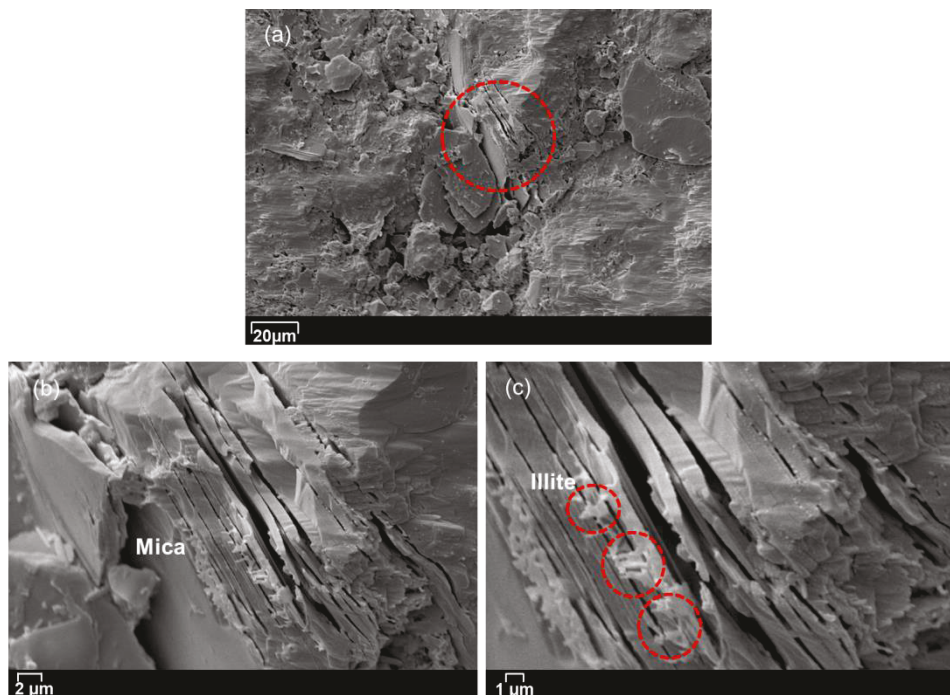


Figure 3.7. (a) An SEM image taken from core plug 2, (b) magnified view of mica located in the rock sample, and (c) fibrous illite accumulated on the mica surface.

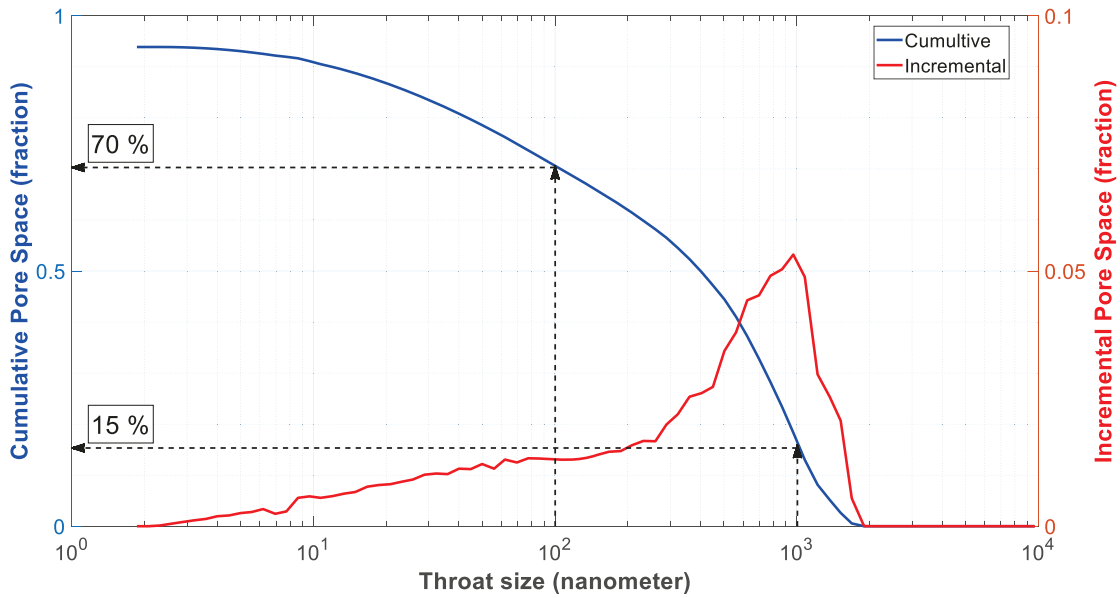


Figure 3.8. Pore-throat size distribution of core plug 2 (depth of 1758.26 m) measured by MICP method. 23%, 55%, and 15% of pores have the throat radius smaller than 100 nm, in the range of 100-1000 nm, and larger than 1000 nm, respectively.

To understand how mineral heterogeneity affects the wetting behavior of the rock samples, we apply the DLVO theory in the next section to understand the intermolecular forces between rock minerals, water and oil at the pore scale. Surface charges of the minerals influence the double layer forces between oil and minerals coated with an electrolyte solution. The surface charge of minerals strongly depends on pH of the solution and dissolution ability of minerals into the aqueous electrolyte solutions [142, 143]. To account for surface charge of the minerals, we decouple the minerals forming the MT core plugs into types 1-4. Type 1 represents quartz and feldspars as these minerals are mainly composed of Si and O elements and show negative surface charge in an electrolyte solution at the neutral pH. Type 2 represents calcite and dolomite as these minerals are mainly composed of Ca, C, and O elements and show positive surface charge in an electrolyte solution at the neutral pH. Type 3 represents kaolinite and smectite as the main clay contents in the rock sample. Type 4 represents organic contents. We select pure quartz slides, SiO_2 , and pure calcite crystal, CaCO_3 , as representatives of type 1 and type 2 minerals, respectively. The variations of surface charge of quartz and carbonates at different pH values have been studied before [142-145].

3.6.2. Step 2: DLVO Theory and Wettability

3.6.2.1. The Mixed-wet Behavior of the Dry Core Plugs

In the previous section, we explained that some pores are surrounded by clays (illite/mica and illite/smectite) as shown in zone 1 of **Figure 3.6** and others are surrounded by different minerals. In this section, we calculate and compare the total disjoining pressure for different minerals to investigate the effect of mineral heterogeneity on wetting behavior of solid surface/air/water and solid surface/air/oil systems. Although the Rock-Eval analysis conducted on the MT rock samples used in this study shows no evidence of organic matter, the SEM/EDS analysis shows the existence of organic contents in these samples. The organic contents shown in SEM analysis may be the heavy oil components deposited on the pore walls. We consider the hydrocarbon residue (HR) as a component in all DLVO calculations. In the literature, the Hamaker constant of the hydrocarbon reported in the literature is ranged from 4.5×10^{-20} J (n-Octane) to 10.0×10^{-20} J (crystal). We assume that the highest Hamaker constant value reported in the literature (i.e. hydrocarbon crystal) is for HR. **Table 3.4** lists the Hamaker constants of water and minerals used for calculation of van der Waals forces. We also investigate the effect of oil Hamaker constants ranging from 4.5×10^{-20} J to 9.0×10^{-20} J (

Table 3.5) on total disjoining pressure for all systems.

Table 3.4. Hamaker constants of materials used for calculation of van der Waals forces [114, 146, 147].

Material	Hamaker Constant, $A_H (\times 10^{-20})$ J
Water	3.7
Quartz	6.5
Calcite	12.0
Clays	16.3
HR	10.0

Table 3.5. Oil Hamaker constants used for calculation of van der Waals forces [114, 146].

Oil	Hamaker Constant, $A_H (\times 10^{-20})$ J
Hydrocarbon (crystal)	10
n-Octane	4.5
n-Dodecane	5.0
n-Hexadecane	5.2
Heavy oil-1	6.0

Heavy oil-2	7.0
Heavy oil-3	8.0
Heavy oil-4	9.0

Figure 3.9 shows the disjoining pressure-distance profiles for dry pure calcite, pure quartz, pure clays, HR, and MT rock sample exposed to the oil (lowest and highest oil Hamaker constants) and water. Disjoining pressure-distance profiles for the oil imbibition into the dry core plugs when $4.5 \times 10^{-20} \text{ J} \leq A_{H(\text{oil})} \leq 9.0 \times 10^{-20} \text{ J}$ are presented in **Appendix B**. First, the calculated disjoining pressure-distance profiles show the strong attractive forces between the minerals, water, and oil for all cases. Negative disjoining pressure values calculated for the separation distance ranging from 1 Å to 30 Å indicate that there are strong van der Waals attractive forces between the minerals, water and oil. Second, the attractive forces in the solid surface/air/oil system are higher than those in the solid surface/air/water system for all minerals, indicating the higher wetting affinity toward oil compared with water. The oil contact angles calculated for all minerals are zero when $4.5 \times 10^{-20} \text{ J} \leq A_{H(\text{oil})} \leq 9.0 \times 10^{-20} \text{ J}$, indicating the strong attraction between the oil and the solid surfaces. The results of oil contact angle measurements conducted in our previous study [100] showed that oil droplets completely spread on the rock surface. **Table 3.6** lists the calculated water contact angles using Eq. 11 for all minerals. The water contact angles measured on dry rock samples in our previous study are in the range of 17°-61°. Calculated oil and water contact angles suggest higher wetting affinity towards oil. This is in agreement with the measured wetting affinity indices calculated based on the spontaneous imbibition of oil and water into the MT core plugs [100]. The oil wetting indices for all samples are slightly higher than those for the water. Third, the total disjoining pressure becomes more negative when the oil Hamaker constant increases, indicating the stronger attraction between the solid surface and heavier oil components.

Table 3.6. Calculated contact angles using Eq. 11 for solid surface/air/water system.

Mineral	Water contact angle
Pure quartz	26.83°
Pure calcite	31.56°
Pure clays	32.68°
HR	30.08°
MT rock surface	29.28°

In the next step, we investigate the impact of mineralogy on the disjoining pressure-distance profile. **Figure 3.10** shows the disjoining pressure-distance profiles for all the minerals when water and oil imbibe into the dry core plugs. We only present the disjoining pressure profiles for oil when $A_{H(\text{oil})} = 4.5 \times 10^{-20}$ J and $A_{H(\text{oil})} = 9.0 \times 10^{-20}$ J. Disjoining pressure-distance profiles for the oil with other Hamaker constant values are presented in the Supplementary Document. First, all minerals show the similar general trend for disjoining pressure-distance profile for both oil and water. This observation suggests the similar wetting affinity of minerals toward oil and brine in the dry conditions as we discussed earlier. Second, the difference in mineralogy does not significantly affect the wettability for the solid/air/oil and the solid/air/water systems since the differences between calculated disjoining pressure values are insignificant for each system. In summary, the calculated disjoining pressures and contact angles are in agreement with the mix-wet behavior suggested by the results of spontaneous imbibition tests conducted on the dry core plugs.

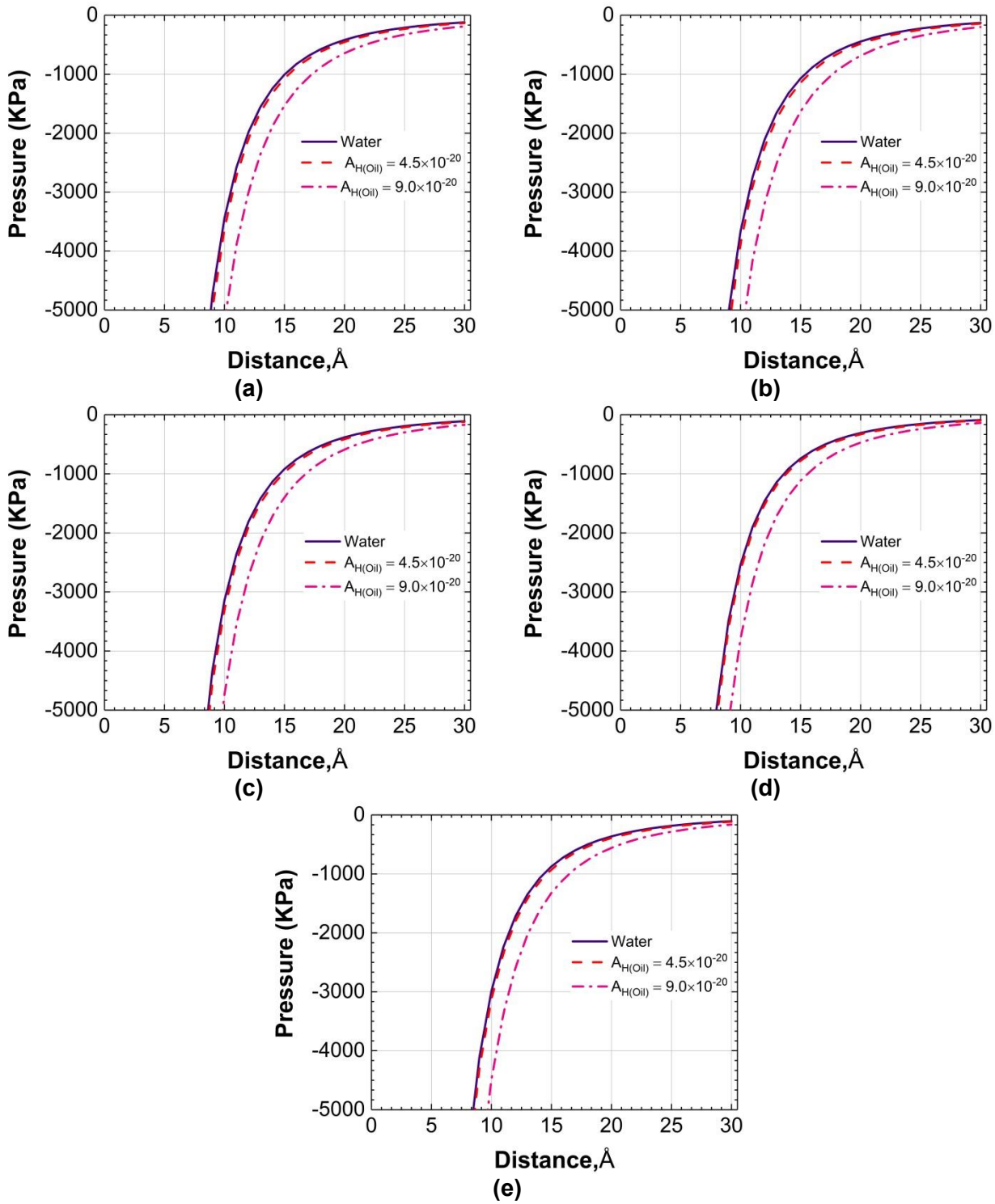


Figure 3.9. Calculated disjoining pressure versus separation distance for (a) pure calcite, (b) clays, (c) HR, (d) pure quartz, and (e) the MT rock sample.

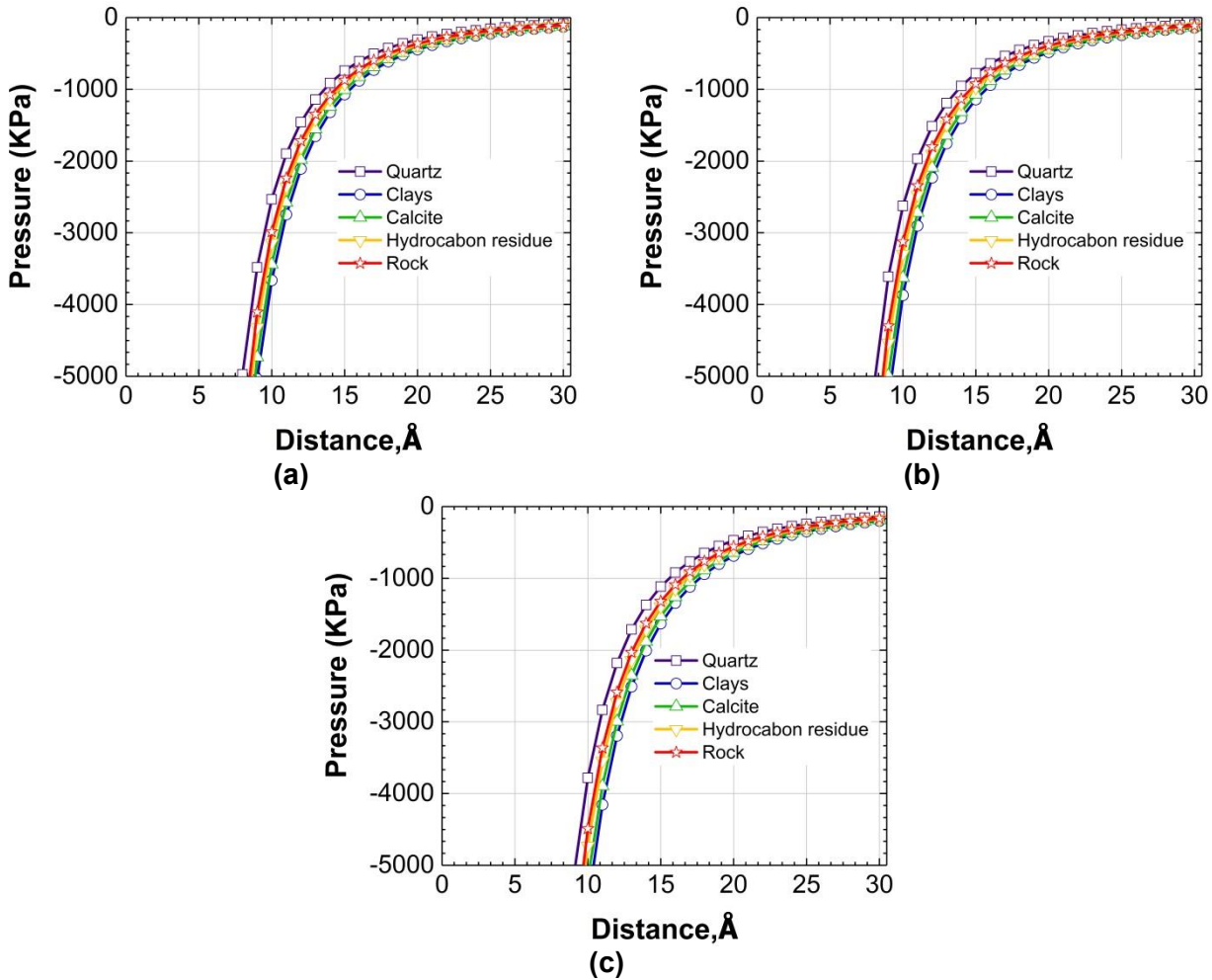


Figure 3.10. Calculated disjoining pressure versus separation distance for (a) water imbibition into the dry core plugs and (b) oil imbibition into the dry core plugs when $A_{H(oil)} = 4.5 \times 10^{-20}$ J, and (c) oil imbibition into the dry core plugs when $A_{H(oil)} = 9.0 \times 10^{-20}$ J.

3.6.2.2. Water Imbibition into the Oil-saturated Core Plugs

To explain the observation of water imbibition into the oil-saturated core plugs [100], we apply the DLVO theory and assume that 1) the oil covers the rock surface and there is no thin film of water on the rock surface, and 2) the electrostatic interactions (double layer forces) within the oil film are neglected [81].

Figure 3.11 shows the disjoining pressure-distance profile calculated for the solid surface/oil/water system when $A_{H(oil)} = 4.5 \times 10^{-20}$ J. The positive total disjoining pressure over the whole range of separation distance suggests the strong attraction between the oil film and the solid surface. The strong attraction for the separation distance (h) $< 5\text{ Å}$ is related to the strong structural forces. When $h > 5\text{ Å}$, the disjoining pressure drops rapidly

and becomes less than 200 KPa for the oil films thicker than 10 Å. The calculated oil contact angles using Eq. 11 for all minerals are zero indicating the complete oil-wet behavior when $A_{H(oil)} = 4.5 \times 10^{-20}$ J. Quartz has the lowest disjoining pressure values among all solid surfaces as shown in **Figure 3.11**, indicating that quartz is more prone to contact with water compared with other minerals. Therefore, water can contact quartz (33-51 wt% concentration in the MT core plugs) and cover the quartz surface easier than others (21-41.5 wt% concentration). The Hamaker constant for clays ($A_{H(clays)} = 16.3 \times 10^{-20}$ J) is higher than that for other minerals, suggesting strong van der Waals attraction between the oil film and clays, and the stable oil film for clay/oil/water system. Note that non-DLVO forces such as hydrophobic forces and hydrogen bonding are not considered in these calculations.

Figure 3.12 shows the disjoining pressure-distance profile for the solid surface/oil/water surface when $A_{H(oil)} = 9.0 \times 10^{-20}$ J. The total disjoining pressure for quartz is negative when $1 \text{ \AA} < h < 30 \text{ \AA}$, indicating that the oil film is unstable and oil can be spontaneously replaced by the water. When the oil becomes heavy, denoted by increasing the oil Hamaker constant, oil detachment from the quartz surface becomes easier compared with other minerals. However, the total disjoining pressure for other minerals is still positive showing the stability of the oil film attached to the mineral surface. In conclusion, the stability of the oil film covering the solid surface is strongly controlled by the geometric mean of Hamaker constants (Eq. 4). The total disjoining pressure-distance profiles for all minerals are presented in the Supplementary Document for the solid surface/oil/water system when $4.5 \times 10^{-20} \text{ J} < A_{H(oil)} < 9.0 \times 10^{-20} \text{ J}$.

The results of disjoining pressure calculations cannot explain the observation of spontaneous oil production by water imbibition into the oil-saturated core plugs. The existence of water film covering the rock surface or salts precipitated on the rock surface can affect the stability of the oil film. Although the cores were initially dry, the existence of water film or precipitated salts on the rock surface can make the rock surface water-wet and facilitate the water imbibition into the multi-mineral pores. Therefore, the assumption that there is no water film on the rock surface may not be valid in reality. Moreover, the Hamaker constant of minerals assumed from the literature are not foolproof. To have a better understanding of the wetting behavior of

heterogeneous rock samples, more experimental data on the Hamaker constant of different minerals and contribution of non-DLVO forces are required.

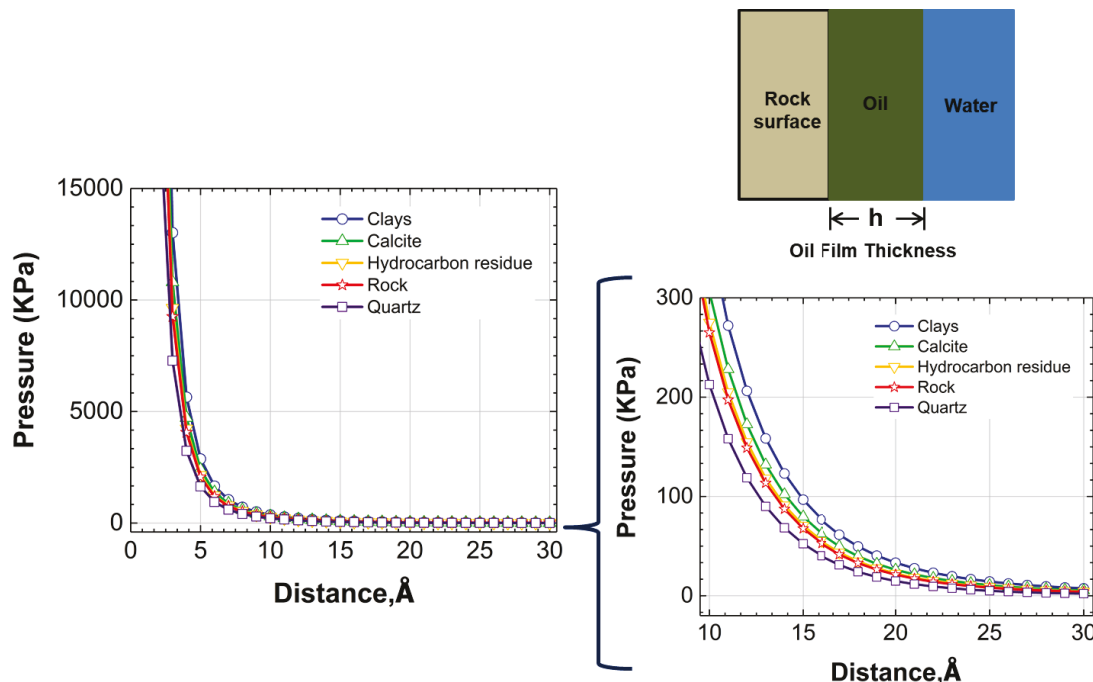


Figure 3.11. The total disjoining pressure for the solid surface/oil/water system when $A_{H(\text{oil})} = 4.5 \times 10^{-20} \text{ J}$.

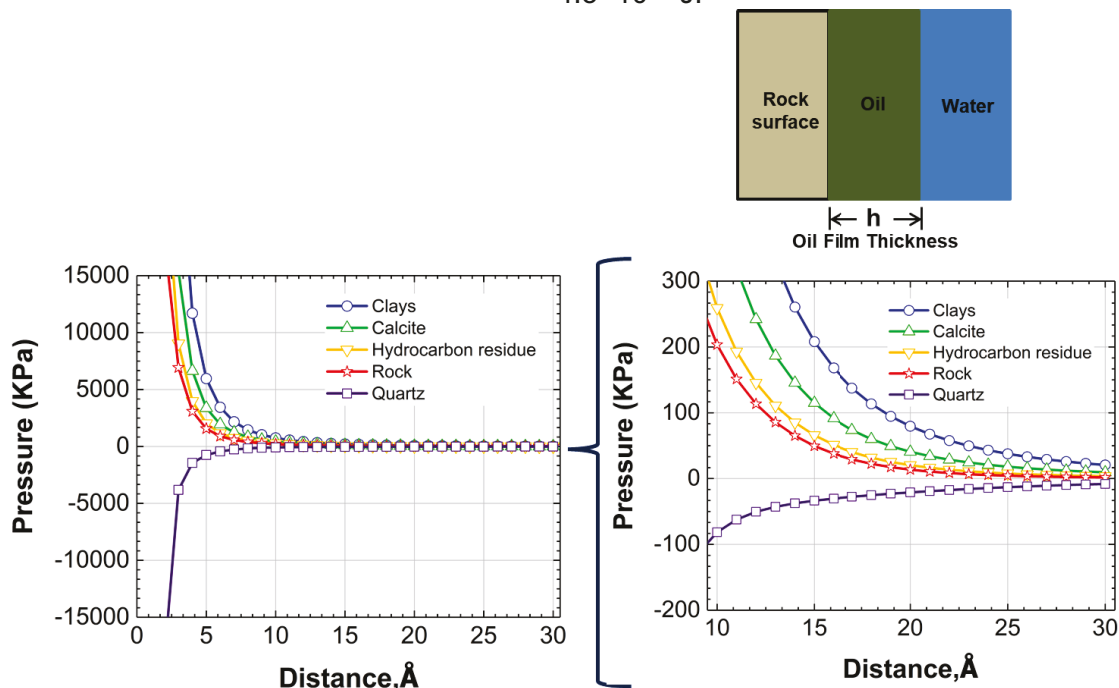


Figure 3.12. The total disjoining pressure for the solid surface/oil/water system when $A_{H(\text{oil})} = 9.0 \times 10^{-20} \text{ J}$.

3.6.2.3. Oil Imbibition into the Water-saturated Core Plugs

To explain why the oil cannot imbibe into the water-saturated core plugs during the spontaneous imbibition tests [100], we evaluate the stability of the water film covering the rock grains when the water-saturated core plugs are exposed to the oil. To calculate the disjoining pressure of a rock/water/oil system, we first measure the zeta potential of rock/water and water/oil pairs; then we calculate the double layer forces (Eq. 6) using the reduced surface potentials calculated for each pair (Eq. 8). **Table 3.7** lists the zeta potential values measured with the Malvern Zetasizer for five different systems. Finally, we add the double layer forces to the van der Waals and structural forces calculated from Eqs. 3 and 9, respectively, to evaluate the total disjoining pressure for each mineral.

Table 3.7. Zeta potential (ζ_i) values measured for the solid powder/water and water/oil pairs.

Pair	Zeta potential (mV)
Water/oil	-49.90±1.60
MT rock/water	-21.00±0.43
Pure calcite/water	-4.08±1.76
Pure quartz/water	-35.30±1.34
Pure clays/water	-50.00±2.23
HR/water	+5.00±0.78

Figure 3.13 shows the disjoining pressure-distance profiles for the solid surface/water/oil system when $A_{H(oil)} = 4.5 \times 10^{-20}$ J. P_t between the solid surface (i.e. calcite, quartz, clays, HR, and the rock) and the water layer is strongly positive when the water film thickness is less than 4 Å, meaning that water completely spreads on the solid surface. The strong repulsive structural forces between the surfaces and the oil lead to the large values of P_t when $h < 4$ Å. By increasing the water film thickness, P_t drops significantly to the minimum disjoining pressure value at $h = 5$ Å. At the minimum disjoining pressure point, the attractive forces are dominant. By increasing the water film thickness ($h > 5$ Å), the negative P_t decreases, indicating less attractions between the oil and the surface. When $h > 10$ Å, the disjoining pressure trend becomes dependent on the mineralogy. Quartz and clays show the most stable ($P_t > 0$) water film among all minerals. In contrast, calcite and HR show the most unstable ($P_t < 0$) water films among all minerals. The attractions between the oil and HR (and calcite) surfaces are higher

than those between the water and HR (and calcite) surfaces. The water film can be ruptured easier on the pore walls composed of HR and calcite compared with those composed of quartz and clays.

Figure 3.14 shows the disjoining pressure-distance profile for the solid surface/water/oil system when $A_{H(oil)} = 9.0 \times 10^{-20}$ J. The general trend of disjoining pressure is similar to the trend observed in **Figure 3.13**. The magnitude of total disjoining pressure increases by increasing the oil Hamaker constant ($A_{H(oil)}$), indicating stronger attraction between the oil and solid surface. The possibility of water film rupture increases by increasing the oil Hamaker constant. This suggests that the existence of heavy oil components can destabilize the water film, deposit on the solid surface partially, and make the solid surface less water-wet. The total disjoining pressure-distance profiles for all minerals are presented in the **Appendix B** for the solid surface/water/oil system when 4.5×10^{-20} J $< A_{H(oil)} < 9.0 \times 10^{-20}$ J.

It is expected that oil imbibes into the pores surrounded by carbonates (calcite and dolomite) and HR. However, the spontaneous imbibition results do not show noticeable water production when the water-saturated core plugs are soaked in the oil. First, higher concentration of quartz in the MT core plugs (33-51 wt%) compared with that of carbonates (21-41.5 wt%) can be a reason that oil cannot access the pores surrounded by carbonates during spontaneous imbibition tests. Second, the water-wet behavior of the multi-mineral pores may be explained by the existence of clays. Coating the surface of carbonates minerals with clays may mask the oil-wet behavior of these minerals.

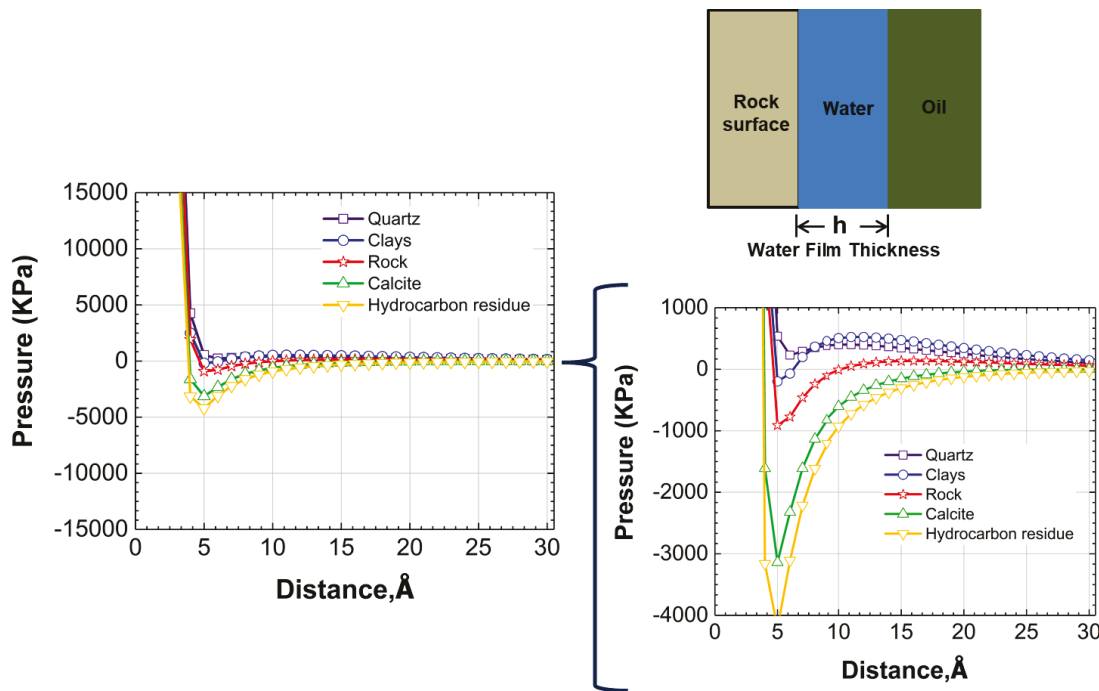


Figure 3.13. The total disjoining pressure-distance profile for the solid surface/water/oil when $A_{H(oil)} = 4.5 \times 10^{-20} \text{ J}$.

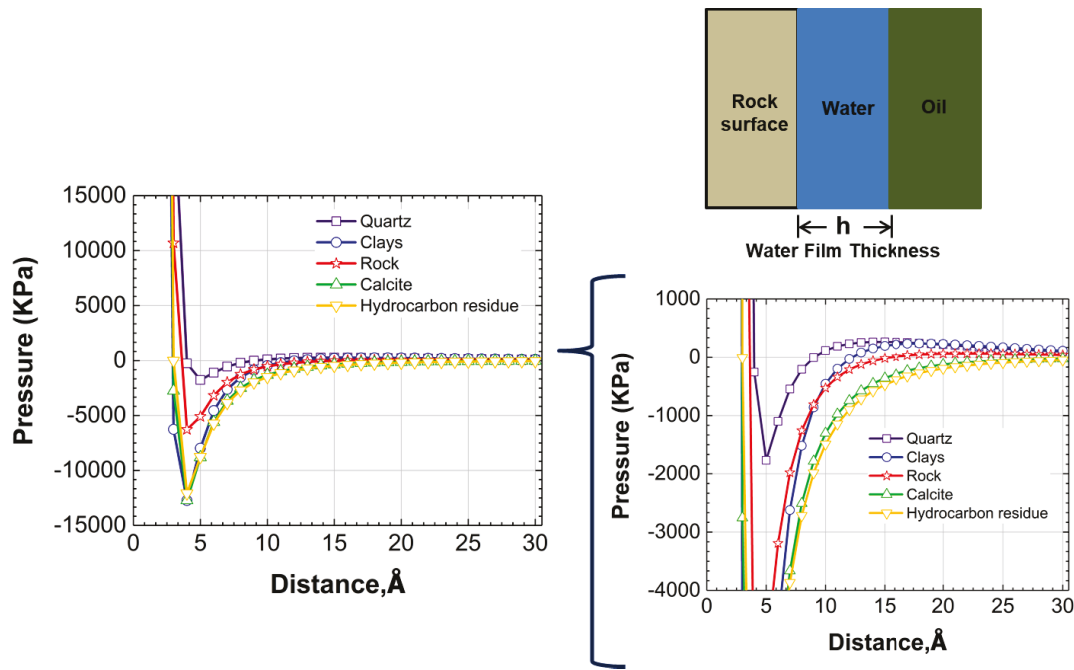


Figure 3.14. The total disjoining pressure-distance profile for the solid surface/water/oil when $A_{H(oil)} = 9.0 \times 10^{-20} \text{ J}$.

Table 3.8 lists the water contact angles calculated for the solid surface/water/oil system when $4.5 \times 10^{-20} \text{ J} < A_{H(\text{oil})} < 9.0 \times 10^{-20} \text{ J}$. The water contact angles increase when $A_{H(\text{oil})}$ increases for all minerals except for quartz. This means that the minerals become less water-wet when the oil becomes heavy. One reason is the increase of van der Waals attraction between the oil and the minerals due to the increase of oil Hamaker constant. However, the water contact angles on the quartz surface are zero over the range of oil Hamaker constants. This indicates that quartz is strongly water-wet even when $A_{H(\text{oil})}$ increases. Moreover, calcite and HR show the highest water contact angles compared with other minerals, suggesting less water-wet behavior. In summary, the water contact angles calculated for the minerals are in the water-wet state. Therefore, the MT rock samples tend to be water-wet.

Table 3.8. The water contact angles calculated for solid surface/water/oil systems using Eq. 11.

Mineral	Water contact angle, θ_w						
	$A_{H(\text{oil})}, \times 10^{-20} \text{ J}$						
	4.5	5.0	5.2	6.0	7.0	8.0	9.0
Quartz	0.0	0.0	0.0	0.0	0.0	0.0	0.0
Clays	0.0	0.0	0.0	4.6	9.2	12.1	14.2
HR	13.3	14.1	14.4	15.5	16.7	17.7	18.6
Calcite	10.7	12.0	12.4	13.9	15.5	16.9	18.1
Rock	0	4.0	4.9	7.3	9.4	11.0	12.3

The contribution of F_{vdw} , F_{edl} , and F_s to the total disjoining pressure for all systems is presented in **Appendix B** to show how significant these forces are in each rock-fluid system.

3.6.3. Step 3: AFM Analysis

Here, we present the results of adhesion forces measured between the tip of the cantilever and different minerals. The adhesion forces measured for different minerals show how strong the attractive forces are between a solid surface and the uncoated standard silicon tip. The purpose is to compare the trend of adhesion forces for pure minerals and the real rock surface. Moreover, pore-scale visualizations of the minerals are presented in this section. Measurement of adhesion forces is not flawless especially for conducting the measurement at the ambient air conditions. First, capillary bridging can significantly alter the magnitude of adhesion forces. This is because of water

condensation in nanoscale separation formed around the tip-substrate contact area [129]. The magnitude of capillary forces formed by the condensed water bridge depends on the humidity level and the wetting characteristics of the interacting surfaces [148]. On the other hand, capillary condensation shows the relative degree of wettability. Adhesion forces can be measured at the ambient air conditions to distinguish between hydrophobic and hydrophilic groups [149, 150]. Caution should be taken to interpret the results obtained at the ambient air conditions, because it is difficult to exclude or account for the presence of capillary forces. Therefore, the forces reported in this study are summation of adhesion and capillary forces. The effects of capillary forces can be eliminated by conducting the experiments in liquid instead of air [151, 152].

Second, static charging can influence the measured values of adhesion forces between electrically non-conductive surfaces in dry conditions. Surface coating with gold and treatment with thiol are proposed to reduce the charging effect [148, 149]. Although, the effect of surface charging can be mitigated by surface treatment, these treatments can affect (i) roughness of the surface by gold coating, and (ii) adhesion forces by functionalizing the surface. The main purpose of the AFM analysis conducted in this study is to understand how different the adhesion forces are between pure minerals and natural rock thin sections.

Figure 3.15 shows different types of images taken from the pure quartz slide and a generic force-distance profile measured for a selected point on the quartz slide. To make sure that the forces measured by AFM analysis are representative of adhesion forces, we select 100 points on each scan area and repeat the force measurements for at least four scan areas of each mineral. Then, we report the mean and standard deviation values of adhesion forces for each mineral.

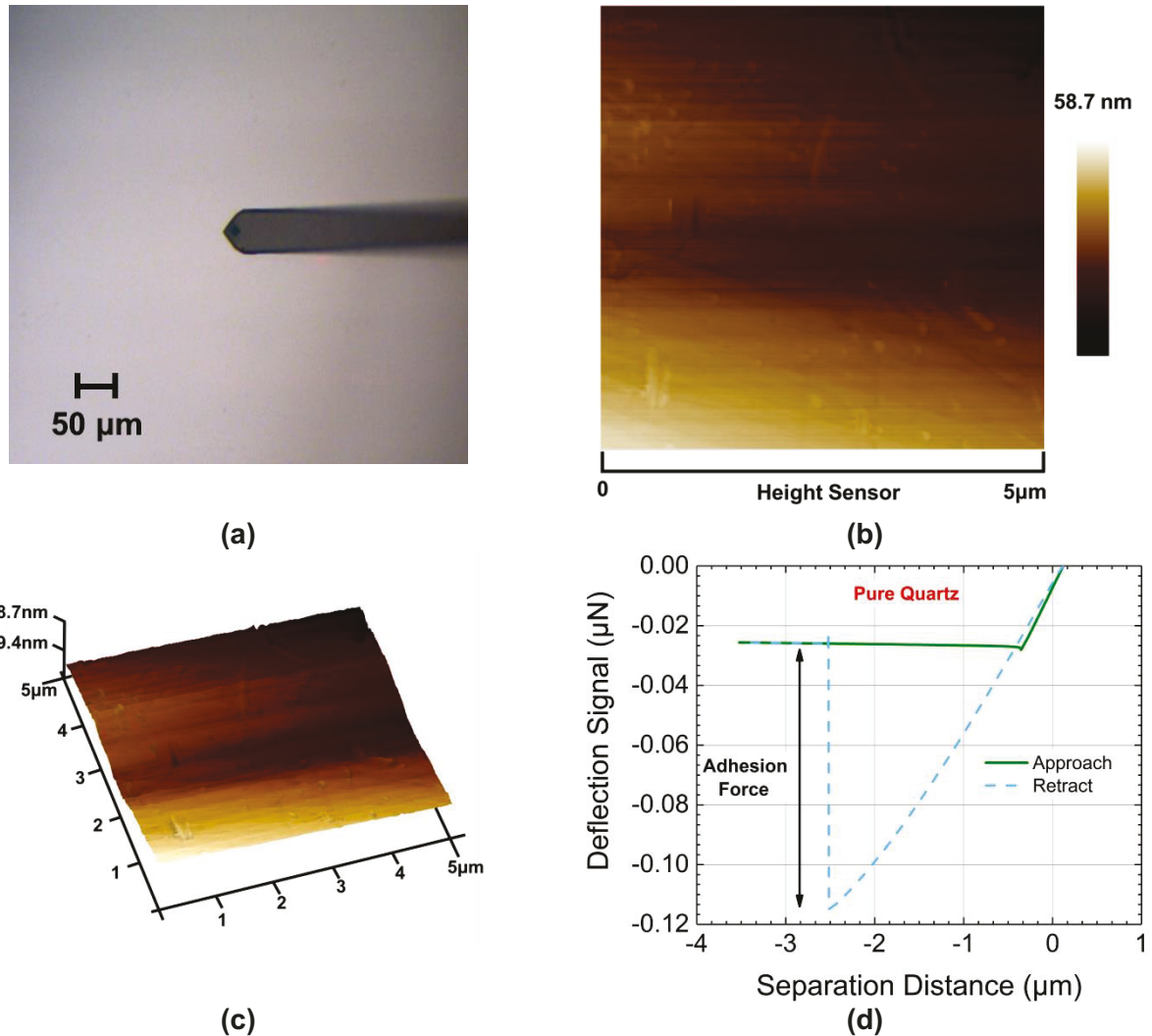


Figure 3.15. (a) A light image of quartz slide and a tip contacting the surface, (b) an AFM height mode (forward) image taken from the pure quartz slide, (c) 3D surface topography of the quartz slide, and (d) the force-distance profile for a point marked on the quartz slide.

Next, we perform AFM analysis on pure calcite crystal and the MT thin section as shown in **Figure 3.16** and **Figure 3.17**, respectively. Comparing **Figures 3.15-3.17** shows that the quartz surface is smoother than the calcite surface and the MT thin section. Mineral heterogeneity leads to the non-uniform structure in the MT thin section (**Figure 3.17b**), which shows a rough surface compared with quartz and calcite surfaces. 3D surface topography of the MT thin section shows several wrinkled shapes known as a ridge-and-valley structure. Valleys represent the pores located in the thin section and can be analyzed to determine the depth of the pores. The roughness of the rock surface affects the wetting behavior [153-155]. When the roughness ratio for a

solid surface ($\phi = \frac{A_{real}}{A_{smooth}}$) becomes more than 1, the apparent contact angle for hydrophilic and hydrophobic surfaces decreases (more water-wet) and increases (more oil-wet), respectively. Consequently, the roughness of the thin section observed in **Figure 3.17b** can affect the wetting affinity of the rock sample.

To characterize AFM images at the microscopic scale three parameters are defined: mean roughness (R_a), RMS value (R_q), and ζ scale. The mean roughness and RMS value are defined as [105]

$$R_a = \frac{\sum_{i=1}^N |h_i - \bar{h}|}{N} \quad (12)$$

$$R_q = \sqrt{\frac{\sum_{i=1}^N |h_i - \bar{h}|^2}{N}} \quad (13)$$

where h_i , \bar{h} , and N are elevation of a data point i , the mean elevation, and number of data points in the image, respectively. The RMS of an AFM image is the root mean square average of the height deviation taken from the mean data points. The ζ scale also represents the vertical distance between highest and lowest points in the image.

Table 3.9 lists the statistical roughness analysis performed on pure quartz slide, pure calcite crystal and MT thin section. Note that R_a and R_q evaluated for pure quartz, pure calcite, and the MT thin section may not represent the roughness of pore walls in the core plugs. Since each AFM instrument has a limited capacity for detecting the surface roughness, all solid surfaces should be smooth. Therefore, smooth surfaces used in this study may not represent the real pore walls. Rougher surfaces are expected for pore walls of real cores.

Table 3.9. Roughness analysis of the minerals in dry conditions

Sample	R_a, nm	R_q, nm	ζ scale, nm
Pure quartz	3.67	4.56	58.70
Pure calcite	0.19	0.26	1.80
Montney thin section	40.00	51.20	431.10

To conduct the force measurements on the MT thin section, we select different spots to consider the heterogeneities in the thin section. **Figures 3.15d, 3.16d, and 3.17d** show a force-distance profile for a point marked on the pure quartz, pure calcite, and the MT thin section, respectively. The adhesion forces for quartz surface are higher than those

for calcite and the thin section. **Table 3.10** lists the mean values of adhesion forces measured for more than 400 points selected from each sample. Higher surface tensions of pure quartz than calcite is a reason for higher adhesion forces between the tip of the cantilever and the solid surface. The surface tension for pure quartz and pure calcite are 280-1200 mN/m and 32 mN/m, respectively [156, 157]. More details about the impact of surface tension on adhesion forces are presented elsewhere [129, 158]. Moreover, as it is expected $(\bar{F}_{adh})_{calcite} < (\bar{F}_{adh})_{MT \ thin \ section} < (\bar{F}_{adh})_{quartz}$ because the MT thin section is mainly composed of quartz and carbonates.

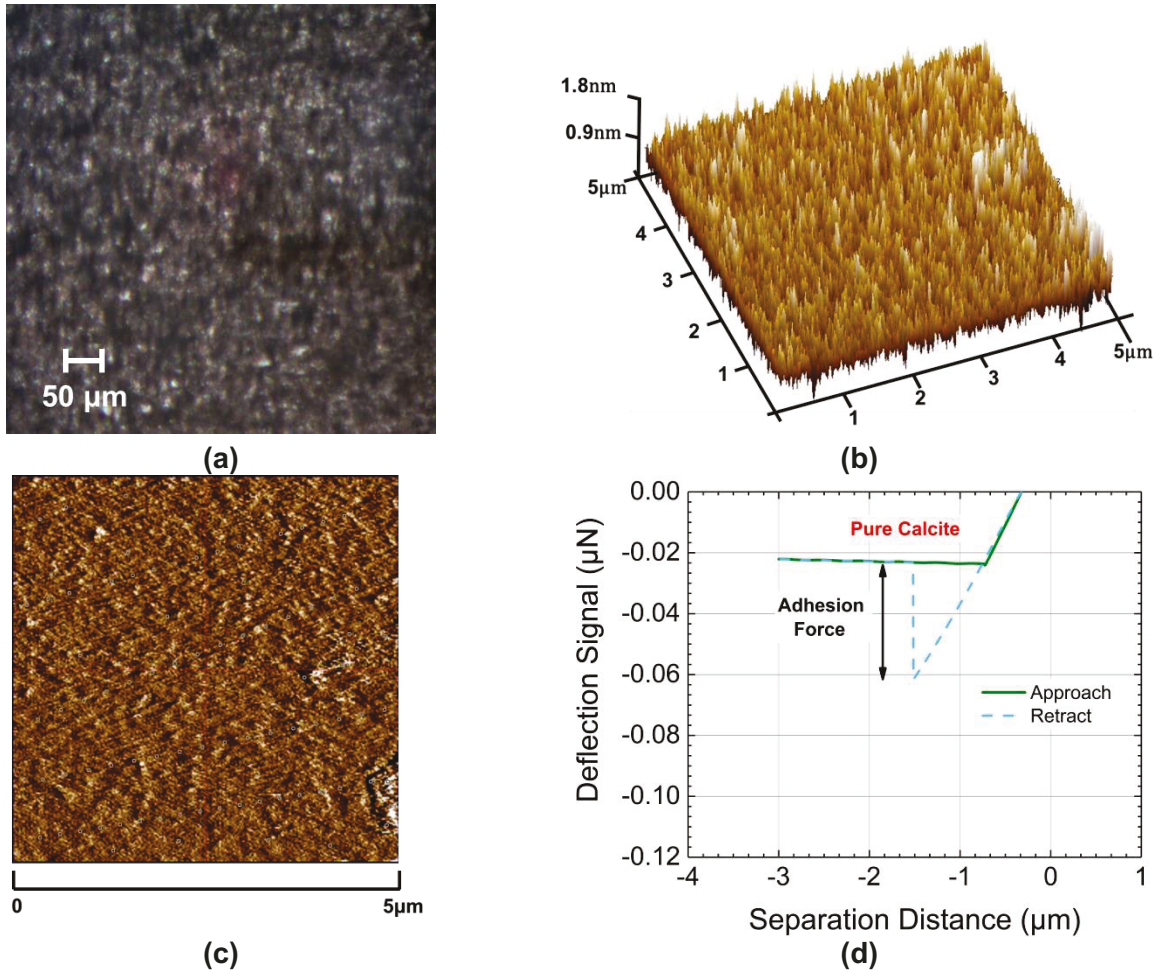


Figure 3.16. (a) A light image of the calcite crystal, (b) 3D surface topography of the calcite crystal, (c) marked points on a pure calcite crystal used for force measurement, and (d) a force-distance profile for a point marked on the calcite surface.

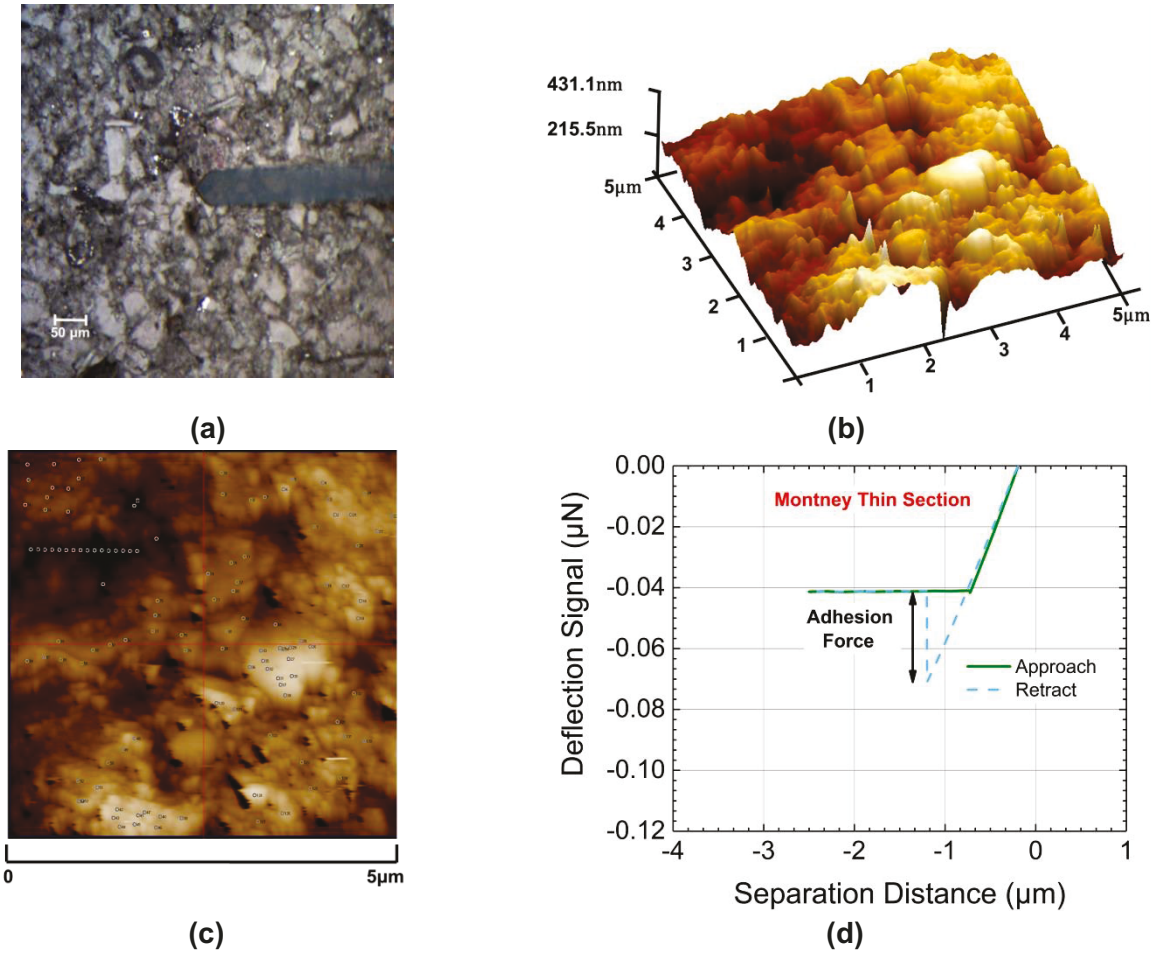


Figure 3.17. (a) A light image of the Montney thin section, (b) 3D surface topography of the Montney thin section, (c) marked points on the thin section used for force measurement, and (d) a force-distance profile for a point marked on the tin section.

Table 3.10. The adhesion forces measured between the tip of the cantilever and the pure quartz, pure calcite, and the MT thin section.

Sample	Mean adhesion forces, \bar{F}_{adh} , (μN)
Pure quartz	-0.101000±0.004450
Pure calcite	-0.056018±0.003490
Montney thin section	-0.070815±0.006203

Adhesion forces reported in the literature for quartz at the ambient air conditions cover a wide range of values. The magnitude of the adhesion forces for quartz are ranged from $0.021\pm0.006 \mu\text{N}$ to 0.032 ± 0.005 [159], and from $0.015 \mu\text{N}$ to $0.060 \mu\text{N}$ [148]. Several studies have investigated the adhesive forces for the cleaved calcite crystals immersed in different liquids [130, 157, 160-162]. There are a few studies reported in the literature investigating the adhesion forces for calcite at the ambient air conditions. Røyne et al.

[161] showed that the adhesion forces of calcite surface measured at the ambient air conditions are 1 to 2 orders of magnitude higher than those measured in pure glycol, ranging between 0.002 μN and 0.02 μN .

The adhesion forces measured in this study are different from those reported in the literature. One reason is that different materials (i.e. calcite and quartz) and tips have been used here. Surface roughness and humidity also strongly affect the adhesion forces [148, 163, 164]. Compared to a smooth flat surface, larger and smaller adhesive forces are reported for concave and convex surfaces, respectively [165].

There are two limitations regarding the force measurement at the ambient air conditions. First, the adhesion forces measured in air are larger than those measured in liquid. Second, the adhesion forces measured in air may not represent the real reservoir conditions because the surface of rock grains is exposed to aqueous and oleic phases at reservoir conditions. In the liquid mode of force measurement, double layer repulsion is another term which is added to the adhesion force in addition to attractive forces (i.e. van der Waals forces). Although the effect of double layer forces is significant especially for the short range of separation distance, the magnitude of double layer forces decreases by increasing the salinity of water. Since the total salinity of reservoir brine is very high ($>100,000$ ppm) the contribution of double layer forces is expected to be relatively low. In summary, the adhesion force for the MT thin section composed of multi-mineral pores is between the values for pure quartz and calcite.

3.7. Conclusions

In this study, different sets of experiments were conducted to investigate the effects of mineral heterogeneity and intermolecular forces on wetting behavior of tight rocks from core-scale to pore-scale. First, we reviewed the results of previous spontaneous imbibition tests conducted on downhole core plugs collected from the Montney Formation. Then, we explained the spontaneous imbibition results by using the disjoining pressure-distance profiles calculated based on the DLVO theory. Finally, we investigated the effect of mineralogy on the adhesion forces measured by AFM analysis. Here is the summary of the main conclusions:

- The results of pore-scale visualizations (thin section and SEM/EDS analyses) show the existence of multi-mineral pores with mixed-wet characteristics. To

explain the effect of mineral heterogeneity on wetting behavior, we investigated the stability of thin water films covering the rock surface using the DLVO theory.

- The disjoining pressure values calculated based on the DLVO theory for the dry core plugs suggest similar wetting affinities of the rock samples toward oil and water which agrees with the spontaneous imbibition results.
- The disjoining pressures calculated for the solid surface/oil/water system show the strong van der Waals attraction between the oil film and all minerals except quartz surface, indicating the stable oil film covering the minerals (except quartz). The oil film attached to the quartz surface is destabilized when $A_{H(oil)} \geq 8 \times 10^{-20}$ J. Therefore, the water imbibition into the oil-saturated core plugs can be explained by the water imbibition into the pores surrounded by quartz grains. However, the oil film is completely attached to the other minerals.
- The contact angles calculated for the solid surface/water/oil system is in the range of water-wet state which can be explained by the stability of water film covering the rock surface. This explains why oil cannot imbibe into water-saturated core plugs, based on previous experiments.
- AFM measurements show that the adhesion forces between the tip and the quartz surface are higher than those between the tip and the calcite surface. The adhesion forces measured for the MT rock sample are between those measured for quartz and calcite, showing the effect of mineral heterogeneity in the MT rock sample.

Chapter 4 CO₂-Oil Interactions in Tight Rocks: An Experimental Study

4.1. Introduction

Hydraulic fracturing and horizontal drilling technologies have substantially increased oil production from unconventional resources during the last decade. Although the volume of hydrocarbon in-place is significantly high in unconventional resources, the primary oil recovery factor is 3-10 % of initial oil in-place [166-171]. The oil production rate is affected by reservoir properties such as permeability, pressure, wettability, oil API, initial oil saturation and operational parameters such as fracturing stages, fracture conductivity and wellbore radius. Recently, different EOR techniques including gas injection [170, 172-175] and chemical injection [15, 48, 176, 177] have been studied to improve the oil recovery from unconventional resources. Among all injection fluids, CO₂ has several benefits in terms of improving oil recovery [178-185] and mitigation of greenhouse gas emissions by CO₂ sequestration [186-188]. These advantages have made CO₂ injection an attractive EOR technique for tight and shale oil formations.

CO₂ flooding may not be applied on unconventional resources due to a very low injectivity of CO₂ [189]. In addition, complex natural and induced fractures in such reservoirs may result in early breakthrough of injected gas in production wells that leads to low volumetric sweep efficiency and bypassing of the oil in the matrix system [190]. Most EOR processes need at least one well for injection of EOR fluid and one well for production [189]; while EOR processes in unconventional resources are mostly designed to be conducted as a cyclic process in single fractured wells [191]. The results of previous studies [185, 189, 192-194] show that there is a potential to increase final oil recovery up to 85 % of the original oil in-place by conducting cyclic CO₂ process in unconventional resources.

A CO₂ fracturing operation can be considered as a cyclic CO₂ process if the well is soaked after the fracturing operation. To understand how cyclic CO₂ process can result in improved oil recovery in tight formations, it is essential to investigate the interactions between injected CO₂ and oil in the matrix. The cyclic CO₂ process is mainly composed

of three steps: 1) CO₂ injection, 2) soaking the well for a specific period of time to allow dissipation of the injected CO₂ into the formation, and 3) hydrocarbon production. We conduct a series of experiments to understand: 1) how dissolution of CO₂ into the oil at the bulk-phase conditions can change the physical properties of the CO₂-oil mixture and, 2) how CO₂ can interact with oil in the oil-saturated cores and lead to improved oil recovery.

The objective of this study is to understand CO₂-oil interactions at different experimental conditions, and explain how these interactions can lead to improved oil recovery. In this study, we investigate: 1) the CO₂-oil interactions at the bulk-phase conditions using a PVT cell and a custom-designed visual cell, 2) the oil recovery from oil-saturated core plugs soaked in CO₂, 3) the oil recovery from oil-saturated core plugs by conducting the cyclic CO₂ process. **Figure 4.1** shows the workflow of this study which is divided into two sections: 1) experiments conducted at the bulk-phase conditions to visualize and evaluate the CO₂-oil interactions, 2) experiments conducted in the porous media to evaluate the oil recovery after soaking with CO₂. In the first step, we conduct constant composition expansion (CCE) tests using a PVT cell to evaluate the bubble-point pressure and swelling factor of the CO₂-oil mixture. Then, we visualize the CO₂-oil interface at reservoir conditions (P=2000 psig and T=50°C) using a custom-designed visual cell and investigate the possibility of oil expansion and asphaltene precipitation. We conduct SEM (Scanning Electron Microscopy) /EDS (energy x-ray dispersive spectroscopy) analysis on solid precipitates deposited after CO₂-oil interactions in the visual cell. In the second step, we investigate the oil recovery from the Montney core plugs soaked with CO₂ in the visual cell. We also use a core flooding apparatus to evaluate the oil recovery factor from the oil-saturated core plugs by conducting the cyclic CO₂ process.

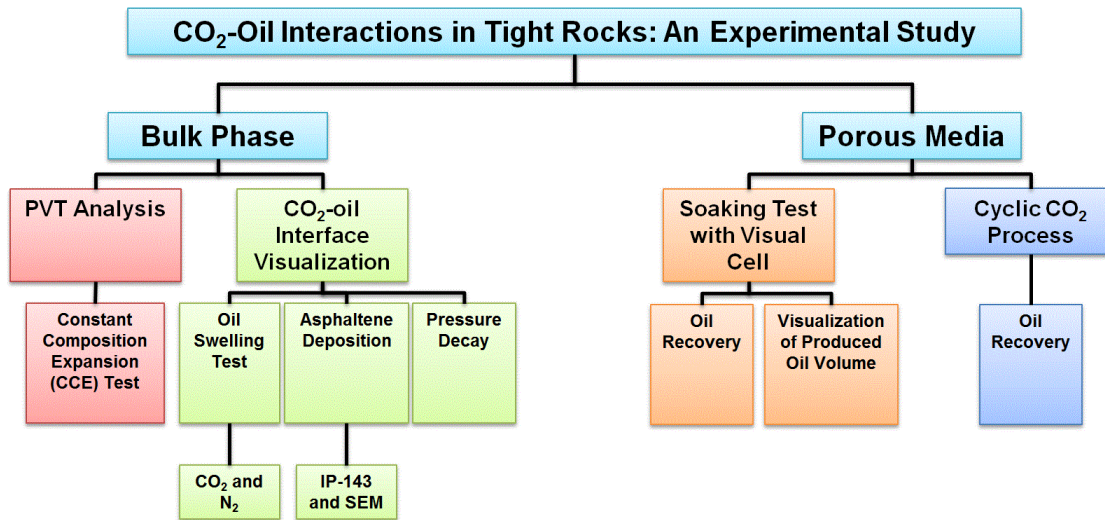


Figure 4.1. The experiments are divided into bulk-phase characterization and flow in porous media.

4.2. Materials

4.2.1. Core Properties

We select four Montney core plugs to conduct this study.

Table 4.1 shows the petrophysical properties of the cores. More details about the petrophysical properties of the core plugs are presented elsewhere [100]. The petrophysical properties are provided by the Core Laboratories service company.

Table 4.1. Petrophysical properties of the Montney core plugs. The diameter of core plugs is 3.8 cm.

Sample No.	Depth (m)	Permeability, K_{Air} , (md)	Porosity, Helium (Fraction)	Grain Density (Kg/m ³)	Length (cm)
S1	1568.89	4.98	0.155	2720	2.36
S2	1569.92	7.53	0.170	2710	2.26
S3	1572.67	2.08	0.140	2690	5.00
S4	1580.64	0.30	0.122	2710	2.22

4.2.2. Fluid Properties

We use Montney crude oil to study the CO₂-oil interactions and conduct CO₂ cyclic experiments. The oil is characterized as light oil ([°]API =37.96). **Table 4.2** lists the physiochemical properties of the oil. **Table 4.3** shows the compositional analysis of the oil measured by simulated distillation test (ASTM 7169). CO₂ with purity of 99.9% (Praxair, Canada) is used in the experiments.

Table 4.2. Physiochemical properties of the Montney crude oil

Property	Value
Color	Dark brown
API (15°C)	37.96
Viscosity at 21°C (cP)	9.6
Surface tension (mN/m)	26.8
Molecular weight (g/mol)	251.78

Table 4.3. Compositional analysis of the Montney crude oil

Component	Wt.%	Component	Wt.%
C ₇	1.03	C ₂₄	5.03
C ₈	1.55	C ₂₆	4.12
C ₁₀	7.55	C ₂₈	3.42
C ₁₁	4.70	C ₃₀	3.24
C ₁₂	4.53	C ₃₂	2.53
C ₁₄	9.94	C ₃₄	2.30
C ₁₆	8.78	C ₃₆	2.15
C ₁₈	8.27	C ₃₈	1.70
C ₂₀	6.55	C ₄₀	1.66
C ₂₂	5.36	C ₄₂₊	15.59

4.3. Methodology

We conduct four different sets of experiments to study CO₂-oil interactions. First, we conduct the CCE experiments using the PVT cell to evaluate the bubble-point pressure and swelling factor of the CO₂-oil mixtures. Second, we visualize the CO₂-oil interface using a custom-designed visual cell. Third, we conduct CO₂ soaking experiments in the visual cell using oil-saturated core plugs. Finally, we conduct cyclic CO₂ process on oil-saturated core plugs using a core flooding apparatus.

4.3.1. CCE Tests

Phase-behavior measurements for CO₂-oil mixture are conducted using a PVT apparatus (PVT-ZS-16-2-2-H/AC, DBR). **Figure 4.2** shows schematic of the apparatus. The PVT cell can stand maximum pressure and temperature of 15,000 psig and 199°C, respectively. The volumetric capacity of the cell is 112 cm³. The dead volume of the PVT system is 1.754 cm³. A floating piston isolates the test fluids from hydraulic oil. A high-pressure positive displacement pump controls the pressure of the hydraulic oil (PMP-500-1-20-HB, DBR). An air bath with an accuracy of ±0.1°C controls the temperature of the PVT cell. The PVT system is equipped with a cathetometer to

measure the height of the test fluids. The uncertainty in volume measurement is ± 0.016 cm³. Heise pressure gauge monitors the pressure of the tests fluids (901A-15K-232P-R5, Ashcroft Inc., Stratford, USA). The uncertainty of the pressure gauge is $\pm 0.07\%$ of full-scale which is 15,000 psig.

We measure the density of the oil at atmospheric pressure and 21°C using Attention Sigma 700 (Biolin Scientific) instrument. The accuracy of the instrument is ± 0.01 kg/m³. Densities of the oil at different pressure and temperature conditions are measured with the PVT cell based on mass balance. The density measurements are conducted at 21-50°C and 50-2000 psig.

We use reference oil density to calculate the density of oil at different experimental conditions (Eq. 1) because injected mass of the oil in the PVT cell is conserved. Since the mass of the oil is constant at all experimental conditions, the product of the oil density multiplied by the oil volume at first experimental conditions equals to that at second experimental conditions. The surface area of the PVT cell is fixed; then, the volume of the oil is proportional to the height of the oil column. Reference density of the oil is measured using Sigma 700 instrument at atmospheric pressure and 21°C.

$$\rho_2 = \frac{V_1}{V_2} \rho_1 = \frac{H_1}{H_2} \rho_1 \quad (1)$$

Here ρ_1 , V_1 , and H_1 are the oil density (Kg/m³), volume (cm³), and height in the PVT cell (cm) at the reference conditions, respectively. ρ_2 , V_2 , and H_2 are the oil density (Kg/m³), volume (cm³), and height in the PVT cell (cm) at a given temperature or pressure.

We conduct seven CCE experiments using the PVT apparatus. We clean the PVT cell with toluene and evacuate the cell by a vacuum pump before running the experiment. The high-pressure CO₂ cylinder is used for CO₂ injection into the PVT cell. First, we inject a specific volume of CO₂ into the cell at room temperature. **Table 4.4** lists the details of experimental conditions for CO₂-oil mixtures. The injected mass of CO₂ is calculated using the volume measured by the cathetometer and density values from literature [195]. Second, a specific amount of the oil is injected into the PVT cell. Then, the injected volume of oil is determined as the difference between the cell volume and CO₂ volume. We assume negligible volume change during mixing of CO₂ and oil for the short time period. Third, we turn on the stirrer to mix the CO₂-oil mixture for 24 hours

and adjust the oven temperature to the set-point for each test. When temperature of the mixture becomes stable at the set-point, we increase the pressure of the mixture until CO₂ is completely dissolved into the oil and a single liquid-phase is formed.

Table 4.4. CO₂ mole% and temperature of CO₂-oil mixtures in CCE tests.

Exp. No.	CO ₂ mole%	Temperature(°C)
1	48.36	50.1
2	58.82	50.1
3	58.82	76.8
4	58.82	90.1
5	71.06	50.1
6	71.06	76.9
7	71.06	90.0

Next, we decrease the pressure step by step and record the swollen oil volume at each pressure. To reach the equilibrium conditions at each pressure, the mixture is stirred. Next, the stirrer is turned off, and the system is kept static until the cell pressure becomes stable. Three and six hours are enough for single-phase and two-phase systems to reach the equilibrium, respectively. Finally, we record swollen oil volume at each pressure when the volume of the mixture does not change, and plot the pressure versus relative volume (V_r) [196-198]. Relative volume at each temperature is defined as a total volume of the CO₂-oil mixture at a desired pressure divided by a total volume of the CO₂-oil mixture at the bubble-point pressure.

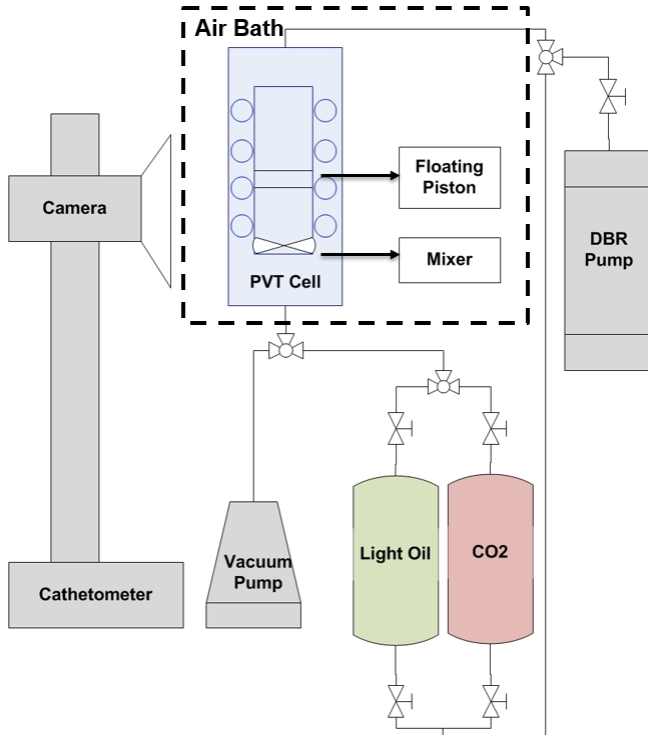


Figure 4.2. Schematic of the PVT cell.

4.3.2. *Visualization of CO₂ - Oil Interactions in Visual Cell*

To visualize CO₂-oil interactions at reservoir conditions, we conduct a series of visualization experiments using oil and CO₂. **Figure 4.3** shows a picture of the custom-designed visual cell which is made of stainless steel and two sight glasses that can stand maximum pressure and temperature of 4000 psig and 200°C, respectively. A heating jacket with an accuracy of $\pm 0.1^\circ\text{C}$ controls the temperature of the visual cell. Omega pressure gauge monitors the pressure of the visual cell (DPG4000 series, Omega). The uncertainty of the pressure gauge is $\pm 0.05\%$ of full-scale which is 4,000 psig. The internal volume of the visual cell is 587 cm³. The sight glasses are used to visualize the fluid-fluid interface. We place a light source in front of one sight glass to show the internal space of the visual cell. We use a camera in front of the second sight glass and visualize the fluid-fluid interface during the experiments.

To start the experiment, we fill almost half of the cell with oil and increase the cell temperature to 50°C (reservoir temperature). When the temperature is stabilized at 50°C, we inject CO₂ into the cell until the pressure reaches 2000 psig (reservoir pressure). Then, we close the injection valve and record the pressure of the mixture

with respect to time. The pressure gradually declines below 2000 psig due to dissolution of CO₂ into the oil phase. We monitor the CO₂-oil interface at 50°C and different pressures to calculate the oil expansion factor (EF). In the next experiment, we replace CO₂ with N₂, to compare the solubility behavior of CO₂ with N₂.

Components of visual cell

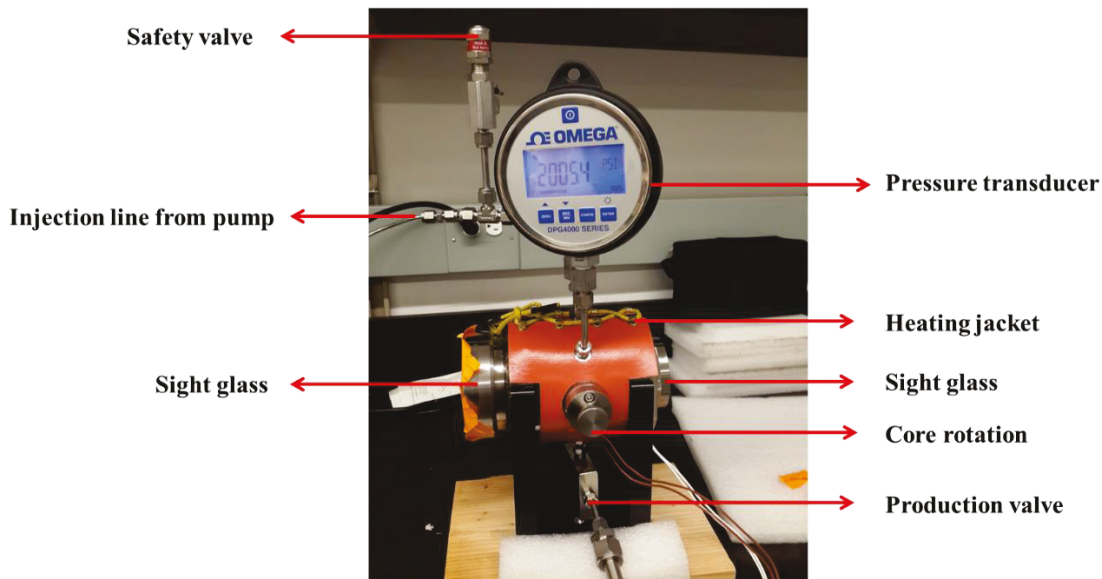


Figure 4.3. Custom-designed visual cell and its components. The diameter of sight glass is 4.8 cm.

4.3.3. CO₂ Soaking Experiments Using Oil-saturated Core Plugs

In this section, we soak the oil-saturated core plugs with CO₂ in the visual cell. We visualize the cross section of the core plugs during the CO₂ soaking tests at 2000 psig and 50°C using the sight glass. The procedure for conducting the soaking experiments is as follows:

- To prepare the oil-saturated samples, we immerse the dry clean core plugs (S1, S2 and S4) into the accumulator filled with the oil at 3000 psig for 2 days. Then, we measure the weight of oil-saturated samples to calculate the initial oil saturation.
- We place the oil-saturated sample in the visual cell (**Figure 4.3**) and increase the temperature of the visual cell to 50°C.
- We inject CO₂ into the visual cell until the pressure of system reaches 2000 psig.

- We soak the core plug in CO₂ for 3 weeks, capture images of the cross section of the core, and record the possible changes of rock surface during the soaking process.
- We take out the core after three weeks and measure the weight of the sample. Finally, we calculate the oil recovery factor based on weight change of the core sample.

We perform the following procedure to prepare the core plugs for conducting the soaking experiments:

- We clean the core plugs with toluene and methanol to remove oleic and aqueous phases in the pore network, respectively.
- We dry the cores in oven at 100°C for three days. Then, we measure the weight of dry cores.
- Prior to saturating the core plugs with fluids, crude oil is filtered using filter paper to remove the solid impurities.

4.3.4. CO₂ Cyclic Process

We conduct CO₂ cyclic tests at (i) 1000 psig and 21°C (room temperature), and (ii) 1400 psig and 50°C (reservoir temperature) using a core flooding apparatus. Core flooding apparatus is composed of a Hassler core holder (Core Lab., US), a dual positive displacement syringe pump (100DX, Teledyne ISCO, US), two high-pressure accumulators, two Omega pressure gauges (DPG409-5KG, Omega, Canada) and a back pressure regulator (KPP series, Swagelok). The Hassler core holder is made of stainless steel and can stand maximum pressure and temperature of 5,000 psig and 150°C, respectively. Cores with diameter of 1.5 inches and length of 2-6 inches can be mounted in the Hassler core holder. The dual ISCO pumps can supply maximum pressure of 10,000 psig. The range of flowrate for the pumps is 0.00001-50 cm³/min. The total capacity of the dual-pump is 206 cc. The uncertainty of the measured pump pressure is ±0.5% of full-scale (10,000 psig). The capacity of each accumulator is 500 cc and can stand the pressure of 10,000 psig. We fill the accumulators with oil and CO₂. Omega pressure gauges measure the confining pressure and inlet pressure of the system. The uncertainty of the pressure gauges is ±0.08% of full-scale (5,000 psig). To conduct the experiment at a higher temperature, the core flooding system is wrapped

with heating tapes and the temperature is controlled using three surface thermocouples connected to a temperature controller (OMEGA).

To perform cyclic CO₂ tests, we use inlet line of the core holder for both CO₂ injection and oil production and close the outlet line of the core holder. **Figure 4.4** shows the schematic view of cyclic CO₂ set-up. We perform the following procedure for cyclic CO₂ tests:

- We mount the clean and dry core plugs in the core holder, and connect the core outlet to the vacuum pump. To avoid air trapping, we apply vacuum on the core plugs until the pressure at the inlet reaches to -9 psig. Then we inject oil from the inlet.
- We inject the oil at a constant injection pressure (4000 psig) to saturate the core plugs. For oil injection, we select constant pressure mode to make sure that the injection pressure is at least 500 psig lower than the confining pressure. The outlet pressure (back pressure) is 0 psig during oil injection. We assume the core plugs are fully saturated with oil when the flow rate stabilizes. We measure the weight of oil-saturated cores, and also measure the contact angles of oil and brine before cyclic CO₂ process.
- To measure the oil contact angle in brine, we immerse the core sample into the brine and inject the oil droplet using a J-shaped needle. Then, we measure the oil contact angle using a high-resolution camera and an LED light source, and analyze the pictures using an image-analyzer software. To measure the brine contact angle in oil, we immerse the core sample into the kerosene because the reservoir oil is not transparent enough to visualize the brine droplet. The procedure is repeated for six droplets to obtain average value and standard deviation.
- We place two oil-saturated core plugs (cores S1 and S3) into the core holder (**Figure 4.4**) and apply the confining pressure of 3000 psig. Since the cores are very tight and the pore volume (PV) is small, we use multiple plugs to increase the total PV. Then, we can measure the produced oil volume accurately using a graduated collector with an accuracy of 0.1 cm³.

- We inject 0.2 PV of pressurized CO₂ at 1000 psig for test 1, and at 1400 psig for test 2 into the cores to produce the oil volume accumulated in the lines (dead volume); then we increase the pressure of the system by CO₂ injection. Then, we close the injection and production valves and soak the samples for 8 hours.
- We start the production period after 8 hours of soaking by reducing the pressure using a back pressure regulator (BPR). We set the production pressure at 400 psig and measure the volume of produced oil using a graduated collector with an accuracy of 0.1 cm³.
- We start the second cycle by injection of CO₂ when the oil production stops in the first cycle. We increase the system pressure from 400 psig to the desired pressure (1000 psig for test 1 and 1400 psig for test 2) by CO₂ injection, and measure the injected volume of CO₂ at each cycle. Then, we stop the pump as soon as the pressure of the system increases to the desired pressure.
- We close the injection valve, and soak the cores with CO₂ for 8 hours.
- We repeat the injection, soaking and production steps for eight cycles.

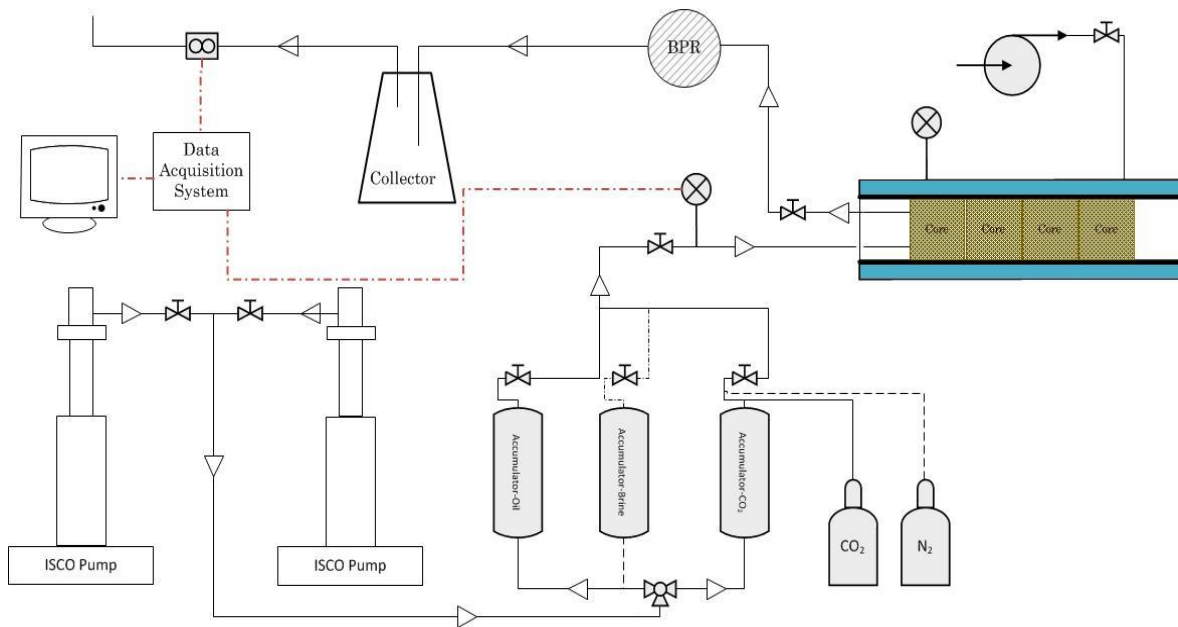


Figure 4.4. Schematic view of the cyclic CO₂ set-up.

4.4. Results and Discussions

Here, we present the results of CO₂-oil interactions at the bulk-phase conditions and in the core plugs. First, we conduct the CCE tests using a PVT cell and evaluate the swelling factor and the bubble-point pressure for different CO₂-oil mixtures. Second, we visualize the CO₂-oil interface at 50°C and 2000 psig in the visual cell to investigate the CO₂-oil interactions at reservoir conditions. We also conduct the similar visualization tests with N₂ to compare the interactions between CO₂-oil and N₂-oil. Then, we analyze the solid precipitates due to CO₂-oil interactions in the visual cell. Third, we investigate the oil recovery from the oil-saturated core plugs soaked with CO₂ in the visual cell. Finally, we present the results of cyclic CO₂ process conducted by a core flooding system.

4.4.1. CCE Tests

Figure 4.5 shows the measured density of the crude oil (ρ_{oil}) at different temperatures (21°C, 35°C and 50°C) and pressures (50-2000 psig). As expected, ρ_{oil} decreases by increasing temperature at a constant pressure, and increases by increasing pressure at a constant temperature. The measured densities can be correlated to pressure and temperature using Tait equation [199, 200]:

$$\rho_{oil}(T, P) = \frac{\rho_0(T, P_0)}{1 - \beta \ln\left(\frac{B + 0.006P}{B + 0.1}\right)} \quad (2)$$

Here, T and P₀ are temperature (K) and reference pressure (0 psig), respectively. ρ_0 , B and β are assumed to be temperature dependent:

$$\rho_0 = a_1 + a_2 T + a_3 T^2 = 376.4873 + 3.3948 T - 6.3000 \times 10^{-3} T^2 \quad (3)$$

$$\beta = c_1 + c_2 T = -0.4026 + 0.0014 T \quad (4)$$

$$B = b_1 + b_2 T^{-1} + b_3 T^{-2} \quad (5)$$

$$= -4.0379 \times 10^3 + 2.6385 \times 10^6 T^{-1} - 4.2596 \times 10^8 T^{-2}$$

The parameters a_1 , a_2 and a_3 in Eq. 3 are determined by fitting the measured densities at the reference pressure. The parameters in Eqs. 4 and 5 are determined by fitting the measured densities at different pressures and temperatures. **Figure 4.6** shows the measured and calculated densities using Eq. 2. We also calculate the average value of

absolute relative deviation (AARD) of the calculated oil density from the experimental data:

$$\%AARD = \frac{1}{N_p} \sum_{i=1}^{N_p} \left| \frac{\rho_{\text{cal}}^{\text{oil}} - \rho_{\text{exp}}^{\text{oil}}}{\rho_{\text{exp}}^{\text{oil}}} \right|_i \times 100 \quad (6)$$

The AARD value is 0.02% which means the density data can be estimated using Tait equation with an acceptable accuracy. ρ_0 values are used to calculate molar concentration of the oil in the CO₂-oil mixture for each CCE test.

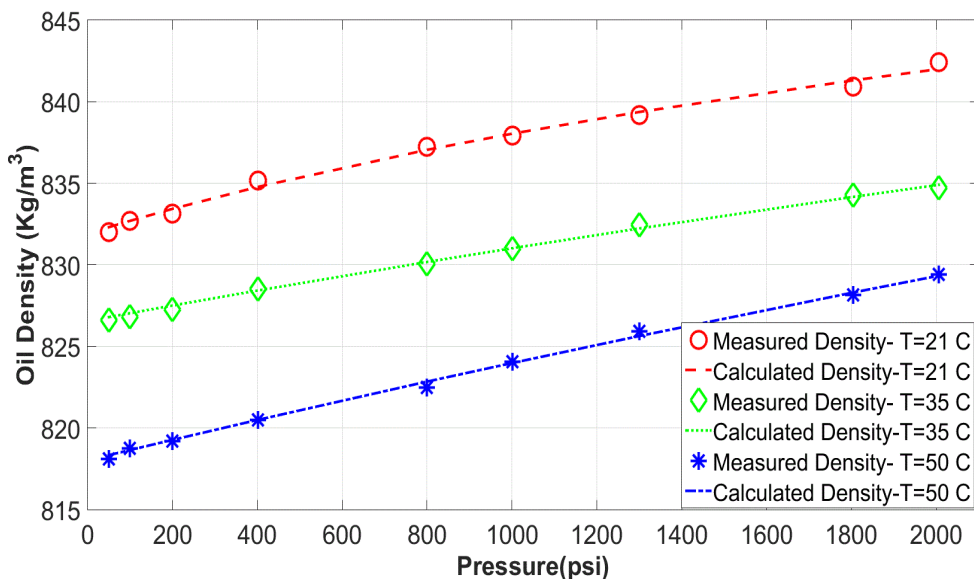


Figure 4.5. Densities of crude oil measured using the PVT cell at different temperatures and pressures.

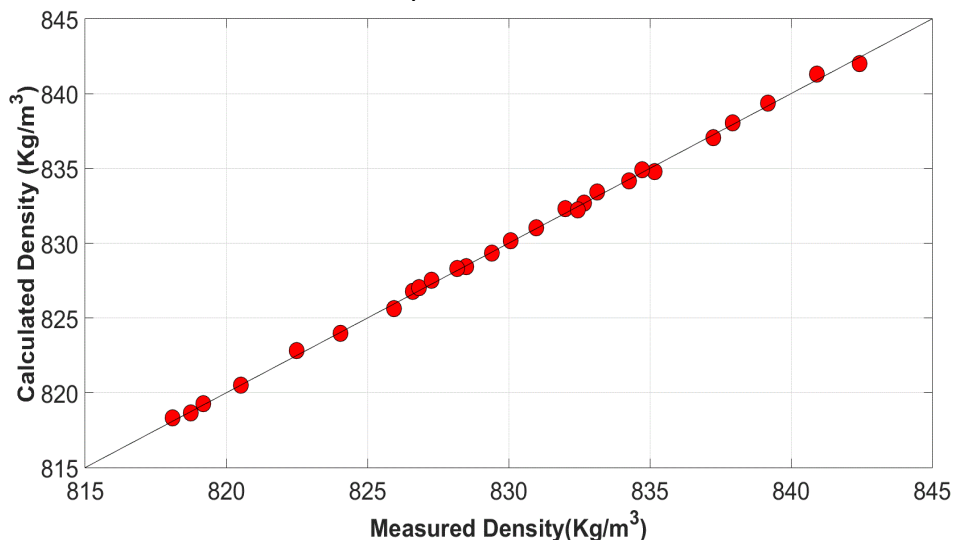


Figure 4.6. Comparison between the measured and calculated oil density.

In the next step, we mixed the oil and CO₂ with different concentrations to conduct CCE tests and define the relative volume (V_r) for CO₂-oil mixtures as:

$$V_r = \frac{(\text{Total volume})_{T \text{ and } P}}{(\text{Total volume})_{T \text{ and } P_b}} \quad (7)$$

Bubble-point pressure (P_b) is the pressure at which the slope of the pressure-volume line changes. At bubble-point pressure, the first bubble of CO₂ releases from the mixture. CO₂ forms a separate gas phase on top of the oil phase when the pressure is gradually decreased.

In **Figure 4.7**, we plot the pressure of CO₂-oil mixture versus V_r for three different CO₂-oil mixtures at 50°C (the reservoir temperature). The P_b of the mixture increases when the concentration of CO₂ in the mixture increases. **Table 4.5** lists P_b values for different CO₂-oil mixtures at different temperatures. The P_b for mixtures with CO₂ mole % of 48.36, 58.82 and 71.06 are 945 psig, 1035 psig and 1302 psig, respectively. The results show that when mixture pressure decreases gradually, the mixture with higher concentration of CO₂ reaches to the bubble-point pressure faster than the other mixtures. For example, the mixture with CO₂ mole % of 71.06 is in the two-phase condition at P=1200 psig while the two other mixtures still form a single-phase.

Figure 4.8 shows the profiles of pressure versus V_r for the CO₂-oil mixtures with CO₂ mole % of 58.82 and 71.06 at three different temperatures (50°C, 76°C and 90°C). For each CO₂ concentration, P_b increases by increasing temperature. The pressure required for dissolving CO₂ in the mixture increases by increasing the temperature. In addition, when the CO₂ concentration increases from 58.82 mole % to 71.06 mole %, P_b increases because the pressure required to dissolve additional CO₂ increases.

The total volume of oil and dissolved CO₂ at bubble-point pressure and temperature, divided by the volume of oil (without CO₂ at the same temperature but at atmospheric pressure) is defined as the swelling factor [201]. We also calculate the swelling factor (SF) of the CO₂-oil mixtures by

$$SF = \frac{(V_{OC})_{T,P_b}}{(V_O)_{T,P_0}} \times \frac{1}{1 - x_{CO_2}} \quad (8)$$

Here, V_{OC} is the molar volume of CO_2 -oil mixture at the bubble-point pressure and temperature, V_O is the molar volume of the oil at atmospheric pressure and bubble-point temperature, and x_{CO_2} is the mole fraction of CO_2 in the mixture.

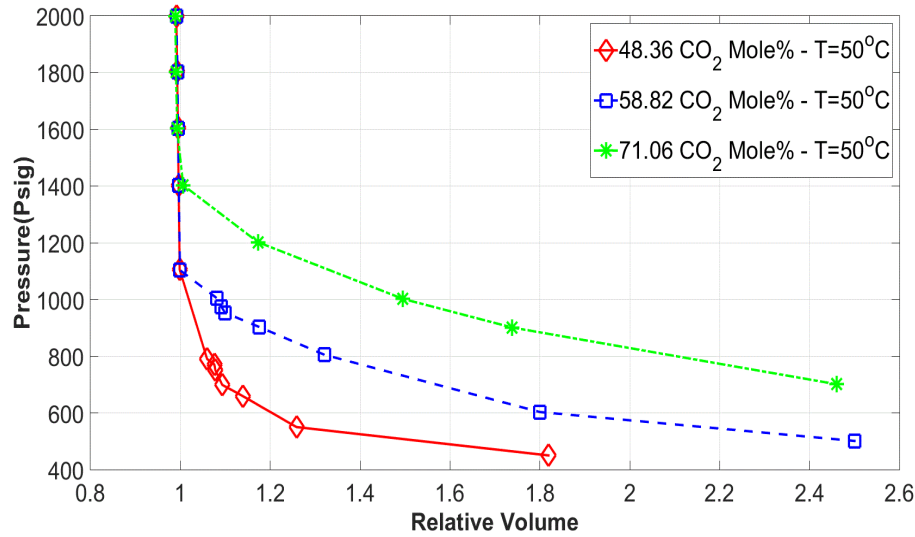


Figure 4.7. Measured relative volume versus pressure at three different concentrations of CO_2 in the mixture at 50°C .

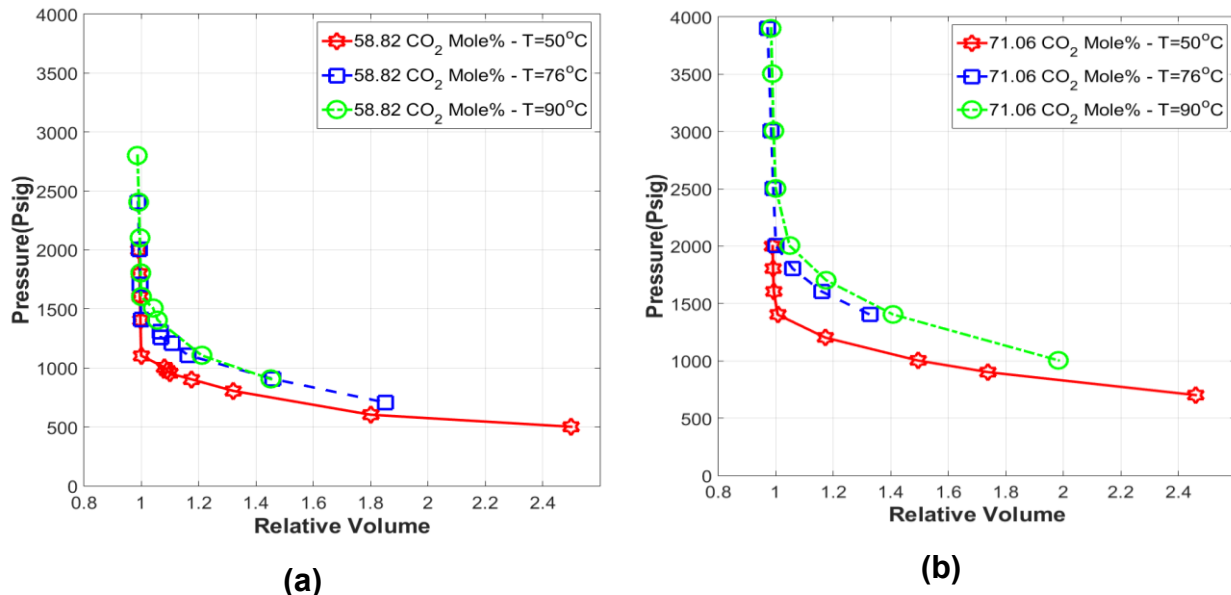


Figure 4.8. Measured relative volume at different temperatures for CO_2 mole % of (a) 58.82 and (b) 71.06.

Table 4.5 lists the calculated values of SF for the mixtures. SF increases by increasing x_{CO_2} . The oil swelling factor increases from 1.211 to 1.390 when x_{CO_2} increases from 48.36 mole % to 71.06 mole % at $T=50^\circ\text{C}$.

Moreover, SF increases by increasing temperature at constant x_{CO_2} . For example, SF for the mixture with $x_{CO_2} = 58.82\%$ increases from 1.243 to 1.262 when the temperature increases from 50°C to 90°C.

Table 4.5. Measured bubble-point pressure and swelling factor obtained from CCE tests

Exp. No.	CO ₂ mole %	Temperature, °C	Bubble-point pressure, psig	SF
1	48.36	50.1	945	1.211
2	58.82	50.1	1035	1.243
3	58.82	76.8	1318	1.254
4	58.82	90.1	1535	1.262
5	71.06	50.1	1302	1.390
6	71.06	76.9	1944	1.398
7	71.06	90.0	2376	1.410

We collect oil samples from each CO₂-oil mixture after CCE tests to measure and compare the oil composition using simulated distillation test. This apparatus separates the oil fractions based on boiling point and measures the mass concentration of each oil fraction. **Figure 4.9** shows the mass concentration of each oil fraction for the mixtures with x_{CO_2} of 48.36 %, 58.82 % and 71.06 % and for the original oil. The general trend for all CO₂-oil mixtures is similar. C₁₄ has the highest concentration for all oil samples, and the concentration of oil fractions heavier than C₁₄ decreases by increasing the carbon number. The weight percent of C₁₀-C₂₀ for the original oil and CO₂-oil mixture with $x_{CO_2}=71.06\%$ are 50 wt.% and 44 wt.%, respectively. The oil samples might become heavier after interactions with CO₂ in the PVT cell due to vaporization of light and intermediate oil components into CO₂ during the CCE tests. When the pressure of the CO₂-oil mixture decreases and CO₂ forms a separate gas phase, light and intermediate oil components evaporate into and enrich the gas phase. Consequently, the concentrations of light and intermediate components (C₁₀-C₂₀) in the oil phase decrease.

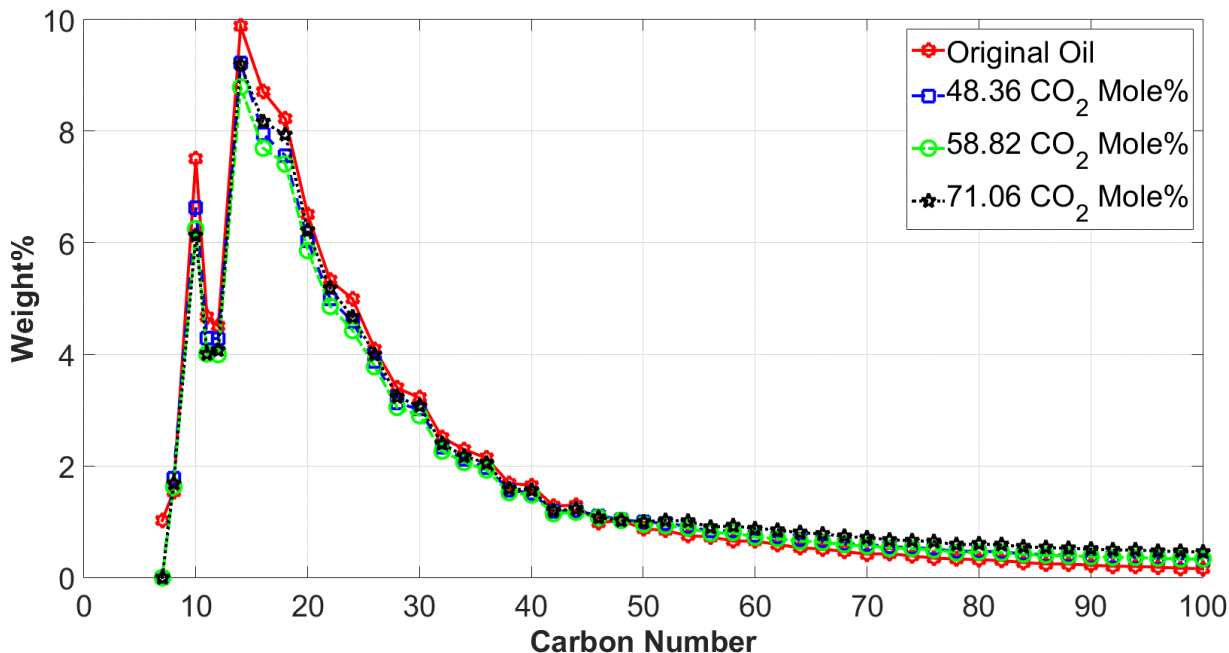


Figure 4.9. Mass fraction of original oil and CO_2 -oil mixtures measured by simulated distillation column.

4.4.2. Visualization of CO_2 -Oil and N_2 -Oil Interactions in the Visual Cell

4.4.2.1. CO_2 -Oil Interactions

In this part, we visualize the CO_2 -oil interface at 50°C and 2000 psig in the visual cell to investigate the CO_2 -oil interactions at reservoir conditions. First, we fill almost half of the cell with 235 cc of oil (0.78 mole) at atmospheric pressure, and increase the temperature from 21°C to 50°C (**Figure 4.10a**). When the temperature is stabilized at 50°C , we inject 6.4 moles of CO_2 into the visual cell until the pressure reaches 2000 psig. It takes 35 minutes to increase the pressure from 0 to 2000 psig by injecting CO_2 using the ISCO pump with flow rate of 25 cc/min. Then, we close the injection valve and record the pressure of the CO_2 -oil mixture, periodically. **Figure 4.10b** shows the CO_2 -oil interface right after closing the injection valve at 50°C and 2000 psig. At this point, the CO_2 -oil mixture is at non-equilibrium conditions, which means the concentrations of CO_2 and oil components in the gas and liquid phases have not reached the stable values. Comparing **Figure 4.10a** with **Figure 4.10b** indicates the oil expansion due to CO_2 dissolution into the oil phase. To quantify oil expansion, we define oil expansion factor (EF) as the oil volume after CO_2 injection divided by the oil volume before CO_2 injection

into the cell (**Figure 4.10a**). The oil EF is defined for both equilibrium and non-equilibrium conditions in the visual cell. At non-equilibrium conditions, the concentrations of CO₂ and oil components in the liquid and gas phases have not reached constant values, leading to variation of visual cell's pressure versus time while those are constant at the equilibrium conditions. It should be mentioned that oil EF in the visual cell experiments is different from oil SF defined by Eq.8 in the PVT cell tests. Oil SF is calculated at bubble-point pressure where single-phase of CO₂-oil mixture is at equilibrium conditions. In the next section, we investigate the convection and diffusion mechanisms to explain the dissolution of CO₂ into the oil phase.

4.4.2.2. Natural Convection Mechanism

Figure 4.10b shows the expanded oil right after closing the CO₂ injection valve at 2000 psig and 50°C. Oil EF in **Figure 4.10b** is equal to 1.23. As previously mentioned, it takes 35 minutes to increase the oil EF from 1.00 to 1.23. After closing the CO₂ injection valve at 2000 psig, we record the pressure decline versus time. As shown in **Figure 4.11**, the pressure of the visual cell declines from 2000 to 1707 psig and reaches equilibrium conditions in 5 hours. During pressure decline, more CO₂ is dissolved in the oil phase and oil EF increases from 1.23 at 2000 psig (**Figure 4.10b**) to 1.32 at 1707 psig (**Figure 4.10c**). CO₂ shows the supercritical behavior at 2000 psig and 50°C with high density of 665.43 Kg/m³. At this pressure and temperature, oil density is 829.40 Kg/m³. Right after CO₂ injection into the visual cell, CO₂ concentration at the CO₂-oil interface is higher than that in the oil bulk-phase. The CO₂ concentration gradient leads to CO₂ dissolution into the oil as soon as it contacts the oil phase. As CO₂ dissolves into the oil phase, the oil density at the interface increases to a value higher than the oil density without any dissolved CO₂ in it [202]. Therefore, the oil density at the CO₂-oil interface is higher than that in the oil bulk-phase. The natural convection phenomenon is defined as downward and upward movements of denser and lighter oils in the oil phase, respectively. The natural convection is the first mechanism for CO₂ dissolution into the oil, leading to: 1) rapid oil expansion right after CO₂ injection into the visual cell (**Figure 4.10b**), and 2) fast equilibrium of CO₂ and oil phase (**Figure 4.11**). To visualize the natural convection within the oil phase as a result of CO₂ dissolution, we replace the

black Montney oil with translucent condensate oil and conduct a similar visualization test.

4.4.2.3. Molecular Diffusion Mechanism

The second mechanism for CO₂ dissolution into the oil phase may be the CO₂ molecular diffusion based on Fick's law of diffusion. Molecular diffusion is a very slow process compared with natural convection [195], and the range of diffusion coefficient in CO₂-oil system is 0.0001-0.01 cm²/s. As a result, slow CO₂ molecular diffusion cannot explain rapid expansion of oil and fast pressure decline shown in **Figures 4.10** and **4.11**, respectively. Overall, the visualization of CO₂-oil interactions at 50°C and reservoir pressure shows that the role of natural convection for dissolution of CO₂ in the oil phase is more pronounced compared with that of molecular diffusion.

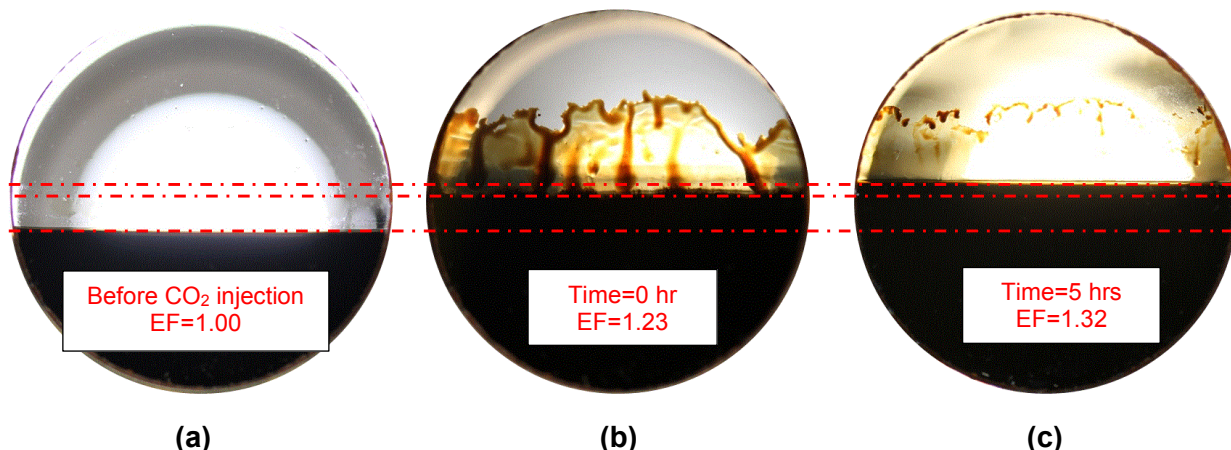


Figure 4.10. CO₂-oil interface at reservoir temperature (50°C). (a) There is 235 cc (0.78 mole) of oil in the cell when there is no CO₂ in the cell at atmospheric pressure (P=0 psig). (b) We inject 6.4 moles of CO₂ to increase the pressure from 0 psig to 2000 psig and then close the CO₂ injection valve. Oil EF is 1.23 at 2000 psig. Rapid expansion of oil after introducing the CO₂ into the visual cell is explained by natural convection mechanism. (c) Due to further CO₂ dissolution into the oil phase, pressure of visual cell declines from 2000 psig to 1707 psig after 5 hours. Rapid pressure decline during 5 hours is explained by convection mechanism. Oil EF is 1.32 at 1707 psig. The dashed line shows the level of CO₂-oil interface at different conditions.

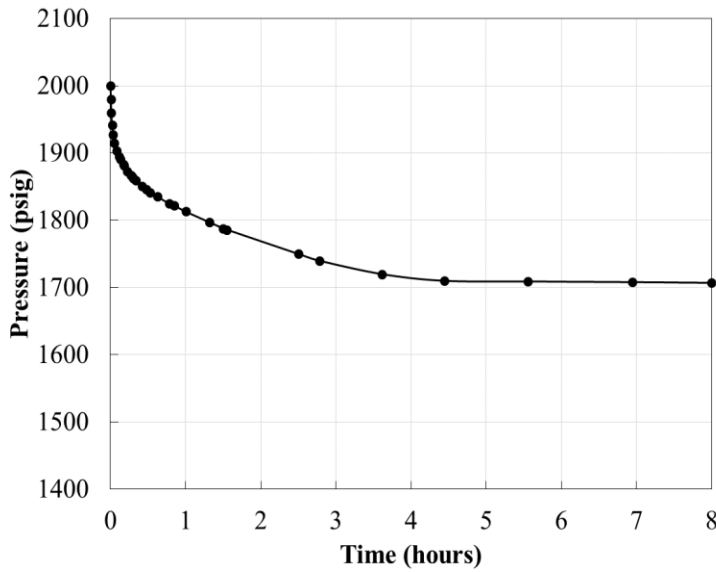


Figure 4.11. Pressure profile of CO₂-oil mixture at 50°C. The pressure of visual cell declines from 2000 psig to 1707 psig after 5 hours. Rapid pressure decline during 5 hours is explained by convection mechanism.

4.4.2.4. N₂-Oil Interactions

To compare the interactions of CO₂ and N₂ with oil, we conduct similar tests using N₂. **Figure 4.12a-c** show the N₂-oil interface at 50°C and different pressures. First, we fill the cell with 295 cc (0.98 mole) of oil at atmospheric pressure (**Figure 4.12a**). Then, we inject 1.46 mole of N₂ to increase the pressure of the visual cell from 0 to 2000 psig. After that, we stop the N₂ injection and close the injection valve. **Figure 4.12b** shows the N₂-oil interface at 50°C and 2000 psig. Comparing **Figure 4.12a** with **Figure 4.12b** shows that oil does not expand after N₂ injection at 2000 psig, and EF is almost 1.0. On the other hand, comparing **Figure 4.10a** with **Figure 4.10b** shows oil EF is 1.23 after CO₂ injection at 2000 psig and 50°C. The solubility of N₂ in the oil is much lower than that of CO₂ at same experimental conditions [203]. One day after closing the N₂ injection valve, the pressure declines from 2000 psig to 1863 psig. However, we do not observe oil expansion even after pressure drop from 2000 psig to 1863 psig. On the other hand, oil SF increases in the CO₂-oil mixture from 1.23 to 1.32 as the pressure declines from 2000 psig to 1707 psig (**Figure 4.10c**). The densities of N₂ and oil at 2000 psig and 50°C are 139.11 and 829.40 Kg/m³, respectively. Right after N₂ injection into the visual cell, N₂ concentration at the N₂-oil interface is higher than that in the oil bulk-phase. The N₂ concentration gradient leads to N₂ dissolution into the oil as soon as it

contacts the oil phase. As the N₂ dissolves in the oil phase, the oil density at the interface decreases to a value lower than the oil density without any dissolved N₂ in it. Therefore, the lighter oil at the N₂-oil interface remains on top of the initial denser oil below the interface, and does not move downward. In other words, natural convection does not happen in N₂-oil experiment and the molecular diffusion due to N₂ concentration gradient is the main mechanism for dissolution of N₂ into the oil phase. In the next step, we inject 0.65 mole of N₂ and increase the pressure of the visual cell from 1863 psig to 3000 psig (**Figure 4.12c**) to observe the possibility of oil expansion due to N₂ dissolution in oil. N₂ density at 3000 psig and 50°C is 200.56 Kg/m³. We do not observe oil expansion even at 3000 psig. However, it does not mean that there is no N₂ dissolution in the oil phase. Pressure decline during N₂-oil interactions and liberation of N₂ bubbles from the oil phase after declining the pressure to atmospheric pressure confirm the dissolution of N₂ in the oil phase. Weaker N₂-oil interactions compared with CO₂-oil interactions results in higher minimum miscibility pressure (MMP) for N₂. MMP is the minimum pressure required to eliminate the interfacial tension (IFT) between oil and injected gas (N₂, CO₂, and etc.). Hawthorne et al. 2016 [204] conducted the capillary rise/vanishing IFT tests to evaluate the MMP between oil and different gases such as CO₂, N₂ and CH₄. The results of MMP measurements at 42°C showed that the MMP between the Bakken oil (API of 38.7°) and CO₂ (1285±37 psig) is much lower than that between the Bakken oil and N₂ (22370±840 psig).

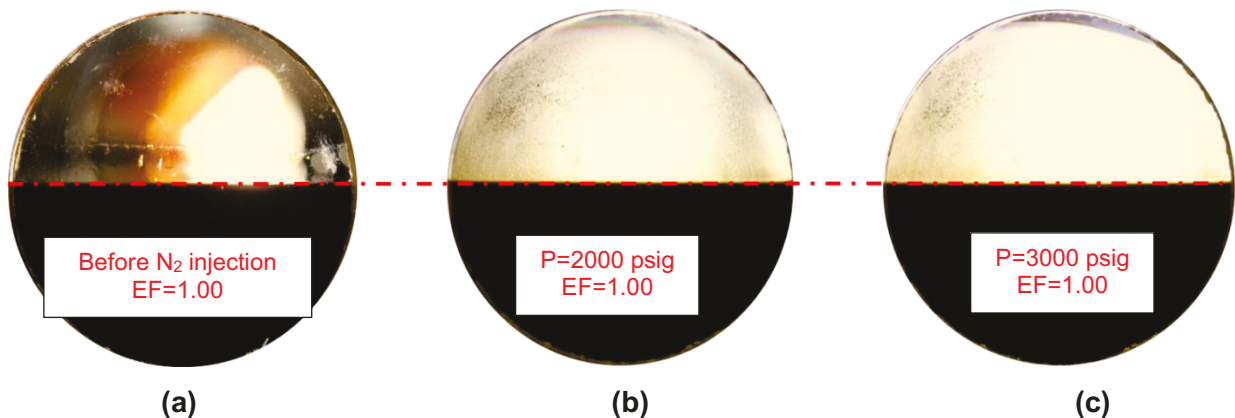


Figure 4.12. N₂-oil interface at reservoir temperature (50°C) and different pressures. (a) There is 295 cc (0.98 mole) of oil in the cell before injecting N₂ at atmospheric pressure (P=0 psig) (b) 1.46 mole of N₂ is injected to increase the atmospheric pressure to 2000 psig. Oil EF is equal to 1.0 at this pressure. (c) We inject 0.65 mole of N₂ to increase the pressure from 1863 psig to 3000 psig. Oil EF is equal to 1.0. The dashed line shows the level of N₂-oil interface at different conditions.

4.4.2.5. Precipitation of Solid Particles due to CO₂-Oil Interactions

We observe the deposition of solid particles during the CO₂-oil interactions at 50°C and 1707 psig. **Figure 4.13a** shows the solid particles accumulated at the CO₂-oil interface and attached on the sight glass (highlighted circles). **Figure 4.13b** shows the mixture of solid precipitates and oil deposited at the bottom of visual cell after the CO₂-oil visualization test. We analyze the precipitates using a high-resolution SEM apparatus (Zeiss EVO M10, Oxford). First, we collect the precipitates and place them in the oven at 50°C for 24 hours. Then, we prepare a uniform thin film of precipitates on a pin stub, and coat the surface of the thin film with gold. Gold coating prevents the charging issue during SEM analysis. **Figure 4.14 a-b** show the secondary electron (SE) and energy x-ray dispersive spectroscopy (EDS) images of the precipitates. SE images are routinely used for analyzing the surface morphology while EDS images are used to show the elemental mapping of the surface. EDS images show the concentration of each element in the sample using the black and white color map. White and black colors represent the lowest and highest concentration of each element, respectively. EDS analysis shows that the solid precipitates are mainly composed of carbon and sulfur. The concentration of carbon is higher than that of sulfur. The results suggest that the precipitates may be asphaltene. Polar asphaltene components can agglomerate and deposit as precipitates when oil contacts CO₂ [205]. Asphaltene is a mixture of organic molecules that vary

widely in composition. Generally, most asphaltenes are composed of 79-88 wt. % carbon, 7-13 wt. % hydrogen, 0-8 wt. % sulfur, 2-8 wt. % oxygen and 0-3 wt. % nitrogen [206]. Arenas-Alatorre et al. [207] conducted SEM/EDS analysis on asphaltenes precipitated from Maya crude oil. The EDS analysis showed that the asphaltene samples are mainly composed of carbon, oxygen and sulfur. To make sure that the precipitates are asphaltene, we conduct IP-143 and measure the n-heptane insoluble asphaltene content of oil samples and precipitates. The procedure of conducting the IP-143 test is explained elsewhere [208]. We use three oil samples and measure their asphaltene contents. We repeat the IP-143 test three times for each oil sample, and report the average wt.% of asphaltene. The average asphaltene content of the oil before and after contact with CO₂ are 2.2 wt.% and 2.1 wt.%, respectively. The small difference between asphaltene content of the oil before and after contact with CO₂ may indicate the asphaltene deposition after CO₂-oil interactions in the visual cell. We also measure the asphaltene content of precipitates deposited at the bottom of visual cell (**Figure 4.13b**). The results show that the average asphaltene content of precipitates is 14.0 wt.% which is almost 6.4 times more than that of the oil before contact with CO₂. **Figure 4.15** shows the n-heptane insoluble asphaltene content of oil accumulated on the filter paper. Asphaltene content of precipitates deposited at the bottom of the cell is high as shown in **Figure 4.15**.

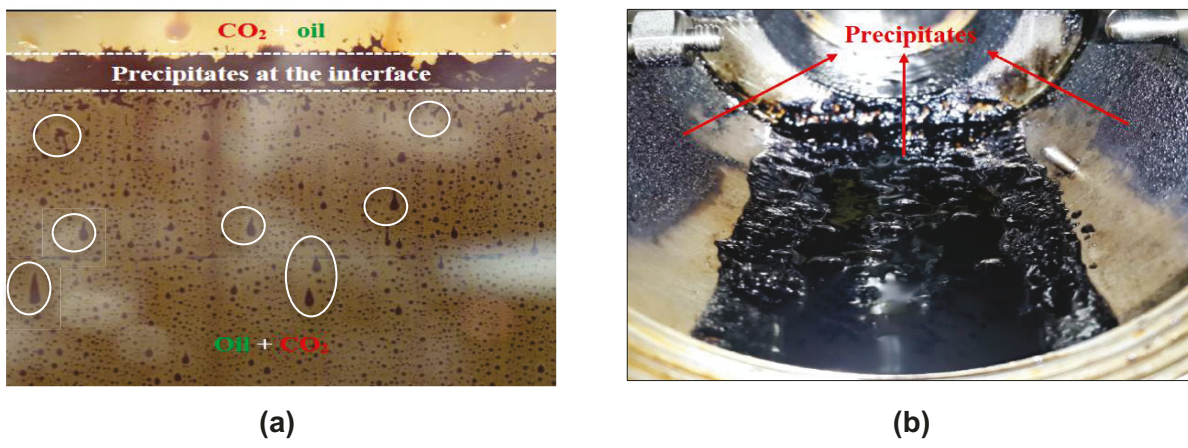


Figure 4.13. (a) Solid precipitates deposited at the CO₂-oil interface at 1707 psig and 50°C. Brown area below CO₂-oil interface is mainly a mixture of oil and CO₂ and black dots highlighted by circles are solid precipitates attached on the sight glass. (b) Solid precipitates mixed with oil deposited at the bottom of visual cell after finishing the CO₂-oil test.

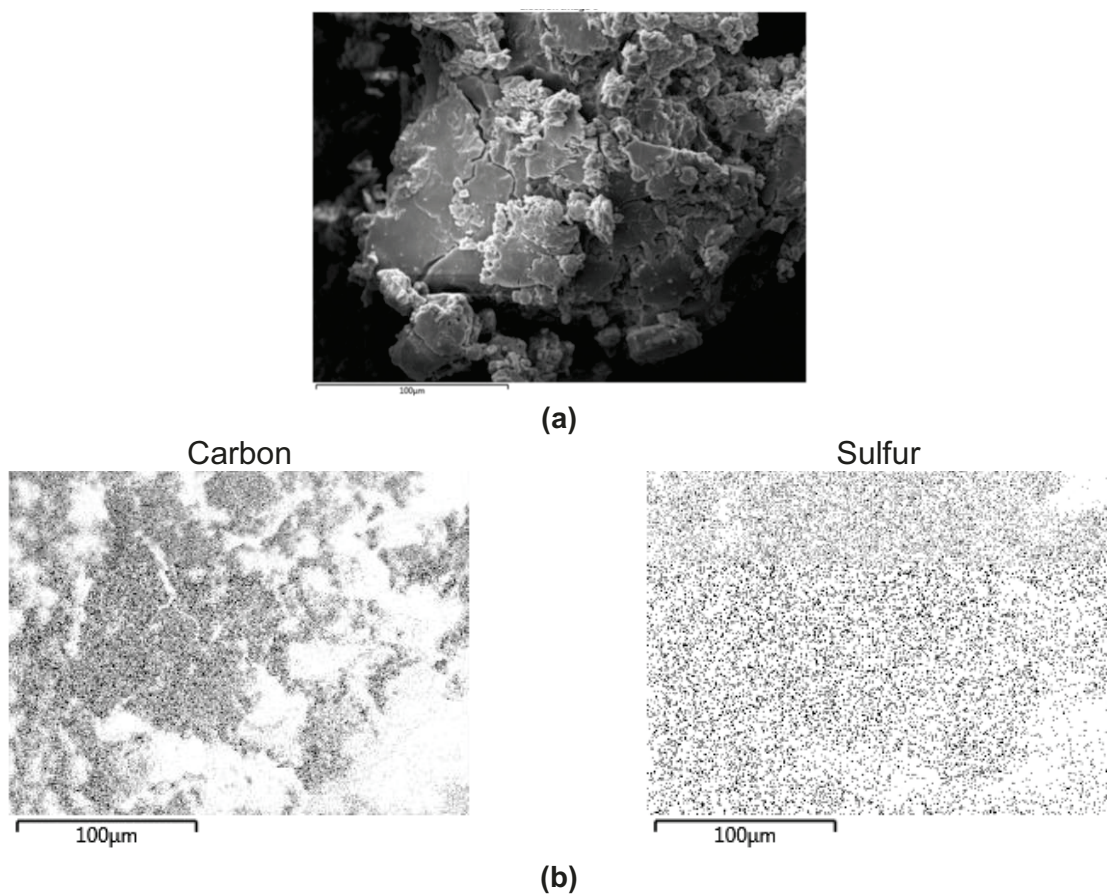


Figure 4.14. (a) SE image and (b) the results of EDS analysis on the solid precipitates. Black and white areas represent the highest and lowest concentrations of each element, respectively.

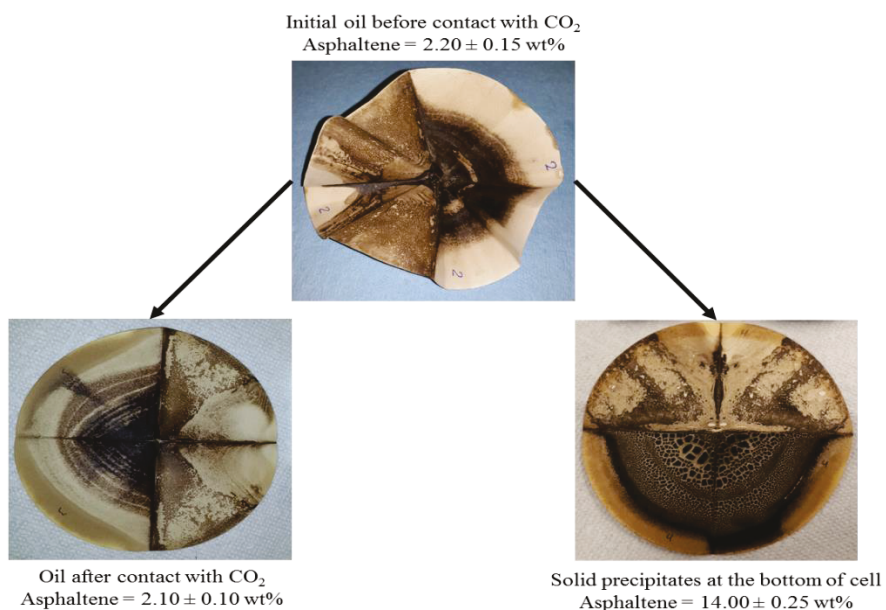


Figure 4.15. Conducting IP-143 test for measuring asphaltene content. The asphaltene content

of oil samples before and after contact with CO₂ are 2.2 and 2.1 wt.%, respectively. The asphaltene content of solid precipitates at the bottom of the visual cell (**Figure 4.13**) is 14.0 wt.%.

4.4.3. CO₂ Soaking Experiments Using Oil-Saturated Core Plugs

In this section, we present the results of soaking tests using oil-saturated core plugs. We place oil-saturated core plugs of S1, S2, and S4 in the visual cell. Then, we adjust the temperature to 50°C and increase the visual cell pressure to 2000 psig by CO₂ injection. The bulk volume of each core sample is almost 25 cm³. We inject 7.9 moles of CO₂ to increase the visual cell pressure to 2000 psig at 50°C. **Table 4.6** lists the initial mole (and initial volume) of oil for each core plug. For example, the initial mole of oil in S1 sample is 0.0102 which is much smaller than that of CO₂ in the visual cell (7.9 moles). After pressurizing the visual cell with CO₂, we visualize the cross section of the core plug and record the possible changes occurring on the rock surface during the soaking process. **Figure 4.16a-d** shows the surface of S1 core sample at four different times. **Figure 4.16a** shows the rock surface right after pressurizing the cell with CO₂. After 1 day of soaking with CO₂, we do not observe any significant changes on the rock surface (**Figure 4.16b**). After 3 days, the color of the rock surface changes from bright grey to dark brown (**Figure 4.16c**), indicating that the oil wets the rock surface. At the same time, we observe condensates attached on the top surface of the visual cell, indicated by yellow spots in **Figure 4.17**. The color of condensates is brighter than the color of original oil. After 5 days, the wet surface becomes dry and, the color of the rock surface changes from dark brown to bright grey (**Figure 4.16d**). The soaking tests last for 3 weeks. After 3 weeks, we turn off the heating jacket to reduce the temperature of the visual cell from 50°C to 21°C. Then, we gradually vent out CO₂. The average rate of pressure decline during CO₂ release is 10 psi/min. We observe yellow condensates accumulated at the bottom of the visual cell during reduction of pressure and temperature while we do not observe any oil production from core plugs during reduction of pressure and temperature. These observations may indicate that the accumulated condensates are mainly oil components vaporized from the oil into the CO₂ bulk phase. Vaporized oil components condense and form a separate liquid-phase

at the bottom of the visual cell when the pressure and temperature decline below the dew point.

Finally, we measure the weight of the core plugs, and the volume of the accumulated condensates at the bottom of the cell after the soaking experiment. **Table 4.6** shows that the oil recovery factor for S1, S2, and S4 are 67.5%, 72.5%, and 73.9%, respectively. The produced oil volume based on the mass balance calculations is higher than the oil volume collected from the bottom of the cell. For example, the produced oil volume based on mass balance calculation and accumulated oil volume at the bottom of the cell for core S1 are 2.07 cc and 1.25 cc, respectively. This observation indicates that a considerable portion of the vaporized oil components may not condense at the bottom of the cell and may vent out with the CO₂ bulk-phase.

Table 4.6. Oil recovery factor for soaking experiments with CO₂. 7.9 moles of CO₂ is required for pressurizing the visual cell to 2000 psig at 50°C.

Sample ID	Depth (m)	K _{Air} (md)	Pore volume (cc)	Initial oil (cc)	Initial oil (mole)	Oil recovery (% initial oil)
S1	1568.89	4.98	4.14	3.07	0.010	67.5
S2	1569.92	7.53	4.35	4.25	0.014	72.5
S4	1580.64	0.30	3.07	1.20	0.004	73.9

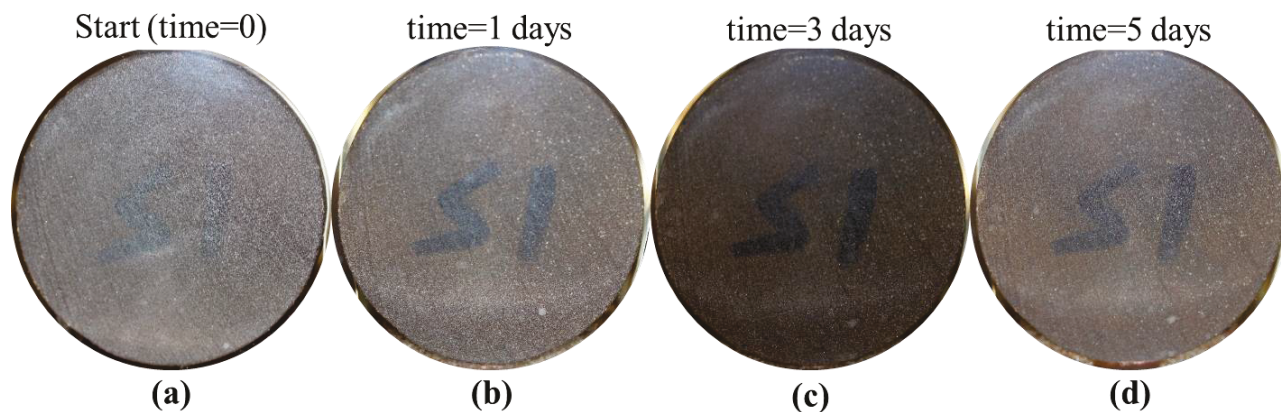


Figure 4.16. Side view of S1 surface soaked in CO₂ at 2000 psig and 50°C at (a) initial state, (b) after 1 day (c) after 3 days, and (d) after 5 days.

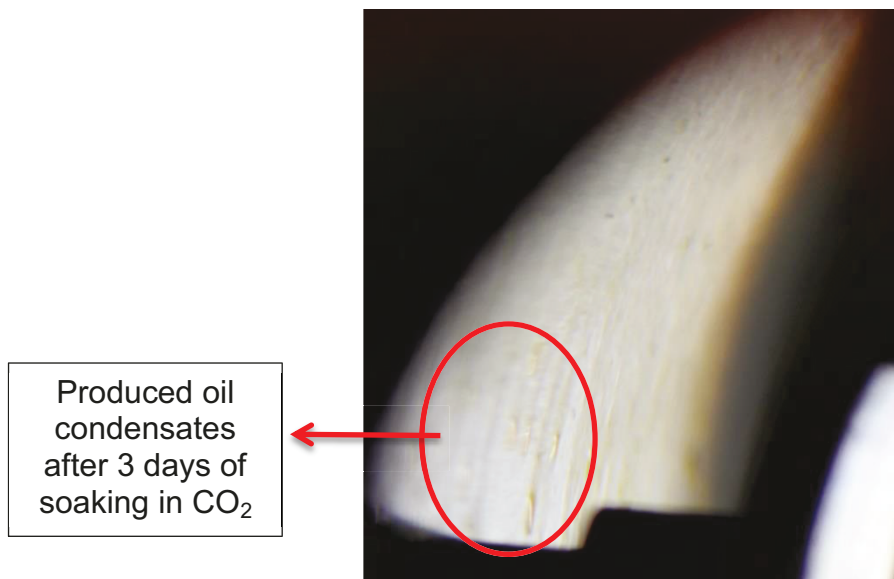


Figure 4.17. Oil droplets condensed on the top surface of the cell during soaking of S1 core sample in CO₂.

In brief, the soaking tests results in the following key observations: 1) the color of the core surface changes during the soaking tests, 2) yellow droplets condense on top of the visual cell, 3) oil components accumulate at the bottom of the visual cell after finishing the test and, 4) oil recovery factor is higher than 67%. The observations suggest that oil-recovery mechanisms include CO₂ diffusion into oil, oil swelling, and oil extraction by CO₂.

- CO₂ has a high potential for dissolution into and expansion of the oil as shown in **Figure 4.10c** and **Table 4.5**. The diffusion is mainly due to CO₂ concentration gradient. Several studies reported the CO₂ diffusion coefficients in one-component pure mineral oils at different pressure and temperature conditions [209-211]. The CO₂ diffusion coefficients are in the range of 1.8×10^{-5} - 12.6×10^{-5} cm²/s. The CO₂ diffusion coefficient into the oil at reservoir conditions is up to 10 times higher than that measured in the laboratory [212]. The diffusion coefficient into oil for supercritical CO₂ is 10-100 times more than that for liquid CO₂ [213]. The range of CO₂ diffusion coefficient into oil is 0.0001-0.01 cm²/s in the soaking tests. Other studies also showed that CO₂ diffusion can be considered as an oil-recovery mechanism in fractured reservoir [211] and tight rocks [214].

- CO_2 diffuses into the oil and results in oil swelling. The saturation of the swollen oil in the core plugs increases. Finally, the swollen oil wets the core surface and changes the color of the core surface. Color change of core surface from bright grey to dark brown in **Figure 4.16c** may imply oil expansion due to CO_2 diffusion. Hawthorne et al. 2013 [171] conducted a series of CO_2 exposure tests using tight rock samples and, proposed a mechanism in which CO_2 permeates into the tight rocks, dissolves into the oil, enhances oil mobilization, and displaces the oil out of the rock surface.
- Oil components expelled out of the core can be vaporized into the CO_2 bulk-phase since large volume of CO_2 is in contact with the oil. For example, the molar ratio of CO_2 to oil for S1 core is 775. High molar ratio of CO_2 to oil leads to vaporization of oil components from oil into CO_2 bulk-phase. Color change of the core surface from dark brown to bright grey in **Figure 4.16d** may suggest vaporization of oil components into CO_2 bulk-phase.

The soaking tests may represent the interactions between oil-saturated matrix and the CO_2 -saturated fracture. In the next step, we investigate the CO_2 -oil interactions in the oil-saturated core plugs in a cyclic CO_2 process. The main differences between CO_2 cyclic process and soaking tests are: 1) the molar ratio of CO_2 to oil in a cyclic process is smaller than that in a CO_2 soaking test (more than 700), 2) the produced oil volume is measured sequentially for each cycle in the cyclic CO_2 process while the total produced oil volume is calculated at the end of the CO_2 soaking test, 3) produced CO_2 containing vaporized oil components is replaced with pure CO_2 in the subsequent cycle of cyclic CO_2 test while CO_2 -oil contact lasts for three weeks without CO_2 replacement in the soaking test, and 4) there is a pressure driven flow in cyclic CO_2 process (injection and drawdown) in addition to diffusion and dissolution of CO_2 into the core plugs while the pressure does not change considerably in the soaking test. Therefore, conducting the cyclic CO_2 process provides a complementary tool to understand the CO_2 -oil interactions at the field scale.

4.4.4. Cyclic CO₂ Process

In previous sections, we visualized and evaluated: 1) swelling factor of the CO₂-oil mixture with different CO₂ concentrations, 2) asphaltene precipitation due to CO₂-oil interactions, 3) vaporization of oil components into the CO₂ during the CO₂ soaking tests, and 4) CO₂ diffusion and dissolution into the oil in the visual cell. To understand how CO₂ interacts with oil in the tight rocks and leads to oil production, we conduct the cyclic CO₂ tests on the Montney core plugs. We perform the cyclic CO₂ process at 1) 1000 psig and 21°C (the room temperature), and 2) 1400 psig and 50°C (the reservoir temperature).

First, we saturate cores S1 and S3 with oil as described in the methodology section. Then, we mount the cores in the core holder in series form and apply a confining pressure 3000 psig. The petrophysical properties of core plugs are listed in Table 1. Next, we conduct the pre-flush step by injecting 0.2 PV of pressurized CO₂ into the cores to displace out the oil in the lines (dead volume). Then, we inject CO₂ to increase the pressure of the cores, close the injection and production valves, and soak the core plugs with CO₂ for 8 hours. After 8 hours, we set the back pressure regulator at 400 psig and open the production valve. The produced oil volume is collected in a graduated collector. We also measure the weight of the core plugs at the end of the cyclic CO₂ process to calculate the final oil recovery by mass balance calculations. The produced oil volume based on mass balance may differ from measured in the graduated collector especially for the experiments conducted at elevated temperatures. Evaporation of light oil components into the CO₂ phase during production period results in discrepancy between the two methods. Produced oil volume collected in a graduated collector is lower than that calculated based on mass balance. Thus, we report the final oil recovery based on the mass balance calculations. To report the oil recovery factor for each cycle, first, we calculate the ratio of the produced oil volume at each cycle to the final collected oil volume. Then, the calculated ratio for each cycle is multiplied by produced oil volume based on mass balance calculations to eliminate the effect of oil evaporation by CO₂. The production period continues until no more oil is produced. When the oil production stops, we start the subsequent cycle by CO₂ injection into the core plugs and increase the pressure of system to the desired pressure. We repeat this procedure for 8 cycles.

We plot the pressure of the system versus time for both cyclic CO₂ tests (**Figure 4.18**). **Figure 4.18** shows the pressure of cyclic CO₂ process during: 1) CO₂ injection step, 2) slowly pressure drop during soaking step, and 3) steeply pressure reduction during production period. Production period takes around 21 minutes for all cycles and after that, we do not observe oil production.

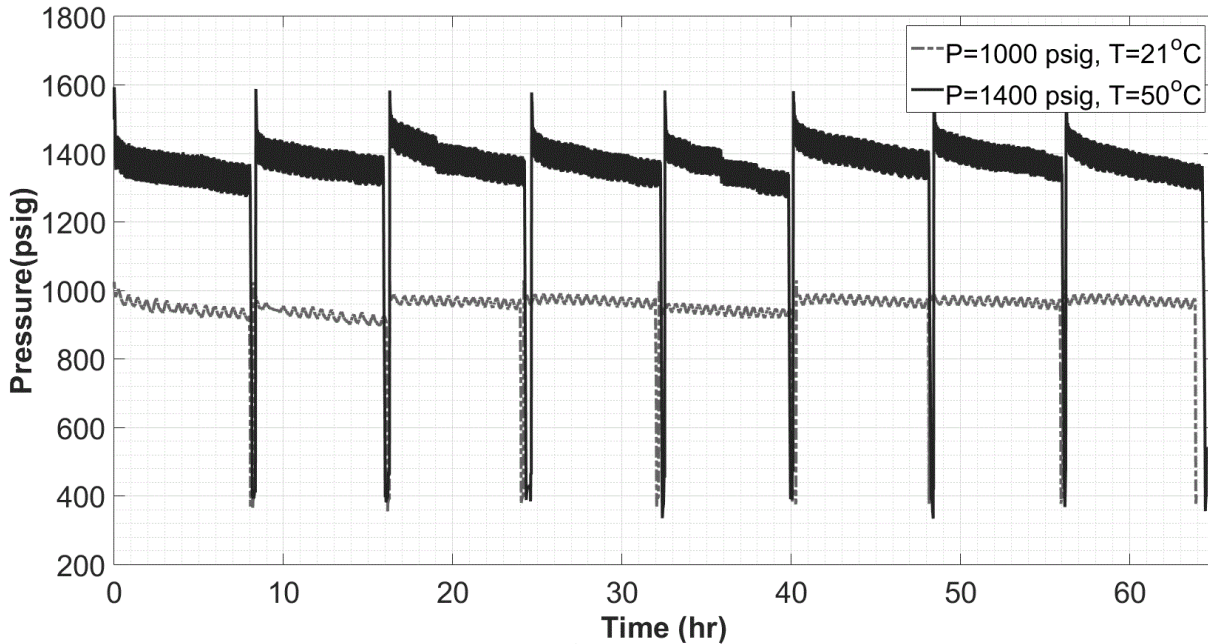


Figure 4.18. Pressure profiles for cyclic CO₂ tests conducted at 1400 psig/50°C and 1000 psig/21°C.

We define normalized injected volume of CO₂ as:

$$V_{CO_2,norm} = \frac{\text{Injected CO}_2 \text{ volume at each cycle}}{\text{Pore volume}} \times 100 \quad (9)$$

Table 4.7 lists the normalized injected volume of CO₂ for each cycle. Since the oil is produced in subsequent cycles, additional CO₂ volume is required to maintain the desired pressure (1000 psig and 1400 psig) for each cycle. The change of injected CO₂ volume for the cycles 1-4 in test 1 is more than that for cycles 5-8 because the oil recovery for the cycles 1-4 is higher than that for cycles 5-8. The injected volume of CO₂ for the first cycle of test 2 is more than that for the first cycle of test 1 due to higher dissolution of CO₂ into oil at higher pressure and temperature. Higher dissolution of CO₂ into the oil results in higher oil recovery in the first cycle of the test 2 compared with that

of the test 1. Higher injected CO₂ volume in the subsequent cycles of test 2 compared with those of test 1 is related to higher oil recovery at higher pressure and temperature. Oil recovery is higher for the test conducted at 1400 psig and 50°C; therefore, there is more room for CO₂ in the subsequent cycle.

Table 4.7. Normalized injected volume of CO₂ for cyclic CO₂ process conducted at 1000 psig/21°C and 1400 psig/50°C.

No. of cycle	V _{CO₂,norm} at 1000 psig and 21°C	V _{CO₂,norm} at 1400 psig and 50°C
1	15.12	18.23
2	34.78	51.02
3	46.59	70.57
4	60.41	73.01
5	63.50	75.25
6	62.97	82.69
7	67.33	85.25
8	71.27	80.77

Figure 4.19 shows the oil production profile for the cyclic CO₂ tests. The final oil recovery for test 1 is 66.00%. The oil recovery factor for first four cycles of the test 1, are 16.97%, 11.31%, 10.37% and 9.43%, respectively. Oil recovery for cycles 1-4 and cycles 5-8 of test 1, are 74% and 26 % of the final recovered oil volume, respectively. The final oil recovery for test 2 is 77.09%. The oil recovery factor for the first four cycles of test 2, are 22.39%, 15.19%, 13.11% and 7.99%, respectively. Oil recovery for cycles 1-4 and cycles 5-8 of test 2, are 76% and 24% of the final recovered oil volume, respectively. The results suggest that the first four cycles show the highest oil recovery in the cyclic CO₂ process. Other studies [175, 185, 215] also concluded that three cycles for cyclic CO₂ process show the highest oil recovery from the cores drilled from tight oil formations located in northwestern China.

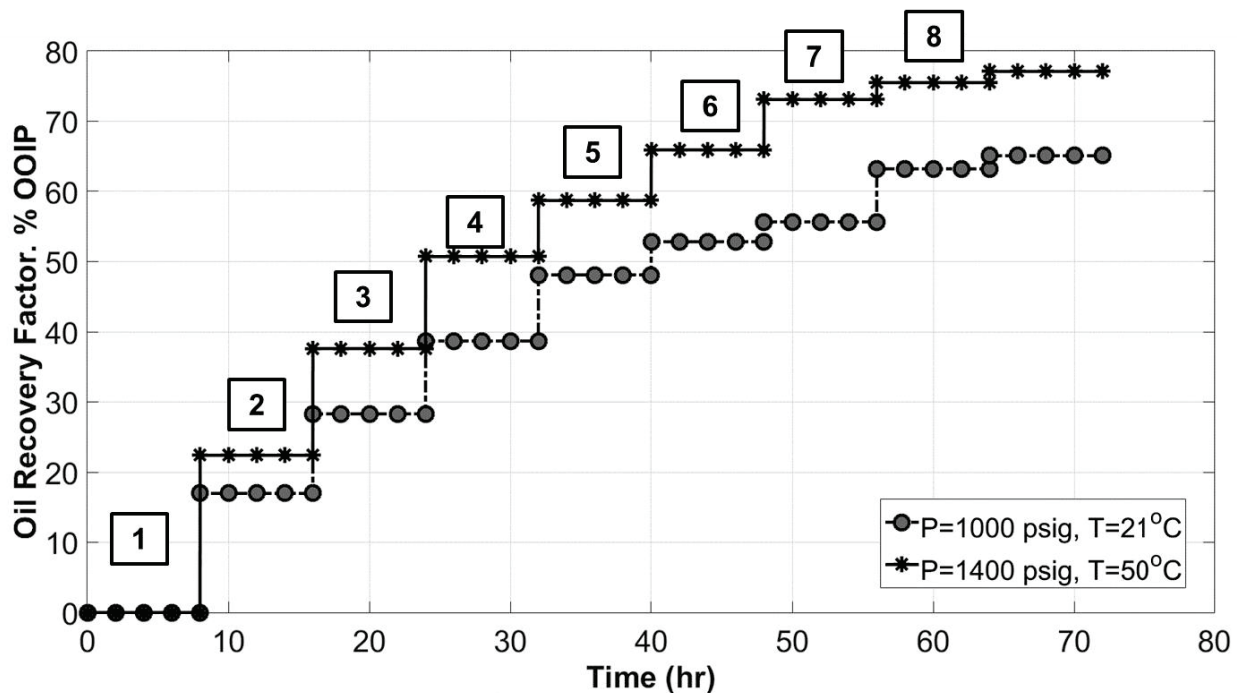


Figure 4.19. Oil production profile for cyclic CO_2 processes at 1000 psig/21°C and 1400 psig/50°C.

We measure the viscosity of oil before and after cyclic CO_2 process using a concentric-cylinder rheometer. We place 0.5 cc of produced oil into the loading cell and measure the oil viscosity. We repeat the oil viscosity measurement three times for each sample. We measure the viscosity of six oil samples and report the average viscosity and the standard deviation.

We collect the produced oil in the graduated cylinder and measure the viscosity of the oil sample immediately after finishing the last cycle of tests (eighth cycle). The oil viscosity before and after cyclic CO_2 process are 9.6 ± 1.3 cp and 2.1 ± 0.64 cp, respectively. One possible reason for the oil viscosity reduction can be the oil dilution after CO_2 -oil interactions in the porous media. The heavy oil components may be deposited in the porous media during soaking time. As a result, the lighter oil can be produced during production period. We conduct the compositional oil analysis using simulated distillation column to compare the composition of the original oil and the oil produced from the first cycle (**Figure 4.20**). **Figure 4.20** shows that the concentration of C₈-C₂₆ for the oil produced from the first cycle is higher than that for the original oil while

the concentration of heavier oil fractions ($> \text{C}_{30}$) for original oil is higher than that for produced oil. The results of the oil compositional analysis indicate that the produced oil becomes lighter after CO_2 -oil interactions in the cyclic CO_2 process.

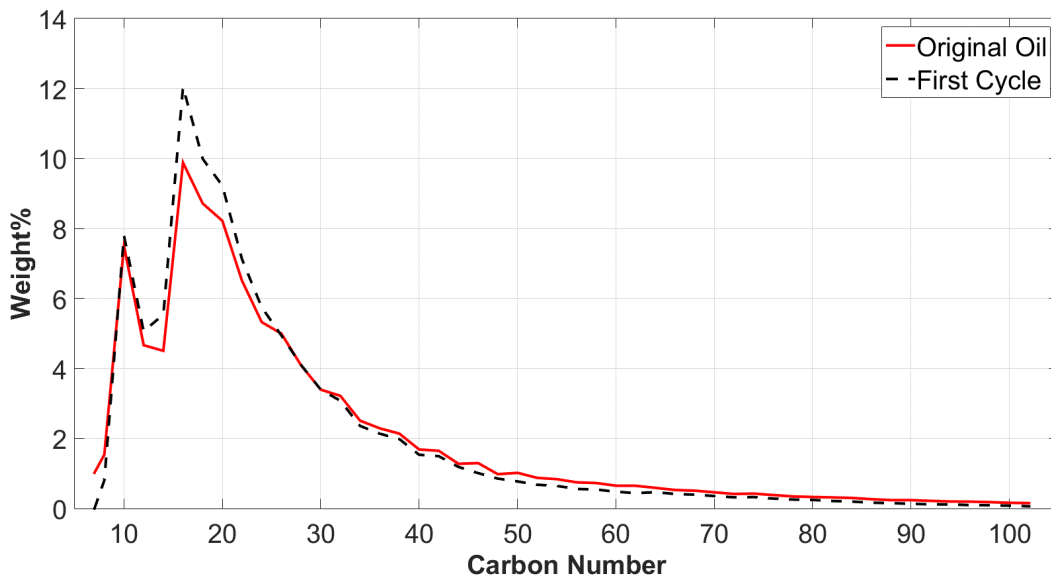


Figure 4.20. Mass fraction of the original oil and the oil produced from the first cycle measured by simulated distillation column.

4.5. Conclusions

We conducted a series of experiments to 1) investigate the swelling factor and bubble-point pressure of the CO_2 -oil mixtures at the bulk-phase conditions using a PVT cell, 2) visualize CO_2 -oil interactions in the visual cell at the reservoir conditions, 3) evaluate the possibility of asphaltene precipitation due to CO_2 -oil interactions in the visual cell, 4) evaluate oil production from oil-saturated core plugs soaked with CO_2 in the visual cell, and 5) investigate the oil recovery during the cyclic CO_2 process. The main conclusions are summarized based on the experimental results as follows:

- The results of CCE tests conducted using the PVT cell show the oil swelling factor increases from 1.211 to 1.390 by increasing the CO_2 concentration from 48.36 mole% to 71.06 mole%. High CO_2 solubility into the oil leads to oil expansion at reservoir conditions. Increasing the temperature of the CO_2 -oil mixture also results in higher oil swelling factor.

- We visualized the oil expansion as a result of CO₂ dissolution at reservoir conditions (2000 psig and 50°C). CO₂ can significantly dissolve into and expand the oil.
- Asphaltene precipitates due to CO₂-oil interactions at the bulk-phase conditions in the visual cell. The results of SEM/EDS analysis show the main components of asphaltene (carbon and sulfur). In addition, the results of IP-143 test confirm the precipitation of asphaltene when the Montney oil interacts with CO₂ at reservoir conditions.
- The results of CO₂ soaking tests show high oil recovery from the oil-saturated Montney core plugs. The key mechanisms for oil production are: 1) oil swelling as a result of CO₂ dissolution into the oil, and 2) evaporation of oil components expelled out of the core into CO₂ bulk-phase.
- The results of cyclic CO₂ tests show the high oil recovery from oil-saturated Montney core plugs (more than 66% of the original oil in-place). The first four cycles recover more than 70% of the total recovered oil from the core plugs.
- In summary, the results of this work suggest that application of CO₂ (as a fracturing fluid in fracturing operations or EOR fluid in the cyclic CO₂ process) may lead to improved oil recovery from the Montney tight oil formation.

Chapter 5 Imbibition Oil Recovery From Tight Rocks by Non-ionic Surfactant Systems

5.1. Introduction

Hydrocarbon production from unconventional resources has been increased by the combination of hydraulic fracturing and horizontal drilling over the past decade [166, 176, 216, 217]. However, the oil recovery factor is usually very low (less than 10% of original oil in-place) for these resources. This is due to their ultra-low permeability, complex pore structure, and oil-wet (or mixed-wet) behavior [15, 218-220]. Recently, different enhanced oil recovery (EOR) methods have been used to increase the oil recovery factor of unconventional resources [212, 221-225]. Success of any EOR methods strongly depends on rock-fluids interactions. Recently, there have been attempts to improve the oil recovery from unconventional resources by modifying the fracturing fluid formulation. Although using produced gas/CO₂ as a fracturing fluid is soaring during the recent years, water is still the common fluid used for fracturing operations [8]. This is because it (i) is cheaper [8], (ii) is more available except some arid areas such as Texas and North Dakota [226], and (iii) requires less well-head facilities compared with non-aqueous fluids.

There is an open question if using additives in the aqueous fracturing fluid can improve oil recovery from tight rocks. Several experimental studies conducted at the lab-scale have shown that adding surface active agents (surfactants) to the aqueous phase can facilitate the counter-current imbibition of the aqueous phase into the matrix, resulting in oil displacement from the matrix and oil recovery improvement [224, 227-234]. The literature is enriched with mechanistic studies conducted on fractured carbonates [235-240], chalks [241-243], and sandstones [244, 245] to understand how surfactant solutions can improve oil recovery [246-253]. The mechanisms proposed for this recovery improvement include (i) IFT reduction between oleic and aqueous phases [133, 250, 254] and (ii) alteration of rock wettability from oil-wet to water-wet [255-260]. However, there is still ongoing debate on how spontaneous imbibition of surfactant solutions can improve oil recovery from tight rocks. These rocks generally have two

unique features that differentiate them from conventional rocks. These features are that (i) a significant portion of their pore-throat size distribution falls into the ultra-low scale (<100 nm) [261-263] and (ii) their pore structure is divided into hydrophilic and hydrophobic networks [264]. Existence of hydrophobic nanopores in organic matter (OM) is responsible for strongly oil-wet behavior of tight rocks [135, 168]. To expel the oil out of hydrophobic network, surfactant solutions should be able to flow through the nanopores in OM, preferentially wet the rock surface, and displace the oil out of these pores.

Considering capillarity as the main driving force for spontaneous imbibition, capillary pressure decreases as the IFT between oleic and aqueous phases (Young-Laplace equation) decreases [239]. For example, Milter and Austad [242], showed that imbibition of surfactant solutions into chalk cores leads to 5% oil recovery factor when the IFT is less than 0.02 mN/m. On the other hand, wettability alteration from oil-wet (or mixed-wet) to water-wet favors aqueous phase imbibition into rocks [265, 266]. The effects of IFT reduction and wettability alteration on oil recovery act in opposite directions during spontaneous imbibition. Therefore, there should be a driving force for micelles formed in surfactant solutions to flow through the hydrophobic pore network and displace the oil out.

Recently, different types of surfactants (anionic, cationic, nonionic, and amphoteric) have been used to improve the imbibition oil-recovery from tight rocks at the lab-scale [224, 267-269]. Alvarez and Schechter [232, 270], suggested that anionic and nonionic-cationic surfactants work better for tight siliceous and carbonates rocks, respectively. However, nonionic surfactants are most common at the field-scale because they are more compatible with other chemicals such as clays stabilizer, biocide, and friction reducers compared with ionic surfactants [271]. Among non-ionic surfactants, octylphenol ethoxylates (OPE) are widely used as detergents, wetting agents, dispersants, and solubilizers in the marketplace [272]. Here, we suggest using mixed non-ionic OPE surfactant solutions composed of oil-soluble surfactant with low hydrophile-lipophile balance (HLB) number and water-soluble surfactant with high HLB number to facilitate the transport of surfactant solution into the hydrophobic pores. The objective of this research is to investigate (i) how OPE solutions affect wettability of tight

rocks and IFT between reservoir fluids and (ii) how mixing of OPE surfactants results in improved oil recovery from tight rocks.

In this study, we conduct different sets of experiments to understand the interactions between single and mixed non-ionic OPE surfactant solutions and oil. First, we measure the surface and interfacial tensions of OPE solutions with different HLB numbers. Second, we measure the particle size distribution of the surfactant solutions to characterize the size of micelles formed in the solutions. Third, we perform the isothermal titration calorimetry (ITC) experiments to evaluate the possibility of surfactant adsorption on the rock surface. Fourth, we conduct liquid/liquid contact angle measurements to investigate the wettability behavior of the rocks exposed to surfactant solutions. Finally, we conduct imbibition oil-recovery experiments using oil-saturated downhole core plugs from the Montney Formation – one of the largest unconventional resources in North America.

5.2. Materials and Methods

5.2.1. Materials

5.2.1.1. Core Properties

Five pairs of downhole core plugs collected from two wells drilled in the Montney Formation (MT) are used in this study. Montney Formation is located in the Western Canadian Sedimentary Basin (WCSB) and is one of the largest economically feasible hydrocarbon resources in North America [273]. The Montney Formation generally comprises siltstone, minor intervals of shaly siltstone and very fine-grained sandstone [274, 275].

Table 5.1.Petrophysical properties of the MT core plugs

Sample No.	Depth, m	Permeability, K_{air} (mD)	Porosity, Helium (Fraction)	Grain Density, g/cm ³
1	2068.39	4.46×10^{-3}	0.049	2.680
2	2074.99	2.82×10^{-3}	0.040	2.710
3	2130.46	3.89×10^{-3}	0.062	2.740
4	2138.85	2.35×10^{-3}	0.066	2.780
5	2149.54	4.42×10^{-3}	0.063	2.680

Nitrogen dry-cutting method is used to cut plugs with 3.81 cm diameter and 7 cm length. **Table 5.1** lists the petrophysical properties of core plugs. X-ray diffraction method is used to evaluate core plug mineralogy. The total organic carbon (TOC) content of the rock powder is measured using Rock-Eval 6 analysis [275]. **Table 5.2** reports the TOC content and mineral composition of the core plugs [218]. The petrophysical properties and mineral composition of rock samples are provided by the Core Laboratories service company.

Table 5.2. TOC content and mineral composition of the core plugs

Mineral (wt %)	Depth, m				
	2068.39	2074.99	2130.46	2138.85	2149.54
Quartz	44	40	48	57	52
K-Feldspar	7	6	7	9	5
Plagioclase	7	5	13	10	15
Calcite	9	11	6	5	5
Dolomite & Fe-Dolomite	11	24	7	12	5
Pyrite	3	3	1	1	1
Fluorapatite	1	1	0	0	0
Illite/Smectite	2	3	0	0	0
Illite/Mica	13	6	15	5	16
Kaolinite	1	0	2	0	1
Chlorite	2	1	2	0	0
TOC	1.67	1.08	0.89	1.3	0.38

5.2.1.2. Surfactants

Surfonic OPE15, OPE70 and OPE100 are surfactants used in this study. They are p,t-octylphenol ethoxylates [$C_8H_{17}C_6H_4(OCH_2CH_2)_nOH$] with n is equal to 1.5, 7 and 10 moles of ethoxylates (EO). These commercial grade surfactants are obtained from Huntsman Corporation and their properties are listed in **Table 5.3**. The reported critical micelle concentration (CMC) of OPE15, OPE70 and OPE100 solutions are 5×10^{-5} , 1.7×10^{-4} and 3.1×10^{-4} molar, respectively [276].

Table 5.3. Properties of tested octylphenol ethoxylate surfactants at 25°C [277].

Name	M.W	EO moles	HLB value	C.M.C. moles/liter	γ , mN/m	Area/molecule nm ²
OPE-15	277	1.7	5.1	5×10^{-5}	30	0.40

OPE-70	519	7	12	1.7×10^{-4}	31	0.52
OPE-100	646	10	13.6	3.1×10^{-4}	35	0.72

5.2.1.3. Fluid Properties

Montney condensate oil is used for saturating the core plugs and measuring the IFT values. It is a light oil (63.6 °API) with viscosity and surface tension of 3.55 cP and 25 mN/m respectively at room temperature (25°C). Also, deionized (DI) water and NaCl salt (Sigma Aldrich) are used to prepare surfactant solutions at different concentrations.

5.2.2. Methods

5.2.2.1. Surface Tension

The surface tension of the surfactant solutions is measured using the ring method in Sigma700 force tensiometer (Attension, Biolin Scientific). The ring is purified by rinsing it with methanol before running the experiment. Next, the ring hanging from an accurate balance (± 0.00001 gr) is immersed into a cell filled with surfactant solution. The instrument records the force required to pull the ring out of the solutions during the experiment. The measurement is repeated 10 times for each solution at 25°C.

5.2.2.2. Interfacial Tension

To evaluate IFT reduction, we measure dynamic IFT between each surfactant solution and oil sample using a spinning drop interfacial tensiometer (SDT, Krüss, Germany). The SDT unit can operate up to a maximum temperature of 120°C with an accuracy of 0.1°C. It measures a wide range of IFT values from 10^{-6} to 2000 mN/m with an accuracy of 10^{-6} mN/m. The SDT is equipped with a capillary tube that is filled with surfactant solutions and an end plug that is filled with an oleic phase. The capillary tube is capped by the end plug. To measure IFT, the capillary tube is mounted in the tensiometer and the rotational speed is gradually increased until an oleic droplet is released. The rotational speed and temperature are set to 10,000 rpm and 25°C, respectively. The ADVANCE™ software is used to analyze the shape of the droplet spinning in the capillary tube and to calculate IFT based on Eq. 1 as given by Vonnegut [278-280]. IFT

values are recorded every 60 seconds until constant values are reached. Each IFT measurement is repeated three times and the mean value is reported.

$$\sigma = \frac{(\rho_1 - \rho_2)\omega^2 R^3}{4} \quad (1)$$

where σ , ρ_1 , ρ_2 , ω , and R are interfacial tension (mN/m), density of aqueous phase (Kg/m^3), density of oleic phase (kg/m^3), angular velocity (radians/s), and radius of the spinning oleic droplet (m) respectively.

5.2.2.3. Dynamic Light Scattering

The size of micelles formed in the aqueous phase is important since the pore-throat size distribution of tight rocks is in the range of nano-scale, $R_{\text{Throat}} < 1,000 \text{ nm}$. To evaluate how large the size of micelles is in the aqueous surfactant solution, we measure the size distribution of micelles formed in the surfactant solutions using Malvern Zetasizer Nano ZS. It works based on dynamic light scattering (DLS) method. This instrument measures micelle diameter ranging from 0.3 nm to 10 μm . Each measurement is repeated three times at room temperature (25°C) and atmospheric pressure (1 atm).

5.2.2.4. Contact Angle

To investigate wettability behavior of rocks, we measure liquid-liquid contact angles using Attention Theta (Biolin Scientific). This instrument is equipped with Navitar lens (1984×1264 pixel resolution, max 3009 FPS) and an LED light source. We polish the surface of end pieces of the MT core plugs (i) to remove dirt attached to the surface of core plugs. Dirt may affect the measured contact angles and (ii) to mitigate the effect of surface roughness on measured contact angles. To polish the surface of end-pieces, we use 240 grit sandpapers. Then, we immerse oil-saturated end-pieces of the core plugs in a cell filled with surfactant solutions. Next, Hamilton syringe and needle system in Attention Theta is used to inject a fixed volume of oil droplet (10 μL) from the bottom of the cell. OneAttention software records contact angles by monitoring the oil droplet shape with time. Each experiment measures contact angles for at least six oil droplets. We report the mean value and standard deviation for each experiment.

5.2.2.5. Isothermal Titration Calorimetry

To evaluate adsorption affinity of the surfactants on rock powder, we perform isothermal titration calorimetry (ITC) experiments using TA Nano ITC 2G (TA, New Castle, DE, USA) at 25°C. First, the sample cell and the ITC syringe are rinsed several times with 18.3 MΩ.cm deionized water (DI) before loading the samples. Second, surfactant solutions are prepared whose concentrations are 10 times higher than CMC values listed in **Table 5.3**. Third, a core plug is crushed and ground to prepare rock powder with a mean particle size of 907±60.57 nm. This is then added to DI water to prepare a suspension with 1 wt% of rock powder. Fourth, the sample cell and ITC syringe are filled with 1mL of suspension and 250 µL of surfactant solutions, respectively. Fifth, 10 µL surfactant solution is injected every 5 minutes into the sample cell. The injection process continues 28 times for each solution. After each injection, the heat released or adsorbed is monitored and analyzed using NanoAnalyze software (TA, New Castle, DE, USA).

5.2.2.6. Spontaneous Imbibition Tests

We perform the imbibition oil-recovery tests to compare the performance of single and mixed solutions on oil recovery improvement from tight rocks. First, dry MT core plugs are placed in oil samples. The weight change of the core plugs is recorded periodically. The spontaneous oil imbibition reaches equilibrium conditions when the weight does not change with time. Second, to make sure that the pore volume is fully filled with the oil, the forced imbibition test is performed. To conduct forced imbibition, external pressure is applied using a continuous pulse-free pump (Vinci Technologies, France) on partially oil-saturated core plugs that are placed in a high pressure accumulator filled with the oil. The weight change of the core plugs soaked for 24 hours in the accumulator at a set pressure of 500 psig is measured. Next, the applied pressure is increased to 2000 psig in 500 psig steps. The forced imbibition is stopped at 2000 psig to avoid the generation of induced fractures in the core plugs. Third, the oil-saturated core plugs are placed in imbibition cells filled with the surfactant solution. The produced oil volume accumulates at the top of the imbibition cell due to buoyancy effect. The collected oil volume is measured periodically using a graduated tube with an accuracy of 0.02 mL.

5.3. Results and Discussions

This section describes the results of experiments conducted to evaluate the performance of single and mixed surfactant solutions on oil recovery improvement from the MT tight rocks.

5.3.1. Surface Tension and Interfacial Tension

Since commercial grade surfactant samples are used in this study, one would expect non-uniform ethoxylation. Therefore, surface tensions of OPE70 and OPE100 solutions are measured in water with different NaCl concentrations (see **Appendix C**). It is not possible to measure the surface tensions of OPE15 solutions due to their extremely low solubilities in water. When the concentrations of OPE70 and OPE100 solutions change from 10^{-6} to 10^{-4} molar, the surface tension decreases from ~ 65 mN/m to ~ 30 mN/m. The CMCs reported by the manufacturer (OPE70: 1.7×10^{-4} and OPE100: 3.09×10^{-4} molar) confirm that the CMCs of OPE70 and OPE100 solutions are around 10^{-4} molar. Moreover, increasing NaCl concentration in water from 1 to 10,000 ppm leads to negligible changes in the CMCs of surfactant solutions measured by Sigma700 force tensiometer.

Mixed surfactant systems are prepared by mixing OPE15 (insoluble in water) with OPE70 (soluble in water) and OPE100 (soluble in water) surfactants solutions (1:1 molar ratio). **Figure 5.1** shows the surface tensions of the mixed surfactant solutions measured by the ring method. The results show that the CMC of mixed solutions is around 1.0×10^{-4} molar. Similar to the single-component surfactant solutions, increasing the NaCl concentration from 1-1,000 ppm does not result in any measurable change in the CMC of mixed solutions. Since these surfactants are non-ionic, we expect that the CMCs of OPE solutions are dependent of electrolyte salinity ranging from 1 to 1,000 ppm [281]. To conduct the spontaneous imbibition tests, we prepare surfactant solutions with the concentration of 10^{-3} molar to make sure that the solutions are above CMCs.

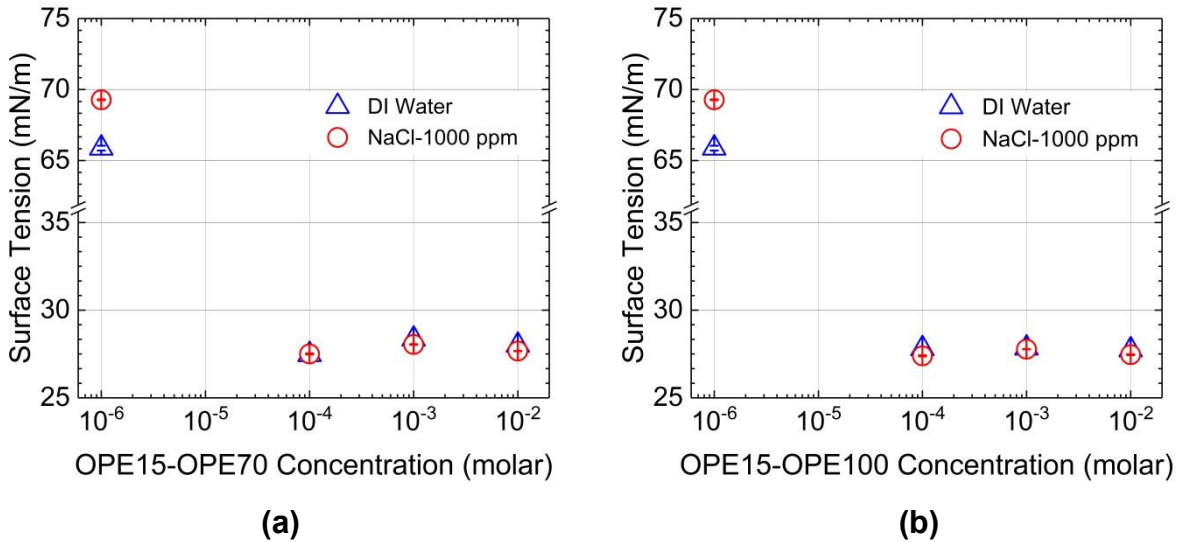


Figure 5.1. Surface tensions of mixed solutions versus surfactant concentrations: (a) OPE15-OPE70 and (b) OPE15-OPE100 with 1:1 mixing ratio.

Figures 5.2 and 5.3 show the IFT values measured for OPE70 and OPE100 solutions prepared at different NaCl concentrations ranging from 1 to 1,000 ppm. The results show that IFT decreases as the surfactant concentration increases. This is due to alignment of surfactant molecules to the oil-water interface. The IFT values for OPE100 solutions with 10^{-3} molar concentration (~ 1 mN/m) are higher than those for OPE70 solutions with 10^{-3} molar concentration (~ 0.5 mN/m). This indicates that the interfacial tension between oil and OPE100 solutions (having surfactants with higher HLB number) is higher than that between oil and OPE70 solutions (having surfactants with lower HLB number). Moreover, the NaCl concentration (1-1,000 ppm) does not significantly change the IFT values for OPE70 and OPE100 solutions. Nevertheless, since the IFTs of 10^{-3} molar OPE70 and OPE100 solutions are significantly higher than 10^{-3} mN/m, one can expect that the capillary pressure is high enough during imbibition oil-recovery process. The results of previous studies [223, 232] suggest that moderate reductions in IFT between surfactant solutions and oil (IFT ~ 0.9 mN/m) results in improved oil recovery from tight rocks (15.0-33.9 % of original oil in-place) during spontaneous imbibition.

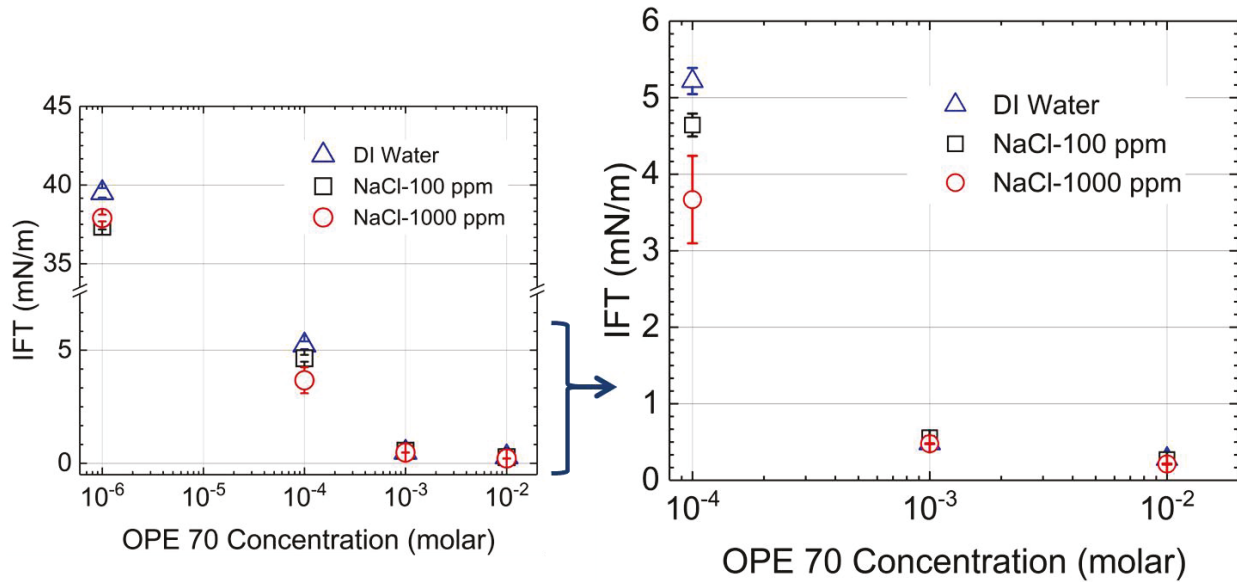


Figure 5.2. IFT measured between the oil and OPE70 solutions versus surfactant concentration

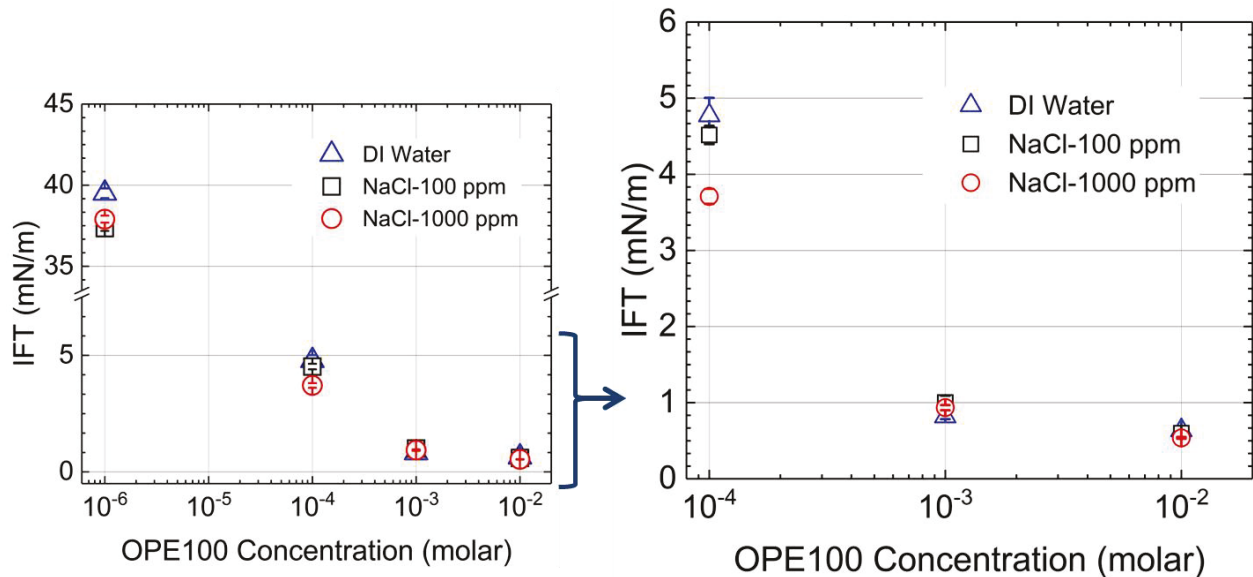


Figure 5.3. IFT measured between the oil and OPE100 solutions versus surfactant concentration

Figure 5.4 shows IFTs between the oil and OPE15-OPE70 and OPE15-OPE100 mixed solutions. A similar trend is observed for IFT-surfactant concentration profiles of the OPE15-OPE70 and OPE15-OPE100 mixed solutions (1:1 molar ratio). First, the IFT values decrease by increasing the surfactant concentration. However, the IFT values do

not reach the minimum (0.5-1 mN/m) at 10^{-3} m concentration. The same behavior was also observed for the interfacial tensions of $C_{12}EO_8-C_{12}EO_2$ mixtures in hexadecane/water systems reported by Rosen and Murphy [282]. Second, adding NaCl into the solution (1000 ppm) does not change the IFT values significantly for mixed surfactant solutions. Yet, mixing OPE-15-OPE-70 and OPE-15-OPE-100 solutions do not change the interfacial tensions significantly compared to OPE70 and OPE100 solutions.

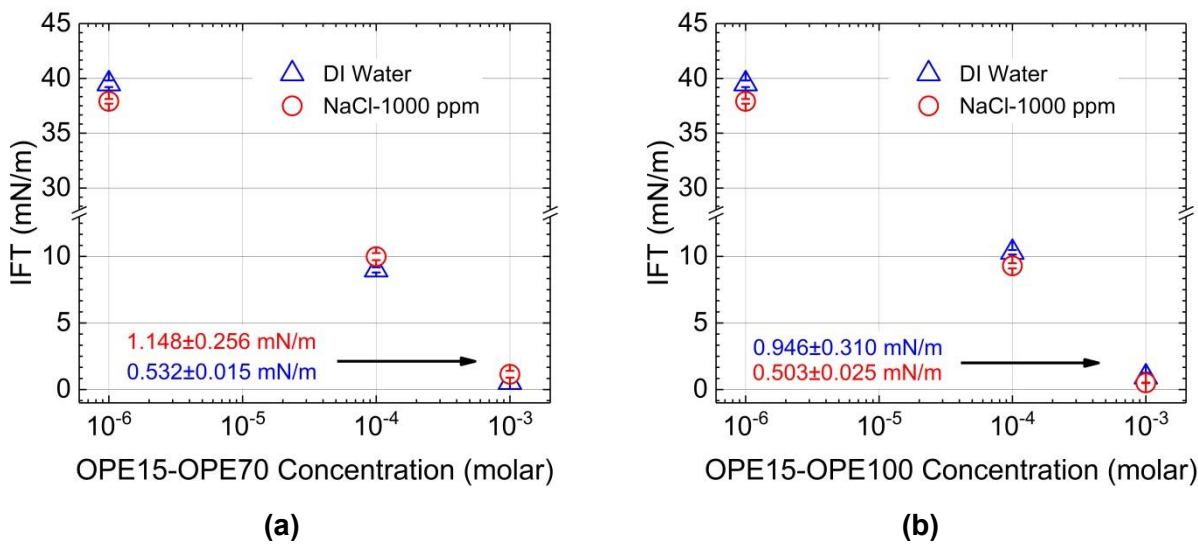


Figure 5.4. IFT values measured between the oil and (a) OPE15-OPE70 and (b) OPE15-OPE100 solutions with 1:1 mixing ratio versus surfactant concentration.

The results of surface tension and interfacial tension measurements suggest the absence of synergistic interactions between the two non-ionic surfactants which have the same tail group (octylphenol) and similar structure but different length of ethoxylate (EO) head groups. In a similar pair of non-ionic surfactants (i.e. $C_{12}EO_8$ and $C_{12}EO_3$), the degree of interactions calculated between two monolayers of mixed surfactants at oil/water interface (β^o) and micelle formation (β^M) for hexadecane/water systems are -0.7 and -0.1, respectively [283]. For a clear case of a strong attractive interaction, β value shall be markedly negative, which is the case for the oppositely charged surfactants.

5.3.2. *Micelle Size Distribution*

To evaluate how large the size of micelles is, we measure the size distribution of micelles formed in the surfactant solutions. The CMCs reported for OPE70 and OPE100 are 1.7×10^{-4} and 3.09×10^{-4} molar, respectively. Therefore, we measure the size of micelles formed in NaCl solutions with surfactant concentration of one and two orders of magnitude higher than CMC. **Figure 5.5** shows the mean size of micelles formed in the OPE70 and OPE100 surfactant solutions prepared in water with different NaCl concentrations ranging from 1 to 1,000 ppm. The size of micelles formed in the OPE70 and OPE100 solutions for different NaCl solutions are in the range of 39.01 ± 1.29 – $100,000 \pm 20,650$ nm and 8.76 ± 0.08 – 13.97 ± 2.00 nm, respectively. The results show that micelles formed in the OPE70 solutions are much larger than those formed in the OPE100 solutions. Since the HLB number of OPE100 is higher than that of OPE70, it is more soluble in aqueous phase and forms smaller micelles. Moreover, the size of micelles formed in OPE70 solutions significantly increases with increasing NaCl concentration. However, the size of micelles formed in the OPE100 does not significantly change with increasing NaCl concentration. Kronberg et al. 2014 [284], showed that the tendency to grow for the size of micelles of non-ionic polyoxyethylene surfactants decreases by increasing the length of EO chain. It means that the size of micelles formed in OPE 70 solutions should be larger than that formed in OPE 100 solutions.

Next, we measure the size of micelles formed in the mixed surfactant solutions to investigate how mixing of OPE surfactants with different HLB numbers affects the size of micelles. **Table 5.4** lists the mean values of micelles formed in the OPE15-OPE70 and OPE15-OPE100 mixed surfactant solutions prepared in DI water and 1000 ppm NaCl solution. The size of micelles formed in the OPE15-OPE70 mixed solution prepared in DI water (180.90 ± 1.62 nm) is larger than that formed in the single OPE70 solution prepared in DI water (39.01 ± 1.29 nm). Compared to OPE70 and OPE100 which are soluble in water, OPE15 is insoluble in water. Therefore, the presence of OPE15 in the mixed surfactant solutions enlarges the resulting mixed micelles. However, the size of micelles formed in the OPE15-OPE70 mixed solution prepared in 1,000 ppm NaCl solution (120.20 ± 6.42) is smaller than that formed in the single OPE70

solution prepared in 1,000 NaCl ppm solution ($100,000 \pm 20,650$ nm). One reason is related to the salt-in effect of NaCl solution described by the Hofmeister series [285, 286]. The presence of Na^+ and Cl^- ions can promote solubilization of hydrophobic components of mixed OPE surfactants into the aqueous phase. Therefore, addition of NaCl into the aqueous solution leads to smaller micelles formed in the OPE15-OPE70 solution.

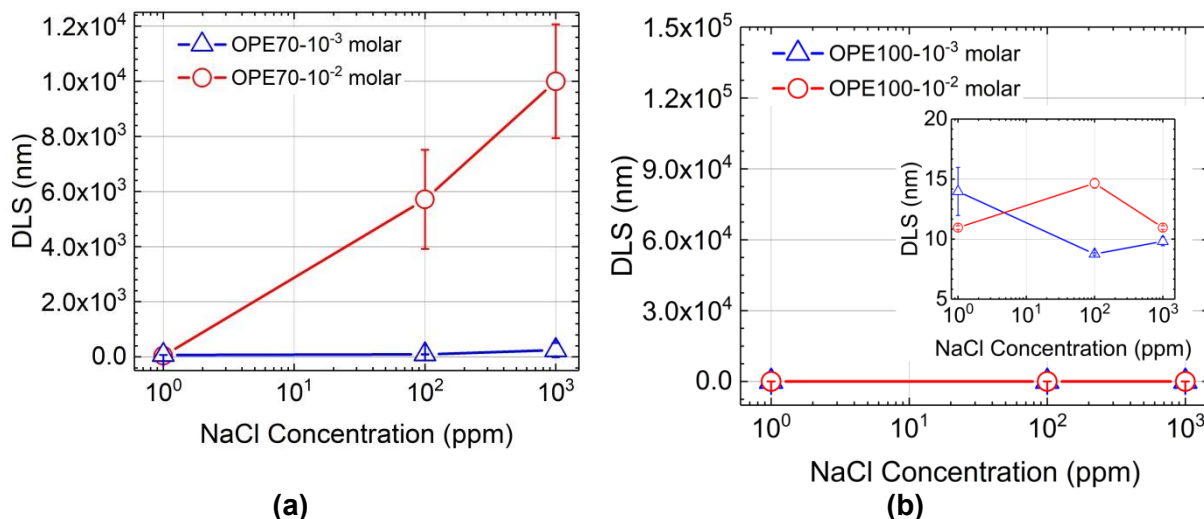


Figure 5.5. Mean size of micelles formed in the (a) OPE70 and (b) OPE100 surfactant solutions versus NaCl concentration.

Moreover, the size of micelles formed in the OPE15-OPE100 solution prepared in DI water and 1,000 ppm NaCl solution is higher than that formed in the OPE100 solutions. The existence of OPE-15 results in formation of larger micelles in the mixed solutions.

Table 5.4. Mean size of micelles formed in the mixed surfactant solutions

Surfactant-1	Surfactant-2	Concentration	NaCl Concentration	Mean of PSD
OP15	OP70	0.001	1	180.90 ± 1.62
OP15	OP70	0.001	1000	120.20 ± 6.42
OP15	OP100	0.001	1	129.20 ± 6.84
OP15	OP100	0.001	1000	173.60 ± 1.10

5.3.3. Isothermal Titration Calorimetry

5.3.3.1. Single Solutions of OPE70 and OPE100

We conduct ITC experiments to determine the adsorption of OPE70, OPE100, OPE15-OPE70, and OPE15-OPE100 solutions on rock powder in aqueous suspensions. First,

we conduct titrations of OPE70 and OPE100 solutions into 1000 ppm NaCl solution (as a reference case). Next, we repeat the experiment by the titration of surfactant solutions into the 1000 ppm NaCl suspension with 1.0 wt % rock particle (RP) concentration.

Figures 5.6a and b show the thermograms for the isothermal titration of OPE70 and OPE100 solutions into 1,000 ppm NaCl solution with and without 1.0% RP suspension, respectively. Each titration step produces a heat signal recorded by the instrument. The recorded enthalpy is due to the heat released from surfactant demicellization and micelle dilution when surfactant concentration ($C_{\text{surfactant}}$) < CMC. As the concentration of surfactant monomers in the cell increases, aggregation starts to occur and only a reduced fraction of injected micelles dissociates into monomers. Therefore, less heat is generated. Micelles do not dissociate into monomers when $C_{\text{surfactant}} > \text{CMC}$, and the heat is generated only from the dilution of micelles. In all cases, there is an exothermic heat production from the titration process. Except the first titration point of OPE100, the titration curves of both OPE70 and OPE100 into 1,000 ppm NaCl solution followed "S shape" profiles. The demicellization of OPE100 is stronger than OPE70. Since the dilution enthalpies for both surfactant micelles and monomers are negligible compared with the enthalpy of demicellization process, the difference in the enthalpy between minimum and maximum heat values is due to the cooperative aggregation of surfactant monomers into micelles. The change of enthalpy due to micellization (ΔH_m) is approximately 8 kJ/mol and 10 kJ/mol for OPE70 and OPE100, respectively. The hydration and excluded volume forces of ethoxylate segments result in hydrophilic repulsions. The formation of micelles by non-ionic OPE surfactants is endothermic because the repulsive forces among ethoxylate chains is higher than the attractive forces among hydrophobic octylphenol groups. Nevertheless, micellization process occurs because it is entropically driven. Due to the longer ethoxylate chain, the hydrophilic repulsion is higher in OPE100 than that in OPE70. This leads to higher micellization enthalpy and CMC solubility.

A different enthalpic process is expected to happen when the suspension of 1wt% RP is prepared in 1,000 ppm NaCl solution as titrate in the sample cell. The titration curves of OPE70 and OPE100 surfactants into the RP suspensions are included in the same plots. The difference between the titration curves of with and without RP is ascribed as

surfactant-rock particles interactions. If there is enough affinity between the surface of the RP and the surfactant, adsorption of surfactant monomers will first take place at the surface of the rock particles. Therefore, more exothermic heat is generated at the early stage of titrations due to the adsorption of OPE70 and OPE100 onto the RP at the beginning of titration process. A plateau is formed after reaching a saturation of surfactant molecules on the RP surface; followed by the demicellization process similar to what observed in the 1,000 ppm NaCl solution without RP.

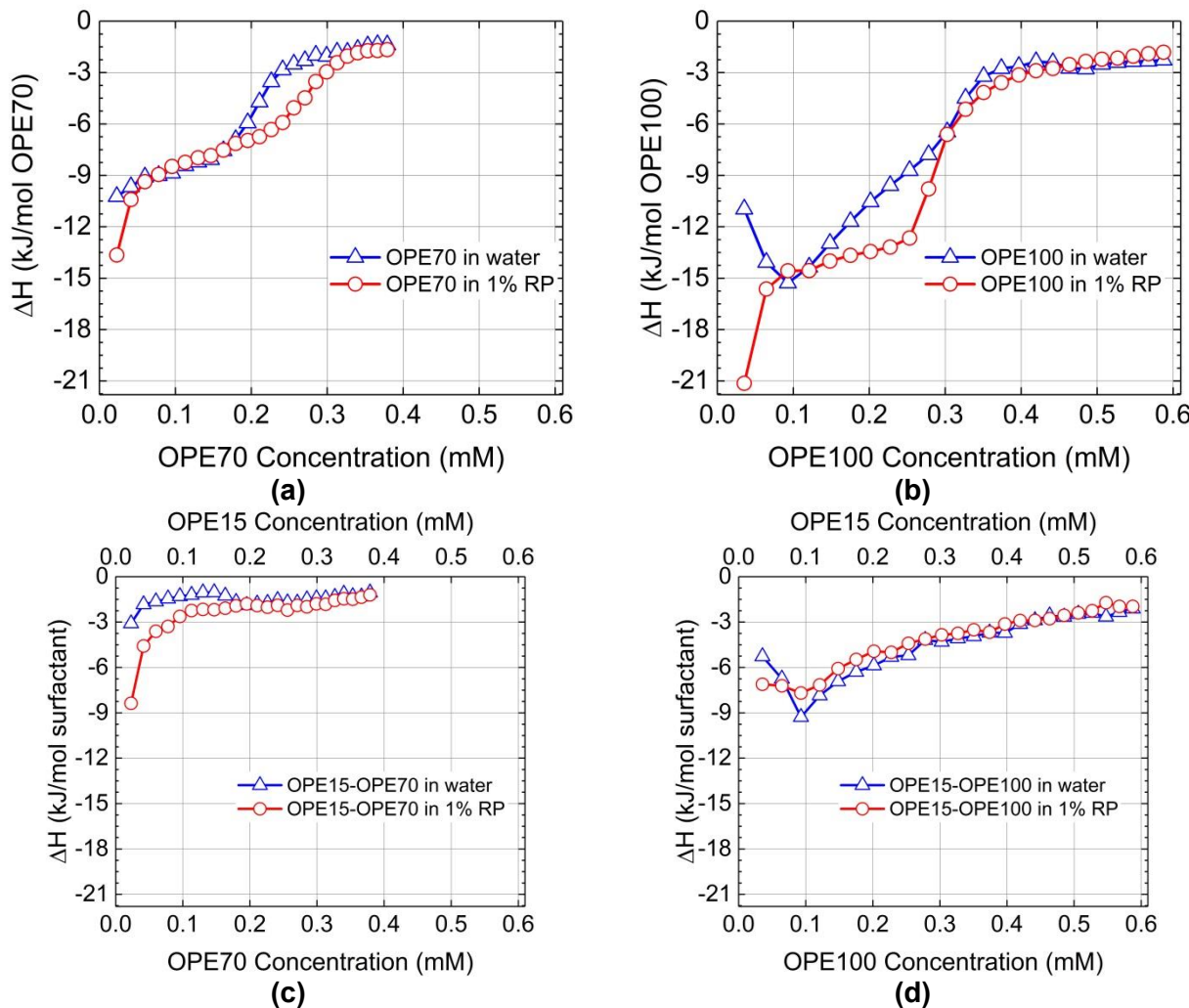


Figure 5.6. ITC curves of (a) OPE70, (b) OPE100, (c) OPE15-OPE70, and (d) OPE15-OPE100 solutions titrated into 1,000 ppm NaCl solution with and without 1% rock particles.

5.3.3.2. Mixed Surfactants

The OPE-15, OPE-70 and OPE-100 surfactants share the same hydrophobic group of ($C_8H_{17}C_6H_4$) with different size of polyoxyethylene chains of $(OCH_2CH_2)_n$.

The chain length of ethoxylates for OPE15, OPE70 and OPE100 are 1.5, 7, and 10 moles, respectively. Therefore, the CMC of OPE15 is more than 10 times lower than that of OPE70 and OPE100. OPE 15 can only be dispersed in the form of mixed micelles in water by adding OPE70 or OPE100.

Figure 5.6c and **5.6d** show the thermograms for the isothermal titration of OPE15-OPE70 and OPE15-OPE100 mixed solutions prepared in 1,000 ppm NaCl solution with and without 1.0% RP suspension, respectively. OPE15 cannot demicellize into its monomers and has no demicellization enthalpy when it is diluted into the 1,000 ppm NaCl solution due to its very short hydrophilic polyoxyethylene chain. When OPE15-OPE70 and OPE15-OPE100 mixed solutions are injected into 1,000 ppm NaCl solution (without RP), OPE15 stays insoluble while OPE70 and OPE100 demicellized in to the solution. Demicellization of OPE70 component for the OPE15-OPE70 mixed solution is less than that of OPE100 for the OPE15-OPE100 mixed solution. OPE100 is a better solubilized agent for OPE15 due to its much longer ethoxylate chain, resulting in better demicellization performance. However, the titration of both OPE15-OPE70 and OPE15-OPE100 mixed solutions show totally different behavior in the presence of RP suspensions. Surfactant mixtures compete for the RP surface. Unlike OPE100, other surfactant solutions (OPE70, OPE15-OPE100, and OPE15-OPE70) show two different thermograms with and without RP particles. Instead of demicellization, OPE15 monomers are first preferentially adsorbed on the RP surface in the case of OPE15-OPE70. **Figure 5.6c** shows a better chromatographic effect, RP surface is enriched in OPE15 whereas the solution is enriched in OPE70.

5.3.4. **Wettability Evaluation**

5.3.4.1. **Contact Angle Measurement**

To evaluate the wettability behavior of rock surface exposed to single and mixed OPE solutions, we perform liquid-liquid contact angle measurements. The reference case is an oil-saturated end-piece of the MT rock sample that is immersed in 1,000 ppm NaCl solution. For the reference case, an oil droplet completely spreads on the rock surface, indicating a strongly oil-wet behavior. In the next step, the contact angle of oil droplets on oil-saturated end-pieces immersed in surfactant solutions is measured. **Figure 5.7**

shows the oil contact angle measured for the 1,000 ppm NaCl solution (reference case) and OPE70 solution with 10^{-2} molar surfactant concentration. The oil contact angle is non-measurable for the reference case due to the spreading of oil droplet on the rock surface when it releases from the J-shape needle placed at the bottom of the cell. **Figure 5.8** shows the oil contact angles measured for different concentrations of single surfactant solutions prepared in 1,000 ppm NaCl solution. The rock surface becomes strongly oil repellent when OPE70 and OPE100 surfactants are added to the aqueous solution. The oil contact angle slightly decreases as surfactant concentration increases meaning that the rock surface becomes less oil-repellent. However, the rock surface shows strongly water-wet behavior even at the highest surfactant concentration (10^{-2} molar).

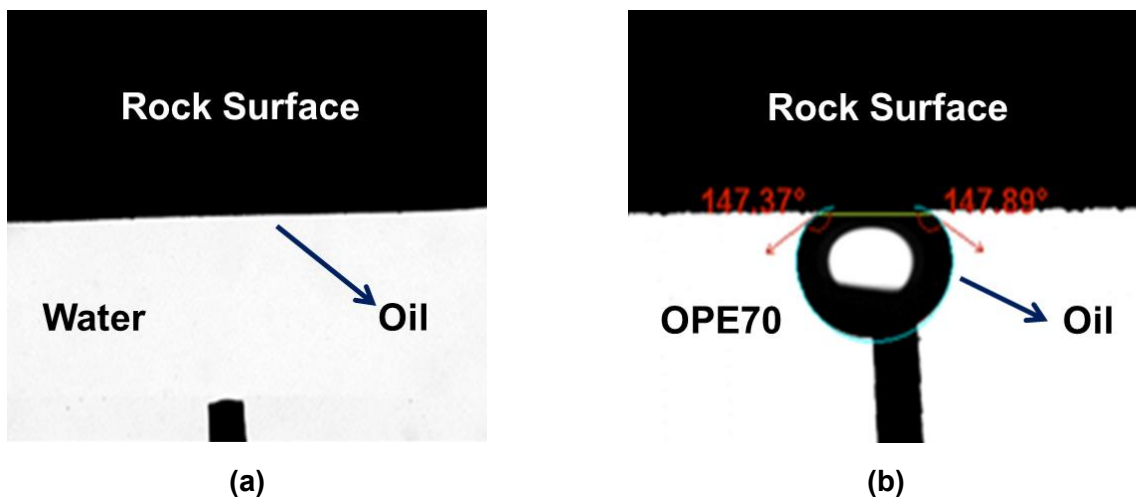


Figure 5.7. Liquid/liquid contact angle of an oil droplet on an end-piece of the MT rock immersed in (a) 1,000 ppm NaCl solution (reference case) and (b) 1,000 ppm NaCl solution with 10^{-2} molar OPE70. The oil droplet completely spreads on the rock surface immersed in 1,000 ppm NaCl solution, indicating strongly oil-wet behavior.

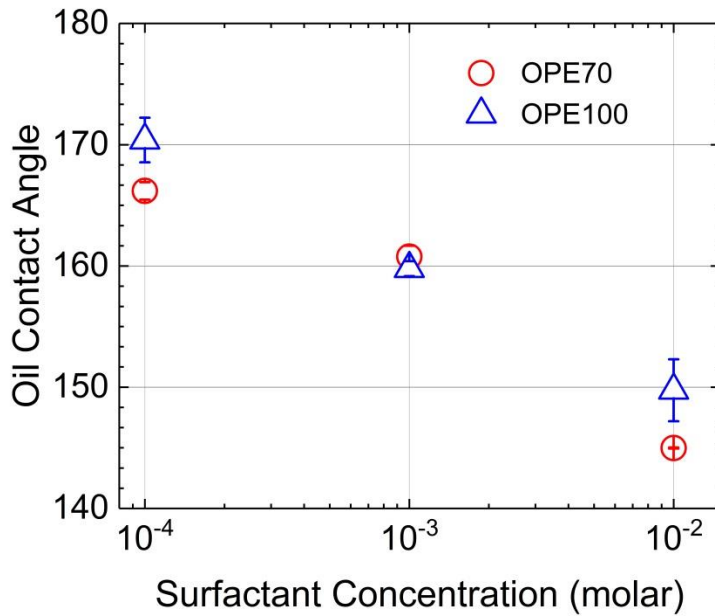


Figure 5.8. Oil contact angle measured on oil-saturated end-pieces of the MT rock samples immersed in OPE70 and OPE100 solutions. Oil droplets completely spread on the surface when the oil-saturated end-pieces are immersed in the water.

Table 5.5 lists the oil contact angles measured for the mixed solutions with 10^{-4} molar concentration. The analysis software could not detect the oil droplet boundary in mixed solutions with 10^{-3} molar concentration because these solutions are not translucent at this concentration. The oil contact angles measured for the mixed solutions suggest that the rock samples are strongly water-wet. In summary, single and mixed surfactant solutions can preferentially wet the oil-saturated rock surface and make it strongly water-wet.

Table 5.5. Oil contact angles measured for the mixed solutions at different concentrations

No.	Type	Surf. Conc. (mole)	NaCl Conc. (ppm)	Oil contact angle
1	OP15-OP100	0.0001	1000	166.78 ± 1.74
2	OP15-OP70	0.0001	1000	152.21 ± 2.20

5.3.4.2. Wetting Behavior

The results of previous sections showed that single and mixed non-ionic OPE solutions (i) reduce IFT between oil and surfactant solutions and (ii) preferentially wet the rock surface. In this section, we explain how the rock surface becomes water-wet in the presence of non-ionic single and mixed surfactant solutions. Wetting behavior are

generally categorize in three ways including spreading, adhesional, and immersional wetting states [287, 288]. Different parameters are defined to measure the driving force for each type of wetting state as: (i) spreading coefficient ($S_{L/S}$), (ii) work of adhesion (W_A), and (iii) immersional free energy ($I_{L/S}$) [288, 289].

In the spreading wetting state, a liquid, which is originally in contact with a solid surface and another fluid, displaces another fluid and spreads on the solid surface. The surface free energy change per unit area for the spreading state in an oil-solid-water system is defined as

$$S_{L/S} = \gamma_{SW} - \gamma_{OW} - \gamma_{SO} \quad (2)$$

where γ_{SW} and γ_{SO} are the solid-water and solid-oil surface tensions, respectively. γ_{OW} is the interfacial tension between oil and water. Since it is not possible to measure γ_{SW} and γ_{SO} independently, Eq. 2 is often combined with the Young-Dupré Eq. 3 to obtain a more useful expression for calculating $S_{L/S}$ as

$$\gamma_{SW} = \gamma_{SO} + \gamma_{OW} \cos \theta_{OWS} \quad (3)$$

$$S_{L/S} = \gamma_{OW} \times (\cos \theta_{OWS} - 1) \quad (4)$$

where θ_{OWS} is the contact angle at the solid-water-oil junction. If $S_{L/S} > 0$, spreading occurs spontaneously. If $\theta_{OWS} = 0$, complete spreading occurs. If $\theta_{OWS} \neq 0$, spontaneous spreading does not occur.

In the adhesional wetting state, a liquid which is not originally in contact with a solid surface makes contact with and adheres to that surface. The work of adhesion (W_A) is a measure used to evaluate the strength of adhesional force between the liquid and the solid surface. W_A is defined as the reversible work required for separating a unit area of a liquid from the solid surface.

$$W_A = \gamma_{SW} + \gamma_{OW} - \gamma_{SO} \quad (5)$$

Combining Eq. 5 with the Young-Dupré Eq. 3 results in

$$W_A = \gamma_{OW} \times (\cos \theta_{OWS} + 1) \quad (6)$$

Finally, in the immersional wetting state, a solid surface which was not previously in contact with the liquid is immersed completely in the liquid. The immersional free energy ($I_{L/S}$) is defined as

$$I_{L/S} = \gamma_{SW} - \gamma_{SO} = (\gamma_{OW} \times \cos \theta_{OWS}) \quad (7)$$

Moreover, $I_{L/S}$ gives an indication of the strength of the capillary force [256]. The capillary pressure is proportional to the immersional free energy as

$$P_C = \frac{2 \times (\gamma_{OW} \times \cos \theta_{OWS})}{r} = \frac{2 \times I_{L/S}}{r} \quad (8)$$

where P_C and r are capillary pressure and pore radius, respectively.

Table 5.6 lists the spreading coefficients ($S_{L/S}$), work of adhesion (W_A), and immersional free energy ($I_{L/S}$) calculated for surfactant solutions prepared in 1,000 ppm NaCl solution. $S_{L/S}$ calculated for the OPE70 and OPE100 solutions (10^{-6} molar) show a strong repulsion between the surfactant solutions and the rock surface. In these cases, the surfactant solution cannot spontaneously spread on the rock surface covered with the oil film. The spreading coefficient significantly decreases as the surfactant concentration increases. The spreading coefficients are very close to zero when $C_{Surfactant} > 10^{-4}$ molar; indicating the complete spreading state. As a result, surfactant solutions can displace the oil film covering the rock surface and spread spontaneously on the rock surface. Finally, the rock surface becomes oil repellent in presence of OPE surfactants as indicated by the measured oil contact angles (**Figure 5.8**).

Table 5.6. Wetting parameters calculated for the OPE70 and OPE100 solutions prepared in 1,000 ppm NaCl solutions.

Surf. Conc. (molar)	NaCl Conc. (ppm)	OPE70			OPE100		
		$S_{L/S}$ (mN/m)	W_A (mN/m)	$I_{L/S}$ (mN/m)	$S_{L/S}$ (mN/m)	W_A (mN/m)	$I_{L/S}$ (mN/m)
10^{-6}	1000	-75.66	0.15	-37.76	-75.66	0.15	-37.76
10^{-4}	1000	-0.11	7.23	3.57	-0.06	7.37	3.66
10^{-3}	1000	-0.03	0.93	0.46	-0.06	1.81	0.88
10^{-2}	1000	-0.04	0.39	0.18	-0.08	1.01	0.47

W_A calculated for all solutions except for 10^{-4} molar surfactant solutions is very low. This means that the adhesion force between the rock surface and surfactants is low. The absence of strong attractive forces between the rock surface and surfactant solutions can be explained by the non-ionic nature of OPE surfactants. Moreover, the IFT values (γ_{OW}) is high (**Figure 5.2** and **Figure 5.3**) when $C_{\text{surfactant}}=10^{-4}$ m, leading to higher W_A for the OPE70 and OPE100 solutions compared with that for others solutions when $C_{\text{Surfactant}}>10^{-4}$ m.

Solutions with 10^{-6} molar concentration of surfactants have high negative $I_{L/S}$ values. This indicates the repulsion between the surfactant solutions and the rock surface covered with the oil film. No surfactant adsorption is expected at this concentration. $I_{L/S}$ is positive and is less than 5 mN/m when $C_{\text{Surfactant}}>10^{-6}$ m, suggesting the existence of capillary-driven force. However, low values of $I_{L/S}$ indicate that the capillary-driven force decreases by increasing the surfactant concentration. In summary, OPE surfactants can effectively spread on and wet the rock surface.

Table 5.7 lists the spreading coefficients ($S_{L/S}$), work of adhesion (W_A), and immersional free energy ($I_{L/S}$) calculated for the mixed solutions prepared in 1,000 ppm NaCl solution. $S_{L/S}$ values calculated for OPE15-OPE70 and OPE15-OPE100 mixed solutions are very close to zero, suggesting the condition of complete spreading. This observation is similar to what we observed for single surfactant solutions. However, W_A for the mixed surfactant solutions is relatively high compared with that for single surfactant solution. This suggests that the mixed surfactant solutions adhere more to the rock surfaces. Higher $I_{L/S}$ calculated for mixed solutions compared with that for single solutions show the higher capillary force promoting the imbibition of the surfactant solutions into the rock samples. We cannot calculate the wetting parameters for mixed solutions with 10^{-3} molar surfactant concentration since it is not possible to measure the oil contact angle. Therefore, the calculated parameters may change at higher concentrations. In summary, the complete spontaneous spreading of surfactants on the rock surface, their high work of adhesion, and high capillary forces are responsible for higher wetting affinity of the rock surface to mixed surfactants compared with single surfactants. In the

next step, we conduct spontaneous imbibition tests using single and mixed solutions prepared in 1,000 ppm NaCl solution.

Table 5.7. Calculated wetting parameters for mixed surfactant solutions

Surf. Conc. (Molar)	NaCl Conc. (ppm)	OPE15-OPE70			OPE15-OPE100		
		$S_{L/S}$ (mN/m)	W_A (mN/m)	$I_{L/S}$ (mN/m)	$S_{L/S}$ (mN/m)	W_A (mN/m)	$I_{L/S}$ (mN/m)
10^{-4}	1000	-1.16	18.82	8.84	-0.25	18.33	9.05

5.3.5. *Imbibition Oil-recovery Test*

In this step, we immerse the oil-saturated downhole core plugs into single and mixed OPE solutions prepared in 1,000 ppm NaCl solution and periodically record the produced oil volume. **Figure 5.9** shows the oil recovery profiles for single and mixed surfactant solutions. The profiles for the single and mixed solutions prepared in DI water are presented in **Appendix C**. First, the oil recovery factor for oil-saturated core plugs soaked in single OPE70 and OPE100 solutions are not significantly different from the reference case. Second, the final oil recovery factor for mixed solutions is higher than that for single surfactant solutions. Third, OPE15-OPE70 mixed solution shows the highest oil recovery factor among all surfactant solutions. The results of previous sections showed that IFT reduction and wettability alteration for all single and mixed surfactant solutions are similar. Therefore, there should be additional mechanisms responsible for the observed difference in oil recovery profiles of the mixed and single surfactant solutions.

First, we investigate the tendency of surfactants adsorption on the oil-wet rock sample to explain the imbibition oil-recovery results. Kronberg et al. [290], showed that adsorption tendency of non-ionic ethoxylate surfactants on a hydrophobic surface increases by decreasing the ethoxylate (EO) chain length. The hydrophobic part of an OPE with shorter EO chain length can escape from the aqueous phase easier than that with longer EO chain length. This escaping tendency of hydrophobic part of a surfactant from the aqueous phase is called hydrophobic effect [290]. The EO chains for OPE15,

OPE70, and OPE100 are 1.7, 7, and 10, respectively (**Table 5.3**). OPE15 is completely insoluble in water since it has the lowest EO chain and the hydrogen bonds between the water molecules and weakly polar hydrophilic part of OPE15 are not strong enough to hold the surfactant soluble in water. However, OPE70 and OPE100 with long EO chains (i) are completely soluble in water and (ii) have less hydrophobic force to adsorb on the rock surface. Note that the hydrophobic force of OPE70 solution is higher than that of OPE100 solution because it has shorter EO chain. Therefore, spontaneous imbibition of OPE70 into the oil-saturated core plugs is expected to be more than OPE100.

The existence of OPE15 (oil-soluble) in the mixed OPE15-OPE70 and OPE15-OPE100 solutions can increase the hydrophobic force of mixed surfactants. As a result, OPE15 as an auxiliary agent (i) facilitates the flow of mixed surfactants into the oleic phase and (ii) promotes the adsorption of mixed surfactants on the rock surface by increasing the hydrophobic force. This can lead to better imbibition of mixed surfactant solutions in the oil-saturated core plugs. Moreover, the shorter EO chain for OPE70 compared with OPE100 in the mixed surfactants leads to higher hydrophobic force of the mixed OPE15-OPE70 solution. The ITC results also suggest that OPE15 monomers in the OPE15-OPE70 solution are first preferentially adsorbed on the rock surface (**Figure 5.6c**). Therefore, it is expected that imbibition of mixed OPE15-OPE70 solution has the highest oil recovery factor.

Second, we investigate the role of surfactant accessibility to the oil-saturated rock samples to explain the imbibition oil-recovery results. The oil recovery profile for the reference case shows that water can spontaneously displace only 5% of initial oil in-place from the oil-saturated core plugs. This suggests that water (without surfactant additives) can imbibe into the hydrophilic pores and expel the oil out up to 5%. However, the hydrophobic pores are inaccessible for the water without surfactant additives due to negative capillary force. In addition to existence of pores in OM, Wood et al. [291], showed that bitumen/pyrobitumen rims coats mineral grains of the MT tight rocks, leading to formation of hydrophobic network in these rocks. Therefore, surfactant solutions should access the hydrophobic pore network to contact with and expel out the oil from the oil-wet pores.

To evaluate surfactant accessibility, the pore-throat size distribution of the cores is measured by conducting mercury injection capillary pressure (MICP) test. **Figure 5.10** shows the cumulative and incremental pore space fractions versus pore-throat radius (R_{throat}) for the five pairs of core plugs used in this study. Over 90% of the pores have a throat radius in the range of 1-100 nm. Since we conduct the spontaneous imbibition tests using surfactant solutions with the concentration (10^{-3} molar) higher than CMCs, the size of micelles formed at this concentration can affect the oil displacement from the pores. Therefore, it is expected that micelles with small size can flow through the pores when $R_{\text{throat}} < 100$ nm, spread on the rock surface covered with the oil, and displace the oil out of narrow pores.

Despite higher hydrophobic force for OPE70 compared with OPE100, the micelles formed in 1,000 ppm NaCl solution are relatively large, $100,000 \pm 20,650$ nm. It is difficult for large micelles to flow through narrow pores and expel the oil. **Figure 5.5b** shows that OPE100 solution forms very small micelles (9.82 ± 0.37 nm) in 1,000 ppm NaCl solution. So, it is expected that these micelles can flow through narrow pores. However, lower hydrophobic force for OPE100 hampers transport of micelles toward oleic phase. Therefore, single non-ionic OPE solutions cannot noticeably improve oil recovery during spontaneous imbibition.

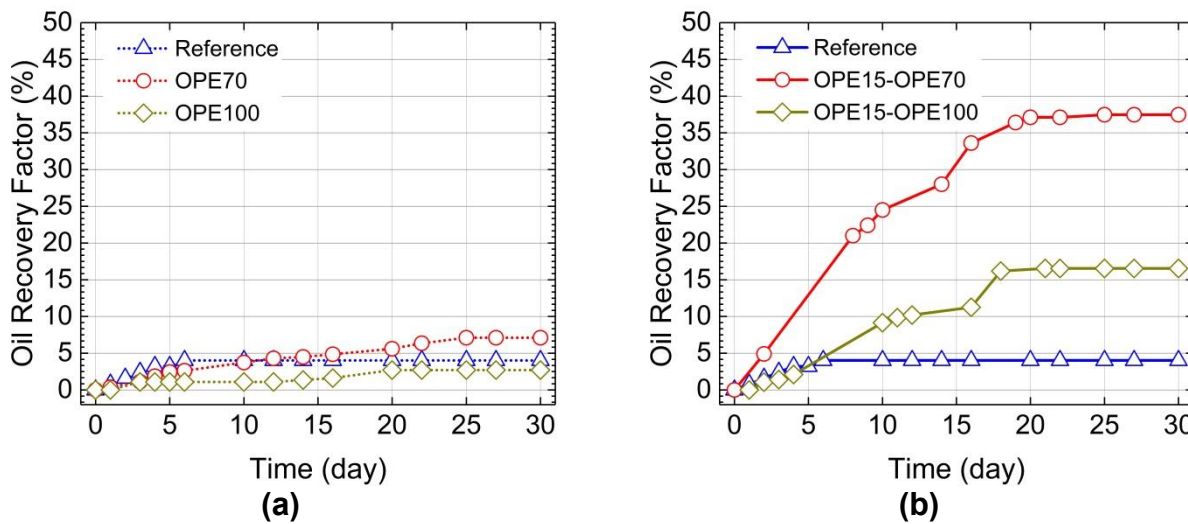
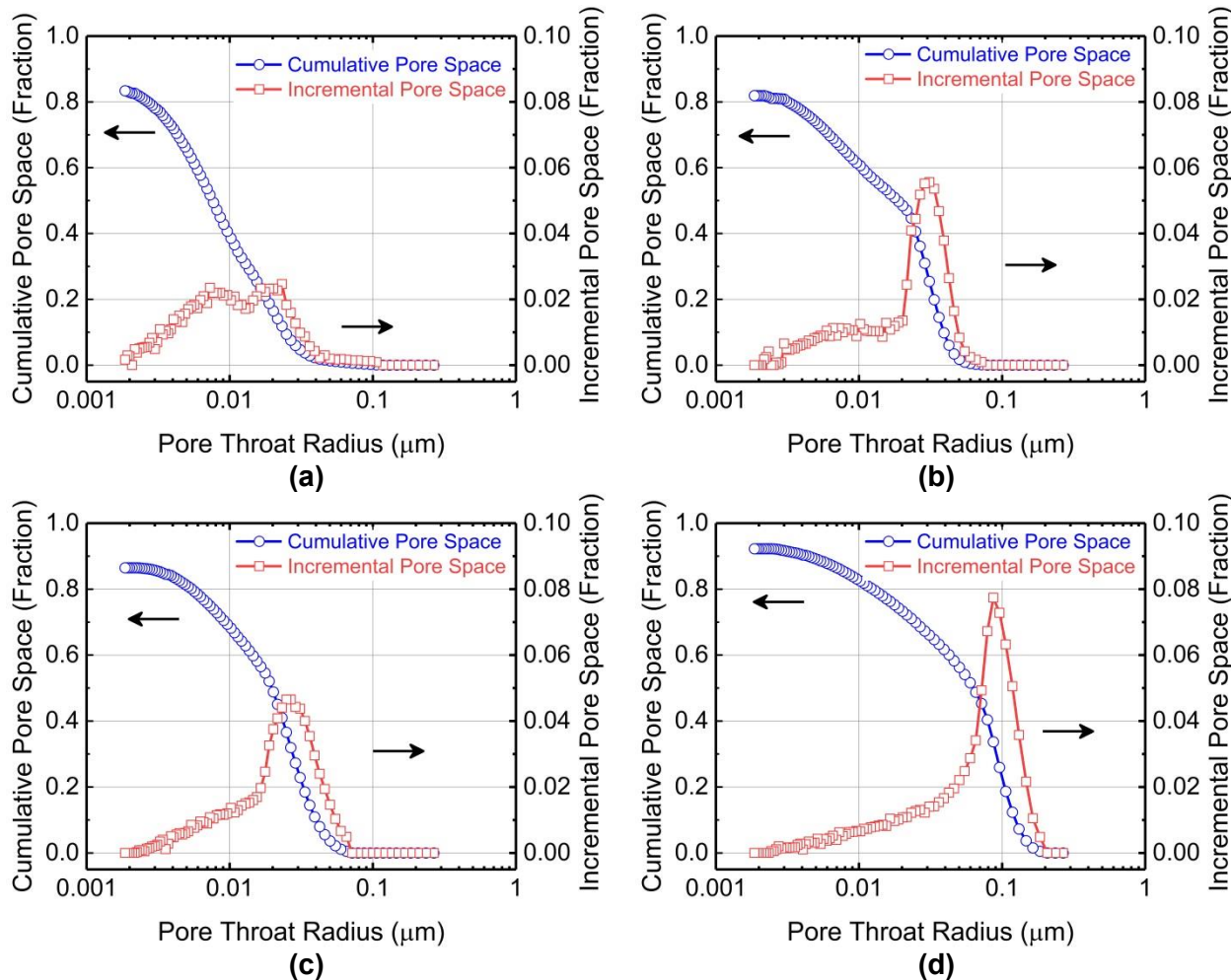


Figure 5.9. Oil recovery-time profiles for (a) single and (b) mixed surfactant solutions prepared in 1,000 ppm NaCl solution.

The oil recovery profiles for OPE15-OPE70 and OPE15-OPE100 solutions show a significant increase in oil recovery compared with single OPE70 and OPE100 solutions

(Figure 5.9b). The size of micelles formed in the mixed solutions is in the range of 100-200 nm as listed in Table 5.4. Small micelles formed in the mixed solutions can flow through narrow pores easier than those formed in the single solutions. Moreover, mixed surfactants have higher hydrophobic forces due to presence of OPE15. Therefore, they can adsorb on the rock surface better than single surfactants. In summary, two mechanisms effectively work in favor of mixing non-ionic OPE surfactants for improving oil recovery from the MT tight rock: (i) the existence of OPE15 increases the hydrophobic force for mixed surfactant solutions, leading to better adsorption of mixed surfactants on the rock surface and making the rock surface water-wet. (ii) Micelles with small size (<200 nm) formed in the mixed solutions can flow through the oil-wet pores easier than single solutions, contact with the oil, and displace the oil from narrow pores.



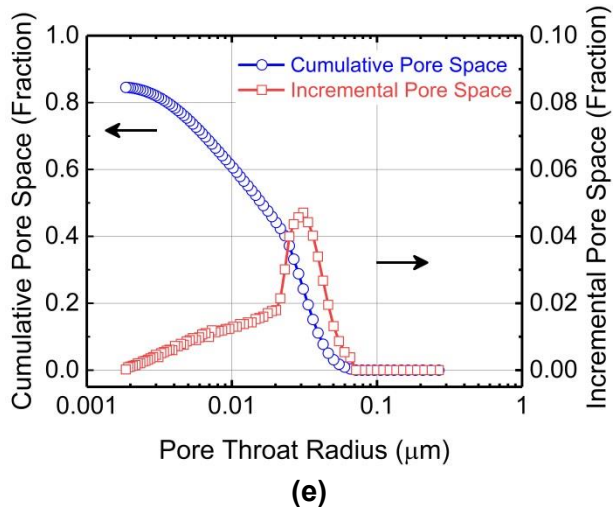


Figure 5.10. Pore size distribution measured by MICP method for the MT core plugs drilled at depth of (a) 2068.39, (b) 2074.99, (c) 2130.46, (d) 2138.85 m, (e) 2149.54 m.

5.4. Conclusions

In this study, different sets of experiments were conducted to investigate the performance of single and mixed non-ionic octylphenol ethoxylates surfactants on oil recovery improvement from tight rocks during spontaneous imbibition. First, we measured the surface and interfacial tensions of single and mixed surfactant solutions with different HLB numbers. Second, we measured the size of micelles formed in the surfactant solutions. Third, we performed ITC experiments to evaluate the possibility of surfactant adsorption on rock surface. Fourth, we conduct liquid/liquid contact angle measurements on the oil-saturated Montney rock samples to investigate the wettability behavior of the rocks exposed to surfactant solutions. Finally, we performed imbibition oil-recovery experiments on oil-saturated downhole core plugs. Here are the main conclusions:

- Both single and mixed OPE solutions have low IFT values. However, the IFTs measured for mixed solutions are not ultra-low. They are in the range of 0.5-1 mN/m at 10^{-3} m surfactant concentration.
- Single OPE surfactant solutions can effectively spread on and wet the rock surface coated with oil film.
- The complete spontaneous spreading of mixed surfactants on the rock surface, their high work of adhesion, and high capillary forces are responsible for higher

wetting affinity of the rock surface to mixed surfactants compared with single surfactants.

- The existence of OPE15 increases the hydrophobic force for mixed surfactant solutions, leading to better adsorption of mixed surfactants on the rock surface and making the rock surface water-wet.
- The size of micelles formed in OPE15-OPE70 and OPE15-OPE100 solutions prepared in 1,000 ppm NaCl solution is in the range of 100-200 nm. The existence of small mixed micelles can facilitate surfactant imbibition into narrow pores ($P_{throat} < 100$ nm) for oil expulsion.
- Mixing OPE15 (oil-soluble with short ethoxylate chain length) with OPE70 and OPE100 (water-soluble with long ethoxylate chain length) leads to improved oil recovery from oil-saturated tight core plugs

Chapter 6 Conclusions and Recommendations

This study investigated (i) the wettability behavior of tight rocks at core-scale (using spontaneous imbibition tests and contact angle measurements) and pore-scale (using AFM, SEM/EDS), (ii) the effect of rock mineralogy on thin film stability using DLVO theory, and (iii) the rock-fluid interactions at different scales (bulk-phase and core-scale) for mixtures of CO₂ and surfactant solutions.

6.1. Conclusions

The key conclusions from this study are summarized as follows:

6.1.1. *Wettability and Surface Forces*

- The DLVO theory (by calculating disjoining pressures and contact angles) is used to explain the effect of mineral heterogeneity on spontaneous imbibition tests performed on Montney downhole core plugs.
- Dry core plugs have similar wetting affinities to oil and water due to the existence of multi-mineral pores observed in pore-scale visualizations.
- Water can spontaneously imbibe into oil-saturated core plugs and expel the oil out. The measured oil recovery is up to 45 %, suggesting higher wetting affinity of core plugs to water compared with oil.
- The disjoining pressures (P_h) calculated for the solid surface/oil/water system can explain the water imbibition into the quartz grains covered with oil film.
- Oil cannot imbibe into the water-saturated core plugs due to the presence of stable water film covering the grains. The contact angles calculated for the solid surface/water/oil system are in the range of water-wet state
- Pore-scale visualizations (thin section, SEM/EDS, and AFM analyses) along with the disjoining pressures and contact angles calculated by applying the DLVO theory can provide a better understanding of wettability behavior for tight rocks.

6.1.2. *CO₂-Oil Interactions*

- High CO₂ solubility in oil leads to high oil swelling factor at reservoir conditions (2000 psig and 50°C) up to 1.390.
- The results of cyclic CO₂ tests show the high oil recovery from oil-saturated Montney core plugs up to 66% of the original oil in-place. The first four cycles recover more than 70% of the total recovered oil from the core plugs.
- The key mechanisms for oil production are: 1) oil swelling as a result of CO₂ dissolution into the oil, and 2) evaporation of oil components expelled out of the core into CO₂ bulk-phase.

6.1.3. *OPE Surfactant Solutions-Oil Interactions*

- Mixing OPE surfactants (having long EO chain) with OPE15 (having short EO chain) improves the oil displacement from narrow hydrophobic pores.
- In addition to (i) decreasing IFTs for single and mixed surfactant solutions and (ii) preferentially wetting the rock surface by single and mixed surfactant solutions, there should be additional driving mechanism for improving oil recovery with mixed surfactants.
- The higher oil recovery factor for the mixed solutions can be explained by (i) improved adsorption tendency of mixed surfactants on the rock surface due to the existence of OPE15, (ii) formation of small micelles (100-200 nm) in OPE15-OPE70 and OPE15-OPE100 solutions.
- The existence of small mixed micelles facilitates surfactant imbibition into narrow pores ($P_{throat} < 100$ nm) for oil expulsion.

6.2. Significance for the Field Application

- A laboratory protocol is developed to evaluate the wettability of tight rocks ranging from core-scale to pore-scale.
- Scaling groups have been applied to predict the oil recovery at the field-scale by use of spontaneous imbibition data.

- Effective mechanisms are proposed for improving the oil recovery factor from tight rocks when CO₂ or mixed non-ionic surfactants contact the oil-saturated rocks.

6.3. Recommendations

Each set of experiment has some limitations affecting the experimental results. The experiments should be conducted at reservoir pressure and temperature to represent the real rock-fluid interactions. Some suggestions for better understanding the controlling mechanisms at the reservoir conditions are presented for the future work in this field:

- Making a visual cell which can work at high temperature/high pressure conditions and conducting the spontaneous imbibition at the reservoir conditions.
- Conducting contact angle measurement at the elevated temperature to consider the effect of temperature on wettability behavior of rocks.
- Measuring the adhesion forces between the minerals in the liquid conditions. Although it is not possible to conduct the force measurement at high pressure, performing the force measurement in presence of water and oil at high temperature can better mimic the rock-fluid interactions at reservoir conditions.
- Investigating the effect of rock grains coating with clays/organic matter on wettability behavior of rock surface using the DLVO theory because coating with clay/organic matter may affect the initial wetting affinity of grains.
- Investigating CO₂-oil interactions in presence of water as CO₂ solubility in water may affect CO₂ solubility in oil and consequently oil displacement from tight rocks.
- Investigating the compatibility of OPE surfactant solution with high saline brine to avoid the formation damage.
- Investigating the cloud point of OPE surfactant since the cloud point of non-ionic surfactants is relatively low. This might affect the performance of surfactant solution at reservoir conditions.

- Conducting more rigorous surfactant-oil interactions at the bulk phase to investigate the possibility of micro-emulsion with OPE surfactant with high salinity brine.

References

1. Zhang, K., et al., *Future Trends for Tight Oil Exploitation*, in *SPE North Africa Technical Conference and Exhibition*. 2015, Society of Petroleum Engineers: Cairo, Egypt. p. 14.
2. Kilian, L., *How the Tight Oil Boom Has Changed Oil and Gasoline Markets*, in *CESifo Working Paper Series 6380*. 2017, CESifo Group Munich.
3. Arthur, J.D.L., B.; Alleman, D., *Modern Shale Gas Development in the United States: A Primer*. 2009: US Department of Energy, Office of Fossil Energy.
4. resources, C.s.f.u., *Tight Oil Fact Sheet*. Last accessed: 2018. p. 2.
5. American Association of Petroleum Geologists, E.M.D., *Unconventional Energy Resources: 2015 Review*. Natural Resources Research, 2015. **24**(4): p. 443-508.
6. association_of_petroleum_producers, C., *Tight Oil: An Emerging Resource Fact Sheet*. 2016. p. 2.
7. Lee, D.S., et al., *A critical evaluation of unconventional gas recovery from the marcellus shale, northeastern United States*. KSCE Journal of Civil Engineering, 2011. **15**(4): p. 679.
8. Middleton, R.S., et al., *Shale gas and non-aqueous fracturing fluids: Opportunities and challenges for supercritical CO₂*. Applied Energy, 2015. **147**: p. 500-509.
9. Resources, C.S.f.U., *Understanding tight oil* Last accessed: 2018.
10. Resources, C.S.f.U., *Water Consumption*. Last accessed: 2018. p. 2.
11. Resources, C.S.f.U., *Fractruing Fluids*. Last accessed: 2018.
12. Frac Focus, C.D.R. *Why Chemicals Are Used*. Last accessed: 2018; Available from: <http://fracfocus.org/chemical-use/why-chemicals-are-used>.
13. Reynolds, M.M., R.C. Bachman, and W.E. Peters, *A Comparison of the Effectiveness of Various Fracture Fluid Systems Used in Multistage Fractured Horizontal Wells: Montney Formation, Unconventional Gas*, in *SPE Hydraulic Fracturing Technology Conference*. 2014, Society of Petroleum Engineers: The Woodlands, Texas, USA. p. 21.
14. Hayes, B., *The Current State of Canadian Unconventional Oil and Gas Plays*, in *The Way Ahead*. 2018, Society of Petroleum Engineer: US.
15. Kathel, P. and K.K. Mohanty, *Wettability Alteration in a Tight Oil Reservoir*. Energy & Fuels, 2013. **27**(11): p. 6460-6468.
16. Manrique, E.J., et al., *EOR: Current Status and Opportunities*, in *SPE Improved Oil Recovery Symposium*. 2010, Society of Petroleum Engineers: Tulsa, Oklahoma, USA. p. 21.
17. Dehghanpour, H., M. Xu, and A. Habibi, *Wettability of Gas Shale Reservoirs*, in *Fundamentals of Gas Shale Reservoirs*, R. Rezaee, Editor. 2015, John Wiley & Sons, Inc. p.

341-359.

18. Donaldson, E.C. and W. Alam, *Wettability*. Wettability. 2008. 1-336.
19. Anderson, W., *Wettability Literature Survey- Part 2: Wettability Measurement*. Journal of Petroleum Technology, 1986. **38**(11): p. 1246-1262.
20. Anderson, W.G., *Wettability Literature Survey- Part 1: Rock/Oil/Brine Interactions and the Effects of Core Handling on Wettability*. Journal of Petroleum Technology, 1986. **38**(10): p. 1125-1144.
21. Anderson, W.G., *Wettability Literature Survey-Part 3: The Effects of Wettability on the Electrical Properties of Porous Media*. Journal of Petroleum Technology, 1986. **38**(12): p. 1371-1378.
22. Anderson, W.G., *Wettability Literature Survey- Part 4: Effects of Wettability on Capillary Pressure*. Journal of Petroleum Technology, 1987. **39**(10): p. 1283-1300.
23. Anderson, W.G., *Wettability Literature Survey Part 5: The Effects of Wettability on Relative Permeability*. Journal of Petroleum Technology, 1987. **39**(11): p. 1453-1468.
24. Anderson, W.G., *Wettability Literature Survey-Part 6: The Effects of Wettability on Waterflooding*. Journal of Petroleum Technology, 1987. **39**(12): p. 1605-1622.
25. Peters, E.J., *Advanced Petrophysics: Volume 2: Dispersion, Interfacial Phenomena/Wettability, Capillarity/Capillary Pressure, Relative Permeability*. Vol. 2. 2012, Palo Alto, California: Live Oak Book Company. 276.
26. Chaturvedi, T., J.M. Schembre, and A.R. Kovscek, *Spontaneous imbibition and wettability characteristics of Powder River Basin coal*. International Journal of Coal Geology, 2009. **77**(1): p. 34-42.
27. Amott, E., *Observations Relating to the Wettability of Porous Rock*. 1959, Society of Petroleum Engineers. p. 7.
28. Donaldson, E.C., R.D. Thomas, and P.B. Lorenz, *Wettability Determination and Its Effect on Recovery Efficiency*. Society of Petroleum Engineers Journal, 1969. **9**(01): p. 13-20.
29. Morrow, N.R., *Wettability and Its Effect on Oil Recovery*. Journal of Petroleum Technology, 1990. **42**(12): p. 1476-1484.
30. Jones, S.C. and W.O. Roszelle, *Graphical Techniques for Determining Relative Permeability From Displacement Experiments*. Journal of Petroleum Technology, 1978. **30**(05): p. 807-817.
31. Brown, R.J.S. and I. Fatt, *Measurements Of Fractional Wettability Of Oil Fields' Rocks By The Nuclear Magnetic Relaxation Method*, in Fall Meeting of the Petroleum Branch of AIME. 1956, Society of Petroleum Engineers: Los Angeles, California. p. 4.
32. Lan, Q., et al., *A comparative investigation of shale wettability: The significance of pore connectivity*. Journal of Natural Gas Science and Engineering, 2015. **27**: p. 1174-1188.

33. Xu, M. and H. Dehghanpour, *Advances in Understanding Wettability of Gas Shales*. Energy & Fuels, 2014. **28**(7): p. 4362-4375.
34. Dehghanpour, H., et al., *Spontaneous Imbibition of Brine and Oil in Gas Shales: Effect of Water Adsorption and Resulting Microfractures*. Energy & Fuels, 2013. **27**(6): p. 3039-3049.
35. Ghanbari, E. and H. Dehghanpour, *Impact of rock fabric on water imbibition and salt diffusion in gas shales*. International Journal of Coal Geology, 2015. **138**: p. 55-67.
36. Makhanov, K., H. Dehghanpour, and E. Kuru, *An Experimental Study of Spontaneous Imbibition in Horn River Shales*, in *SPE Canadian Unconventional Resources Conference*. 2012, Society of Petroleum Engineers: Calgary, Alberta, Canada. p. 14.
37. Montgomery, C., *Fracturing Fluids*, in *ISRM International Conference for Effective and Sustainable Hydraulic Fracturing*. 2013, International Society for Rock Mechanics and Rock Engineering: Brisbane, Australia. p. 23.
38. Bennion, D.B. and F.B. Thomas, *Formation Damage Issues Impacting the Productivity of Low Permeability, Low Initial Water Saturation Gas Producing Formations*. Journal of Energy Resources Technology, 2005. **127**(3): p. 240-247.
39. Cheng, Y., *Impact of Water Dynamics in Fractures on the Performance of Hydraulically Fractured Wells in Gas-Shale Reservoirs*. Journal of Canadian Petroleum Technology, 2012. **51**(02): p. 143-151.
40. Lan, Q., et al., *Water Loss Versus Soaking Time: Spontaneous Imbibition in Tight Rocks*. Energy Technology, 2014. **2**(12): p. 1033-1039.
41. Lan, Q., et al., *Advances in Understanding Wettability of Tight and Shale Gas Formations*, in *SPE Annual Technical Conference and Exhibition*. 2014, Society of Petroleum Engineers: Amsterdam, The Netherlands. p. 19.
42. Makhanov, K., et al., *Liquid uptake of gas shales: A workflow to estimate water loss during shut-in periods after fracturing operations*. Journal of Unconventional Oil and Gas Resources, 2014. **7**: p. 22-32.
43. Roychaudhuri, B., T.T. Tsotsis, and K. Jessen, *An experimental investigation of spontaneous imbibition in gas shales*. Journal of Petroleum Science and Engineering, 2013. **111**: p. 87-97.
44. Wang, M. and J.Y. Leung, *Numerical investigation of fluid-loss mechanisms during hydraulic fracturing flow-back operations in tight reservoirs*. Journal of Petroleum Science and Engineering, 2015. **133**: p. 85-102.
45. Shaoul, J.R., L.F. van Zelm, and C.J. de Pater, *Damage Mechanisms in Unconventional-Gas-Well Stimulation--A New Look at an Old Problem*. SPE Production & Operations, 2011. **26**(04): p. 388-400.
46. Barzegar Alamdari, B., M. Kiani, and H. Kazemi, *Experimental and Numerical Simulation Of Surfactant-Assisted Oil Recovery In Tight Fractured Carbonate Reservoir Cores*, in *SPE Improved Oil Recovery Symposium*. 2012, Society of Petroleum Engineers: Tulsa, Oklahoma,

USA. p. 14.

47. Roychaudhuri, B., et al., *Forced and Spontaneous Imbibition Experiments for Quantifying Surfactant Efficiency in Tight Shales*, in *SPE Western North American and Rocky Mountain Joint Meeting*. 2014, Society of Petroleum Engineers: Denver, Colorado. p. 7.
48. Wang, D., et al., *Wettability Survey in Bakken Shale With Surfactant-Formulation Imbibition*. SPE Reservoir Evaluation & Engineering, 2012. **15**(06): p. 695-705.
49. Dehghanpour, H., et al., *Liquid Intake of Organic Shales*. Energy & Fuels, 2012. **26**(9): p. 5750-5758.
50. Xu, Y., O.A. Adefidipe, and H. Dehghanpour, *Estimating fracture volume using flowback data from the Horn River Basin: A material balance approach*. Journal of Natural Gas Science and Engineering, 2015. **25**: p. 253-270.
51. Ghanbari, E. and H. Dehghanpour, *The fate of fracturing water: A field and simulation study*. Fuel, 2016. **163**: p. 282-294.
52. Davies, G.R., T.F. Moslow, and M.D. Sherwin, *The lower Triassic montney formation, west-central Alberta*. Bulletin of Canadian Petroleum Geology, 1997. **45**(4): p. 474-505.
53. Ghanizadeh, A., et al., *Impact of Solvent-Extraction on Fluid Storage and Transport Properties of Montney Formation*, in *SPE/CSUR Unconventional Resources Conference*. 2015, Society of Petroleum Engineers: Calgary, Alberta, Canada. p. 22.
54. Handy, L.L., *Determination of Effective Capillary Pressures for Porous Media from Imbibition Data*. 1960, Society of Petroleum Engineers. p. 6.
55. Schembre, J.M., et al., *Spontaneous Water Imbibition into Diatomite*, in *SPE Western Regional Meeting*. 1998, Society of Petroleum Engineers: Bakersfield, California. p. 11.
56. Lan, Q., et al., *Wettability of the Montney Tight Gas Formation*, in *SPE/CSUR Unconventional Resources Conference – Canada*. 2014, Society of Petroleum Engineers: Calgary, Alberta, Canada. p. 21.
57. Rezaveisi, M., S. Ayatollahi, and B. Rostami, *Experimental Investigation of Matrix Wettability Effects on Water Imbibition in Fractured Artificial Porous Media*. Journal of Petroleum Science and Engineering, 2012. **86-87**: p. 165-171.
58. Schechter, D.S., D. Zhou, and F.M. Orr, *Low IFT drainage and imbibition*. Journal of Petroleum Science and Engineering, 1994. **11**(4): p. 283-300.
59. Standnes, D.C., et al., *An Evaluation of Spontaneous Imbibition of Water into Oil-Wet Carbonate Reservoir Cores Using a Nonionic and a Cationic Surfactant*. Energy & Fuels, 2002. **16**(6): p. 1557-1564.
60. Mattax, C.C. and J.R. Kyte, *Imbibition Oil Recovery from Fractured, Water-Drive Reservoir*. Society of Petroleum Engineers Journal, 1962. **2**(02): p. 177-184.
61. Schmid, K.S. and S. Geiger, *Universal scaling of spontaneous imbibition for water-wet*

systems. Water Resources Research, 2012. **48**(3).

62. Schmid, K.S. and S. Geiger, *Universal scaling of spontaneous imbibition for arbitrary petrophysical properties: Water-wet and mixed-wet states and Handy's conjecture*. Journal of Petroleum Science and Engineering, 2013. **101**: p. 44-61.
63. Shouxiang, M., N.R. Morrow, and X. Zhang, *Generalized scaling of spontaneous imbibition data for strongly water-wet systems*. Journal of Petroleum Science and Engineering, 1997. **18**(3): p. 165-178.
64. Anderson, W.G., *WETTABILITY LITERATURE SURVEY-PART 1: ROCK/OIL/BRINE INTERACTIONS AND THE EFFECTS OF CORE HANDLING ON WETTABILITY*. JPT, Journal of Petroleum Technology, 1986. **38**(11): p. 1125-1144.
65. Donaldson, E.C. and W. Alam, *CHAPTER 1 - Wettability*, in *Wettability*. 2008, Gulf Publishing Company. p. 1-55.
66. Suicmez, V.S., M. Piri, and M.J. Blunt, *Effects of wettability and pore-level displacement on hydrocarbon trapping*. Advances in Water Resources, 2008. **31**(3): p. 503-512.
67. Bultreys, T., L. Van Hoorebeke, and V. Cnudde, *Simulating secondary waterflooding in heterogeneous rocks with variable wettability using an image-based, multiscale pore network model*. Water Resources Research, 2016. **52**(9): p. 6833-6850.
68. Kallel, W., et al., *Modelling the effect of wettability distributions on oil recovery from microporous carbonate reservoirs*. Advances in Water Resources, 2016. **95**: p. 317-328.
69. Essaid, H.I., B.A. Bekins, and I.M. Cozzarelli, *Organic contaminant transport and fate in the subsurface: Evolution of knowledge and understanding*. Water Resources Research, 2015. **51**(7): p. 4861-4902.
70. Al-Futaisi, A. and T.W. Patzek, *Secondary imbibition in NAPL-invaded mixed-wet sediments*. Journal of Contaminant Hydrology, 2004. **74**(1): p. 61-81.
71. Al-Menhali, A., B. Niu, and S. Krevor, *Capillarity and wetting of carbon dioxide and brine during drainage in Berea sandstone at reservoir conditions*. Water Resources Research, 2015. **51**(10): p. 7895-7914.
72. Iglesias, S., C.H. Pentland, and A. Busch, *CO₂ wettability of seal and reservoir rocks and the implications for carbon geo-sequestration*. Water Resources Research, 2015. **51**(1): p. 729-774.
73. Chaudhary, K., et al., *Pore-scale trapping of supercritical CO₂ and the role of grain wettability and shape*. Geophysical Research Letters, 2013. **40**(15): p. 3878-3882.
74. Chaudhary, K., et al., *Wettability measurement under high P-T conditions using X-ray imaging with application to the brine-supercritical CO₂ system*. Geochemistry, Geophysics, Geosystems, 2015. **16**(9): p. 2858-2864.
75. Peters, E.J., *Advanced Petrophysics*. Vol. Volume 2: Dispersion, Interfacial Phenomena/Wettability, Capillarity/Capillary Pressure, Relative Permeability. 2012: Live Oak

Book Company. 278.

76. Brown, R.J.S. and I. Fatt, *Measurements Of Fractional Wettability Of Oil Fields' Rocks By The Nuclear Magnetic Relaxation Method*, in *Fall Meeting of the Petroleum Branch of AIME*. 1956, Society of Petroleum Engineers: Los Angeles, California.
77. Skauge, A., et al., *Theoretical and experimental evidence of different wettability classes*. Journal of Petroleum Science and Engineering, 2007. **57**(3): p. 321-333.
78. Salathiel, R.A., *Oil Recovery by Surface Film Drainage In Mixed-Wettability Rocks*. Journal of Petroleum Technology, 1973. **25**(10): p. 1216-1224.
79. Anderson, W.G., *WETTABILITY LITERATURE SURVEY - PART 3: THE EFFECTS OF WETTABILITY ON THE ELECTRICAL PROPERTIES OF POROUS MEDIA*. JPT, Journal of Petroleum Technology, 1986. **39**(13): p. 1371-1378.
80. Boinovich, L. and A. Emelyanenko, *Wetting and surface forces*. Advances in Colloid and Interface Science, 2011. **165**(2): p. 60-69.
81. Hirasaki, G.J., *Wettability: Fundamentals and Surface Forces*. SPE Formation Evaluation, 1991. **6**(02): p. 217-226.
82. Nikolai, V.C., B.V. Derjaguin, and V.M. Muller, *Surface Forces*. 1 ed. 1987, Springer Science+Business Media New York: Springer US. XIX, 440.
83. Li, J., et al., *Water Sorption and Distribution Characteristics in Clay and Shale: Effect of Surface Force*. Energy & Fuels, 2016. **30**(11): p. 8863-8874.
84. Binazadeh, M., et al., *Effect of Electrostatic Interactions on Water Uptake of Gas Shales: The Interplay of Solution Ionic Strength and Electrostatic Double Layer*. Energy & Fuels, 2016. **30**(2): p. 992-1001.
85. Roshan, H., et al., *On wettability of shale rocks*. Journal of Colloid and Interface Science, 2016. **475**: p. 104-111.
86. Singh, H., *A critical review of water uptake by shales*. Journal of Natural Gas Science and Engineering, 2016. **34**: p. 751-766.
87. Deglint, H.J., et al., *Live Imaging of Micro-Wettability Experiments Performed for Low-Permeability Oil Reservoirs*. Scientific Reports, 2017. **7**(1).
88. Karimi, S., M. Saidian, and H. Kazemi, *Experimental study of the effect of aging on fluid distribution in Middle Bakken cores*. Journal of Petroleum Science and Engineering, 2018. **166**: p. 1042-1054.
89. Radke, C.J., A.R. Kovscek, and H. Wong, *A Pore-Level Scenario for the Development of Mixed Wettability in Oil Reservoirs*, in *SPE Annual Technical Conference and Exhibition*. 1992, Society of Petroleum Engineers: Washington, D.C.
90. Morrow, N.R., *Interfacial Phenomena in Petroleum Recovery*. Surfactant Science Vol. 36. 1991, New York, USA: MARCEL DEKKER INC. 441.

91. Alshakhs, M.J. and A.R. Kovscek, *Understanding the role of brine ionic composition on oil recovery by assessment of wettability from colloidal forces*. Advances in Colloid and Interface Science, 2016. **233**: p. 126-138.
92. Buckley, J.S., Y. Liu, and S. Monsterleet, *Mechanisms of Wetting Alteration by Crude Oils*. SPE Journal, 1998. **3**(01): p. 54-61.
93. Bradford, S.A. and F.J. Leij, *Predicting Two- and Three-Fluid Capillary Pressure-Saturation Relationships of Porous Media With Fractional Wettability*. Water Resources Research, 1996. **32**(2): p. 251-259.
94. Landry, C.J., Z.T. Karpyan, and O. Ayala, *Relative permeability of homogenous-wet and mixed-wet porous media as determined by pore-scale lattice Boltzmann modeling*. Water Resources Research, 2014. **50**(5): p. 3672-3689.
95. Ryazanov, A.V., K.S. Sorbie, and M.I.J. van Dijke, *Structure of residual oil as a function of wettability using pore-network modelling*. Advances in Water Resources, 2014. **63**: p. 11-21.
96. Valvatne, P.H. and M.J. Blunt, *Predictive pore-scale modeling of two-phase flow in mixed wet media*. Water Resources Research, 2004. **40**(7): p. n/a-n/a.
97. van Dijke, M.I.J., K.S. Sorbie, and S.R. McDougall, *Saturation-dependencies of three-phase relative permeabilities in mixed-wet and fractionally wet systems*. Advances in Water Resources, 2001. **24**(3): p. 365-384.
98. Al-Raoush, R.I., *Impact of Wettability on Pore-Scale Characteristics of Residual Nonaqueous Phase Liquids*. Environmental Science & Technology, 2009. **43**(13): p. 4796-4801.
99. Mirzaei, M., et al., *Prediction of Three-Phase Gravity Drainage from Two-Phase Capillary Pressure Curves*, in *SPE Improved Oil Recovery Symposium*. 2010, Society of Petroleum Engineers: Tulsa, Oklahoma, USA.
100. Habibi, A., et al., *Advances in Understanding Wettability of Tight Oil Formations: A Montney Case Study*. SPE Reservoir Evaluation & Engineering, 2016. **19**(04): p. 583-603.
101. Kumar, M., et al., *Imaging of Pore Scale Distribution of Fluids And Wettability*. Petrophysics, 2009. **50**(04): p. 311-321.
102. Schmatz, J., et al., *Nanoscale imaging of pore-scale fluid-fluid-solid contacts in sandstone*. Geophysical Research Letters, 2015. **42**(7): p. 2189-2195.
103. Singh, K., B. Bijeljic, and M.J. Blunt, *Imaging of oil layers, curvature and contact angle in a mixed-wet and a water-wet carbonate rock*. Water Resources Research, 2016. **52**(3): p. 1716-1728.
104. Javadpour, F., M. Moravvej Farshi, and M. Amrein, *Atomic-Force Microscopy: A New Tool for Gas-Shale Characterization*. Journal of Canadian Petroleum Technology, 2012. **51**(04): p. 236-243.
105. Kumar, K., E. Dao, and K.K. Mohanty, *AFM study of mineral wettability with reservoir oils*. Journal of Colloid and Interface Science, 2005. **289**(1): p. 206-217.

106. Basu, S. and M.M. Sharma, *Characterization of mixed-wettability states in oil reservoirs by atomic force microscopy*. SPE Journal, 1997. **2**(4): p. 427-435.
107. Basu, S. and M.M. Sharma, *Investigating the role of crude-oil components on wettability alteration using atomic force microscopy*. SPE Journal, 1999. **4**(3): p. 235-241.
108. Drummond, C. and J. Israelachvili, *Fundamental studies of crude oil-surface water interactions and its relationship to reservoir wettability*. Journal of Petroleum Science and Engineering, 2004. **45**(1-2): p. 61-81.
109. Edwards, D.E., et al., *Chapter 16: Triassic Strata of the Western Canadian Sedimentary Basin in Geological Atlas of the Western Canada Sedimentary Basin*, G.D. Mossop and I. Shetsen, Editors. 1994, Canadian Society of Petroleum Geologists and Alberta Research Council.
110. Ghanizadeh, A., et al., *Impact of Solvent-Extraction on Fluid Storage and Transport Properties of Montney Formation*, in *SPE/CSUR Unconventional Resources Conference*, 2015, Society of Petroleum Engineers: Calgary, Alberta, Canada.
111. Donaldson, E.C. and W. Alam, *CHAPTER 2 - Surface Forces*, in *Wettability*. 2008, Gulf Publishing Company. p. 57-119.
112. Gregory, J., *Approximate expressions for retarded van der waals interaction*. Journal of Colloid And Interface Science, 1981. **83**(1): p. 138-145.
113. Vincent, B., *The van der Waals attraction between colloid particles having adsorbed layers. II. Calculation of interaction curves*. Journal of Colloid and Interface Science, 1973. **42**(2): p. 270-285.
114. Israelachvili, J.N., *13 - Van der Waals Forces between Particles and Surfaces*, in *Intermolecular and Surface Forces (Third Edition)*. 2011, Academic Press: San Diego. p. 253-289.
115. Bergström, L., *Hamaker constants of inorganic materials*. Advances in Colloid and Interface Science, 1997. **70**(1-3): p. 125-169.
116. Xie, Q., et al., *Ions tuning water flooding experiments and interpretation by thermodynamics of wettability*. Journal of Petroleum Science and Engineering, 2014. **124**: p. 350-358.
117. Al Mahrouqi, D., J. Vinogradov, and M.D. Jackson, *Zeta potential of artificial and natural calcite in aqueous solution*. Advances in Colloid and Interface Science, 2017. **240**: p. 60-76.
118. Gregory, J., *Interaction of unequal double layers at constant charge*. Journal of Colloid and Interface Science, 1975. **51**(1): p. 44-51.
119. Yang, G., et al., *Desorption Mechanism of Asphaltenes in the Presence of Electrolyte and the Extended Derjaguin–Landau–Verwey–Overbeek Theory*. Energy & Fuels, 2015. **29**(7): p. 4272-4280.
120. Wong, H., S. Morris, and C.J. Radke, *Three-dimensional menisci in polygonal*

- capillaries. *Journal of Colloid And Interface Science*, 1992. **148**(2): p. 317-336.
121. Vinogradov, J. and M.D. Jackson, *Zeta potential in intact natural sandstones at elevated temperatures*. *Geophysical Research Letters*, 2015. **42**(15): p. 6287-6294.
122. Al Mahrouqi, D., J. Vinogradov, and M.D. Jackson, *Temperature dependence of the zeta potential in intact natural carbonates*. *Geophysical Research Letters*, 2016. **43**(22): p. 11,578-11,587.
123. Toshia, T., N. Matsushima, and T. Ishido, *Zeta potential measured for an intact granite sample at temperatures to 200°C*. *Geophysical Research Letters*, 2003. **30**(6).
124. Vinogradov, J., M.D. Jackson, and M. Chamerois, *Zeta potential in sandpacks: Effect of temperature, electrolyte pH, ionic strength and divalent cations*. *Colloids and Surfaces A: Physicochemical and Engineering Aspects*, 2018. **553**: p. 259-271.
125. Rodríguez, K. and M. Araujo, *Temperature and pressure effects on zeta potential values of reservoir minerals*. *Journal of Colloid and Interface Science*, 2006. **300**(2): p. 788-794.
126. Van Der Vegte, E.W. and G. Hadzioannou, *Scanning force microscopy with chemical specificity: An extensive study of chemically specific tip-surface interactions and the chemical imaging of surface functional groups*. *Langmuir*, 1997. **13**(16): p. 4357-4368.
127. Butt, H.J., B. Cappella, and M. Kappl, *Force measurements with the atomic force microscope: Technique, interpretation and applications*. *Surface Science Reports*, 2005. **59**(1-6): p. 1-152.
128. Schneider, J., W. Barger, and G.U. Lee, *Nanometer Scale Surface Properties of Supported Lipid Bilayers Measured with Hydrophobic and Hydrophilic Atomic Force Microscope Probes*. *Langmuir*, 2003. **19**(5): p. 1899-1907.
129. Tormoen, G.W., J. Drelich, and E.R. Beach lii, *Analysis of atomic force microscope pull-off forces for gold surfaces portraying nanoscale roughness and specific chemical functionality*. *Journal of Adhesion Science and Technology*, 2004. **18**(1): p. 1-17.
130. Karoussi, O., et al., *AFM study of calcite surface exposed to stearic and heptanoic acids*. *Colloids and Surfaces A: Physicochemical and Engineering Aspects*, 2008. **325**(3): p. 107-114.
131. Bantignies, J.L., C.C.D. Moulin, and H. Dexpert, *Wettability contrasts in kaolinite and illite clays: Characterization by infrared and x-ray absorption spectroscopies*. *Clays and Clay Minerals*, 1997. **45**(2): p. 184-193.
132. Borysenko, A., et al., *Experimental investigations of the wettability of clays and shales*. *Journal of Geophysical Research: Solid Earth*, 2009. **114**(7).
133. Akbarabadi, M., et al., *Nano-scale experimental investigation of in-situ wettability and spontaneous imbibition in ultra-tight reservoir rocks*. *Advances in Water Resources*, 2017. **107**: p. 160-179.
134. Papavasileiou, K.D., et al., *Molecular Dynamics Simulation of Water-Based Fracturing Fluids in Kaolinite Slit Pores*. *The Journal of Physical Chemistry C*, 2018.

135. Siddiqui, M.A.Q., et al., *Current understanding of shale wettability: A review on contact angle measurements*. Earth-Science Reviews, 2018. **181**: p. 1-11.
136. Zhang, L., et al., *Surface Wettability of Basal Surfaces of Clay Minerals: Insights from Molecular Dynamics Simulation*. Energy & Fuels, 2016. **30**(1): p. 149-160.
137. Šolc, R., et al., *Wettability of kaolinite (001) surfaces — Molecular dynamic study*. Geoderma, 2011. **169**: p. 47-54.
138. Greathouse, J.A., et al., *Adsorption of Aqueous Crude Oil Components on the Basal Surfaces of Clay Minerals: Molecular Simulations Including Salinity and Temperature Effects*. The Journal of Physical Chemistry C, 2017. **121**(41): p. 22773-22786.
139. Wilson, M.J., L. Wilson, and I. Patey, *The influence of individual clay minerals on formation damage of reservoir sandstones: A critical review with some new insights*. Clay Minerals, 2014. **49**(2): p. 147-164.
140. Kantorowicz, J.D., *The influence of variations in illite morphology on the permeability of Middle Jurassic Brent Group sandstones, Cormorant Field, UK North Sea*. Marine and Petroleum Geology, 1990. **7**(1): p. 66-74.
141. Pallatt, N., J. Wilson, and B. McHardy, *The Relationship Between Permeability and the Morphology of Diagenetic Illite in Reservoir Rocks*. Journal of Petroleum Technology, 1984. **36**(12): p. 2225-2227.
142. Saraji, S., L. Goual, and M. Piri, *Dynamic adsorption of asphaltenes on quartz and calcite packs in the presence of brine films*. Colloids and Surfaces A: Physicochemical and Engineering Aspects, 2013. **434**: p. 260-267.
143. Somasundaran, P. and G.E. Agar, *The zero point of charge of calcite*. Journal of Colloid And Interface Science, 1967. **24**(4): p. 433-440.
144. Nikolakis, V., M. Tsapatsis, and D.G. Vlachos, *Physicochemical characterization of silicalite-1 surface and its implications on crystal growth*. Langmuir, 2003. **19**(11): p. 4619-4626.
145. Li, H.C. and P.L. De Bruyn, *Electrokinetic and adsorption studies on quartz*. Surface Science, 1966. **5**(2): p. 203-220.
146. Hough, D.B. and L.R. White, *The calculation of hamaker constants from liftshitz theory with applications to wetting phenomena*. Advances in Colloid and Interface Science, 1980. **14**(1): p. 3-41.
147. Tokunaga, T.K., *Physicochemical controls on adsorbed water film thickness in unsaturated geological media*. Water Resources Research, 2011. **47**(8).
148. Jones, R., et al., *Adhesion Forces between Glass and Silicon Surfaces in Air Studied by AFM: Effects of Relative Humidity, Particle Size, Roughness, and Surface Treatment*. Langmuir, 2002. **18**(21): p. 8045-8055.
149. Noy, A., D.V. Vezenov, and C.M. Lieber, *Chemical force microscopy*. Annual Review of Materials Science, 1997. **27**(1): p. 381-421.

150. Wilbur, J.L., et al., *Scanning Force Microscopies Can Image Patterned Self-Assembled Monolayers*. Langmuir, 1995. **11**(3): p. 825-831.
151. Bhushan, B., et al., *Handbook of Micro/Nano Tribology*, ed. B. Bhushan. 1999: Boca Raton: CRC Press.
152. Stifter, T., O. Marti, and B. Bhushan, *Theoretical investigation of the distance dependence of capillary and van der Waals forces in scanning force microscopy*. Physical Review B, 2000. **62**(20): p. 13667-13673.
153. Wenzel, R.N., *RESISTANCE OF SOLID SURFACES TO WETTING BY WATER*. Industrial & Engineering Chemistry, 1936. **28**(8): p. 988-994.
154. Terriza, A., et al., *Roughness assessment and wetting behavior of fluorocarbon surfaces*. Journal of Colloid and Interface Science, 2012. **376**(1): p. 274-282.
155. Kaltenbach, R., D. Diehl, and G.E. Schaumann, *Links between nanoscale and macroscale surface properties of natural root mucilage studied by atomic force microscopy and contact angle*. Journal of Colloid and Interface Science, 2018. **516**: p. 446-455.
156. Parks, G.A., *SURFACE AND INTERFACIAL FREE ENERGIES OF QUARTZ*. Journal of Geophysical Research, 1982. **89**(B6): p. 3997-4008.
157. Sauerer, B., et al., *Quantifying mineral surface energy by scanning force microscopy*. Journal of Colloid and Interface Science, 2016. **472**: p. 237-246.
158. van Oss, C.J., *Interfacial forces in aqueous media*. 2nd Edition ed. 2006, New York, NY: CRC Press, Taylor and Francis Group.
159. Leite, F.L., A. Riul, and P.S.P. Herrmann, *Mapping of adhesion forces on soil minerals in air and water by atomic force spectroscopy (AFS)*. Journal of Adhesion Science and Technology, 2003. **17**(16): p. 2141-2156.
160. Stipp, S.L.S., C.M. Eggleston, and B.S. Nielsen, *Calcite surface structure observed at microtopographic and molecular scales with atomic force microscopy (AFM)*. Geochimica et Cosmochimica Acta, 1994. **58**(14): p. 3023-3033.
161. Røyne, A., K.N. Dalby, and T. Hassenkam, *Repulsive hydration forces between calcite surfaces and their effect on the brittle strength of calcite-bearing rocks*. Geophysical Research Letters, 2015. **42**(12): p. 4786-4794.
162. Ricci, M., et al., *Growth and Dissolution of Calcite in the Presence of Adsorbed Stearic Acid*. Langmuir, 2015. **31**(27): p. 7563-7571.
163. Stifter, T., et al., *Influence of the topography on adhesion measured by SFM*. Applied Physics A, 1998. **66**(1): p. S597-S605.
164. Beach, E.R., et al., *Pull-off force measurements between rough surfaces by atomic force microscopy*. Journal of Colloid and Interface Science, 2002. **247**(1): p. 84-99.
165. Sirghi, L., et al., *Effect of Sample Topography on Adhesive Force in Atomic Force*

Spectroscopy Measurements in Air. Langmuir, 2000. **16**(20): p. 7796-7800.

166. Reynolds, M.M., R.C. Bachman, and W.E. Peters, *A Comparison of the Effectiveness of Various Fracture Fluid Systems Used in Multistage Fractured Horizontal Wells: Montney Formation, Unconventional Gas*, in *SPE Hydraulic Fracturing Technology Conference*. 2014, Society of Petroleum Engineers: The Woodlands, Texas, USA.
167. Javaheri, A., H. Dehghanpour, and J.M. Wood, *Tight rock wettability and its relationship to other petrophysical properties: A Montney case study*. Journal of Earth Science, 2017. **28**(2): p. 381-390.
168. Yassin, M.R., M. Begum, and H. Dehghanpour, *Organic shale wettability and its relationship to other petrophysical properties: A Duvernay case study*. International Journal of Coal Geology, 2017. **169**: p. 74-91.
169. Christensen, J.R., E.H. Stenby, and A. Skauge, *Review of WAG Field Experience*. SPE Reservoir Evaluation & Engineering, 2001. **4**(02): p. 97-106.
170. Hoffman, B.T., *Comparison of Various Gases for Enhanced Recovery from Shale Oil Reservoirs*, in *SPE Improved Oil Recovery Symposium*. 2012, Society of Petroleum Engineers: Tulsa, Oklahoma, USA.
171. Hawthorne, S.B., et al., *Hydrocarbon Mobilization Mechanisms from Upper, Middle, and Lower Bakken Reservoir Rocks Exposed to CO₂*, in *SPE Unconventional Resources Conference Canada*. 2013, Society of Petroleum Engineers: Calgary, Alberta, Canada.
172. Wang, X. and Y. Gu, *Oil Recovery and Permeability Reduction of a Tight Sandstone Reservoir in Immiscible and Miscible CO₂ Flooding Processes*. Industrial & Engineering Chemistry Research, 2011. **50**(4): p. 2388-2399.
173. Han, L. and Y. Gu, *Optimization of miscible CO₂ water-alternating-gas injection in the Bakken formation*. Energy & Fuels, 2014. **28**(11): p. 6811-6819.
174. Yu, Y., X. Meng, and J.J. Sheng, *Experimental and numerical evaluation of the potential of improving oil recovery from shale plugs by nitrogen gas flooding*. Journal of Unconventional Oil and Gas Resources, 2016. **15**: p. 56-65.
175. Pu, W., et al., *Experimental investigation of CO₂ huff-n-puff process for enhancing oil recovery in tight reservoirs*. Chemical Engineering Research and Design, 2016. **111**: p. 269-276.
176. He, K., et al., *Evaluation of surfactant performance in fracturing fluids for enhanced well productivity in unconventional reservoirs using Rock-on-a-Chip approach*. Journal of Petroleum Science and Engineering, 2015. **135**: p. 531-541.
177. Xu, L., K. He, and C. Nguyen, *Insights into Surfactant Containing Fracturing Fluids Inducing Microcracks and Spontaneously Imbibing in Shale Rocks*, in *SPE/CSUR Unconventional Resources Conference*. 2015, Society of Petroleum Engineers: Calgary, Alberta, Canada.
178. Odi, U., *Analysis and Potential of CO₂ Huff-n-Puff for Near Wellbore Condensate*

Removal and Enhanced Gas Recovery, in *SPE Annual Technical Conference and Exhibition*. 2012, Society of Petroleum Engineers: San Antonio, Texas, USA.

179. Jiang, J., Y. Shao, and R.M. Younis, *Development of a Multi-Continuum Multi-Component Model for Enhanced Gas Recovery and CO₂ Storage in Fractured Shale Gas Reservoirs*, in *SPE Improved Oil Recovery Symposium*. 2014, Society of Petroleum Engineers: Tulsa, Oklahoma, USA.
180. Heller, R. and M. Zoback, *Adsorption of methane and carbon dioxide on gas shale and pure mineral samples*. *Journal of Unconventional Oil and Gas Resources*, 2014. **8**: p. 14-24.
181. Gong, Y. and Y. Gu, *Miscible CO₂ Simultaneous Water-and-Gas (CO₂-SWAG) Injection in the Bakken Formation*. *Energy & Fuels*, 2015. **29**(9): p. 5655-5665.
182. Alharthy, N., et al., *Enhanced Oil Recovery in Liquid-Rich Shale Reservoirs: Laboratory to Field*, in *SPE Annual Technical Conference and Exhibition*. 2015, Society of Petroleum Engineers: Houston, Texas, USA.
183. Lu, J., et al., *Alteration of Bakken reservoir rock during CO₂-based fracturing—An autoclave reaction experiment*. *Journal of Unconventional Oil and Gas Resources*, 2016. **14**: p. 72-85.
184. Cudjoe, S., et al., *A comprehensive approach to sweet-spot mapping for hydraulic fracturing and CO₂ huff-n-puff injection in Chattanooga shale formation*. *Journal of Natural Gas Science and Engineering*, 2016. **33**: p. 1201-1218.
185. Ma, J., et al., *Enhanced light oil recovery from tight formations through CO₂ huff 'n' puff processes*. *Fuel*, 2015. **154**: p. 35-44.
186. Liu, F., et al., *Assessing the feasibility of CO₂ storage in the New Albany Shale (Devonian–Mississippian) with potential enhanced gas recovery using reservoir simulation*. *International Journal of Greenhouse Gas Control*, 2013. **17**: p. 111-126.
187. Levine, J.S., et al., *U.S. DOE NETL methodology for estimating the prospective CO₂ storage resource of shales at the national and regional scale*. *International Journal of Greenhouse Gas Control*, 2016. **51**: p. 81-94.
188. Yu, Z., et al., *Petrological characterization and reactive transport simulation of a high-water-cut oil reservoir in the Southern Songliao Basin, Eastern China for CO₂ sequestration*. *International Journal of Greenhouse Gas Control*, 2015. **37**: p. 191-212.
189. Gamadi, T.D., et al., *An Experimental Study of Cyclic CO₂ Injection to Improve Shale Oil Recovery*, in *SPE Improved Oil Recovery Symposium*. 2014, Society of Petroleum Engineers: Tulsa, Oklahoma, USA.
190. Sheng, J.J., *Enhanced oil recovery in shale reservoirs by gas injection*. *Journal of Natural Gas Science and Engineering*, 2015. **22**: p. 252-259.
191. Chen, C., M. Balhoff, and K.K. Mohanty, *Effect of reservoir heterogeneity on primary recovery and CO_n huff 'n' puff recovery in shale-oil reservoirs*. *SPE Reservoir Evaluation and Engineering*, 2014. **17**(3): p. 404-413.

192. Wang, Z., et al., *Optimizing Cyclic CO₂ Injection for Low-permeability Oil Reservoirs through Experimental Study*, in *SPE Unconventional Resources Conference Canada*. 2013, Society of Petroleum Engineers: Calgary, Alberta, Canada.
193. Song, C. and D. Yang, *Performance Evaluation of CO₂ Huff-n-Puff Processes in Tight Oil Formations*, in *SPE Unconventional Resources Conference Canada*. 2013, Society of Petroleum Engineers: Calgary, Alberta, Canada.
194. Tang, G.-Q., et al., *An Experimental Study on Supercritical CO₂ Injection in Fractured Tight Reservoir to Enhance Oil Recovery*, in *Unconventional Resources Technology Conference*. 2016, Unconventional Resources Technology Conference: San Antonio, Texas, USA.
195. Bird, R.B., W.E. Stewart, and E.N. Lightfoot, *Transport phenomena* John Wiley & Sons, New York, 2002.
196. Gao, J., R. Okuno, and H.A. Li. *An experimental study of multiphase behavior for n-butane/bitumen/water mixtures*. in *Society of Petroleum Engineers - SPE Canada Heavy Oil Technical Conference*. 2016.
197. Danesh, A., *PVT and phase behaviour of petroleum reservoir fluids*. Vol. 47. 1998: Elsevier.
198. Pedersen, K.S., P.L. Christensen, and J.A. Shaikh, *Phase Behavior of Petroleum Reservoir Fluids, 2nd Edition*. Phase Behavior of Petroleum Reservoir Fluids, 2nd Edition. 2015, Boca Raton: Crc Press-Taylor & Francis Group. 1-446.
199. Dymond, J.H. and R. Malhotra, *The Tait equation: 100 years on*. International Journal of Thermophysics, 1988. **9**(6): p. 941-951.
200. Gonçalves, F.A.M.M., et al., *PVT, viscosity, and surface tension of ethanol: New measurements and literature data evaluation*. The Journal of Chemical Thermodynamics, 2010. **42**(8): p. 1039-1049.
201. Teja, A.S. and S.I. Sandler, *A Corresponding States equation for saturated liquid densities. II. Applications to the calculation of swelling factors of CO₂—crude oil systems*. AIChE Journal, 1980. **26**(3): p. 341-345.
202. Crawford, H.R., et al., *Carbon Dioxide - A Multipurpose Additive for Effective Well Stimulation*. Journal of Petroleum Technology, 1963. **15**(03): p. 237-242.
203. Bahralolom, I.M. and F.M. Orr, Jr., *Solubility and Extraction in Multiple-Contact Miscible Displacements: Comparison of N₂ and CO₂ Flow Visualization Experiments*. SPE Reservoir Engineering, 1988. **3**(01): p. 213-219.
204. Hawthorne, S.B., et al., *Rapid and Simple Capillary-Rise/Vanishing Interfacial Tension Method To Determine Crude Oil Minimum Miscibility Pressure: Pure and Mixed CO₂, Methane, and Ethane*. Energy & Fuels, 2016. **30**(8): p. 6365-6372.
205. Kokal, S.L. and S.G. Sayegh, *Asphaltenes: The Cholesterol Of Petroleum*, in *Middle East Oil Show*. 1995, Society of Petroleum Engineers: Bahrain.

206. Speight, J.G., *Petroleum asphaltenes - Part 1: Asphaltenes, resins and the structure of petroleum*. Oil and Gas Science and Technology, 2004. **59**(5): p. 467-477.
207. Arenas-Alatorre, J., P.S. Schabes-Retchkiman, and V. Rodriguez-Lugo, *Electron Microscopy Characterization of Crystalline Nanostructures Present in Asphaltene*. Energy & Fuels, 2016. **30**(5): p. 3752-3757.
208. Gonçalves, M.L.A., et al., *Influence of asphaltenes on coke formation during the thermal cracking of different Brazilian distillation residues*. Fuel, 2007. **86**(4): p. 619-623.
209. Renner, T.A., *Measurement and Correlation of Diffusion Coefficients for CO₂ and Rich-Gas Applications*. 1988. **3**(2): p. 517-523.
210. Grogan, A.T., et al., *Diffusion of CO₂ at Reservoir Conditions: Models and Measurements*. SPE Reservoir Engineering, 1988. **3**(01): p. 93-102.
211. Eide, Ø., et al., *Visualization of Carbon Dioxide Enhanced Oil Recovery by Diffusion in Fractured Chalk*. SPE Journal, 2016. **21**(01).
212. Yu, W., et al., *CO₂ injection for enhanced oil recovery in Bakken tight oil reservoirs*. Fuel, 2015. **159**: p. 354-363.
213. Promod Kumar , K.L.M., *Handbook of microemulsion science and technology*. 1999, New York: Marcel Dekker. 864.
214. Jin, L., et al., *Improving Oil Recovery by Use of Carbon Dioxide in the Bakken Unconventional System: A Laboratory Investigation*. SPE Reservoir Evaluation & Engineering, 2016.
215. Ma, J., et al., *Study of cyclic CO₂ injection for low-pressure light oil recovery under reservoir conditions*. Fuel, 2016. **174**: p. 296-306.
216. Reynolds, M., et al., *The Full Montney - A Critical Review of Well Performance by Production Analysis of Over 2,000 Montney Multi-Stage Fractured Horizontal Gas Wells*, in *SPE/CSUR Unconventional Resources Conference*. 2015, Society of Petroleum Engineers: Calgary, Alberta, Canada.
217. Administration, U.S.E.I., *Drilling productivity report*. 2018: Washington, DC. p. 11.
218. Lan, Q., et al., *Wettability of the Montney tight gas formation*. SPE Reservoir Evaluation and Engineering, 2015. **18**(3): p. 417-431.
219. Habibi, A., et al., *Understanding Rock-Fluid Interactions in the Montney Tight Oil Play*, in *SPE/CSUR Unconventional Resources Conference*. 2015, Society of Petroleum Engineers: Calgary, Alberta, Canada.
220. Habibi, A., et al., *Advances in Understanding Wettability of Tight Oil Formations: A Montney Case Study*. 2016.
221. Habibi, A., et al., *Experimental investigation of CO₂-oil interactions in tight rocks: A Montney case study*. Fuel, 2017. **203**: p. 853-867.

222. Jin, L., et al., *Advancing CO₂ enhanced oil recovery and storage in unconventional oil play—Experimental studies on Bakken shales*. Applied Energy, 2017. **208**: p. 171-183.
223. Sheng, J.J., *What type of surfactants should be used to enhance spontaneous imbibition in shale and tight reservoirs?* Journal of Petroleum Science and Engineering, 2017. **159**: p. 635-643.
224. Nguyen, D., et al., *Evaluation of Surfactants for Oil Recovery Potential in Shale Reservoirs*, in *SPE Improved Oil Recovery Symposium*. 2014, Society of Petroleum Engineers: Tulsa, Oklahoma, USA.
225. Wang, D., et al., *Wettability Survey in Bakken Shale With Surfactant-Formulation Imbibition*. 2012.
226. Hargreaves, S., *Drought strains US oil production*. CNNMoney, 2012: p. 31.
227. Roychaudhuri, B., et al., *Forced and Spontaneous Imbibition Experiments for Quantifying Surfactant Efficiency in Tight Shales*, in *SPE Western North American and Rocky Mountain Joint Meeting*. 2014, Society of Petroleum Engineers: Denver, Colorado, USA.
228. Shuler, P.J., et al., *Chemical Process for Improved Oil Recovery From Bakken Shale*, in *Canadian Unconventional Resources Conference*. 2011, Society of Petroleum Engineers: Calgary, Alberta, Canada.
229. Sun, Y., B. Bai, and M. Wei, *Microfracture and surfactant impact on linear cocurrent brine imbibition in gas-saturated shale*. Energy and Fuels, 2015. **29**(3): p. 1438-1446.
230. Wang, D., et al., *Surfactant Formulation Study For Bakken Shale Imbibition*, in *SPE Annual Technical Conference and Exhibition*. 2011, Society of Petroleum Engineers: Denver, Colorado, USA.
231. Zhou, J., et al., *Enhancing Well Stimulation with Improved Salt Tolerant Surfactant for Bakken Formation*, in *SPE Improved Oil Recovery Symposium*. 2014, Society of Petroleum Engineers: Tulsa, Oklahoma, USA.
232. Alvarez, J.O. and D.S. Schechter, *Improving oil recovery in the Wolfcamp unconventional liquid reservoir using surfactants in completion fluids*. Journal of Petroleum Science and Engineering, 2017. **157**: p. 806-815.
233. Zhou, Z., et al., *Experimental and numerical study on spontaneous imbibition of fracturing fluids in the horn river shale gas formation*. SPE Drilling and Completion, 2016. **31**(3): p. 168-177.
234. Liang, T., et al., *Enhancing Hydrocarbon Permeability After Hydraulic Fracturing: Laboratory Evaluations of Shut-Ins and Surfactant Additives*. SPE Journal, 2017. **22**(04): p. 1011-1023.
235. Standnes, D.C. and T. Austad, *Nontoxic low-cost amines as wettability alteration chemicals in carbonates*. Journal of Petroleum Science and Engineering, 2003. **39**(3): p. 431-446.

236. Standnes, D.C. and T. Austad, *Wettability alteration in carbonates: Interaction between cationic surfactant and carboxylates as a key factor in wettability alteration from oil-wet to water-wet conditions*. Colloids and Surfaces A: Physicochemical and Engineering Aspects, 2003. **216**(1): p. 243-259.
237. Austad, T. and D.C. Standnes, *Spontaneous imbibition of water into oil-wet carbonates*. Journal of Petroleum Science and Engineering, 2003. **39**(3): p. 363-376.
238. Zhang, P. and T. Austad, *Wettability and oil recovery from carbonates: Effects of temperature and potential determining ions*. Colloids and Surfaces A: Physicochemical and Engineering Aspects, 2006. **279**(1): p. 179-187.
239. Adibhatla, B. and K.K. Mohanty, *Parametric analysis of surfactant-aided imbibition in fractured carbonates*. Journal of Colloid and Interface Science, 2008. **317**(2): p. 513-522.
240. Mirzaei, M., D.A. DiCarlo, and G.A. Pope, *Visualization and Analysis of Surfactant Imbibition Into Oil-Wet Fractured Cores*. SPE Journal, 2016. **21**(01): p. 101-111.
241. Zhang, P., M.T. Tweheyo, and T. Austad, *Wettability alteration and improved oil recovery by spontaneous imbibition of seawater into chalk: Impact of the potential determining ions Ca²⁺, Mg²⁺, and SO₄²⁻*. Colloids and Surfaces A: Physicochemical and Engineering Aspects, 2007. **301**(1): p. 199-208.
242. Milter, J. and T. Austad, *Chemical flooding of oil reservoirs 7. Oil expulsion by spontaneous imbibition of brine with and without surfactant in mixed-wet, low permeability chalk material*. Colloids and Surfaces A: Physicochemical and Engineering Aspects, 1996. **117**(1): p. 109-115.
243. Standnes, D.C. and T. Austad, *Wettability alteration in chalk: 2. Mechanism for wettability alteration from oil-wet to water-wet using surfactants*. Journal of Petroleum Science and Engineering, 2000. **28**(3): p. 123-143.
244. Hirasaki, G., C.A. Miller, and M. Puerto, *Recent Advances in Surfactant EOR*. SPE Journal, 2011. **16**(04): p. 889-907.
245. Larson, R.G., H.T. Davis, and L.E. Scriven, *Elementary Mechanisms of Oil Recovery by Chemical Methods*. Journal of Petroleum Technology, 1982. **34**(02): p. 243-258.
246. Sheng, J.J., *Status of surfactant EOR technology*. Petroleum, 2015. **1**(2): p. 97-105.
247. Alvarado, V. and E. Manrique, *Enhanced oil recovery: An update review*. Energies, 2010. **3**(9): p. 1529-1575.
248. Pons-Jiménez, M., et al., *Theoretical and experimental insights on the true impact of C₁₂TAC cationic surfactant in enhanced oil recovery for heavy oil carbonate reservoirs*. Colloids and Surfaces A: Physicochemical and Engineering Aspects, 2014. **455**(1): p. 76-91.
249. Pal, S., et al., *Review of surfactant-assisted chemical enhanced oil recovery for carbonate reservoirs: challenges and future perspectives*. Petroleum Science, 2018. **15**(1): p. 77-102.

250. Kamal, M.S., I.A. Hussein, and A.S. Sultan, *Review on Surfactant Flooding: Phase Behavior, Retention, IFT, and Field Applications*. Energy and Fuels, 2017. **31**(8): p. 7701-7720.
251. Kamal, M.S., *A Review of Gemini Surfactants: Potential Application in Enhanced Oil Recovery*. Journal of Surfactants and Detergents, 2016. **19**(2): p. 223-236.
252. Babadagli, T. and Y. Boluk, *Oil recovery performances of surfactant solutions by capillary imbibition*. Journal of Colloid and Interface Science, 2005. **282**(1): p. 162-175.
253. Yarveicy, H. and A. Haghtalab, *Effect of amphoteric surfactant on phase behavior of hydrocarbon-electrolyte-water system-an application in enhanced oil recovery*. Journal of Dispersion Science and Technology, 2018. **39**(4): p. 522-530.
254. Mirchi, V., et al., *A Systematic Study on the Impact of Surfactant Chain Length on Dynamic Interfacial Properties in Porous Media: Implications for Enhanced Oil Recovery*. Industrial & Engineering Chemistry Research, 2017. **56**(46): p. 13677-13695.
255. Alvarez, J.O. and D.S. Schechter, *Application of wettability alteration in the exploitation of unconventional liquid resources*. Petroleum Exploration and Development, 2016. **43**(5): p. 832-840.
256. Zhou, L., S. Das, and B.R. Ellis, *Effect of Surfactant Adsorption on the Wettability Alteration of Gas-Bearing Shales*. Environmental Engineering Science, 2016. **33**(10): p. 766-777.
257. Hou, B.F., Y.F. Wang, and Y. Huang, *Mechanistic study of wettability alteration of oil-wet sandstone surface using different surfactants*. Applied Surface Science, 2015. **330**: p. 56-64.
258. Jarrahian, K., et al., *Wettability alteration of carbonate rocks by surfactants: A mechanistic study*. Colloids and Surfaces A: Physicochemical and Engineering Aspects, 2012. **410**: p. 1-10.
259. Abdulelah, H., S.M. Mahmood, and A. Al-Mutarreb, *Effect of Anionic Surfactant on Wettability of Shale and Its Implication on Gas Adsorption/Desorption Behavior*. Energy and Fuels, 2018. **32**(2): p. 1423-1432.
260. Nwiduee, L.N., et al., *Wettability alteration of oil-wet limestone using surfactant-nanoparticle formulation*. Journal of Colloid and Interface Science, 2017. **504**: p. 334-345.
261. Hou, Y., et al., *The effects of shale composition and pore structure on gas adsorption potential in highly mature marine shales, Lower Paleozoic, central Yangtze, China*. Canadian Journal of Earth Sciences, 2017. **54**(10): p. 1033-1048.
262. Dong, T. and N.B. Harris, *Pore size distribution and morphology in the horn river shale, middle and upper Devonian, northeastern British Columbia, Canada*. AAPG Memoir, 2013(102): p. 67-79.
263. Liu, K., et al., *Nanoscale pore structure characterization of the Bakken shale in the USA*. Fuel, 2017. **209**: p. 567-578.
264. Javaheri, A., A. Habibi, and H. Dehghanpour, *Imbibition oil recovery from tight rocks with*

dual-wet pore-network. Journal of Petroleum Science and Engineering, 2018.

265. Spinler, E.A. and B.A. Baldwin, *Surfactant Induced Wettability Alteration in Porous Media*, in *Surfactants: Fundamentals and Applications in the Petroleum Industry*, L.L. Schramm, Editor. 2000, Cambridge University Press: Cambridge. p. 159-202.
266. Morrow, N.R. and G. Mason, *Recovery of oil by spontaneous imbibition*. Current Opinion in Colloid & Interface Science, 2001. **6**(4): p. 321-337.
267. B. Alamdari, B., et al., *Understanding the Oil Recovery Mechanism in Mixed-Wet Unconventional Reservoirs: Uniqueness and Challenges of Developing Chemical Formulations*, in *SPE Improved Oil Recovery Conference*. 2018, Society of Petroleum Engineers: Tulsa, Oklahoma, USA. p. 12.
268. Zhang, J., D. Wang, and R. Butler, *Optimal Salinity Study to Support Surfactant Imbibition into the Bakken Shale*, in *SPE Unconventional Resources Conference Canada*. 2013, Society of Petroleum Engineers: Calgary, Alberta, Canada.
269. Wang, D., et al., *Wettability survey in bakken shale with surfactant-formulation imbibition*. SPE Reservoir Evaluation and Engineering, 2012. **15**(6): p. 695-705.
270. Alvarez, J.O., I.W.R. Saputra, and D.S. Schechter, *Potential of Improving Oil Recovery with Surfactant Additives to Completion Fluids for the Bakken*. Energy and Fuels, 2017. **31**(6): p. 5982-5994.
271. He, K. and L. Xu, *Unique Mixtures of Anionic/Cationic Surfactants: A New Approach to Enhance Surfactant Performance in Liquids-Rich Shale Reservoirs*, in *SPE International Conference on Oilfield Chemistry*. 2017, Society of Petroleum Engineers: Montgomery, Texas, USA.
272. Ying, G.-G., B. Williams, and R. Kookana, *Environmental fate of alkylphenols and alkylphenol ethoxylates—a review*. Environment International, 2002. **28**(3): p. 215-226.
273. Keneti, A. and R.C.K. Wong, *Investigation of Anisotropic Behavior of Montney Shale Under Indirect Tensile Strength Test*, in *Canadian Unconventional Resources and International Petroleum Conference*. 2010, Society of Petroleum Engineers: Calgary, Alberta, Canada.
274. Wood, J., *Water Distribution in the Montney Tight Gas Play of the Western Canadian Sedimentary Basin: Significance for Resource Evaluation*. 2013.
275. Sanei, H., et al., *Characterization of organic matter fractions in an unconventional tight gas siltstone reservoir*. International Journal of Coal Geology, 2015. **150-151**: p. 296-305.
276. corporation, H., *Performance products: Metalworking chemicals, product information*. 2005: The Woodlands, Texas, US. p. 58.
277. Crook, E.H., G.F. Trebbi, and D.B. Fordyce, *Thermodynamic Properties of Solutions of Homogeneous p,t-Octylphenoxyethoxyethanols (OPE1-10)*. The Journal of Physical Chemistry, 1964. **68**(12): p. 3592-3599.
278. Vonnegut, B., *Rotating bubble method for the determination of surface and interfacial*

tensions. *Review of Scientific Instruments*, 1942. **13**(1): p. 6-9.

279. Viades-Trejo, J. and J. Gracia-Fadrique, *Spinning drop method. From Young-Laplace to Vonnegut*. Colloids and Surfaces A: Physicochemical and Engineering Aspects, 2007. **302**(1-3): p. 549-552.

280. Princen, H.M., I.Y.Z. Zia, and S.G. Mason, *Measurement of interfacial tension from the shape of a rotating drop*. *Journal of Colloid And Interface Science*, 1967. **23**(1): p. 99-107.

281. Kronberg, B., K. Holmberg, and B. Lindman, *Surfactant Self-Assembly*, in *Surface Chemistry of Surfactants and Polymers*. 2014, John Wiley & Sons, Ltd. p. 75-94.

282. Rosen, M.J. and D.S. Murphy, *Effect of the nonaqueous phase on interfacial properties of surfactants. 2. Individual and mixed nonionic surfactants in hydrocarbon/water systems*. *Langmuir*, 1991. **7**(11): p. 2630-2635.

283. Rosen, M.J., *Reduction of Surface and Interfacial Tension by Surfactants*, in *Surfactants and Interfacial Phenomena*, M.J. Rosen, Editor. 2004, Wiley. p. 208-242.

284. Kronberg, B., K. Holmberg, and B. Lindman, *Surfactants and Polymers Containing Oxyethylene Groups Show a Complex Behavior in Surface Chemistry of Surfactants and Polymers*. 2014, John Wiley & Sons, Ltd. p. 137-152.

285. Collins, K.D. and M.W. Washabaugh, *The Hofmeister effect and the behaviour of water at interfaces*. *Quarterly Reviews of Biophysics*, 1985. **18**(4): p. 323-422.

286. Kronberg, B., K. Holmberg, and B. Lindman, *Types of Surfactants, their Synthesis, and Applications*, in *Surface Chemistry of Surfactants and Polymers*. 2014, John Wiley & Sons, Ltd. p. 1-47.

287. Osterhof, H.J. and F.E. Bartell, *Three Fundamental Types of Wetting. Adhesion Tension as the Measure of the Degree of Wetting*. *The Journal of Physical Chemistry*, 1929. **34**(7): p. 1399-1411.

288. Rosen, M.J. and J.T. Kunjappu, *Wetting and Its Modification by Surfactants*, in *Surfactants and Interfacial Phenomena*. 2012, John Wiley & Sons, Inc. p. 272-307.

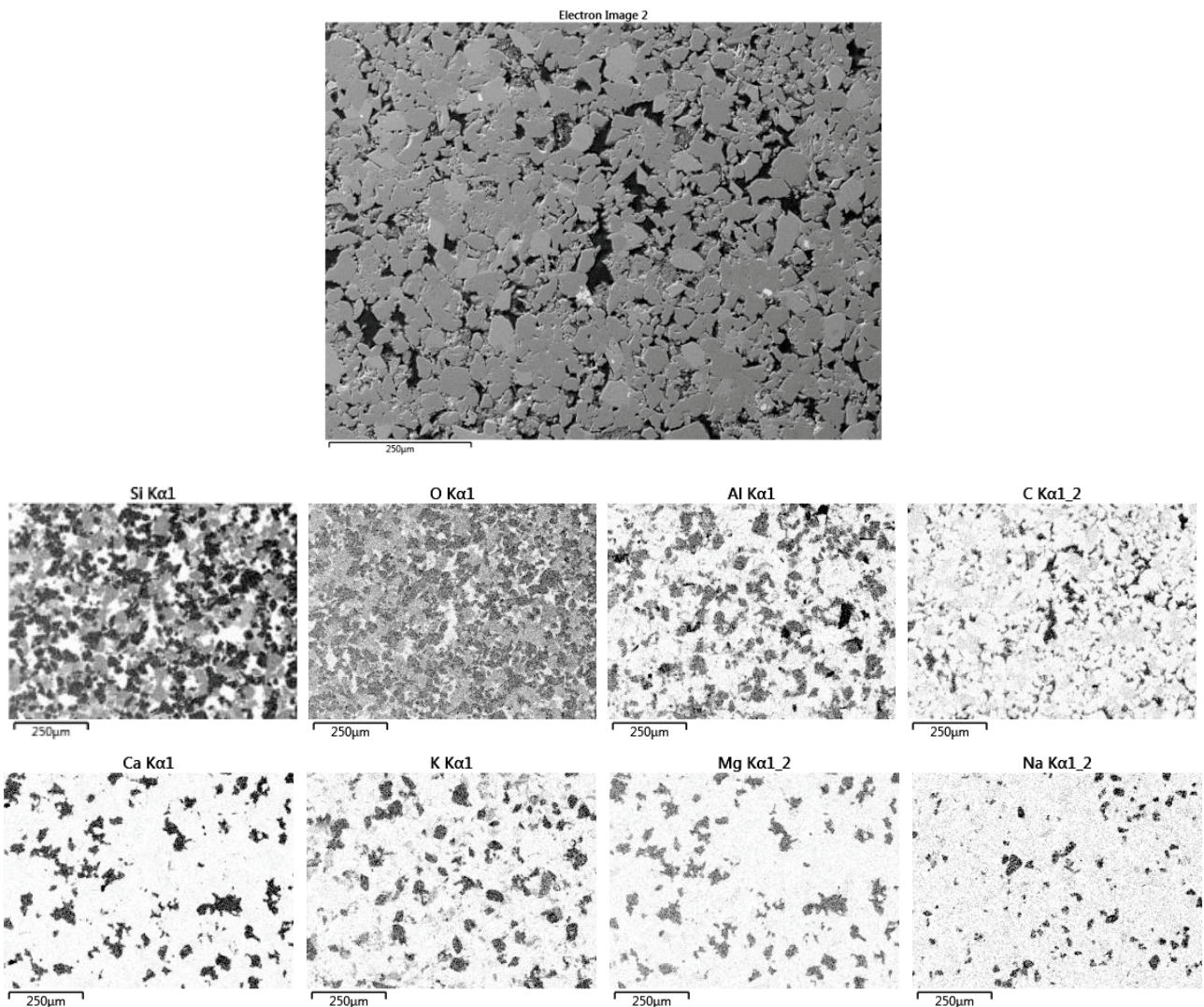
289. Cambiella, Á., et al., *Interfacial properties of oil-in-water emulsions designed to be used as metalworking fluids*. Colloids and Surfaces A: Physicochemical and Engineering Aspects, 2007. **305**(1): p. 112-119.

290. Kronberg, B., K. Holmberg, and B. Lindman, *Surfactant Adsorption at Solid Surfaces* in *Surface Chemistry of Surfactants and Polymers*. 2014, John Wiley & Sons, Ltd. p. 153-173.

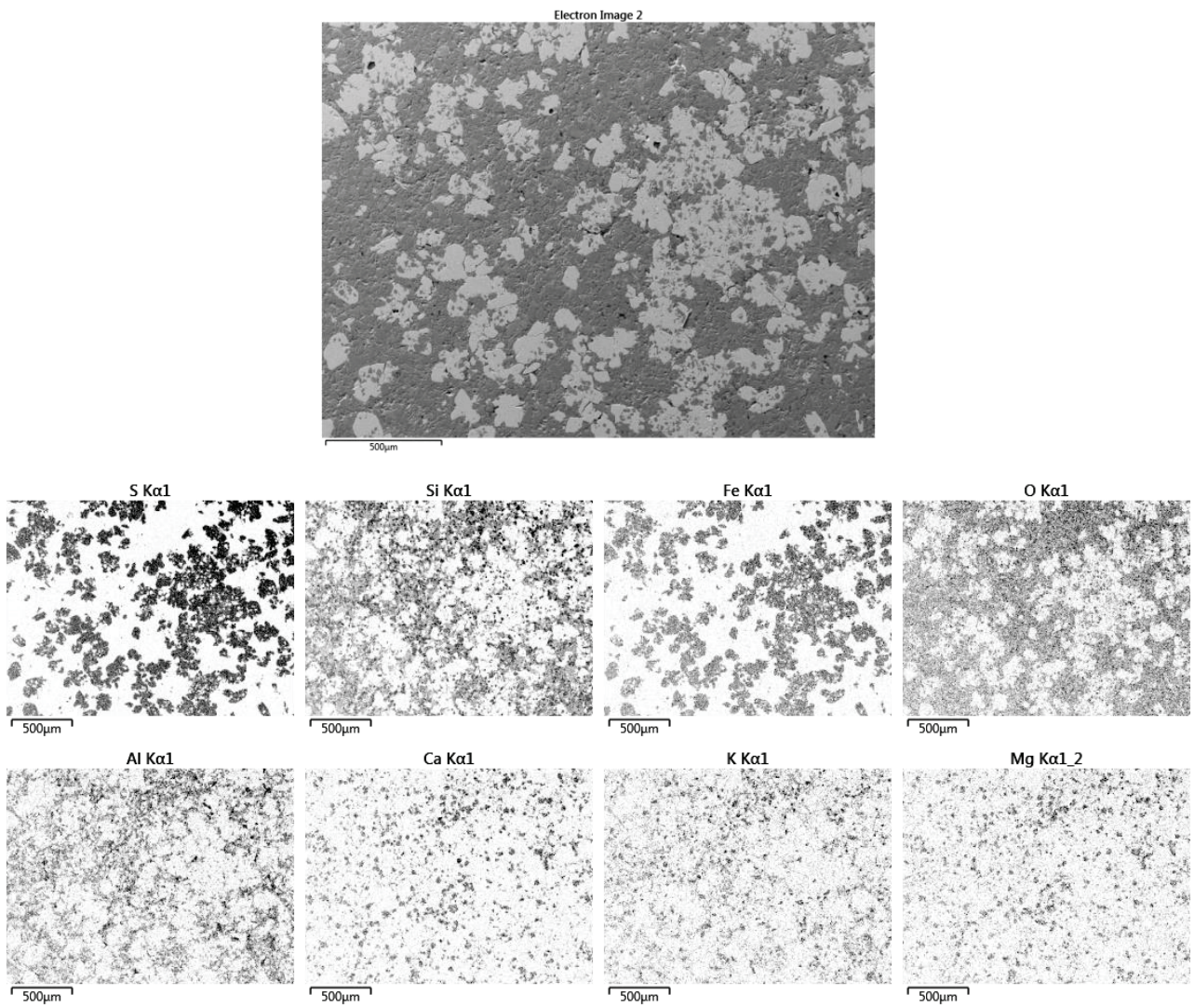
291. Wood, J.M., et al., *Solid bitumen in the Montney Formation: Diagnostic petrographic characteristics and significance for hydrocarbon migration*. *International Journal of Coal Geology*, 2018. **198**: p. 48-62.

Appendix A: SEM Images of Layered Core Plugs

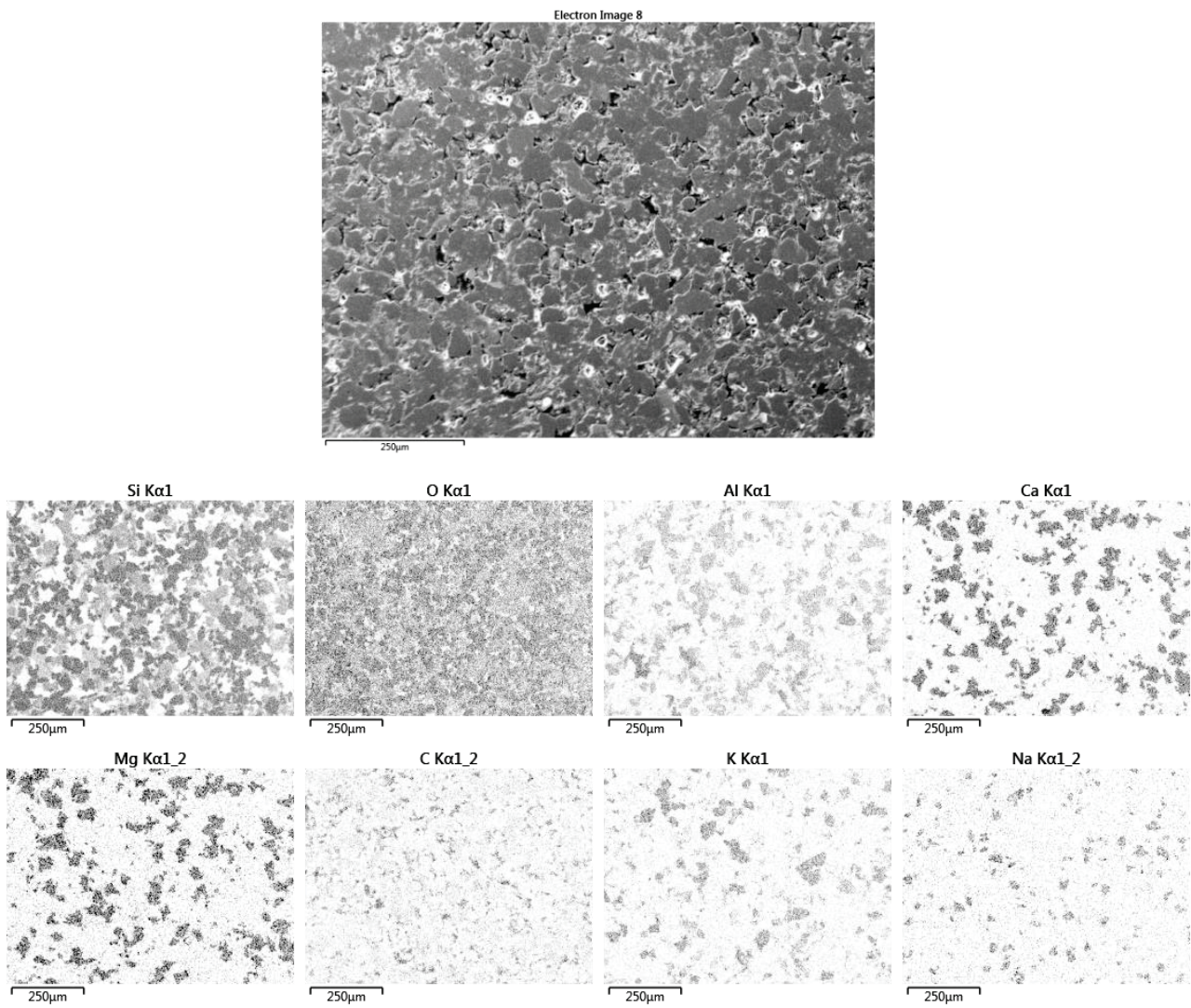
The following figures show the results of SEM/EDS analyses conducted on the three different thick layers shown in **Figure 2.25**.



Appendix A1. SEM/EDS analysis shows that layer 1 is mainly composed of quartz, feldspar, and carbonate grains.

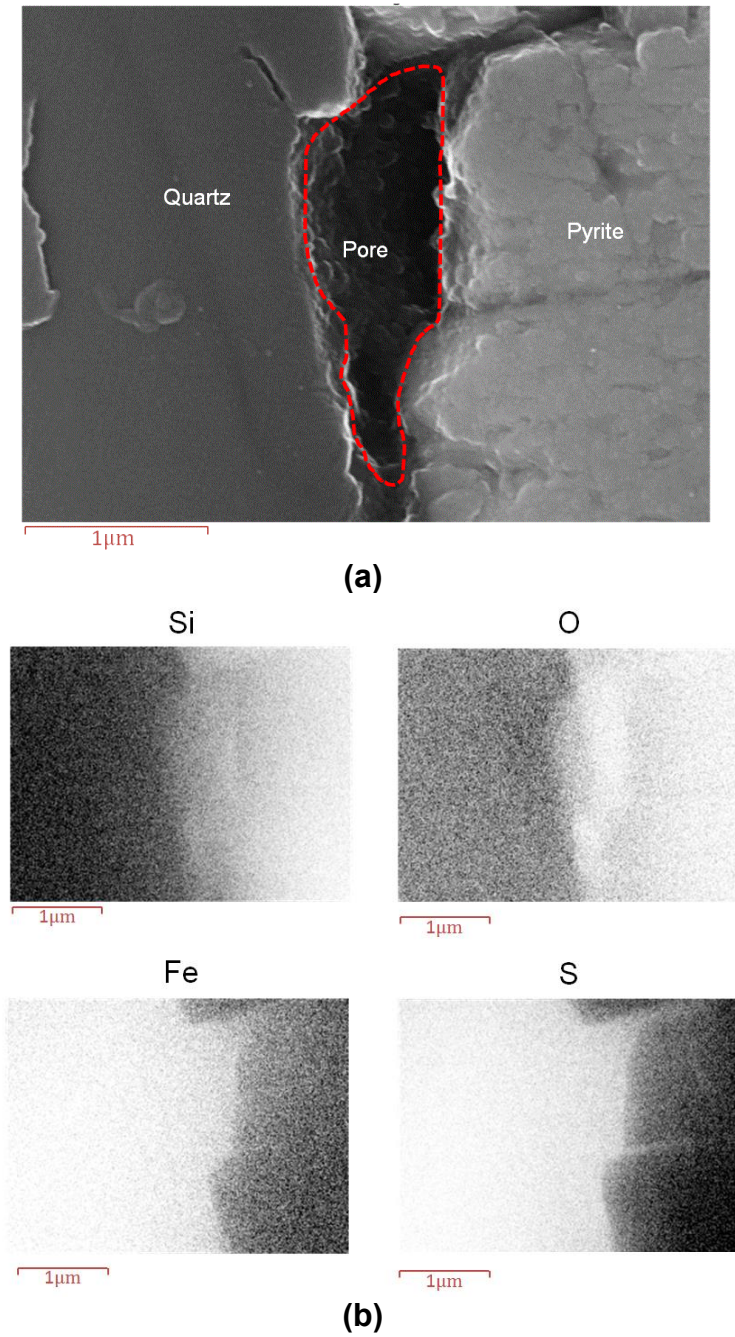


Appendix A2. SEM/EDS analysis shows that layer 2 is mainly composed of pyrite, quartz, and feldspar.

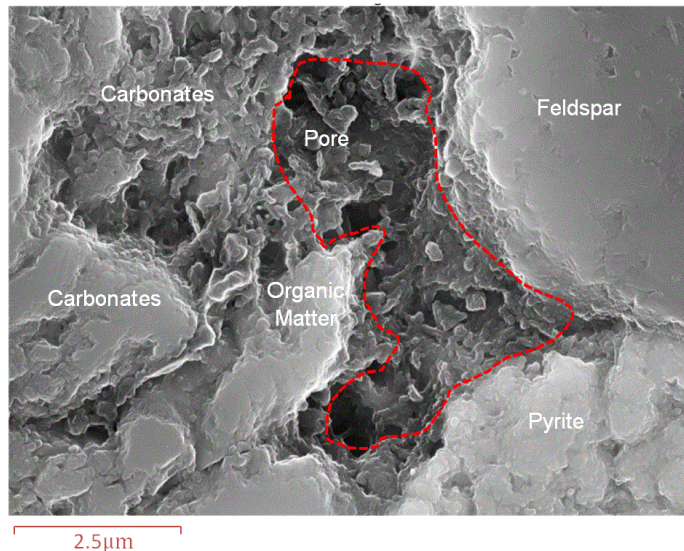


Appendix A3. SEM/EDS analysis shows layer 3 is composed of quartz, feldspar, carbonates, and organic matter.

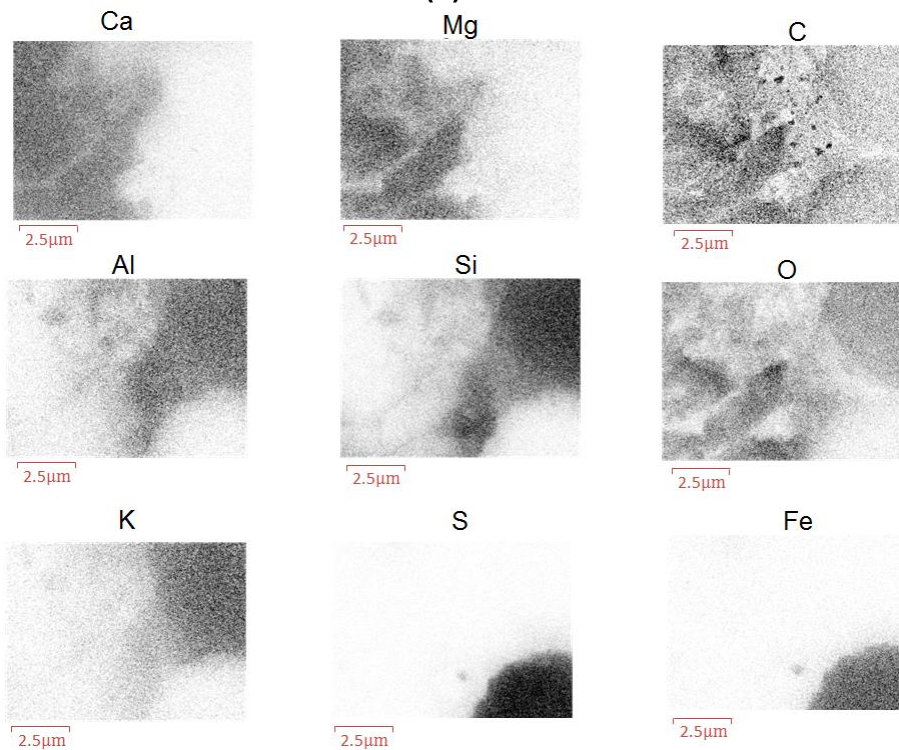
Appendix B: Surface Forces



Appendix B1. (a) SEM image of a multi-mineral pore from core plug 3 (2380.24 m) and (b) its elemental mapping. The concentration of Si and O is high at the left side of the pore while the concentration of Fe and S is high at the right side of the pore. Therefore, the highlighted pore in this figure is surrounded by quartz (left side) and pyrite (FeS_2) (right side).

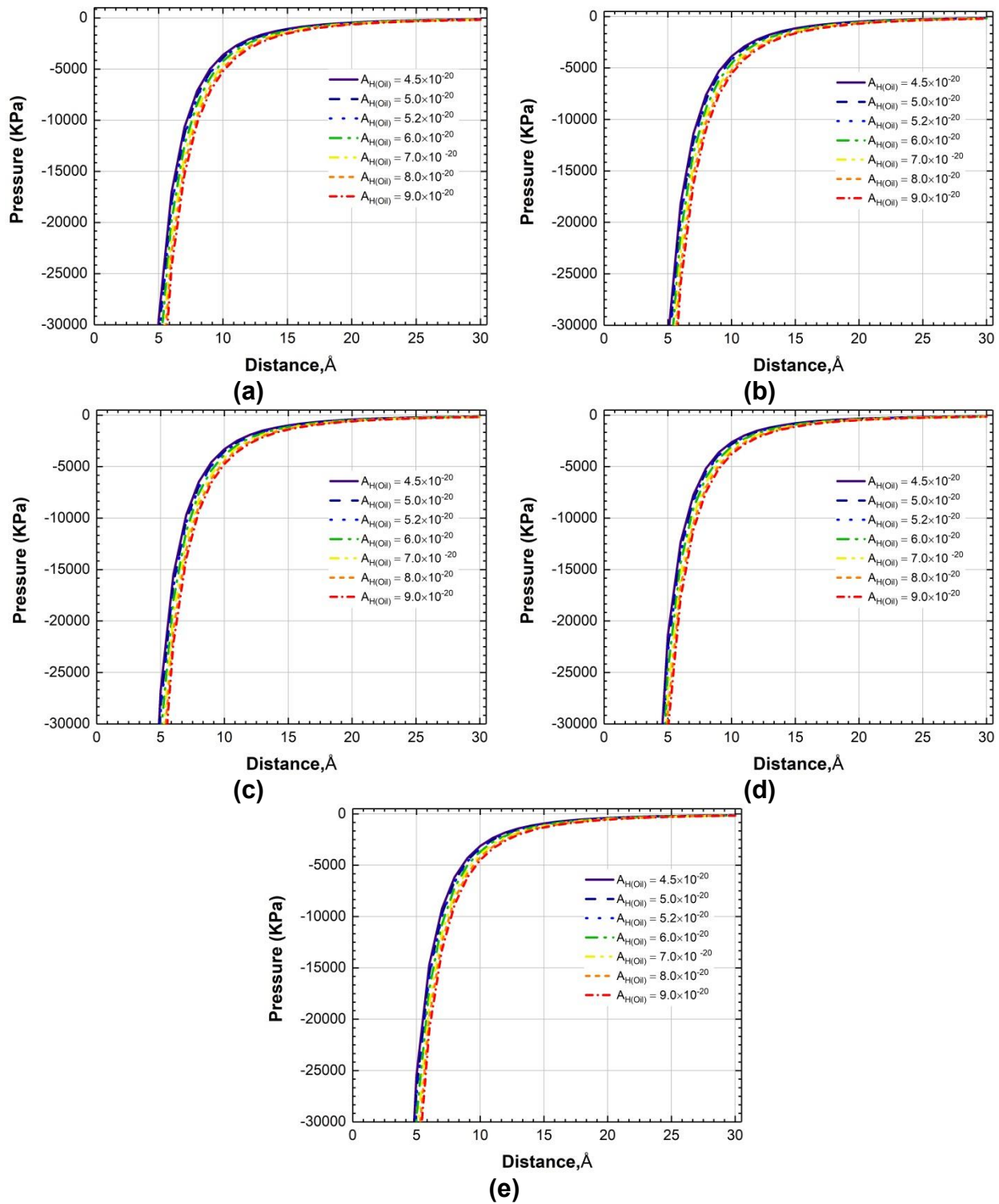


(a)

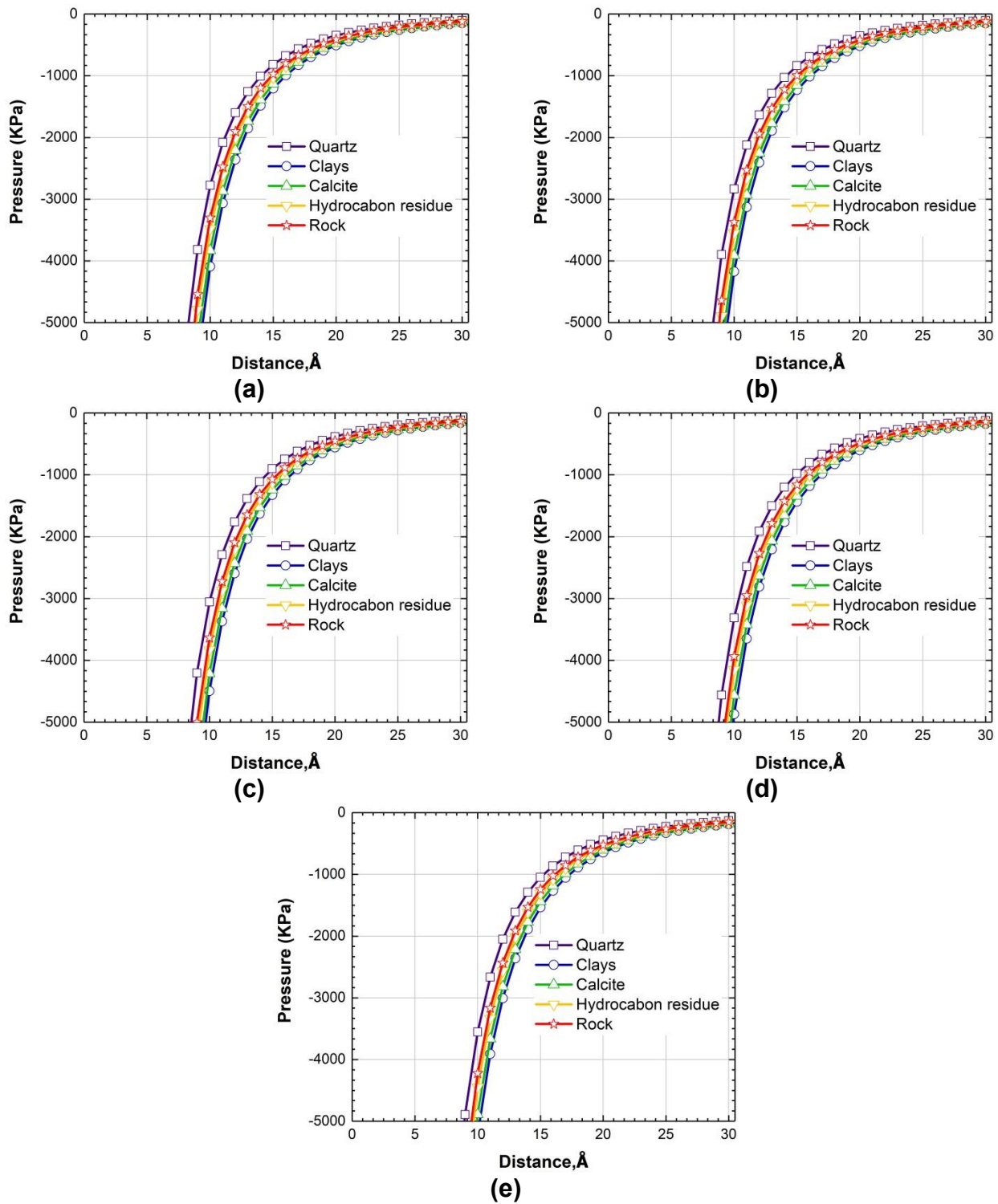


(b)

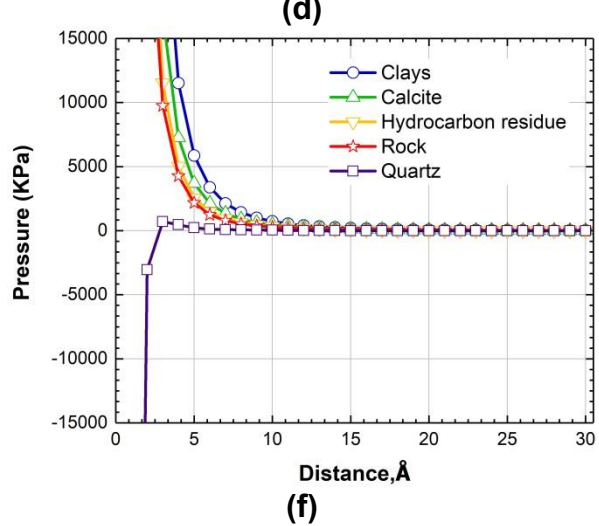
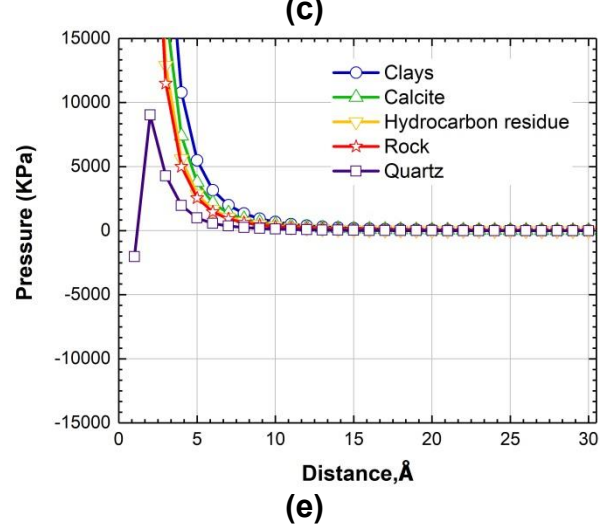
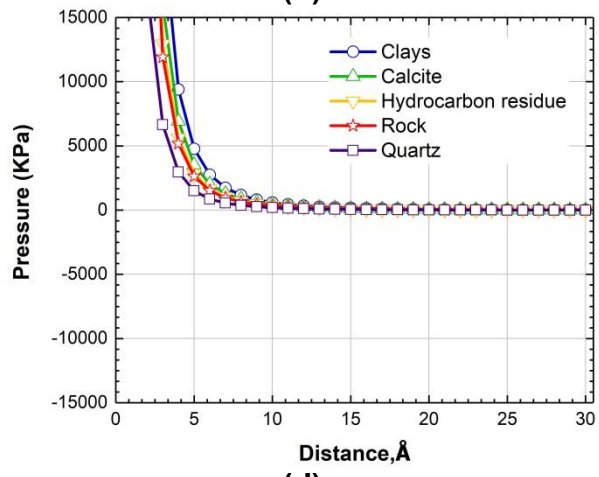
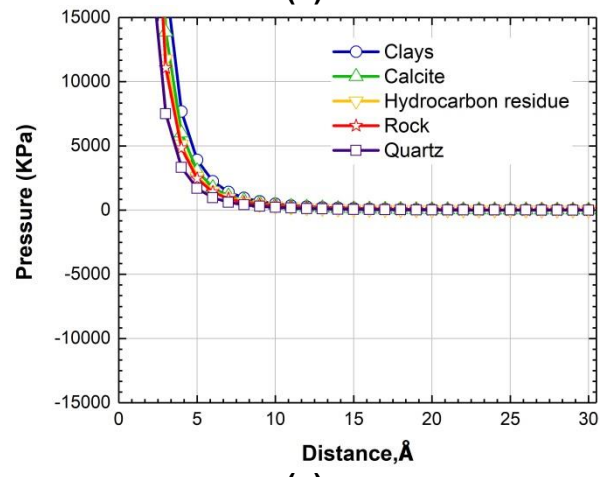
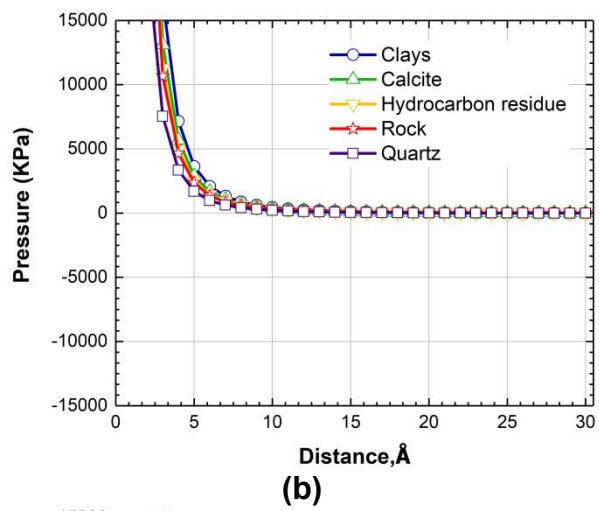
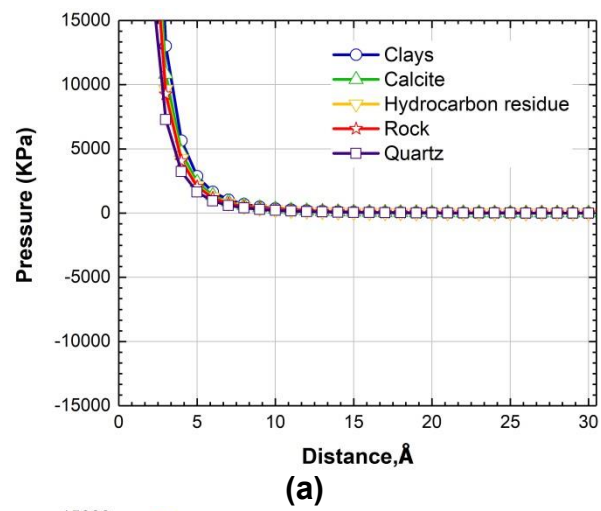
Appendix B2. (a) SEM image of multi-mineral pores from core plug 5 (2393.94 m) and (b) its elemental mapping. Pores are surrounded by carbonates, feldspars and pyrite. The concentration of carbonates in the left side of the figure is high as shown by black color in Ca, Mg, C and O elemental maps. The concentration of feldspars is relatively high in the upper right side of pores as shown by black color in Al, Si, O and K elemental maps. Concentration of pyrite at the lower corner of pores is high as shown by black color in Fe and S elemental maps.

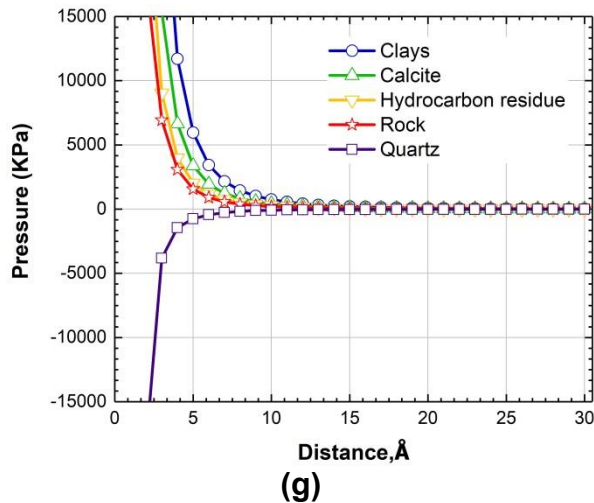


Appendix B3. The total disjoining pressure-distance profiles calculated for (a) calcite, (b) clays, (c) HR, (d) quartz, and (e) the MT rock surface for the solid surface/air/oil system.

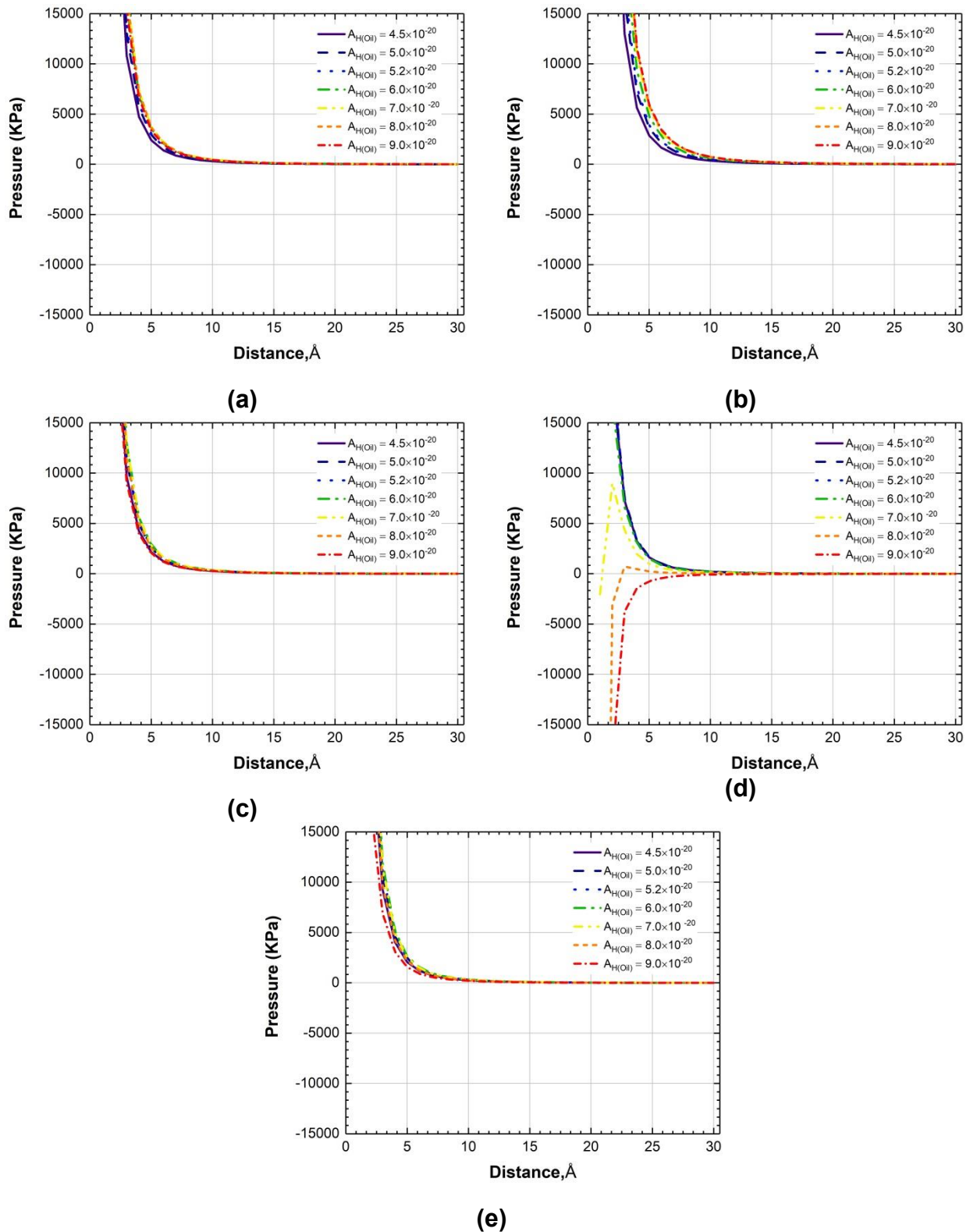


Appendix B4. The total disjoining pressure-distance profiles calculated for the solid surface/air/oil system when (a) $A_{H(oil)} = 5.0 \times 10^{-20} \text{ J}$, (b) $A_{H(oil)} = 5.2 \times 10^{-20} \text{ J}$, (c) $A_{H(oil)} = 6.0 \times 10^{-20} \text{ J}$, (d) $A_{H(oil)} = 7 \times 10^{-20} \text{ J}$, and (e) $A_{H(oil)} = 8 \times 10^{-20} \text{ J}$.

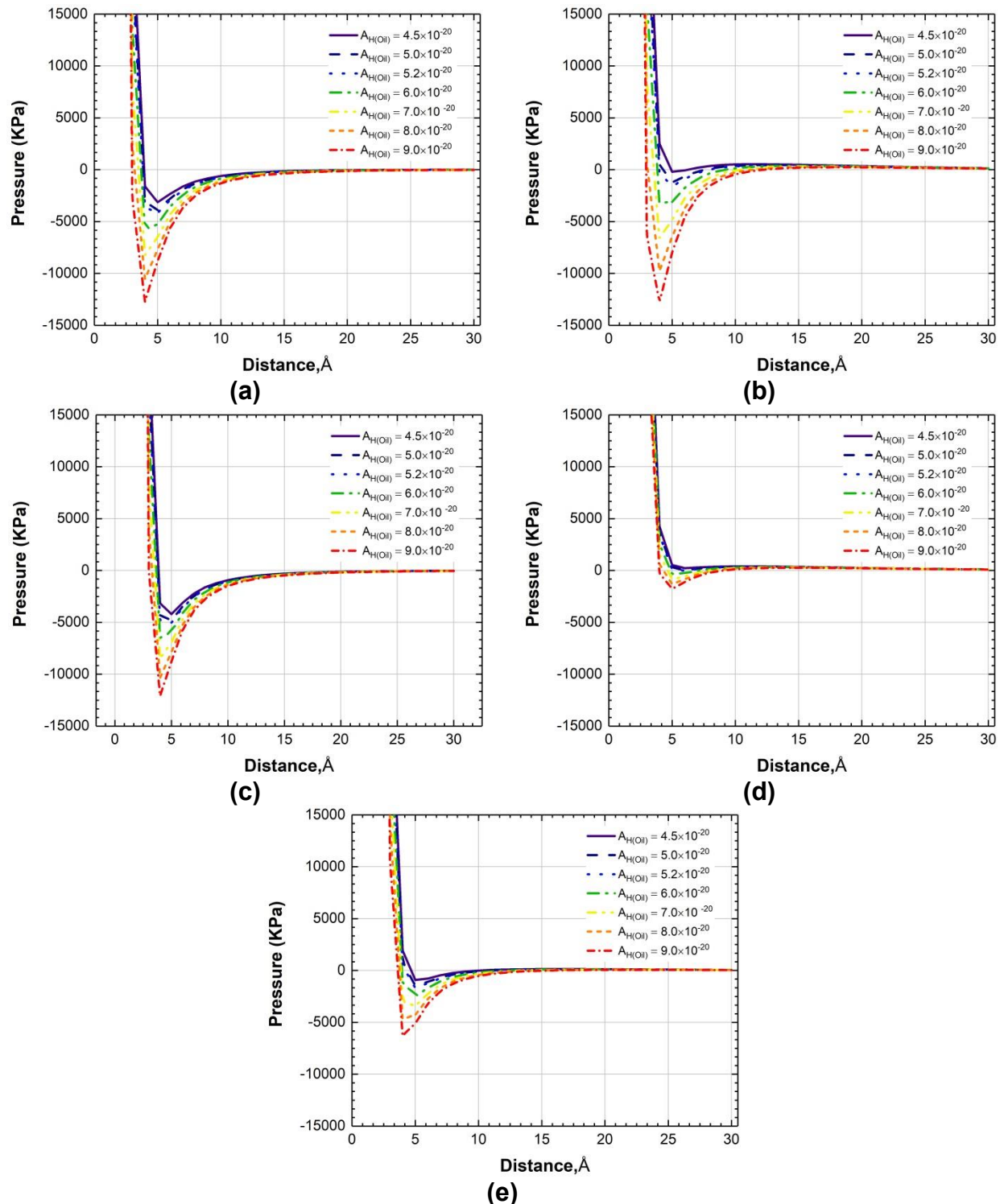




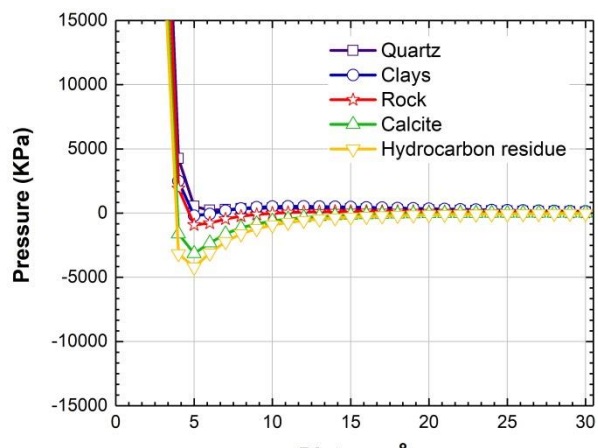
Appendix B5. The total disjoining pressure-distance profiles calculated for the solid surface/oil/water system when (a) $A_{H(oil)} = 4.5 \times 10^{-20} \text{ J}$, (b) $A_{H(oil)} = 5.0 \times 10^{-20} \text{ J}$, (c) $A_{H(oil)} = 5.2 \times 10^{-20} \text{ J}$, (d) $A_{H(oil)} = 6.0 \times 10^{-20} \text{ J}$, (e) $A_{H(oil)} = 7 \times 10^{-20} \text{ J}$, (f) $A_{H(oil)} = 8 \times 10^{-20} \text{ J}$, and (g) $A_{H(oil)} = 9 \times 10^{-20} \text{ J}$.



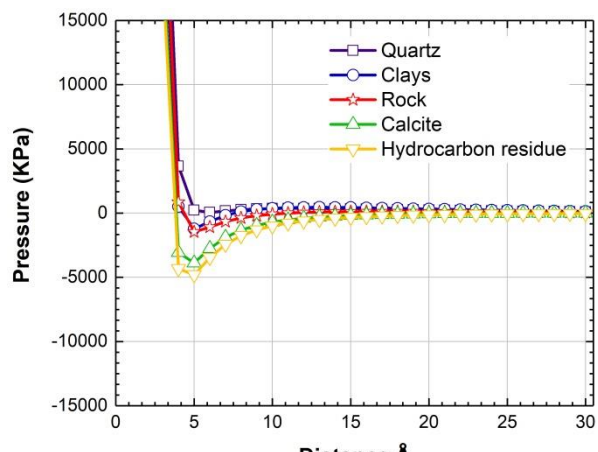
Appendix B6. The total disjoining pressure-distance profiles calculated for pure (a) calcite, (b) clays, (c) HR, (d) quartz, and (e) rock surface for the solid surface/oil/water system.



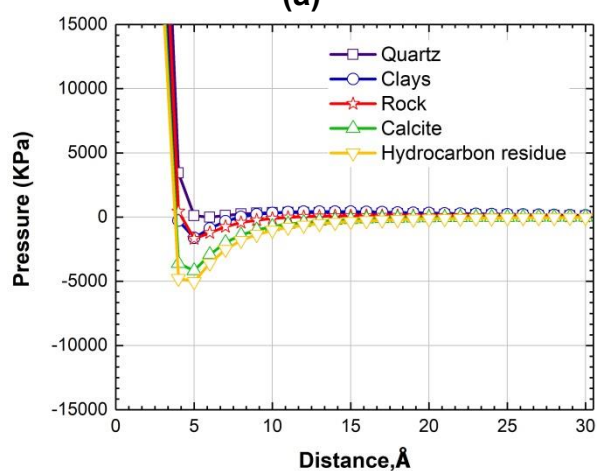
Appendix B7. The total disjoining pressure –distance profiles calculated for pure (a) calcite, (b) clays, (c) HR, (d) quartz, and (e) rock surface for the solid surface/water/oil system.



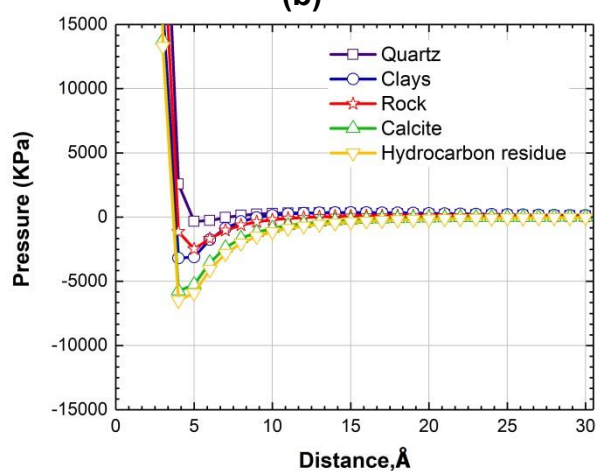
(a)



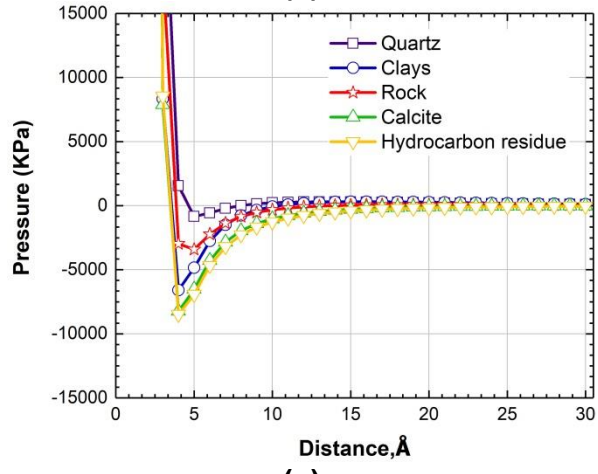
(b)



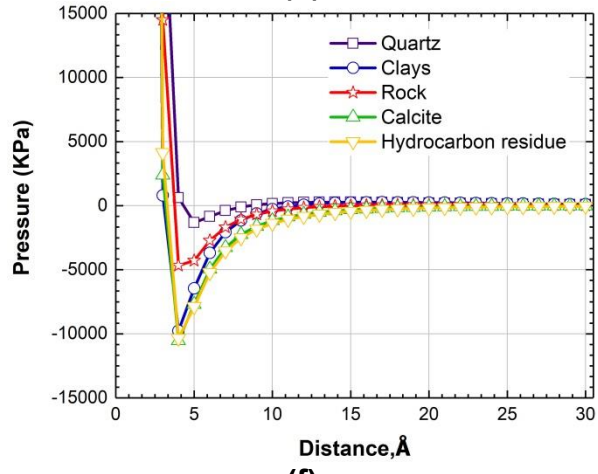
(c)



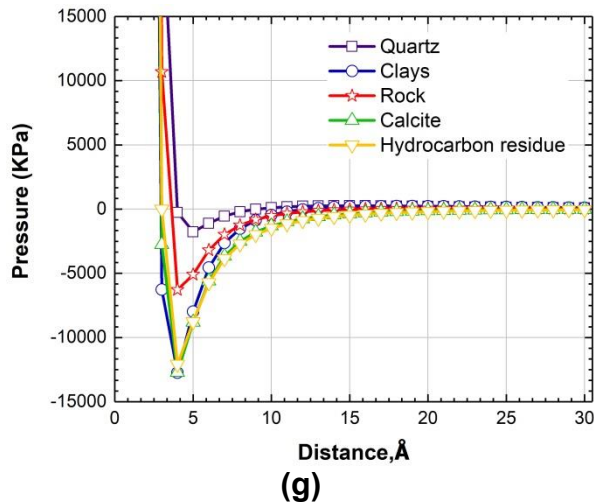
(d)



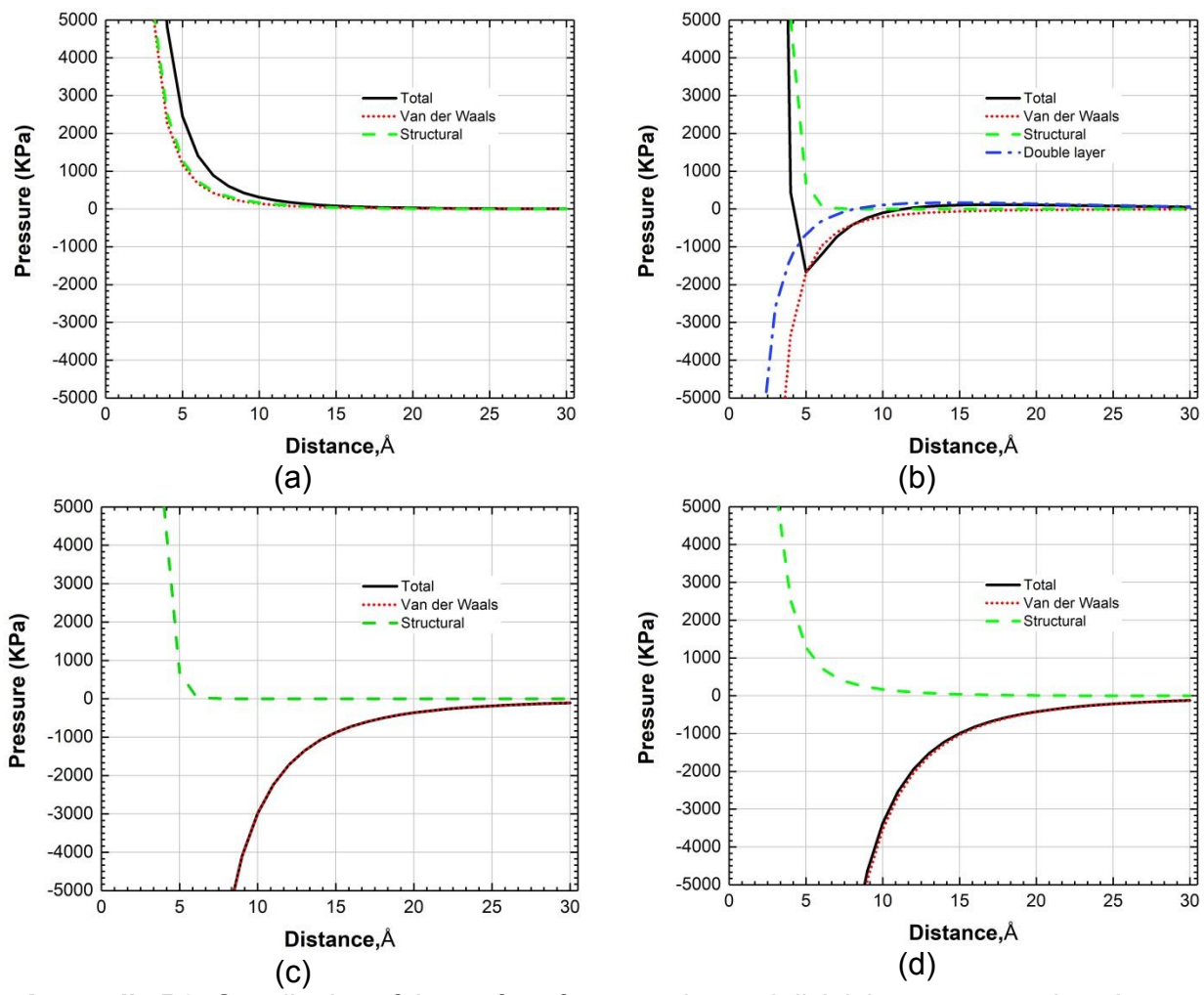
(e)



(f)

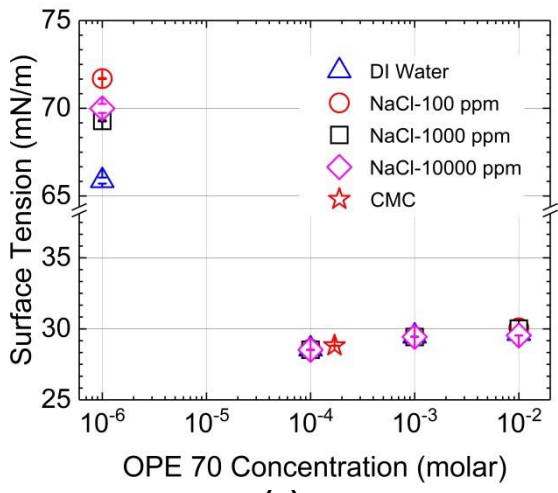


Appendix B8. The total disjoining pressure-distance profiles calculated for (a) $A_{H(\text{oil})} = 4.5 \times 10^{-20}$ J, (b) $A_{H(\text{oil})} = 5.0 \times 10^{-20}$ J, (c) $A_{H(\text{oil})} = 5.2 \times 10^{-20}$ J, (d) $A_{H(\text{oil})} = 6.0 \times 10^{-20}$ J, (e) $A_{H(\text{oil})} = 7 \times 10^{-20}$ J, (f) $A_{H(\text{oil})} = 8 \times 10^{-20}$ J, and (g) $A_{H(\text{oil})} = 9 \times 10^{-20}$ J for the solid surface/water/oil system.

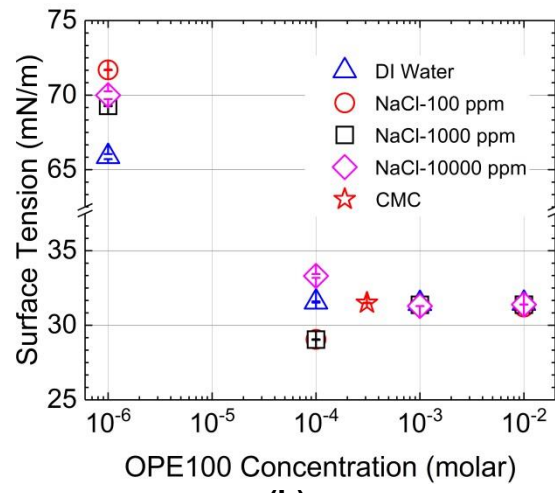


Appendix B9. Contribution of the surface forces to the total disjoining pressure when $A_{H(\text{oil})} = 5.2 \times 10^{-20} \text{ J}$ for (a) the rock surface/air/oil, (b) the rock surface/air/water, (c) the rock surface/oil/water, and (d) the rock surface/water/oil systems.

Appendix C: Surface Tension of Surfactant Solutions

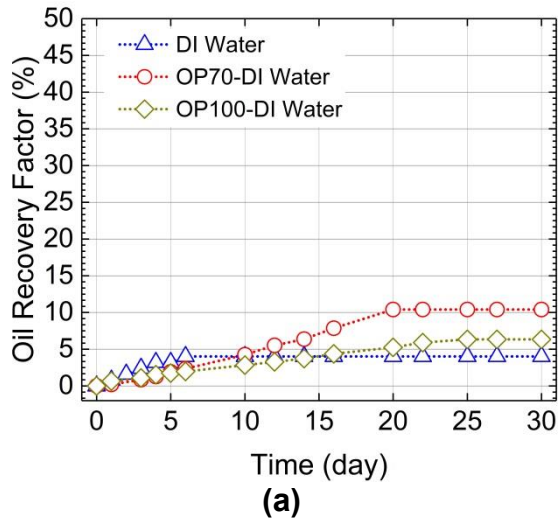


(a)

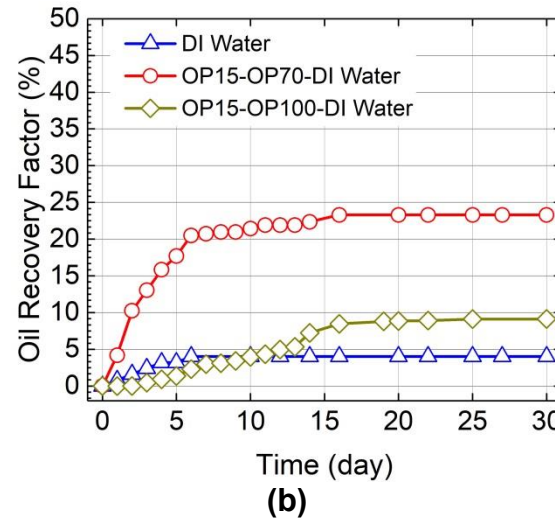


(b)

Appendix C1. Surface tension measured for the surfactant solutions prepared with (a) OPE70 and (b) OPE100.



(a)



(b)

Appendix C2. Oil recovery-time curves for (a) single and (b) mixed surfactant solutions prepared in DI water.